

THE PRECAMBRIAN GEOLOGY OF AN  
AREA BETWEEN MESSINA AND TSHIPISE  
LIMPOPO MOBILE BELT

---

Peter Charles Brammer Horrocks

A Dissertation Submitted to the Faculty of Science,  
University of the Witwatersrand, Johannesburg,  
for the degree of Doctor of Philosophy.

Johannesburg 1981

ABSTRACT

An area of about 200 'sq km has been mapped at a scale of 1 : 25 000 between Messina and Tshipise. Subsequent laboratory work has included petrographic, whole-rock and mineral analysis in order to describe the Precambrian rock-types and lithologies, their structure, and their metamorphic history.

The Precambrian lithologies underlying the study area consist of grey banded basement gneisses of granodioritic composition, together with a large variety of supracrustal rock-types. These include quartzo-feldspathic gneiss, Singelele-type granitoid gneiss, garnet-cordierite-sillimonite gneiss, sapphirine-bearing rock, garnet-orthopyroxene-plagioclase symplectite, pyroxenitic amphibolite, quartzite, banded magnetite quartzite, amphibolite, calc-silicate gneiss and marble. These supracrustal rocks may belong to a geosynclinal-type series of deposited or extruded lithologies. Intrusive rocks of the Messina Layered Intrusion consist of gabbroic and anorthositic gneiss. Metapyroxenites and serpentinites also occur. Both ancient deformed and younger fabric-free mafic dykes transect this stratigraphy.

Polyphase deformation has produced complex and intense folding of the area. Early isoclinal and ductile folds, now manifest as tight intrafolial folds, have been refolded around later structures. Most fold hinges plunge moderately to the

south-west. Considerable flattening, attenuation and along-strike boudinaging of the units occurs in the region, probably as a result of regional simple shear. The asymmetry of the folds in the region suggest that this simple shear was left lateral.

Pearce-type variation diagrams for data from the Messina Layered Intrusion show plagioclase fractionation trends, and support the argument that these rocks are of plutonic igneous origin. The anorthosites were the earliest cumulates, with the gabbros forming by subsequent fractionation. Rayleigh's law indicates that about 70 per cent fractionation has occurred in these rocks. The parental liquid appears to have been anomalously enriched in rubidium.

The supracrustal units have experienced a high-grade metamorphism between about 3 100 m.y. ago and 2 400 m.y. ago. The P-T conditions for this metamorphism range from about 9 kbar and 900°C at the 'peak' of the metamorphism, to about 4 kbar and 650°C, and thus represents a retrogression within the field of medium pressure granulites. Earlier high-pressure granulite metamorphism is indicated by assemblages reported from other regions in the Central Zone of the Limpopo Mobile Belt. These data suggest that the supracrustal rocks were subjected to burial into regions of the lower crust up to 40 km depth, and geothermal gradients between 15°C/km and 35°C/km were experienced. Water

activities were low during this high-grade metamorphism, with water making up not more than 10 per cent of the fluid present during this event. The onset of relative tectonic stability and the end of high-grade metamorphism was achieved by about 2 200 m.y. ago.



I declare that this thesis is my own, unaided work.

It is being submitted for the degree of Doctor of Philosophy  
in the University of the Witwatersrand, Johannesburg. It  
has not been submitted before for any degree or examination  
in any other University.

*[Handwritten signature]*

---

23<sup>rd</sup> day of OCTOBER 1981.

ACKNOWLEDGEMENTS

T.N. Clifford is thanked for supervising this project and for providing continuous encouragement and support. Sponsorship of this study by the Council for Scientific and Industrial Research as part of the South African contribution to the International Geodynamics Project is gratefully acknowledged.

Numerous colleagues provided encouragement, support, help, constructive discussion and criticism to whom the author is indebted. These include M.A.G. Andreoli, J.M. Barton, G. Davies, M.J. De Wit, R.E.P. Fripp, C. Guerin, M.J. Hudson, G.J.M. Kitching, P.A. Killy, J. Lilly, K. Lilly, M.S. McCarthy, T.S. McCarthy, J.R. McIver, N. McLean, M.A. Miles, P. Richardson, R. Rickard, M. Taylor and M.K. Watkeys.

Special thanks are due to W. Schreyer, J.G. Ramsay, A.B. Thompson, D.J. Ellis and C. Simpson for their support and advice during part of the time while this study was in preparation.

The Messina (Transvaal) Development Company, and in particular members of its Geology Department at Messina are thanked for their logistic support during the periods of field work for this study in 1975 - 1977.

Mrs Elaine Towsey is also thanked for typing the thesis.

CONTENTS

ABSTRACT	..	..	..	..	..	..	(ii)
DECLARATION	..	..	..	..	..	..	(v)
ACKNOWLEDGEMENTS	..	..	..	..	..	..	(vi)
CHAPTER 1: INTRODUCTION	..	..	..	..	..	..	1
Regional setting of the Limpopo Mobile Belt	..	..	..	..	..	..	1
The geology of the Central Zone in the Messina area	..	..	..	..	..	..	3
Geochronological review	..	..	..	..	..	..	8
Statement of purpose and work done	..	..	..	..	..	..	12
Previous work in the area studied	..	..	..	..	..	..	14
CHAPTER 2: ROCK TYPES AND LITHOLOGIES	..	..	..	..	..	..	18
Introduction	..	..	..	..	..	..	18
Basement gneisses	..	..	..	..	..	..	18
Quartzo-feldspathic gneisses	..	..	..	..	..	..	22
Singelele-type granitoid gneiss	..	..	..	..	..	..	26
Garnet-cordierite-sillimanite gneiss and varieties	..	..	..	..	..	..	28
Pyroxene amphibolite	..	..	..	..	..	..	41
Quartzite and banded magnetite quartzite	..	..	..	..	..	..	48
Calc-silicate gneiss and marble	..	..	..	..	..	..	56
Metapyroxenite and serpentinite	..	..	..	..	..	..	57
Gabbroic and anorthositic gneisses of the Messina Layered Intrusion	..	..	..	..	..	..	63
Discussion	..	..	..	..	..	..	68
CHAPTER 3: STRUCTURE	..	..	..	..	..	..	76
Introduction	..	..	..	..	..	..	76
Large scale structure	..	..	..	..	..	..	76
Small scale structures	..	..	..	..	..	..	87
Faults	..	..	..	..	..	..	95
Discussion	..	..	..	..	..	..	96

CHAPTER 4: THE MESSINA LAYERED INTRUSION	..	..	..	..	103
Introduction	..	..	..	..	103
Geological setting	..	..	..	..	104
Compositional variation of a unit sampled on Shangani					105
Pearce diagrams	..	..	..	..	109
Rb, Sr and K <sub>2</sub> O relationships	..	..	..	..	117
Discussion	..	..	..	..	122
CHAPTER 5: METAMORPHISM	..	..	..	..	124
Introduction	..	..	..	..	124
Solubility of aluminium in orthopyroxene	..	..	..	..	124
Aluminium and titanium in hornblende	..	..	..	..	126
Parameters of metamorphism	..	..	..	..	128
Garnet-cordierite-sillimanite gneiss	..	..	..	..	131
Sapphirine-bearing rocks	..	..	..	..	136
Garnet-orthopyroxene-plagioclase symplectite	..	..	..	..	146
Garnet zonation in the pelitic rock-types	..	..	..	..	154
Pyroxenitic amphibolites	..	..	..	..	173
Intrusive rocks	..	..	..	..	182
Water activity	..	..	..	..	184
The P-T field - a synthesis	..	..	..	..	187
CHAPTER 6: CONCLUSIONS	..	..	..	..	195
APPENDIX 1: ANALYTICAL TECHNIQUES	..	..	..	..	1.1
Whole-rock analysis	..	..	..	..	1.1
Electron probe microanalysis	..	..	..	..	1.1
APPENDIX 2: ELECTRON PROBE ANALYTICAL DATA	..	..	..	..	2.1
Introduction	..	..	..	..	2.1
Feldspar	..	..	..	..	2.2
Mica	..	..	..	..	2.3

Amphibole	..	..	..	..	..	2.3
Pyroxene ...	..	..	..	..	..	2.4
Garnet ..	..	..	..	..	..	2.6
Cordierite	..	..	..	..	..	2.7
Sapphirine	..	..	..	..	..	2.7
Spinel ..	..	..	..	..	..	2.9
Outline chart	..	..	..	..	..	2.9
TABLES 2.1 - 2.23	..	..	..	..	..	2.10
APPENDIX 3: METAMORPHIC PARAMETERS	..	..	..	..	..	3.1
Introduction	..	..	..	..	..	3.1
Orthopyroxene-clinopyroxene thermometry	..	..	..	..	..	3.1
Garnet-orthopyroxene barometry and thermometry	..	..	..	..	..	3.7
Garnet-clinopyroxene thermometry	..	..	..	..	..	3.10
Biotite-garnet thermometry	..	..	..	..	..	3.16
Garnet-cordierite thermometry and barometry	..	..	..	..	..	3.20
Two-feldspar thermometry	..	..	..	..	..	3.28
Coexisting plagioclase - clinopyroxene - quartz	..	..	..	..	..	3.30
Water activity	..	..	..	..	..	3.39

## REFERENCES

## MAPS IN REAR POCKET

- 1       Field Map (1 : 25 000)
- 2       Interpretation and Sample Localities (1 : 50 000)

## CHAPTER 1: INTRODUCTION

### Regional setting of the Limpopo Mobile Belt

The Limpopo Mobile Belt is an approximately linear ENE trending region underlain by Precambrian rocks which have undergone high-grade regional metamorphism and intense polyphase deformation (MacGregor, 1953). The main rock-types found within the belt include a variety of basement gneisses, porphyritic gneisses, granitoid gneisses, gabbroic and anorthositic gneisses, and supracrustal paragneisses.

The belt is situated between the Rhodesian Croton in the north and the Kaapvaal Croton in the south (Figure 1), and is approximately 500 km in length and 250 km in width. The belt is overlain in the east by younger Umkondo and Karoo strata, and by the 500 - 1 100 m.y. north-south trending Mocambique Belt (Clifford, 1970). In the west, it is also overlain by younger Proterozoic and Karoo strata and Tertiary sands in Botswana, although some workers consider the belt to terminate in this region (Key and Hutton, 1976). In this thesis, the northern margin of the belt is defined by an orthopyroxene isograd, marking the first appearance of granulite facies rocks in a southwards direction into the belt (Robertson, 1968 and 1973; see also Rhodesia Geological 1 : 1 000 000 Map Seventh Edition, 1977). Similarly, the southern margin of the belt has been defined by an orthopyroxene isograd caused by a northward

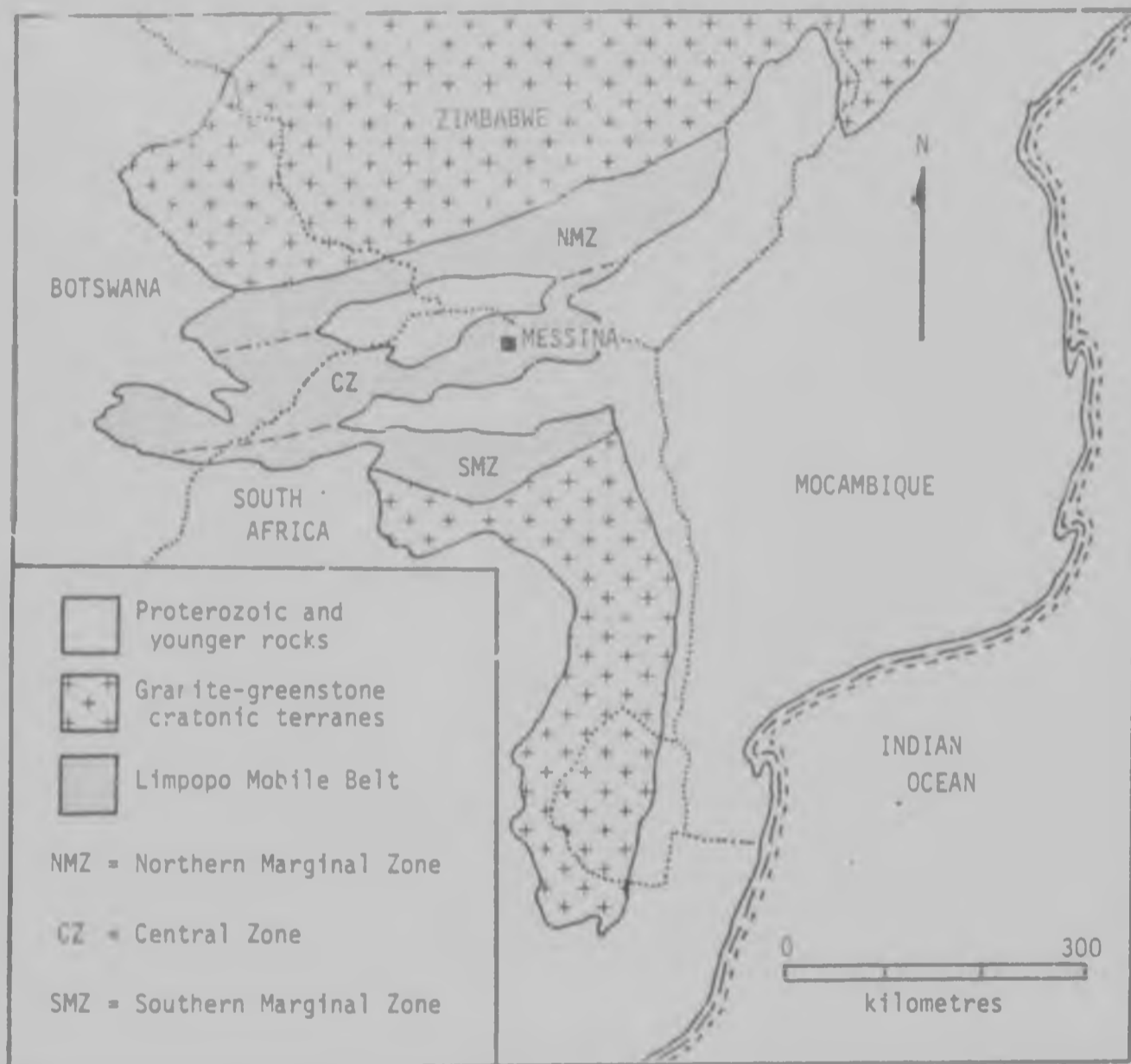


Figure 1: A simplified geological map of part of southern Africa showing the location of Messina and the Limpopo Mobile Belt (after Horrocks, 1980).

crease in metamorphism of the Kaapvaal Craton into the belt (Du Toit and Van Keenan, 1977).

A distinct zonation has been recognized within the belt (Figure 1) where Northern and Southern Marginal Zones between 500 and 100 km in width are separated by a Central Zone between 100 and 150 km in width. Major zones of shearing and transcurrent dislocation form their boundaries. The northern margin of the belt is characterized by fault zones and shear zones which are sub-parallel to the length of the belt, and which separate the Limpopo gneisses from the granite-greenstone terrane of the Rhodesian Craton in the north. The fault and shear zones are steeply dipping and mylonitic, with horizontal displacements of up to 40 km (Coward, 1976; Coward *et al.* 1976). The southern margin of the belt is somewhat obscured by the fault-bounded Proterozoic sediments and volcanics of the Soutpansberg Group (Jansen, 1975, 1976 and 1977; Barker, 1976). However, no fundamental structural or stratigraphic breaks have been recognized between the belt and the Kaapvaal Craton, since the earliest deformations were regional horizontal compressions affecting both the belt and the Kaapvaal Craton (Graham, 1974; Coward *et al.* 1976).

#### The geology of the Central Zone in the Messina area

The Central Zone contains complexly infolded supracrustal, porphyritic and granitoid gneisses, some of which are regarded



as representing a basement (Bahnemann, 1972; Fripp, 1981a, b, c). This zone has been sub-divided into three regions in the Messina area (Figure 2) namely, the Bulai Belt, the Cross-Folded Belt and the Linear Belt. The Bulai Belt occurs north-west of Messina and is underlain by the porphyritic Bulai Gneiss and in places, a grey banded gneiss which has been regarded as a basement from which the Bulai Gneiss may have been remobilized (Bahnemann, 1972). Other charnockitic, enderbitic and various paragneisses also occur (Watkeys, 1979). South-east of the Bulai Belt in the vicinity of Messina, complexly folded layers of the supracrustal paragneisses are infolded together with these 'basement' rocks and other orthogneisses to make up the Cross-Folded Belt (Bahnemann, 1972). Further to the south-east, the Linear Belt occurs, and contains essentially similar lithologies as the Cross-Folded Belt, but here the strata are markedly attenuated and deformed to trend in the regionally pervasive ENE direction (Bahnemann, 1972).

The basement gneisses, termed the Sand River Gneisses, comprise a variety of banded gneisses of charnockitic, enderbitic, monzonitic, tonalitic and granodioritic compositions, and contain little or no garnet. These rocks occur over a wide region in the central part of the Limpopo Mobile Belt, particularly west and north-west of Messina and Beit Bridge

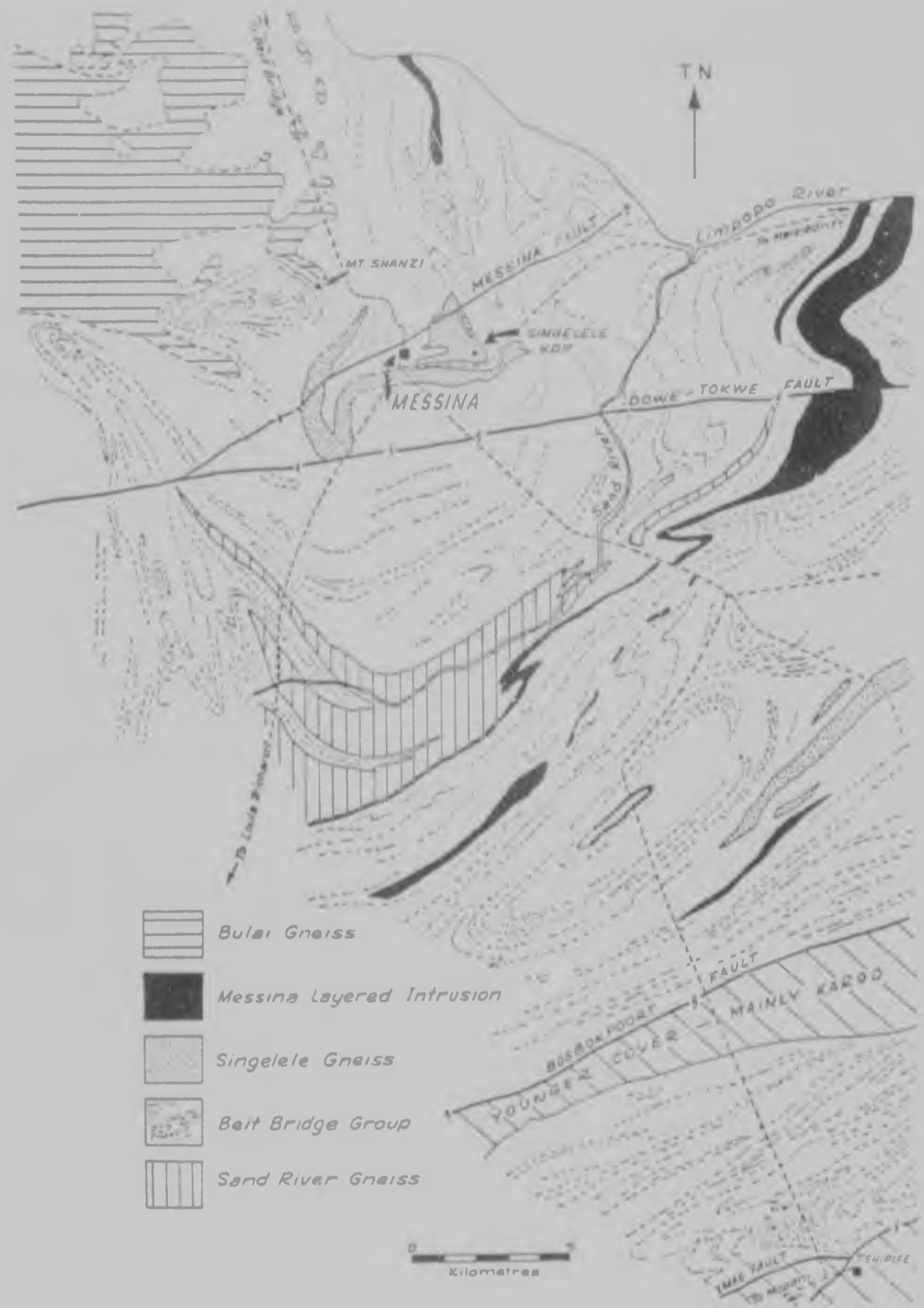


Figure 2: A simplified geological map of the area between Messina and Tsh'ise in the Central Zone of the Limpopo Mobile Belt (after Horrocks, 1981).

(Bahnmann, 1972; Watkeys, 1977; Light et al., 1977; Light and Watkeys, 1978; Watkeys, 1979). In the vicinity of the Sand River (Figure 2), the Sand River Gneisses are infolded with the supracrustal gneisses (Fripp, 1981a, 1981b, and 1981c). Here they occur as hypersthene bearing granodiorite and quartz diorite gneisses and are characterized by cross-cutting ancient deformed tholeiitic dykes.

The porphyritic Bulai Gneiss also occurs over a large area west and north-west of Messina (Figure 2) and is characterized by large phenocrysts of alkali feldspar. These gneisses commonly occur at the interface between basement and supracrustal gneisses, and have been considered to be remobilized from the basement, and to be intrusive and batholithic in form (Bahnmann, 1972). In places, a strong tectonic fabric is developed by the alignment of the phenocrysts and other mineral grains, and the rock commonly contains inclusions of supracrustal and dyke-like rocks.

The supracrustal rocks are essentially paragneisses and commonly contain garnet. They include a large variety of mainly quartzo-feldspathic gneisses which contain varying proportions of amphibole, mica, pyroxene, garnet, cordierite and sillimanite. Also, quartzite, banded magnetite quartzite, pyroxenitic amphibolite, calc-silicate gneiss and marble occur. The carbonate and calc-silicate rocks became distinctly more

abundant towards Tshipise, about 30 km south-east of Messina (Figure 2). These paragneisses underlie large areas south and east of Messina (Figure 2) within the Cross-Folded and Linear Belts, and have been known as the Messina Formation (Söhnge, 1946; Söhnge et al., 1948) although basement *sensu stricto* was not distinguished. Revised stratigraphic nomenclature has been proposed (Geological Survey of South Africa, in preparation) where the basement lithologies are grouped under the term Sand River Gneisses, and the supracrustal lithologies are grouped together as the Beit Bridge Complex.

The Singelele Gneiss (Söhnge, 1946; Bahnemann, 1972 and 1973; Fripp et al., 1979) is a concordant granitoid gneiss which forms prominent outcrops immediately south-east of Messina (Figure 2). The rock is silica-rich with ribbon-like grains and aggregates of quartz parallel to the tectonic fabric. It weathers to a distinctive reddish colour, and is pre-tectonic in age being affected by all the deformations recognized in the supracrustal rocks (Fripp et al., 1979). Some workers regard this lithology as remobilized at least in part from the other supracrustal rock-types and to be intrusive in nature (Bahnemann, 1972 and 1973) while others consider the rock to be a conformable and integral part of the supracrustal stratigraphy (Fripp et al., 1979).

Layered anorthositic and gabbroic gneisses occur as

generally conformable sill-like intrusives throughout the Central Zone (Barton et al., 1979a). They are phase-layered, and in places contain thin discontinuous units of chromitite and titaniferous magnetitite (Söhne, 1946). Most workers agree that these lithologies are derived by plutonic igneous processes, though some consider that at least in part they may have been derived from metamorphosed calcareous sediments (Bahnemann, 1970). Relict cumulate textures and phase and graded layering are common features of these rocks (Hor et al., 1975; Barton et al., 1979a) while units of metapyroxenite and serpentinite, although not always spatially associated with the anorthositic rocks, may belong in the same suite. These rocks have been collectively grouped under the term Messina Layered Intrusion (Barton et al., 1979a).

Pre- and post-tectonic dykes of tholeiitic compositions are common throughout the region. Pre-tectonic dykes are characterized by mineral fabrics and metamorphic reaction margins with their host rocks, while post-tectonic dykes are fabric-free. Several ages of dyke intrusion are recognized (Barton et al. 1977; Barton, 1979; Barton et al., 1981).

#### Geochronological review

Analytical isotopic work in the region has enabled a geochronological framework to be suggested for the Precambrian history of the Messina area (Barton and Ryan, 1977). The

techniques utilize Rb, Sr and Pb whole-rock isotope systematics and U-Pb zircon methods, and in the Rb-Sr ages, a  $^{87}\text{Rb}$  decay constant of  $1.42 \times 10^{-11} \text{ yr}^{-1}$  has been used. All dates published which use other decay constant have been recalculated for consistency. The relevant age determinations discussed here are summarized in Table 1.

The Sand River Gneisses ('basement') have yielded a Rb-Sr whole-rock age of  $3786 \pm 61$  m.y. with an initial  $^{87}\text{Sr}/^{86}\text{Sr}$  ratio of  $0.70122 \pm 0.00016$  (all errors are two standard deviations) which has been interpreted as reflecting a homogenization of the Sr isotopes during a metamorphism (Barton et al., 1978). Thus, this age which is probably associated with a tectonic fabric (Fripp, 1981a, 1981b, 1981c) defines the oldest rocks to occur in the Central Zone of the Limpopo Mobile Belt, and as such, they may be compared to the Isua supracrustal rocks and the Amitsoq gneisses in Greenland (Bridgewater et al., 1976).

Two suites of ancient deformed tholeiitic dyke intrusion have been recognized in the region (Barton et al., 1977). The oldest of these has been dated at about 3570 m.y. by the Rb-Sr whole-rock isochron method, and these dykes have only been recognized to intrude the Sand River Gneisses. The younger suite of dykes has given an age of about 3060 m.y. by the Rb-Sr whole-rock isochron method and these dykes are

Table 1: Summary of geochronological events in the Messina area of the Limpopo Mobile Belt

Age m.y.	Isotope System	Interpretation
2200	Rb-Sr	Dolerite dyke intrusion - end of high-grade metamorphism and the onset of relative tectonic stability.
2430	Pb-Pb	Metamorphism of Singelele Gneiss on the Farm Ostend southeast of Messina.
2460	Rb-Sr	As above.
2600	Rb-Sr	Metamorphism of the Singelele Gneiss at the type area near Messina.
3060	Rb-Sr	Suite of ancient deformed tholeiitic dykes which intrude the Sand River Gneisses, the Beit Bridge Complex and the Messina Layered Intrusion.
3150	Rb-Sr	Metamorphism of the Messina Layered Intrusion - probable peak of the high grade metamorphism.
3270	Pb-Pb	Probable age of the emplacement of the Messina Layered Intrusion.
-	-	Deposition and/or extrusion of the supracrustal rocks of the Beit Bridge Complex between 3570 and 3270 m.y. ago.
3570	Rb-Sr	Suite of ancient deformed tholeiitic dykes which intrude the Sand River Gneisses only.
3790	Rb-Sr	Metamorphism of the Sand River Gneisses.
?	-	Formation of the Sand River Gneisses.

- 1: All ages are derived from whole-rock isochrons.
- 2: See text for references and sources of data.
- 3: All Rb-Sr ages are calculated using a decay constant of  $1,42 \times 10^{-11} \text{ yr}^{-1}$  for  $^{87}\text{Rb}$ .

recognized in the Sand River Gneisses, the Beit Bridge Complex and the Messina Layered Intrusion. The latter has been dated by two different methods. A Pb-Pb whole-rock isochron for the anorthositic and gabbroic rocks has given an age of about 3 270 m.y. (Barton, 1981), while a Rb-Sr whole-rock isochron has yielded an age of about 3 150 m.y. (Barton et al., 1979a) which probably reflects a metamorphic event. Since the Beit Bridge Complex of supracrustal rocks is cut by the Messina Layered Complex, this suggests that the supracrustal lithologies were deposited and/or extruded sometime between 3 570 m.y. and 3 270 m.y. The Bulai Gneiss is dated at about 2 700 m.y. by the Rb-Sr whole-rock isochron method, and this date has been interpreted as the time of intrusion or remobilisation of this unit (Barton et al., 1979b). Age determinations by the same method on the Singelele Gneiss have suggested a date of about 2 600 m.y. and this age has been interpreted as a metamorphic age of the previously formed supracrustal granitoid (Fripp et al., 1979; Barton et al., 1979b). However, this metamorphic age was obtained from samples collected at the type locality near Messina. Other samples collected on the Form Ostend about 15 km south-east of Messina (from within the mapping area of this study) gave whole-rock Rb-Sr isochron age of  $2\,461 \pm 19$  m.y. with a very high initial ratio of  $0,8308 \pm 0,0003$ . This supports the interpretation that these ages for the



Singelele Gneiss are metamorphic, since large initial ratios are characteristic of rehomogenisation of Sr isotopes during metamorphism. Close correlation with a Pb-Pb whole-rock isochron of about 2 430 m.y. was obtained using the Ostend samples.

An undeformed and unmetamorphosed dolerite dyke which occupies a fault plane on the Farm Heuningfontein about 15 km south-east of Messina has yielded a whole-rock Rb-Sr isochron age of about 2 200 m.y. This suggests that the end of high-grade metamorphism and the onset of relative tectonic stability was achieved by this time (Barton, 1979).

#### Statement of purpose and work done

This study is a field oriented study aimed at preparing a geological map and describing the Precambrian geology of an area situated within the Central Zone of the Limpopo Mobile Belt, south-east of Messina (Figure 1). This area lies between the Sand River in the north-west and the Bosbokpoort Fault in the south-east, and lies on either side of the main road linking Messina and Tshipise in the northern Transvaal (Figure 2). This research forms part of the South African national contribution to the International Geodynamics Project. Within this programme, three groups have been working in the Limpopo Mobile Belt: the Departments of Geology at the University of the Witwatersrand and the Rand Afrikaans

University responsible for field mapping, structural analysis, geochemistry and metamorphic petrology, and the Bernard Price Institute of Geophysical Research responsible for geochronology and isotope geochemistry. These studies have been aimed at establishing a framework for understanding the relationships among the various igneous, sedimentological and metamorphic events recognizable in the field. The objective of the South African participation in this project has been to undertake research on the dynamics and dynamic history of the earth with emphasis on deep-seated phenomena. In addition, it was hoped to provide clues to the chemical pattern of evolution of the mantle and crust in an area exposing elements encompassing a major part of early earth history.

An area of approximately 200 sq km has been mapped using aerial photographs in the field. These data have been compiled onto a base map at an approximate scale of 1 : 25 000 to produce a field map (map 1 in rear pocket). Also, an interpretive map at a scale of 1 : 50 000 has been prepared to illustrate the structural attitudes and sample localities (map 2 in rear pocket). A representative sample collection of 140 specimens has been made from which over eighty petrographic thin-sections were prepared. Full silicate analyses were carried out on over thirty-five samples using X-ray fluorescence for major elements. Rb, Sr and Ba trace element abundances were also

determined in selected samples. After the examination of the thin-sections, over twenty samples were selected from which polished thin-sections were prepared to enable electron probe microanalyses to be made of selected mineral grains. Over 70 analyses were completed using a Cambridge Microscan 5 instrument at the Department of Geochemistry, University of Cape Town, while over 250 mineral analyses were completed using an ARL-SEMQ instrument in the Department of Geology, University of the Witwatersrand.

Previous work in the area studied

The first systematic study of the geology in the area was a regional mapping programme by the Geological Survey of South Africa (Söhnge, 1946; Söhnge et al., 1948). The region was mapped at a scale of 1 : 50 000 using aerial photographs, and was regarded at that time as being underlain by rocks belonging to a Precambrian 'basement complex'. Most of the rock types that occur in the area were recognized, though the distinction between basement and supracrustal *sensu stricto* was not made, and the rocks were collectively called the Messina Formation. It was concluded that primary textures and structures were effectively obscured by the tectonic and metamorphic conditions that had prevailed in the area. Also, many types of granitoid gneiss were considered to have had sedimentary origins.

More recently, a review has been completed of the geology around Messina and a paleogeological interpretive map prepared (Bahnemann, 1972). The stratigraphy, metamorphism, and structure of the area was investigated, and basement and supracrustal elements of the stratigraphy were recognized. Metamorphic conditions were considered to have reached pressures in excess of 6 kbar and possibly as high as 10 kbar, while temperatures exceeded 625°C. Thus it was concluded that the metamorphism reached a high grade and was uniform over large areas. The deformation in the area was regarded as having a 'plastic' (sic) nature, with 'plastic folding' occurring at the height of the metamorphism. Deformation occurred in response to a regional shearing parallel to the ENE trend of the Limpopo Mobile Belt. Early and late folds, as well as intersecting fold directions and interference structures were recognized.

Two chemical analyses of Singelele Gneiss are reported for samples collected from within the area of the study reported here (Bahnemann, 1973). Consideration was given to the petrography of this rock, and to the process of anatexis, and it was concluded that the Singelele Gneiss may owe its origin to partial melting of the basement and supracrustal rocks in antiformal areas, resulting in potash feldspar and silica-rich melts, to produce the Singelele Gneiss, leaving

'restite' of anorthositic gneiss, calc-silicate gneiss and amphibolite which occur in the supracrustal rocks surrounding areas which contain Singelele Gneiss. The presence of numerous quartz-feldspar veins in these lithologies was used as further evidence of this process. The starting materials before anatexis were considered to have included shales, calcareous shales and marls. Temperatures of more than 625°C and pressures approaching 10 kbar were required for this melting event, based on the experimental data of Winkler, von Platen and others (see Winkler, 1974). However, subsequent trace element fractionation studies on granitic melting using Rb, Sr and Ba (McCarthy, 1977) has revealed the presence of both restite and anatectite fractions within the Singelele Gneiss itself.

A mineralogical study was carried out on garnets from the Messina area, with the aim of showing that their composition may reflect the metamorphic grade (Bahnemann, 1975). This investigation included the analysis of nine garnets, one of which was collected from a leucocratic granitic gneiss on the Farm Randjesfontein within the area studied. Using experimental data of Currie (1971), equilibrium temperatures of 635°C and pressures of about 6 kbar were suggested. However, using other experimental data (Hensen and Green, 1973), temperatures between 850°C and 900°C, and pressures from 9 to 10 kbar have been obtained (Horrocks, 1975).

Geochronological work has been completed on samples collected during the course of the present investigation (Barton, 1979; Barton et al., 1979a, and b) and are reviewed elsewhere.

## CHAPTER 2: ROCK TYPES AND LITHOLOGIES

### Introduction

In this section, the results from the field and laboratory examination of the different rock types encountered in the area under study are presented. Aspects of their field characteristics, petrography, whole-rock and mineral chemistry are also discussed. Analytical procedures are described in Appendix 1.

The following rock types and lithologies have been recognized as follows: basement gneisses, quartzo-feldspathic gneisses, Singelele-type granitoid gneiss, garnet-cordierite-sillimanite gneiss and varieties, pyroxenitic amphibolite, quartzite and banded magnetite quartzite, calc-silicate gneiss and marble, metapyroxenite and serpentinite, and the gabbroic and anorthositic gneisses of the Messina Layered Intrusion. The basement gneisses have been so called on the basis of correlation with similar gneisses in the Sand River area (Fripp, 1981a-c) while all other rock types excluding the metapyroxenite, serpentinite and the Messina Layered Intrusion are considered to represent a supracrustal sequence (ibid.). In addition, dolerite dykes of various ages are abundant, and pegmatites occur in some of the serpentinite bodies.

### Basement gneisses

The basement gneisses (i.e. Sand River Gneisses) have been

recognized at three localities in the study area. One outcrop was observed on the Farm Oorsprong, and other outcrops occur on the Farm Middelbult (see Map 1 in rear pocket). These gneisses are grey in colour and weakly banded, and are transected by both melanocratic and leucocratic dykes together with numerous leucocratic veins (Figure 3). They characteristically form smooth whale-back pavement outcrops.

The grey gneiss is medium grained with the mineral grains averaging about 1 mm in diameter. Mineral banding is typically 2 or 3 mm in thickness and varies from more quartz and feldspar rich compositions to those with more abundant mica. Red garnets about 1 mm in size are dispersed in small quantities,

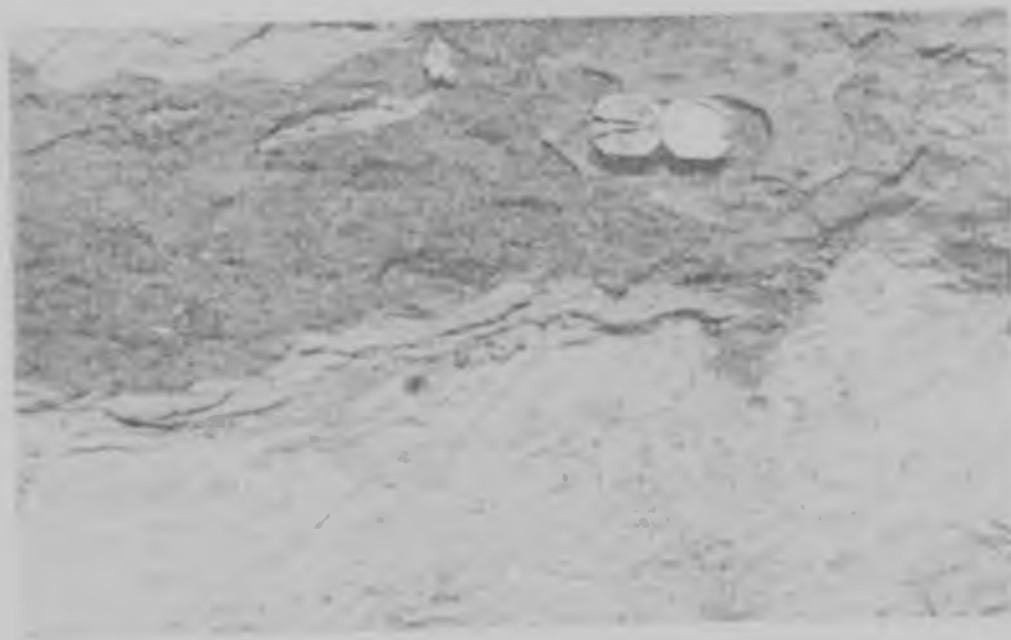


Figure 3: Deformed melanocratic dyke transecting grey banded basement gneisses on the farm Middelbult, about 5 km east of the main Messina-Tshipise road (Map 1 in rear pocket).



while prismatic black amphiboles up to 3 mm in length and about 1 mm in diameter are visible on weathered surfaces, and impart a linear fabric to the rocks. In thin section, the following typical mineral assemblage occurs: 40 per cent quartz, 30 per cent andesine, 15 per cent microcline, 10 per cent biotite, 3 per cent alteration minerals, 2 per cent garnet and accessory apatite. This assemblage is granodioritic in composition with biotite as the predominant ferromagnesian mineral. In addition to its obvious concentration in layers, biotite occasionally forms skeletal grains and clusters of oriented flakes in quartz. It often replaces an earlier mafic mineral, possibly orthoamphibole or orthopyroxene, which now remains in places in an amorphous and altered state. The quartz and feldspar form a granoblastic texture in which the xenoblastic grains have irregular polygonal boundaries. The microcline is a perthite with exsolved beads and stringers of plagioclase.

The cross-cutting melanocratic dykes are dark and even grained rocks with a general grain size of 1 or 2 mm in diameter. They have the following average modal mineralogy: 45 per cent tremolite amphibole, 35 per cent andesine; 10 per cent hypersthene, 5 per cent biotite, 5 per cent quartz and accessory opaque minerals. The rock preserves prograde orthopyroxene textures where weakly pleochroic hypersthene can be seen to be in a reaction relationship with the amphibole, and in places encloses

small optically continuous crystals of amphibole (Figure 4). However, biotite and hypersthene only coexist in the dyke along its boundaries with leucocratic veins.



Figure 4: Prograde orthopyroxene (opx) in a melanocratic dyke in basement gneiss on the Farm Oorsprong (about 250 m east of the main Messina-Tsh.pise road - Map 1 in rear pocket), which contains optically continuous amphibole (hnb) in a matrix of feldspar (plag). Scale bar is about 0,5 mm.

Elsewhere, biotite does not appear in the dyke.

The leucocratic veins are sub-parallel to parallel to the mineral banding in the gneiss, and are usually a few centimetres in thickness. They are deformed together with the mineral banding, and display cusped boundaries which are convex outwards into the grey basement gneisses, indicating that their viscosity was greater than that of the gneisses during the deformation. The veins are dioritic in composition with the following

average modal assemblage: 60 per cent andesine, 30 per cent quartz, and 10 per cent biotite. Biotite is the only ferromagnesian mineral to occur in the veins, while the quartz and feldspar show even grained polygonal textures.

A whole-rock analysis of the basement gneiss is presented in Table 2. The sample (22-6-B) from the Farm Oorsprong (Map 2 in rear pocket) was chosen to contain as few veins as possible. The rock is predominantly felsic being mainly composed of  $\text{SiO}_2$ ,  $\text{Al}_2\text{O}_3$ ,  $\text{Na}_2\text{O}$ ,  $\text{K}_2\text{O}$  and  $\text{CaO}$ . Femic components comprise less than 4 per cent of the rock. The rock is corundum normative with over 32 per cent normative quartz, while the only ferromagnesian mineral to appear in the norm is orthopyroxene in an amount of less than 3 per cent by weight.

Comprehensive whole-rock and mineral geochemical data for these basement rocks have been presented by a complimentary study of the Sand River Gneisses from the type area (Fripp, 1981a, 1981b, 1981c).

#### Quartzo-feldspathic gneisses

These gneisses are ubiquitous in the study area and underlie most of the region (see Map 1 in rear pocket). They weather readily and occupy much of the flat country or valley floors where they are largely covered by sand, soil and rubble. They show considerable heterogeneity in the proportions of their constituent minerals which include mica, amphibole, pyroxene,

Table 2: Whole-rock analyses of basement, quartzo-feldspathic and Singelele type gneisses and their C.I.P.W. norms

	1	2	3	4	5	6	7	8	9	10	Singelele Average	1σ
SiO <sub>2</sub>	72,61	75,81	80,28	73,21	78,94	78,33	78,96	78,90	78,80	79,21	78,79	0,32
TiO <sub>2</sub>	0,38	0,02	0,06	0,24	0,09	0,11	0,12	0,14	0,12	0,12	0,02	0,02
Al <sub>2</sub> O <sub>3</sub>	14,95	14,22	11,92	13,91	11,56	11,23	11,11	11,33	10,92	11,13	11,21	0,22
Fe <sub>2</sub> O <sub>3</sub>	2,54	0,51	0,58	2,04	1,37	1,92	1,85	1,78	2,23	2,11	1,88	0,30
MnO	0,03	0,03	0,01	0,01	-	-	-	-	-	0,01	-	-
MgO	0,62	-	0,03	0,46	0,11	0,08	0,08	0,04	0,05	0,05	0,07	0,03
CaO	2,78	1,45	2,48	1,53	0,64	0,48	0,42	0,47	0,42	0,50	0,49	0,08
Na <sub>2</sub> O	3,73	4,02	3,59	2,63	3,54	3,43	2,84	3,06	3,09	3,18	3,19	0,26
K <sub>2</sub> O	2,90	4,03	1,68	5,23	4,37	4,54	5,03	4,80	4,70	4,36	4,63	0,26
P <sub>2</sub> O <sub>5</sub>	0,11	0,07	0,05	0,07	0,02	0,03	0,04	0,05	0,04	0,04	0,04	0,01
LOI	0,16	0,05	0,22	0,27	0,17	0,09	0,24	0,15	0,18	0,19	0,17	0,05
Total	100,81	100,21	100,90	99,60	100,81	100,24	100,69	100,30	100,57	100,90	100,59	0,27
Rb ppm.	74	55	25	105	114	118	143	129	120	93	120	17
Sr ppm.	222	75	113	130	28	21	26	27	24	21	25	3
Ba ppm.	741	316	199	956	629	620	681	700	775	623	671	61
quartz	32,68	33,89	47,43	34,02	39,66	39,55	41,70	40,97	41,34	42,24	40,90	-
corundum	0,88	0,77	-	1,31	-	-	0,32	0,36	0,08	0,36	0,15	-
orthoclase	17,03	23,79	9,87	31,13	25,67	26,80	29,60	28,33	27,67	25,59	27,25	-
albite	31,35	33,97	30,18	22,40	29,76	28,98	23,92	25,85	26,04	26,71	26,87	-
anorthite	12,98	6,72	11,37	7,18	2,72	1,82	1,81	2,00	1,81	2,02	2,16	-
diopside	-	-	0,13	-	0,09	0,07	-	-	-	-	-	-
hedenbergite	-	-	0,32	-	0,17	0,24	-	-	-	-	-	-
enstatite	1,53	-	0,01	1,15	0,23	0,17	0,20	0,10	0,12	0,12	0,17	-
ferrosilite	0,75	0,28	0,04	0,70	0,51	0,72	0,81	0,76	0,98	0,95	0,81	-
magnetite	1,83	0,38	0,42	1,49	0,98	1,39	1,33	1,29	1,60	1,51	1,36	-
ilmenite	0,72	0,04	0,11	0,46	0,71	0,21	0,23	0,23	0,27	0,23	0,23	-
apatite	0,25	0,16	0,12	0,16	0,05	0,07	0,09	0,12	0,09	0,09	0,09	-

- 1: grey banded basement gneiss (22-6-B) - Farm Oorsprong.
- 2: dyke-like quartzo-feldspathic gneiss (77) - Farm Aitonville.
- 3: dyke-like quartzo-feldspathic gneiss (29-1-7B) - Farm Heuningfontein.
- 4: adamolitic quartzo-feldspathic gneiss (18-6-A) - Farm Veenen.
- 5 to 10: Singelele-type granitoid gneiss (B76-85 to B76-90) - Farm Ostend.

Analyst: P.C. Horrocks  
 Total Fe determined as Fe<sub>2</sub>O<sub>3</sub>  
 LOI = loss on ignition.

and garnet in addition to quartz and feldspar. The quartz commonly forms aggregates of grains fused into ribbon-like structures typical of high grade metamorphic rocks. Grain sizes are variable from 1 to 5 mm for the leucocratic minerals and 1 to 2 mm for the melanocratic minerals. In places, more leucocratic varieties of this lithology can be seen to form discrete layers and dyke-like bodies which transect other quartzo-feldspathic units that contain more abundant melanocratic minerals.

Three modal assemblages are presented below to demonstrate the range of compositions which occur. The first is a leucocratic dyke-like body that transects the other quartzo-feldspathic types, and has a granitic mineralogy: 50 per cent microcline, 40 per cent quartz, 5 per cent albite and 5 per cent almandine. This rock has a granoblastic texture and is largely recrystallized. The quartz grains commonly display concave inward cusped boundaries, and have clear rather than undulose extinction. The garnet has been identified as being predominantly almandine by powder X-ray diffraction techniques, while the microcline is perthitic.

A second typical variety of these rocks is adamellitic in composition, with alkali feldspar constituting between 33 per cent and 66 per cent of the total feldspar. The average modal

composition is: 35 per cent microcline, 30 per cent quartz, 20 per cent andesine, 10 per cent biotite, 3 per cent garnet, 1 per cent chlorite, accessory opaque minerals, sillimanite and phlogopite. The garnet in these varieties is typically zoned and poikiloblastic. Their cores commonly contain numerous small blebs of quartz while biotite crystals interpenetrate and coexist with an outer zone. The sillimanite replaces the pale mica and their longest crystallographic axes are colinear. These two minerals occur in only minor quantities. Some biotite laths are replaced by chlorite which in turn have abundant opaque minerals exsolved along their lamellae.

A third variety of the gneiss is dioritic with the following mineral composition: 65 per cent labradorite, 20 per cent quartz, 10 per cent augite, 1 per cent orthopyroxene, 2 per cent tremolitic amphibole, 2 per cent opaque minerals and accessory monazite. Replacement relationships and reactions are commonly observed in this lithology. In places, the clinopyroxene and opaque minerals are seen rimmed by the greenish amphibole. The minor amounts of pleochroic hypersthene containing inclusions of small optically continuous grains of amphibole show prograde reactions where it replaces amphibole in the presence of quartz. This amphibole-pyroxene reaction can also be observed with the pale green weakly pleochroic clinopyroxene. Some idioblastic grains of metamict monazite also occur.

Three whole-rock analyses of these gneisses are included in Table 2. Samples 77 and 29-1-7B are leucocratic dyke-like units which in places can be seen to cross-cut the other quartzofeldspathic lithologies. Sample 18-6-A contains more ferromagnesian minerals, and is adamellitic in composition. These rocks all have high  $\text{SiO}_2$  contents which vary from about 73 per cent to 80 per cent, and variable alkali ratios. This reflects the heterogeneous nature of these rock-types. The normative assemblages are similarly variable. Sample 29-1-7B with over 80 per cent  $\text{SiO}_2$  is not corundum normative, but contains normative clinopyroxene. In addition, this sample shows over 47 per cent normative quartz reflecting its high  $\text{SiO}_2$  content.

#### Singelele-type granitoid gneiss

This granitoid gneiss occurs on the Farms Kopjesfontein, Ostend, Trotsky, Lenin and Senator (see Map 1 in rear pocket), and forms prominent hills of large rounded boulders on Ostend. It is characterized by a reddish weathering colour and a coarse grain size, with some minerals reaching 5 mm in diameter. The rock is quartz rich, where aggregates of quartz grains produce flat ribbon-like structures which accentuate the planar fabric. The feldspar produces the reddish colour, while small amounts of platy biotite form the predominant melanocratic mineral in the rock. Weathered surfaces commonly display a characteristic

pattern of irregular polygonal cracks.

The rock has the composition of a granite as follows: 50 per cent quartz, 40 per cent microcline, 3 per cent plagioclase, 5 per cent biotite, 2 per cent chloritized amphibole, accessory zircon and accessory opaque minerals. Myrmekite commonly occurs in the plagioclase grains and can usually be seen to terminate against the boundary with an alkali feldspar grain. Some plagioclase-biotite grain boundaries show the development of later smaller plagioclase grains. Both the biotite and opaque mineral exhibit skeletal grain textures, while some quartz grains show cusped boundaries which are concave inwards. Amphiboles are rare, and are commonly altered in chlorite. The zircon grains show two distinct morphologies: idiomorphic grains, commonly metamict with radiating cracks and cloudy coronas, and smaller corroded grains which are numerically more abundant.

Table 2 shows 6 whole-rock analyses of this rock type, that have also been used for isotope and geochronological studies (Barton *et al.*, 1979b). These samples were collected over a limited area at one locality on the Farm Ostend (Map 2 in rear pocket) and all have a similar composition. This has been used to test the 'repeatability' of the analytical technique (Appendix 1), and average values with single standard deviations have been calculated (Table 2). The rock is characterized by



high  $\text{SiO}_2$  values, typically over 78 per cent. Calcic components are minor, less than 4 per cent on average, while  $\text{K}_2\text{O}$  is the most abundant alkali (up to 5 per cent). Rb and Sr trace element abundances have also been determined using the 'isotope dilution' technique (Barton et al., 1979b), and in general closely agree with those values determined by X-ray fluorescence used in this study. An exception is sample B76-89 which displays some considerable isotopic heterogeneity. The samples all contain normative quartz (about 40 per cent), though unlike the others, samples B76-85 and B76-86 are not corundum normative, but show small amounts of normative clinopyroxene (less than 0.4 per cent). All samples contain normative orthopyroxene (about 1 per cent). The normative feldspar is largely alkaline, with only minor quantities of anorthite being calculated (about 4 per cent of the total feldspar). Normative potash and sodic feldspars are in nearly equal proportions.

#### Garnet-cordierite-sillimanite gneiss and varieties

These gneisses form a variety of units in general interlayered and infolded with the quartzo-feldspathic gneisses (see Map 1 in rear pocket). Apart from the more common garnet-cordierite-sillimanite gneiss, corundum-bearing, sillimanite bearing, sapphirine-bearing and symplectite-bearing varieties occur. They are characterized by a large number of mineral

phases and commonly exhibit a well developed mineral layering. Biotite-rich and leucocratic layers alternate, and vary from a few millimetres to a few centimetres in thickness. Garnet porphyroblasts are characteristic, and range up to a centimetre in diameter, with the biotite and sillimanite showing wrap-around structures. Some varieties contain abundant sillimanite, and at some localities, for example on the farm Randjesfontein (Map 1 in rear pocket), are monominerallic, and have been quarried for commercial purposes. The sillimanite occurs as clusters of needle-like grains up to 3 cm in length, and these commonly reveal small kink-bands and shear-zones in the rock. Other varieties are corundum bearing, and have also been quarried on the farm Randjesfontein. The corundum grains range up to 1 cm in diameter, and are commonly set in a matrix of biotite which wraps around the corundum porphyroblasts. Spinel and sapphirine bearing varieties usually occur as small outcrops of very limited extent within a country rock made up of the more typical garnet-cordierite-sillimanite gneiss where they form tough, coarse and uneven grained rocks which have extremely irregular weathered surfaces and contain garnets up to 2 cm in diameter.

A considerable variation in mineral assemblages occur in these rocks, and some samples may contain more than 9 different phases. An example of a mode for a typical garnet-cordierite-sillimanite gneiss is: 5 - 10 per cent garnet, 10 - 20 per cent

cordierite; 5 - 10 per cent sillimanite, 10 - 25 per cent biotite, 20 - 25 per cent oligoclase, 15 - 25 per cent quartz, 5 - 15 per cent K-feldspar and accessory opaque minerals. The garnet is porphyroblastic with poikiloblastic cores containing quartz, plagioclase, sillimanite and biotite inclusions. In places the garnet has quartz myrmekites which radiate outwards into cordierite. Quartz myrmekites are generally abundant, and are present in quartz, plagioclase and cordierite hosts. The cordierite is well twinned and poikiloblastic, and typically contains biotite and sillimanite grains. This suggests that the following reaction reported by Holdaway and Lee (1977) has occurred in these rocks:



Also, the reaction described by Currie (1971) is typical of these rocks, where cordierite and garnet share common grain boundaries and both contain quartz and sillimanite inclusions:



Both the K-feldspar and the plagioclase display perthitic and antiperthitic textures respectively, but are seldom poikiloblastic.

The sillimanite occurs in two morphologies as (i) clusters of small needle-like grains within the garnet and cordierite; and (ii) larger columnar grains usually occurring within cordierite only where the sillimanite replaces the biotite (Figure 5).

A corundum bearing variety of these gneisses has the following typical modal assemblage: 40 per cent corundum, 35



Figure 5:: Sillimanite (sill) replacing biotite (biot) in cordierite from a garnet-cordierite-sillimanite gneiss on the Farm Artonvilla (7 km east of Messina - see Horrocks, 1975). Scale bar is approximately 0,5 mm.

per cent biotite, 18 per cent alteration minerals, 5 per cent phlogopite, 2 per cent hornblende, accessory opaque minerals, and accessory allanite. The corundum forms porphyroblasts up to 1 cm in diameter and contains inclusions of brown amphibole and colourless mica (phlogopite). In places, the corundum displays a distinct zonation revealed by cloudy traces of sub-microscopic particles incorporated during crystal growth. Biotite laths wrap around the corundum, and also occur as scattered prismatic grains in an amorphous groundmass of the alteration products, which include sericitic micas and clay minerals probably after a feldspar.

The almost monominerallic sillimanite rock contains

prismatic grains of sillimanite which are generally needle-like in form. However, larger columnar grains of sillimanite cross-cut the smaller needles and probably represent a second stage of sillimanite crystallization. Also, biotite which may comprise up to 10 per cent of the rock occurs in similar replacement relationships as illustrated in Figure 5. Late stage greenish coloured very fine grained quartz is locally present in amounts up to 5 per cent, while accessory spinel and opaque minerals are also present. Small kink-bands and shear-zones deform the sillimanite needles on a microscopic scale, and in some of the shear-zones, the larger columnar grains occur with their longest axes parallel to the zone's edge.

The sapphirine bearing varieties are generally characterized by the presence of spinel, corundum and bronzite. A typical mineral assemblage is as follows: 30 per cent biotite/phlogopite, 30 per cent cordierite, 10 per cent sapphirine, 10 per cent garnet, 5 per cent hercynite, 5 per cent alteration minerals, 4 per cent hypersthene/bronzite, 4 per cent amphibole (gedrite), 2 per cent corundum, accessory opaque minerals. Important mineral parageneses which preserve complex reaction textures are a feature of these varieties. Canals of cordierite, sapphirine and spinel separate garnet from corundum which are never seen in contact. In the same thin section, the isotropic green spinel, hercynite, can be observed to coexist with cordierite, and in

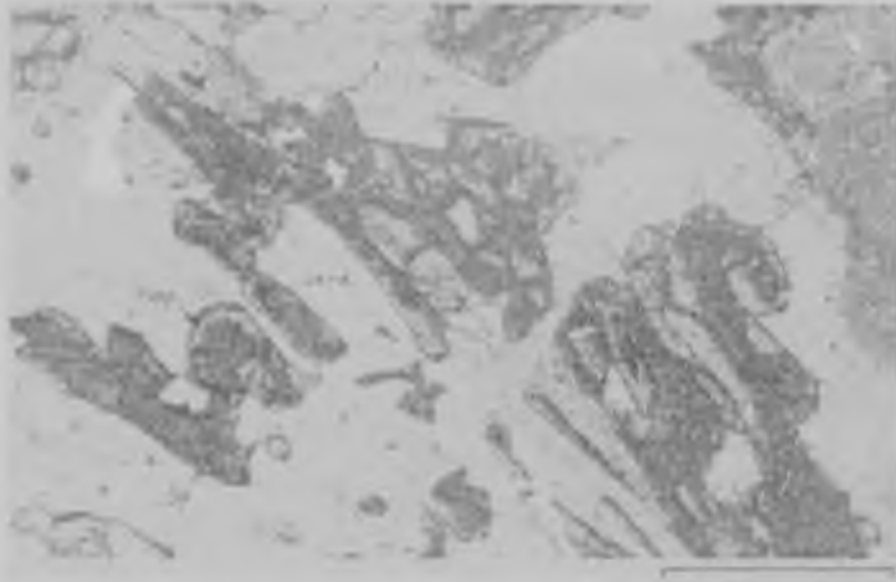


Figure 6: Sapphirine (sapp) overgrowing hercynite (sp) in cordierite (cord) from a sapphirine rock on the Farm Randjesfontein (2 km north-east of the main Messina-Tshipise road - Map 1 in rear pocket). The scale bar is approximately 0,5 mm.

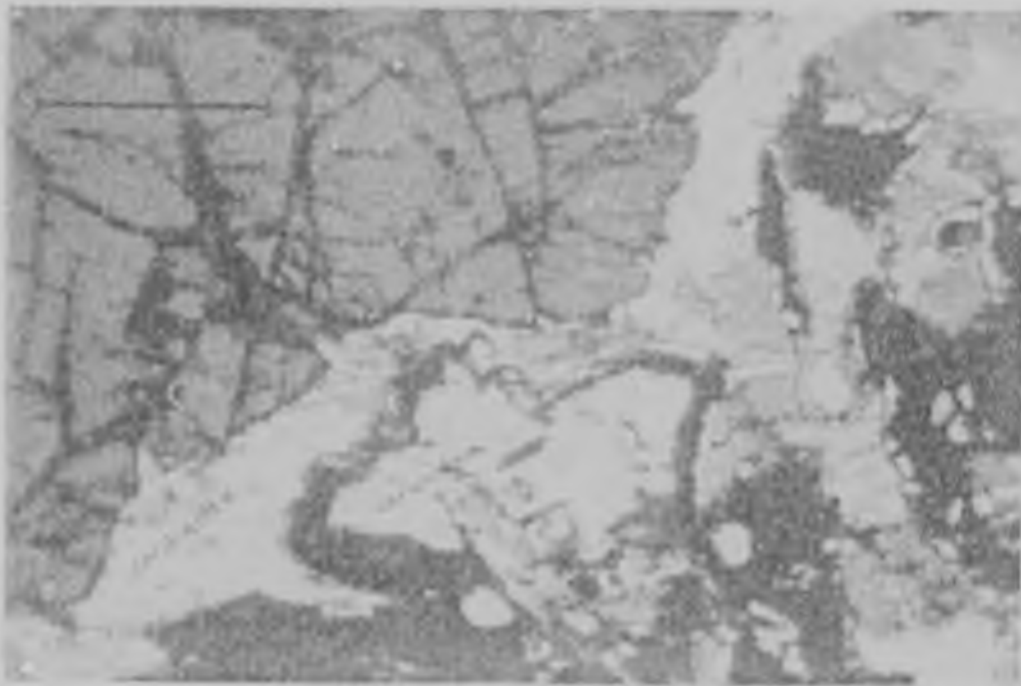


Figure 7: Reaction rims of spinel (sp), sapphirine and cordierite separating corundum and garnet, in sapphirine rock from the Farm Randjesfontein (2 km north-east of the main Messina-Tshipise road - Map 1 in rear pocket). The scale bar is approximately 0,5 mm.

adjacent areas to be 'armoured' from cordierite by a thin rim of sapphirine (Figure 6). Where corundum is present, it is always rimmed by the hercynite, which is in turn rimmed by sapphirine. The sapphirine is then separated from the garnet by larger canals of cordierite (Figure 7). Bronzite also occurs in these rocks, and coexists with both garnet and cordierite (Figure 8). The amphibole in the rock consists of pale brown gedrite, and shows particularly well developed cleavage traces. It forms porphyroblasts up to a few millimetres in diameter, and commonly includes small granules of orthopyroxene.

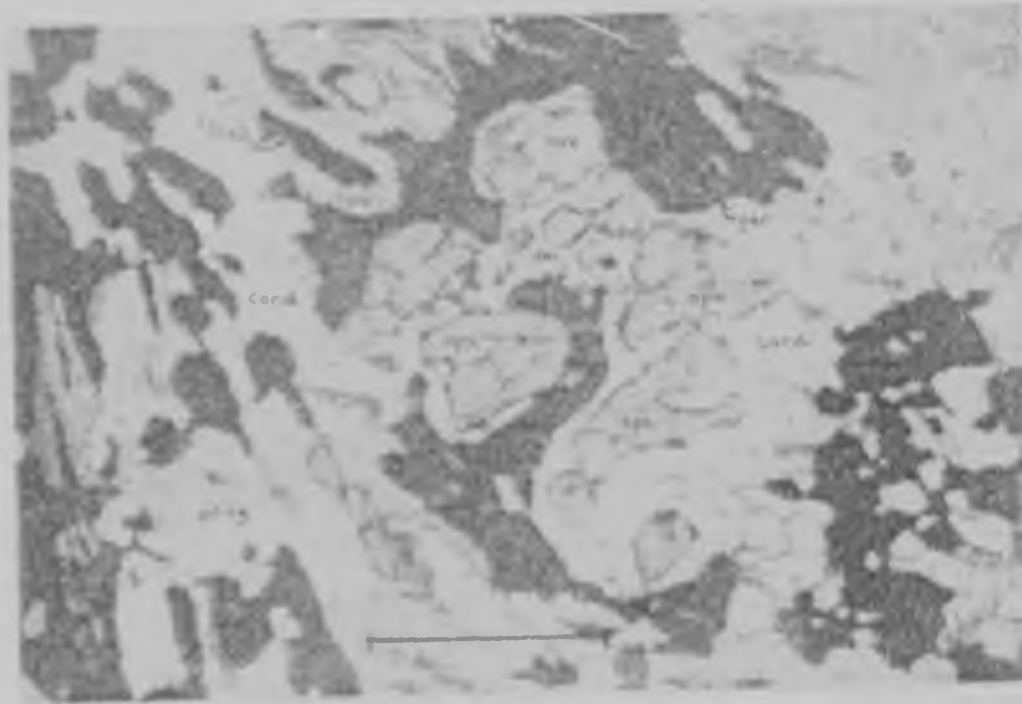


Figure 8: Reaction texture of garnet (gar) which coexists with both orthopyroxene (opx), cordierite (cord) and plagioclase (plag) in a sapphirine rock from the Farm Randjesfontein (2 km north-east of the main Messina-Tshipise road - Map 1 in rear pocket). The scale bar is about 0,5 mm.

Certain types of these gneisses, particularly those in close spatial association with the sapphirine bearing varieties preserve symplectitic textures. These contain vermicular orthopyroxene hosted within either cordierite or plagioclase. In samples with sapphirine, the orthopyroxene occurs intimately associated with biotite and may even completely overgrow the biotite (Figure 9). These minerals are then most commonly



Figure 9: Symplectite consisting of vermicular orthopyroxene (opx), biotite (biot), and cordierite (cord), in a sapphirine rock from the Farm Randjesfontein (2 km north-east of the main Messina-Tshipise road - Map 1 in rear pocket). The scale bar is approximately 0,5 mm.

hosted in cordierite. In the case of symplectites containing vermicules of orthopyroxene hosted in plagioclase, the orthopyroxenes occur radiating outwards from a garnet porphyroblast (Figure 10), and in some specimens, the garnet

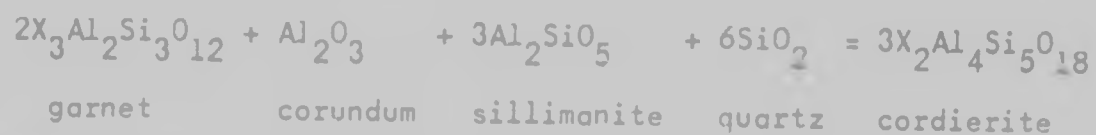


may be entirely absent with only spherical 'knots' of the orthopyroxene in plagioclase remaining.



Figure 10: Symplectite consisting of radiating vermicular orthopyroxene (opx) in plagioclase (plag) around a garnet porphyroblast (gar) in a symplectite rock from the Farm Randjesfontein (2 km north-east of the main Messina-Tshipise road - Map 1 in rear pocket). The scale bar is approximately 0,5 mm.

In summary, these textures may be ascribed to the following reactions. Corundum and garnet appear to be the earliest formed metamorphic minerals, and are separated by a reaction rim of mainly cordierite (Figure 7):

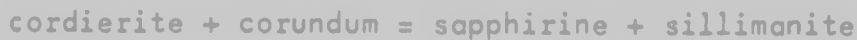


This reaction consumes alumino-silicate and quartz, which is supported by the fact that sillimanite and quartz are common

inclusions within the garnet and cordierite in all varieties of these gneisses. Also, the association of enstatite + kyanite + quartz has been described from rocks in the Central Zone of the Limpopo Mobile Belt (Chinner and Sweatman, 1968) and suggests that reactions similar to:



may have been responsible for the breakdown of an earlier assemblage such as enstatite + kyanite + corundum + quartz + garnet into new phases, for example garnet + cordierite + spinel + sapphirine. Sapphirine forming reactions which may be applicable in the area under study have been studied by Seifert (1974) and include:



However, sapphirine is always 'armoured' from the corundum by spinel probably by the reaction:



Such reactions are considered by Leyreloup et.al. (1975) to occur during retrograde transitions to low pressure granulite facies in felsic rocks at high temperatures.

Whole-rock and mineral geochemical data have been obtained for these garnet-cordierite-sillimanite gneisses and their related sapphirine, spinel, corundum and symplectitic varieties. The whole-rock analytical data are presented in Table 3, whilst

Table 3: Whole-rock analyses of garnet-cordierite-sillimanite gneiss and related varieties

	1	2	3	4	5
SiO <sub>2</sub>	54,99	55,02	31,01	46,29	29,33
TiO <sub>2</sub>	0,81	0,84	0,98	1,22	0,96
Al <sub>2</sub> O <sub>3</sub>	20,76	21,60	36,08	17,22	31,41
FeO	10,47	9,88	11,58	16,78	12,58
MnO	0,12	0,12	0,01	0,16	0,03
MgO	5,92	6,96	14,31	10,05	23,21
CaO	1,08	1,08	0,63	6,92	0,14
Na <sub>2</sub> O	1,17	1,07	0,51	0,80	1,05
K <sub>2</sub> O	2,85	2,71	2,02	0,35	-
P <sub>2</sub> O <sub>5</sub>	0,06	0,07	0,12	0,20	0,16
LOI	0,84	0,77	2,57	0,33	1,20
Total	100,07	100,11	99,82	100,32	100,07

- 1: garnet-cordierite-sillimanite gneiss (21-7-F) - Farm Boschrand.
- 2: garnet-cordierite-sillimanite gneiss (21-7-G) - Farm Boschrand.
- 3: sapphirine bearing rock (2-8-12) - Farm Randjesfontein.
- 4: garnet-orthopyroxene-plagioclase symplectite (2-8-10) - Farm Randjesfontein.
- 5: cordierite-spinel-corundum rock (2-8-1) - Farm Chirundu.

Analyst: P.C. Horrocks  
 Total iron determined as FeO  
 LOI = loss on ignition

the mineral analytical data (electron probe microanalyses) are presented in Appendix 2.

The whole-rock analyses for these rocks show some great variability. The garnet-cordierite-sillimanite gneiss (nos. 1 and 2, Table 3) are essentially pelitic in composition (see Pettijohn, 1957, p.106) with  $\text{SiO}_2$ ,  $\text{Al}_2\text{O}_3$ , FeO and MgO comprising more than 90 per cent of the rock. However, compared to the compositions of typical shales, these gneisses show relative depletions in the lithophile components ( $\text{SiO}_2$ ,  $\text{Al}_2\text{O}_3$ , CaO,  $\text{Na}_2\text{O}$  and  $\text{K}_2\text{O}$ ) while the siderophile components (FeO, MgO) are relatively enriched. The sapphirine, spinel and corundum bearing lithologies (nos. 3 and 5, Table 3) display this trend in an even greater degree, with the exception of  $\text{Al}_2\text{O}_3$  which is high in these rocks relative to the garnet-cordierite-sillimanite gneiss country rock. Silica and the alkalis (CaO,  $\text{Na}_2\text{O}$  and  $\text{K}_2\text{O}$ ) are depleted, while the  $\text{Al}_2\text{O}_3$ , FeO and MgO are enriched by significant amounts, for example the  $\text{Al}_2\text{O}_3$  is enriched from about 21 per cent in the garnet-cordierite-sillimanite gneiss to about 36 per cent in the sapphirine bearing rock (see Table 3). The symplectite (no.4, Table 3) is depleted in  $\text{SiO}_2$  and  $\text{Al}_2\text{O}_3$  while enriched in FeO, MgO and CaO relative to the garnet-cordierite-sillimanite gneisses. In the case of CaO, this enrichment is from about 1 per cent CaO to about 7 per cent CaO.

Numerous electron probe microanalyses of minerals from

these lithologies are presented in Appendix 2. These have been used in applying various geothermometers and geobarometers in order to establish some physical conditions of the metamorphism, and in a study of compositional zonation in garnet. These topics are discussed in more detail later in this report. Suffice it to say here that the minerals analysed from the garnet-cordierite-sillimanite gneiss include feldspar, mica, garnet and cordierite. The mica is generally phlogopite with  $Mg/Mg+Fe$  ratios approaching 0,7 but phlogopite in contact with garnet is generally more magnesian than those grains isolated from the garnet. The garnet shows a distinctive zonation in Mg and Fe which is generally concentric to the margins of the porphyroblasts, and varies from about  $Alm_{55}Py_{45}$  at the grain cores to about  $Alm_{70}Py_{30}$  at the grain margins. Grossular and spessartine forms negligible proportions of the garnet in the garnet-cordierite-sillimanite gneiss. However, in the symplectite, grossular forms up to 20 per cent of the garnet, and zoning is much less marked. The sapphirine bearing varieties contain garnet which displays similar compositions and zoning to that in the garnet-cordierite-sillimanite gneiss. The cordierite is generally unzoned, and has typical  $Mg/Mg+Fe$  ratios of about 0,8. In addition to these minerals, sapphirine, spinel, gedrite and orthopyroxene analyses have been obtained from the sapphirine and other varieties of these rocks (see

Appendix 2). In these samples, the mica is also phlogopitic, with  $TiO_2$  contents up to 2,5 per cent which contrasts with about 1,5 per cent in the garnet-cordierite-sillimanite gneiss. The orthopyroxene is typically bronzite in the sapphirine rocks, with a  $Mg/Mg+Fe$  ratio of about 0,7 or higher.

#### Pyroxenitic amphibolite

Amphibolitic gneisses are common (see Map 1 in rear pocket) but display considerable variety in their field appearance and constituent mineral components. Although termed 'amphibolites' as a field term by many workers in the region, these rocks contain in general appreciable amounts of pyroxene, which can produce brown and reddish colours in outcrop as opposed to those more blackish melanocratic varieties with less pyroxene and more amphibole. The rock weathers easily, and typically occurs interlayered and infolded with quartzite, banded magnetite quartzite and also some pod-like serpentinites. This association of rock-types is characteristic in the area. However, they also occur together with the quartzo-feldspathic gneisses where they are more leucocratic and generally contain more biotite. They are even grained rocks with grain sizes ranging from 1 to 3 mm in diameter. Many varieties are distinctly garnetiferous, and take on a characteristic 'spotted' appearance, in which the 'spots' are a few centimetres in diameter, and often comprise garnet centres with aggregates of plagioclase grains forming

naloos. In some samples, idioblastic outlines can be detected, while others are deformed into ellipsoidal bodies within the rock. These textures and structures occur elsewhere in high-grade metamorphic provinces, and have even been used as palaeo-strain gauges (Schwerdtner et al., 1974).

These rocks are mainly pyroxene-amphibole-plagioclase assemblages, and two modes are presented below, the first in a garnet-free variety, while the second contains garnet: 10 - 40 per cent andesine, 25 - 50 per cent hornblende, 0-35 per cent hypersthene, 0 - 25 per cent diopside, 0 - 20 per cent biotite, 3 - 15 per cent quartz, 0 - 5 per cent opaque minerals, 0 - 5 per cent chlorite, 0 - 5 per cent sphene; and 5 per cent labradorite, 75 per cent hornblende, 10 per cent hypersthene, 2 per cent diopside, 1 per cent biotite, 5 per cent quartz, 5 per cent garnet. The proportions of these phases vary considerably from locality to locality, and the above only represent typical assemblages. Many samples contain clinopyroxene without any orthopyroxene, and commonly, the diopside rims the hornblende, and blebs of optically continuous hornblende may be included within pyroxene grains. However, the diopside can also be rimmed by the hornblende, suggesting that both prograde and retrograde relationships are preserved between these minerals. In the prograde relationship, orthopyroxene forms along grain boundaries between adjacent amphibole grains (Figure 11)

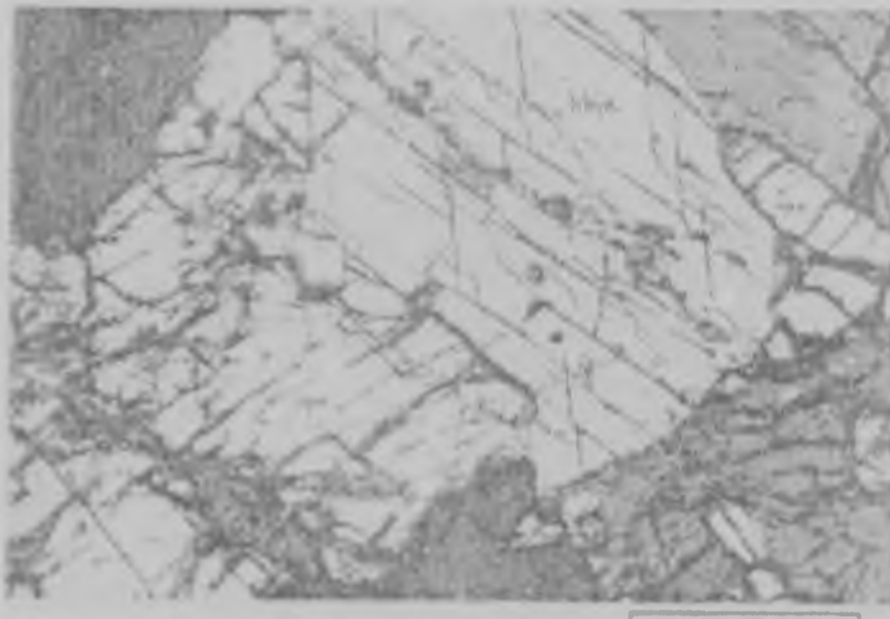
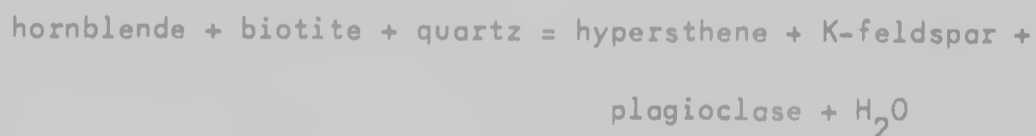


Figure 11: Prograde orthopyroxene (opx) replacing hornblende (hble) along grain boundaries in a pyroxenitic amphibolite from the Farm Artonvilla (7 km east of Messina - see Horrocks, 1975). Scale bar is about 0,5 mm.

where it consumes the amphibole and may contain optically continuous inclusions of hornblende. Alternatively, poikiloblastic grains of hornblende may be seen to contain optically continuous inclusions of pyroxene (Figure 12) reflecting the retrograde relationship. These textures always occur in the presence of plagioclase and quartz, and suggest that they may have been formed by the following reactions described by De Waard (1965):





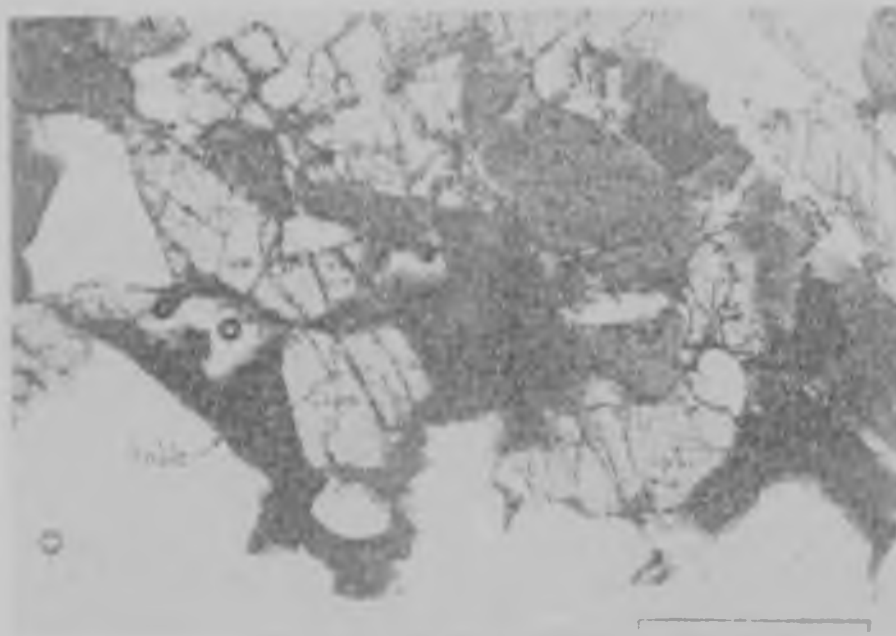


Figure 12: Retrograde hornblende (hnble) containing optically continuous inclusions of clinopyroxene (cpx) in a pyroxenitic amphibolite from the Farm Artonvilla (7 km east of Messina - see Horrocks, 1975). Scale bar about 0,5 mm.

which are both reversible reactions controlled not only by pressure and temperature, but also by the partial pressure of water at the time of the metamorphism, which may be estimated using the following reaction (S.W. Richardson, pers. comm.):



Garnet bearing assemblages in these rocks have two forms: either (i) garnet may occur in coexistence with the amphibole and pyroxene; or (ii) the garnet may occur with distinctive kelyphytic coronas as is the case in hornblende-rich varieties (Figures 13 and 14) which impart the characteristic 'spotted' appearance to the hand specimen. In the former, the following reaction may in part account for the texture observed (De Waard, 1965):

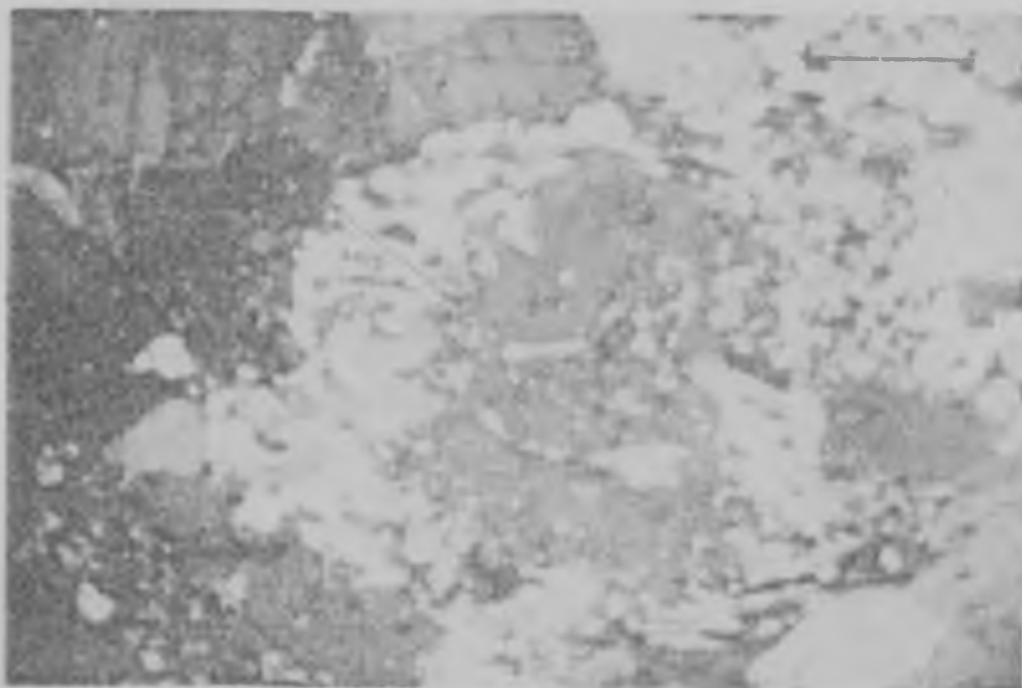


Figure 13: Kelyphitic corona texture about garnet (gar) in an amphibole-rich pyroxenitic amphibolite from the Farm Artonvilla (7 km east of Messina - see Horrocks, 1975). The scale bar is approximately 0,5 mm.



Figure 14: Kelyphitic aggregates of altered plagioclase, amphibole and clinopyroxene in an amphibole-rich pyroxenitic amphibolite from the Farm Artonvilla (7 km east of Messina - see Horrocks, 1975). The scale bar is about 0,5 mm.

hornblende + almandine + quartz = hypersthene + plagioclase + H<sub>2</sub>O

However, in the kelyphitic textures, the garnet is 'armoured' from the hornblende by a rim composed mainly of plagioclase, but which also contains inclusions of clinopyroxene and hornblende.

This suggests a reaction which may have the form:

hornblende + garnet = plagioclase + pyroxene + H<sub>2</sub>O

The presence of garnet in these assemblages may be ascribed to an earlier reaction described by Green and Ringwood (1967):

orthopyroxene + plagioclase = garnet + clinopyroxene + quartz  
which signifies their transition from lower pressure granulites to higher pressure granulites.

Whole-rock geochemical data for these rock-types are presented in Table 4 together with their respective C.I.P.W. normative assemblages. They reveal the calcic nature of these lithologies, and pyroxene, plagioclase and quartz are the major normative minerals calculated. Hornblende is not calculated in a C.I.P.W. norm. Magnetite and ilmenite are important constituents, and in some samples comprise over 7 per cent of the normative assemblage.

Electron probe microanalyses of minerals from these rocks (see Appendix 2) have been obtained for the application of various geobarometers and geothermometers. In addition, the activity of water may be calculated using these mineral parageneses. Data for feldspars, orthopyroxenes, clinopyroxenes

Table 4: Whole-rock analyses of pyroxenitic amphibolites and their C.I.P.W. norms

	1	2	3	4	5	6	7	8	9	10	Average of 3 to 10	1σ
SiO <sub>2</sub>	57.58	61.57	49.92	49.98	48.39	48.72	50.32	49.47	49.97	46.92	49.21	1.14
TiO <sub>2</sub>	1.18	0.88	1.50	1.26	1.09	1.57	1.35	1.26	1.01	1.08	1.27	0.20
Al <sub>2</sub> O <sub>3</sub>	13.48	15.75	13.74	14.62	15.07	13.57	14.52	14.39	15.04	15.41	14.55	0.64
Fe <sub>2</sub> O <sub>3</sub>	4.45	7.08	15.40	13.18	12.38	16.00	14.45	13.57	12.28	13.93	13.90	1.34
MnO	0.08	0.11	0.26	0.39	0.30	0.44	0.35	0.46	0.39	0.28	0.36	0.07
MgO	5.35	3.51	6.48	6.98	7.99	6.54	6.41	7.06	8.00	8.07	7.19	0.72
CaO	13.17	6.29	9.98	9.83	9.81	9.64	9.35	8.78	9.46	9.87	9.47	0.46
Na <sub>2</sub> O	2.63	3.10	1.77	2.29	2.22	1.70	1.87	2.38	1.74	1.64	1.95	0.30
K <sub>2</sub> O	0.33	1.71	1.03	1.46	1.19	1.02	1.17	1.48	1.29	1.22	1.23	0.17
P <sub>2</sub> O <sub>5</sub>	-	0.20	0.09	0.08	0.06	0.10	0.08	0.09	0.06	0.04	0.08	0.02
LOI	0.86	0.33	0.72	1.10	1.69	0.78	0.93	1.22	1.66	1.72	1.23	0.42
Total	99.15	100.53	100.89	100.17	100.21	100.08	100.80	100.16	100.90	100.18	100.42	0.37
Rb ppm.	11	44	-	-	-	-	-	-	-	-	-	-
Sr ppm.	163	356	-	-	-	-	-	-	-	-	-	-
Bo ppm.	53.3	469	-	-	-	-	-	-	-	-	-	-
K/Rb	300	389	-	-	-	-	-	-	-	-	-	-
Rb/Sr	0.07	0.11	-	-	-	-	-	-	-	-	-	-
quartz	12.08	16.38	1.48	-	-	0.60	1.63	-	-	-	-	-
orthoclase	1.99	10.05	6.03	8.66	7.13	6.02	6.87	8.80	7.63	7.30	-	-
albite	22.64	26.08	14.84	19.45	19.03	14.37	15.72	20.26	14.74	14.04	-	-
anorthite	24.41	23.86	26.25	25.38	27.98	26.33	27.58	24.34	29.43	31.44	-	-
diopside	26.63	2.69	9.33	8.30	9.78	8.54	7.67	8.57	8.47	8.46	-	-
hedenbergite	6.92	2.14	9.12	6.58	7.52	8.72	7.24	8.01	5.58	6.20	-	-
enstatite	1.31	7.44	11.66	10.91	4.68	12.30	12.30	8.65	15.42	7.66	-	-
ferrosilite	0.41	7.20	13.86	10.53	4.38	15.29	14.10	8.60	12.36	6.82	-	-
forsterite	-	-	-	2.27	7.66	-	-	4.28	0.41	6.13	-	-
fayalite	-	-	-	1.57	7.45	-	-	3.06	0.35	5.68	-	-
magnetite	1.31	2.05	4.42	2.82	2.17	4.63	4.16	2.90	3.57	4.09	-	-
ilmenite	2.28	1.66	2.82	1.80	2.10	2.98	2.55	1.80	1.92	2.08	-	-
apatite	0.02	0.46	0.21	0.17	0.14	0.23	0.18	0.19	0.14	0.09	-	-

1: pyroxenitic amphibolite (28-5-K) - Farm Shangani.  
 2: pyroxenitic amphibolite (18-6-C) - Farm Vaenan.  
 3 - 10: pyroxenitic amphibolite (B77-44 to B77-51) - Farm Magdala.

Analyst: P.C. Horrocks  
 Total Fe determined as Fe<sub>2</sub>O<sub>3</sub>  
 LOI = loss of ignition.

hornblendes and garnets which are in coexistence are presented in Appendix 2. The garnet is generally unzoned, in contrast to those in the garnet-cordierite-sillimanite gneiss and typically gives Mg/Mg+Fe ratios of about 0,2. Grossular forms an important component of these garnets in amounts up to 30 per cent in addition to almandine and pyrope.

#### Quartzite and banded magnetite quartzite

The quartzites form prominent ridges in the area, particularly in the north-western region (see Map 1 in rear pocket) where they are typically interlayered with considerable thicknesses of pyroxenitic amphibolite. Boudins of banded magnetite quartzite and bodies of garnet quartzite, serpentinite and pyroxenite also occur in close and characteristic association with the quartzites. Although the quartzites are only a few metres thick, the abundant float and scree material obscures the outcrop of other lithologies, and creates a false impression of the thickness of the quartzite units.

The quartzite is largely recrystallized, and in many outcrops assumes a milky vein-quartz appearance. In places, the rock contains disseminated leucocratic and melanocratic minerals ranging from 1 to 3 mm in size. At some localities, for example on the Farm Dover, the quartzite is distinctly sillimanite bearing which imparts a marked linear fabric to the rock. An unusual garnet quartzite occurs on the Farm Heuningfontein

interlayered with other quartzo-feldspathic and amphibolitic gneisses, and is composed of quartz scattered with garnet grains ranging up to 8 mm in diameter.

In thin section, other disseminated minerals apart from quartz include oligoclase, biotite, orthopyroxene which in places contains inclusions of clinopyroxene and amphibole, amphibole, clinopyroxene, rutile needles, sillimanite and sericitic micas. These disseminated minerals range up to 3 mm in size, and occur both along quartz grain boundaries and included within quartz grains. They often produce a microscopic fabric due to the alignment of their longest dimensions (Figure 15). The plagioclase commonly displays intense sericitization,



Figure 15: Rutile needles in quartz in a quartzite from the Farm Artonvilla (7 km east of Messina - see Horrocks, 1975). Scale bar is approximately 0,5 mm.

while the quartz grain boundaries are typically dusted with iron oxides and sericitic mica flakes. The equidimensional shapes and polygonization of the quartz grains suggest that they are largely recrystallized, and they show little or no undulose extinction. However, deformation bands are common in these rocks within the larger quartz grains (Figure 16) and are revealed by their small optical orientation differences. Trails of fluid inclusions are also common in the quartz grains.

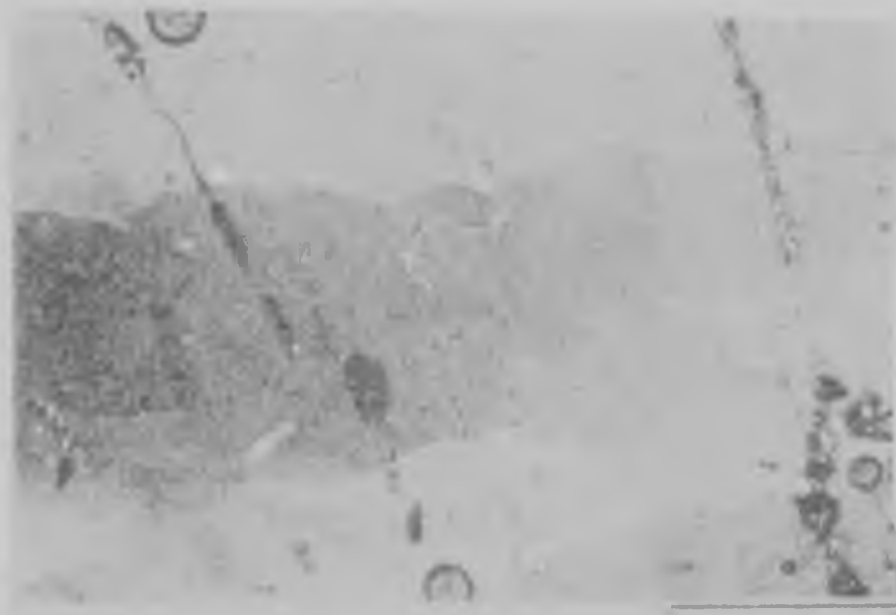


Figure 16: Deformation band in a quartz grain in a quartzite from the Farm Artonvilla (7 km east of Messina - see Horrocks, 1975). The scale bar is about 0,5 mm.

The garnet quartzite which crops out on the Farm Heuningfontein is notable for the large garnet porphyroblasts which range up to 5 mm in diameter. The rock has the following approximate modal composition: 30 per cent garnet, 60 per cent

quartz, 5 per cent andesine, 2 per cent hornblende, 1 per cent clinopyroxene, 2 per cent alteration minerals, accessory opaque minerals and accessory allanite. The garnet forms distinctive atoll structures in places, with idioblastic outlines and quartz-filled cores (Figure 17). The other silicate minerals are commonly obscured by alteration products. Abundant metamict allanite grains are dispersed in the quartz and show radial fractures and trails of fluid inclusions surrounding them and penetrating the adjacent minerals (Figure 18). Deformation bands are also present in this rock-type.

The banded magnetite quartzite is mainly developed within pyroxenitic amphibolite units interlayered with the quartzite in the north and north-west of the study area (see Map 1 in rear

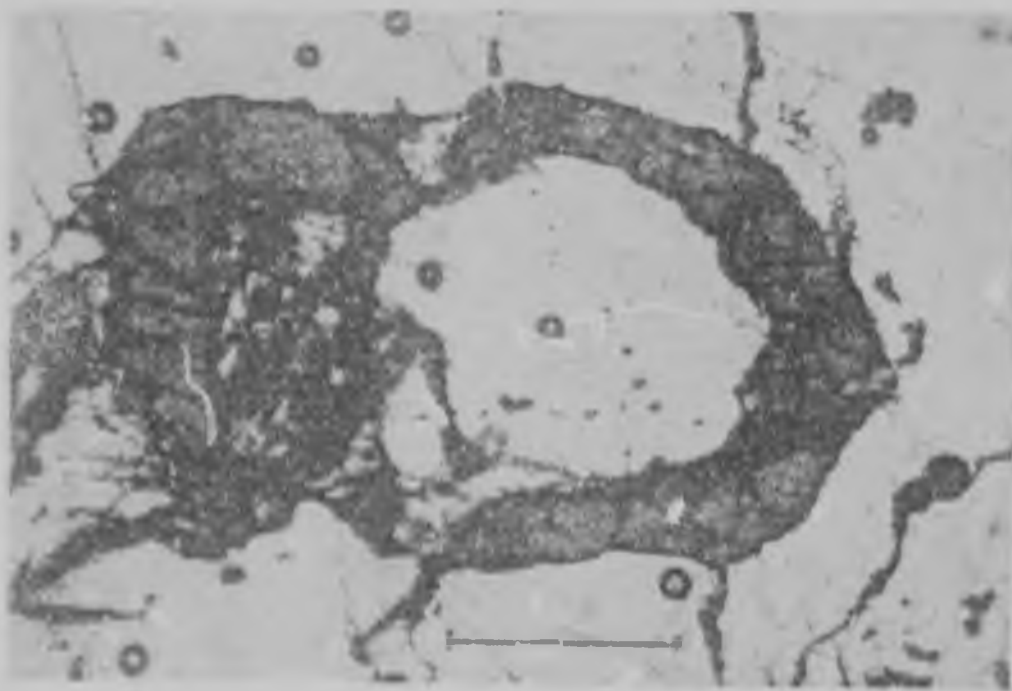


Figure 17: Atoll structure of garnet in a garnet quartzite from the Farm Heuningfontein (2 km west of the main Messina-Tshipise road - see Map 1 in rear pocket). Scale bar is about 0,5 mm.



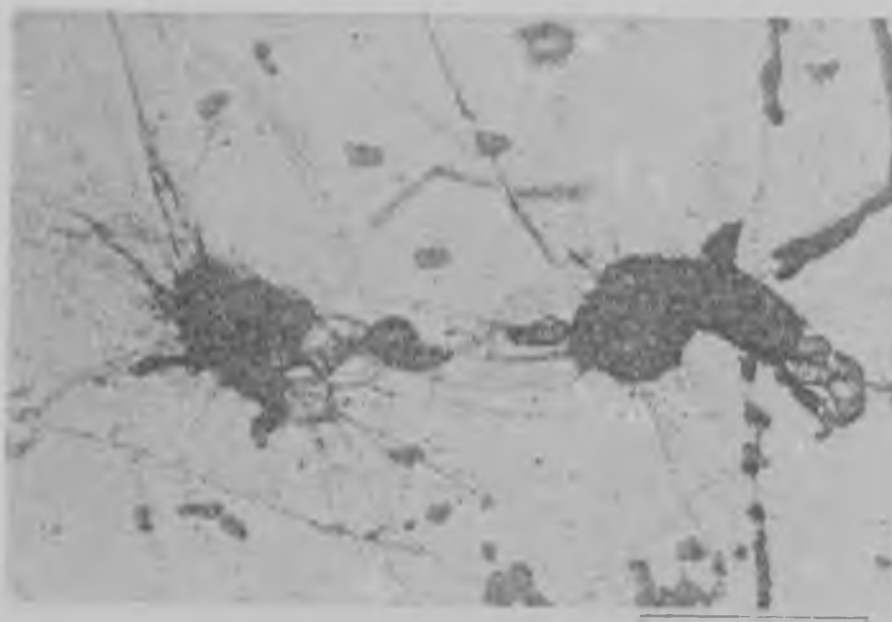


Figure 18: Metamict allanite grains in a garnet quartzite from the Farm Heuningfontein (2 km west of the main Messina-Tshipise road - see Map 1 in rear pocket). The scale bar is approximately 0,5 mm.

pocket). The rock is notable for the presence of well developed and well exposed minor fold structures. The rock also forms a useful marker horizon. The rock has a high viscosity in comparison to the surrounding lithologies, which are mainly pyroxenitic amphibolite, and hence is extensively boudinaged during the obvious attenuation these lithologies have experienced. Thus units of this rock-type occur over an extensive but discontinuous strike length. The rock contains fine laminations from 1 to 4 mm in thickness made up of alternating quartz and magnetite layers.

This fine banding in these rocks can be clearly seen in thin section (Figure 19). The magnetite grains are typically

idioblastic and detached from each other giving the rock a very granular appearance. The layers have the appearance of being 'graded' (Figure 19) with sharply bounded 'bottom' surfaces from which the densely packed and fine grained magnetite grades upwards, becoming more coarse grained, and less densely packed with an increasing proportion of interstitial quartz. The quartz grains are recrystallized with little or no undulose extinction, and are characterized by a cloudy appearance due to large amounts of submicroscopic particles, probably iron oxides, bubbles and fluid inclusion trails (Figure 20).

A more massively recrystallized haematitic ore occurs within a unit of this rock type on the Farm Heuningfontein (see Map 1 in rear pocket) and in the past has been mined for its iron content, as have other localities of this rock type in the area under study. In places, amphibole asbestos occurs with fibres ranging up to 5 cm in length. Also, highly altered amphiboles and small radiating clusters of sillimanite needles up to 1 cm in length occur with this ore.

A whole-rock analysis of a sample of this rock type from the Farm Heuningfontein is presented in Table 5. Over 95 per cent of the rock is made up of silica and iron oxide.  $TiO_2$  makes up a very low proportion of this rock (0,01 per cent) and distinguishes these rocks from the chromium and titanium bearing magnetitites occurring within the intrusive rocks of the Messina Layered Intrusion (Söhnge, 1946; Barton et al., 1979a).  $Na_2O$

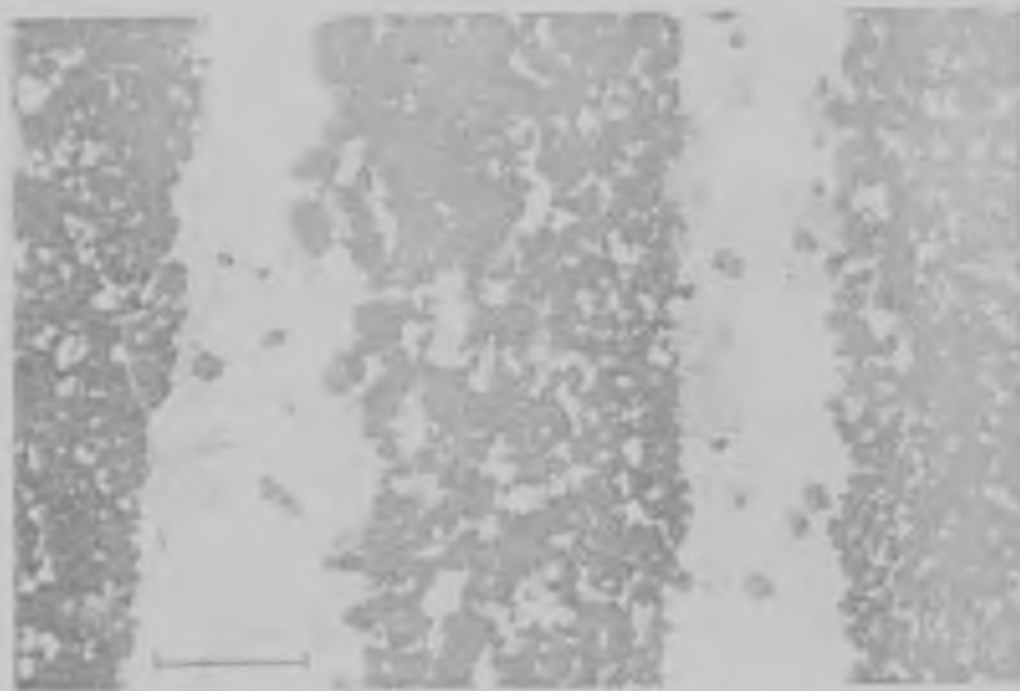


Figure 19: Laminations in a banded magnetite quartzite from the Farm Heuningfontein (1 km west of the main Messina-Tshipise road - see Map 1 in rear pocket). Note the graded grain size of magnetite granules within the laminations. The scale bar is approximately 0,5 mm.

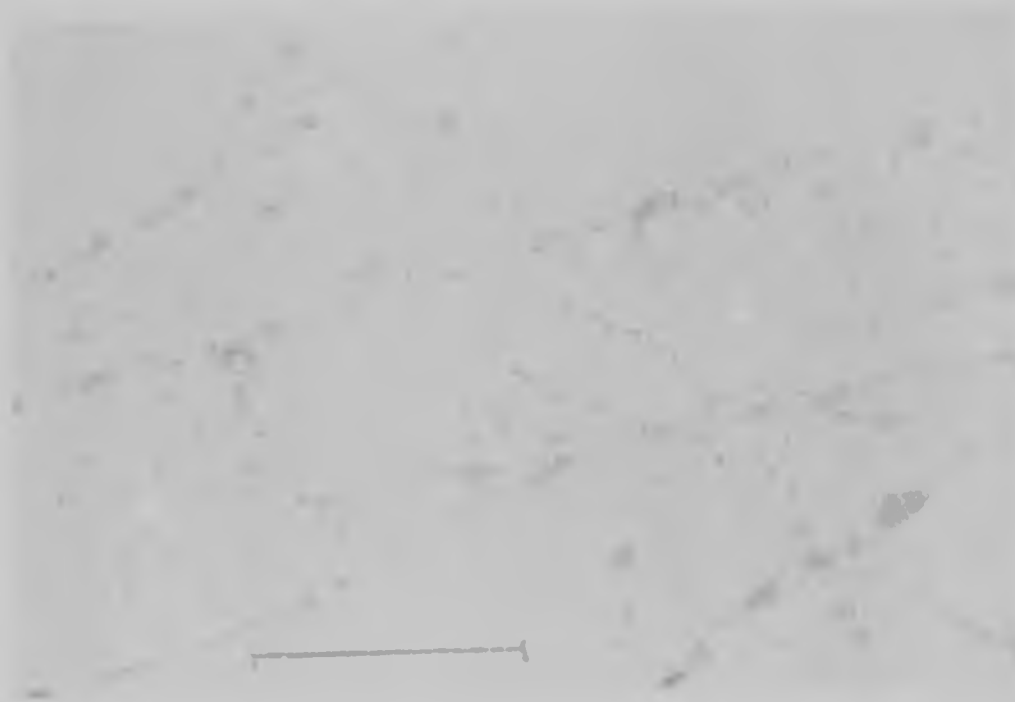


Figure 20: Fluid inclusions, some of which contain gas bubbles, in a banded magnetite quartzite from the Farm Heuningfontein (1 km west of the main Messina-Tshipise road - see Map 1 in rear pocket). The scale bar is about 0,05 mm.

Table 5: A whole-rock analysis of a banded magnetite quartzite  
(sample no.4-2-13, Farm Heuningfontein - see Map 2 in rear  
pocket)

SiO <sub>2</sub>	47,81
TiO <sub>2</sub>	0,01
Al <sub>2</sub> O <sub>3</sub>	0,59
FeO	45,18
MnO	0,06
MgO	0,91
CaO	0,09
Na <sub>2</sub> O	4,57
K <sub>2</sub> O	-
P <sub>2</sub> O <sub>5</sub>	0,04
LOI	0,53
Total	99,79

Analyst: P.C.B. Horrocks  
 Total iron determined as FeO  
 LOI = loss on ignition

forms a significant amount in the rock (over 4,5 per cent) and is probably associated with altered plagioclase which occurs in small quantities in these rocks.

#### Calc-silicate gneiss and marble

The calc-silicate gneiss characteristically forms prominent outcrops due to its resistance to weathering. These rocks are well banded with bands usually only a few millimetres in thickness made up of alternating melanocratic and leucocratic layers. Like the banded magnetite quartzite, this rock is characterized by minor fold structures and is useful as a structural and as a mapping marker horizon. The mineral grains are of uniform size ranging from 1 to 3 mm in diameter, although some massive greyish coloured varieties containing carbonate minerals also occur, usually adjacent to units of marble.

The mineralogical composition of calc-silicate varieties occurring in the area under study is as follows: 45 - 55 per cent labradorite, 10 - 35 per cent diopside, 0 - 20 per cent hornblende, 0 - 15 per cent calcite, 0 - 10 per cent quartz, 0 - 5 per cent biotite, accessory opaque minerals and accessory zircon. They are characterized by abundant calcic plagioclase and weakly pleochroic pale green diopside. The plagioclase is frequently heavily altered and replaced by sericitic micas, while some samples contain numerous zircons which are generally free of metamict texture.

Marbles are not abundant in the area mapped, but occur much more frequently in the south-east in the vicinity of the village of Tshipise (Figure 2). The main occurrence in the study area forms prominent ridges in the south-east of the area parallel to and just north-west of the Bosbokpoort Fault (see Map 1 in rear pocket). Minor quantities of carbonate-bearing rocks also occur on the Farms Shangani and Boulogne (see Map 1 in rear pocket). The interlocking carbonate grains up to 4 mm in diameter give the rock a coarsely crystalline texture. The silicate minerals, often heavily altered, range up to 5 mm in diameter and impart a speckled appearance to the rock. This lithology weathers positively in the dry climate of the area.

In thin section, the marbles typically comprise about 30 per cent ferromagnesian silicates and 70 per cent carbonate material. The greenish silicates are heavily serpentinized olivines, now entirely composed of serpentine whose development resulted in magnetite exsolution. The Alizarin Red S test (sodium alizarinsulphonate in dilute hydrochloric acid) produced a reddish violet stain when applied to the carbonate grains, indicating that the composition is largely calcitic ( $\text{CaCO}_3$ ).

#### Metapyroxenite and serpentinite

The metapyroxenites, termed 'perknites' by Söhngé (1946), form good outcrops due to their resistance to weathering. The rock is hard and brittle, forming small hillocks of dark reddish

brown to black sharp-edged boulders. The pyroxenite is coarse grained and contains reddish pyroxene megacrysts up to 2 cm in diameter. The serpentinites, in contrast, weather more readily and form poor outcrops usually covered with a rubble of whitish and greyish coloured boulders. In places, the serpentinite preserves original pyroxene occurring in layers up to 2 cm thick and is only partially serpentitized. Both of these rock types occur as pod-like or boudin-like bodies. In general, they are confined to a zone in the north, north-west and west of the area (see Map 1 in rear pocket) which contains the most extensive outcrops of quartzite, banded magnetite quartzite and pyroxenitic amphibolite. Three relatively large outcrops of these rock-types occur within the region:

1. An oval shaped body about 400 by 700 m in size is exposed on the Farm Shangani (see Map 1 in rear pocket). This locality displays amphibolitization, and the major part of the rock is made up of amphibole grains ranging up to 5 mm in size. Peripheral pyroxenites rim the outcrop. Several pegmatites cut the rock, some of which display green malachite staining.
2. An outcrop 600 to 1 500 m occurs on the Farms Veenen and Dover enclosed by quartzites (see Map 1 in rear pocket). A few small veins of amphibole asbestos, usually less than 1 cm thick, cut through the serpentitized portions of the body, while numerous small pods and outlying lenses of pyroxenite and

serpentinite occur in the surrounding area adjacent to the large outcrop.

3. On the Farm Middelbult, an outcrop of 600 by 1 100 m in size occurs. It is strongly serpentized and cut by numerous pegmatites.

In the reddish coarse grained metapyroxenites, thin sections reveal distinctive orthopyroxene megacrysts. These are poikiloblastic hypersthene, and commonly contain inclusions of clinopyroxene and the green spinel hercynite (Figure 21). The matrix to these hypersthene is made up of smaller equant grains of clinopyroxene, with scattered spinels and pale-brown amphiboles.

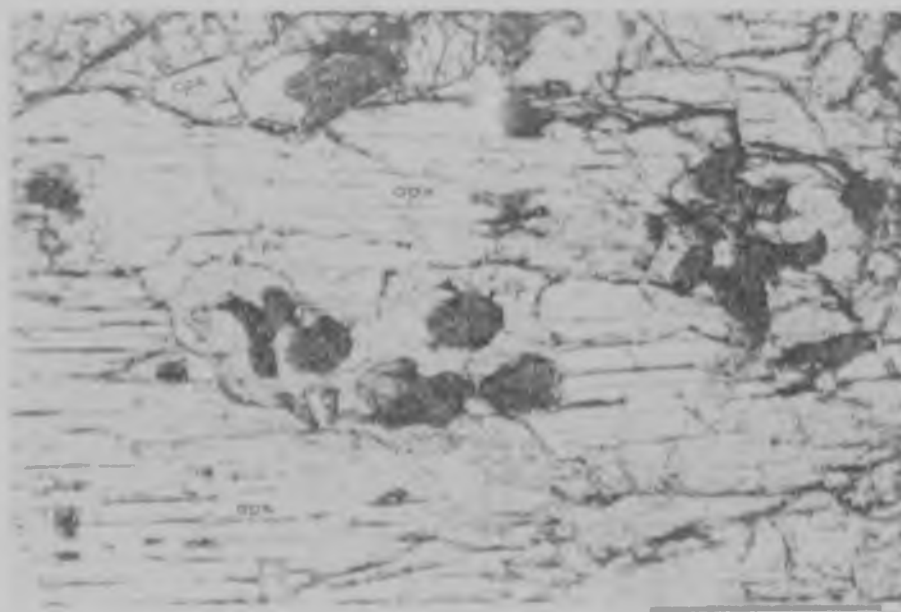


Figure 21: Poikiloblastic hypersthene megacryst (opx) containing clinopyroxene (cpx) and hercynite inclusions (sp), in a metapyroxenite from the Farm Artonvilla (7 km east of Messina - see Horrocks, 1975). The scale bar is about 0,5 mm.



The amphibolitized variety occurring on Farm Shangani is essentially monominerallic in places. Pale amphiboles with cleavage planes either poorly developed or absent produce a recrystallized granoblastic texture, with well-formed  $120^\circ$  triple point junctions between the idioblastic grains (Figure 22). An X-ray powder diffraction scan on this mineral revealed tremolite 'peaks' suggesting that this rock has resulted from a hydrous alteration. Some samples contain minor amounts of an altered clinopyroxene, and highly altered and sericitized plagioclase which occurs along the amphibole grain boundaries and in the interstices.



Figure 22: Recrystallized tremolitic amphibole in an amphibolitized metapyroxenite from the Farm Shangani (4 km west of the main Mossina-Tshipise road - see Map 1 in rear pocket). The scale bar is about 0,5 mm.

The serpentinites contain variable amounts of pyroxene and amphibole, many of which are obscured by hydrous alteration products. The degree of serpentinization is variable from sample to sample, with some showing complete replacement textures of serpentine and magnetite. The magnetite is exsolved along certain serpentine lamellae and reveals ghost outlines of previous cleavage planes in what was mainly pyroxene, but possibly also olivine grains. In places, orthopyroxene remnants occur surrounded by serpentine (Figure 23) perhaps reflecting the reaction:



Figure 23: Serpentine (serp) replacing orthopyroxene (opx) in a serpentinite from the Farm Heuningfontein (500 m west of the main Messina -Tshipise road - see Map 1 in rear pocket). The scale bar is approximately 0,5 mm. Abundant hornblende (hnble) occurs in this rock.

Some samples are composed almost entirely of amphibole and pyroxene and are only cut in places by thin layers of serpentine up to 1 mm thick (Figure 24). In this case, only non-hydrous minerals such as pyroxene appear to be affected by the serpentinization process while already hydrous minerals such as amphibole have remained stable and unaffected by the growth of serpentine. This process enhances any mineralogical layering existing in the rock.



Figure 24: Serpentine (serp) occurring in thin bands in a serpentinite from the Farm Heuningfontein (500 m west of the main Messina-Tshipise road - see Map 1 in rear pocket). Note the magnetite (mag) exsolution outlining earlier grain shapes (probably pyroxene) while the amphibole (hnbld) is un-serpentinized. The scale bar is about 0,5 mm.

Whole-rock and mineral geochemical data for these rocks is presented in a complementary study (Fripp, 1981c). Additional mineral analyses obtained in this study are presented in

Appendix 2 and include electron probe microanalyses of orthopyroxene, clinopyroxene, amphibole and spinel. These data are discussed later in relation to various methods of geothermometry.

#### Gabbroic and anorthositic gneisses of the Messina Layered Intrusion

These rocks which belong to the Messina Layered Intrusion (Barton et al., 1979a) comprise a variety of plagioclase bearing units in the study area. They form sheet-like layers which appear to be concordant with the supracrustal stratigraphy over most of the area. They reach a maximum thickness of about 2 km in outcrop in the northern part of the area on the Farm Boschrand (see Map 1 in rear pocket) where the body contains a central axis of tightly folded units of pyroxenite, quartzite, banded magnetite quartzite, calc-silicate and other paragneisses up to a maximum thickness of about 25 m. Towards the south, the anorthositic and gabbroic gneisses thin appreciably and become boudinaged in places, such as on the Farms Dover, Veenen and Heuningfontein (see Map 1 in rear pocket). On the Farm Shangani, the unit displays a compositional symmetry across its width (about 500 m). More melanocratic gabbroic varieties occur along its margins with the country rock, while the centre contains a more monominerallic plagioclase anorthositic rock.

In places, magnetite occurs within the anorthositic rocks such as on the Farm Boulogne and Boschrand (see Map 1 in rear pocket). The magnetite is clearly distinguishable from the banded magnetite quartzite which occurs within the surrounding gneisses in that it has a more massive and crystalline appearance and lacks the presence of quartz and the finely banded laminations characteristic of the latter. The magnetite grains are up to 4 mm in diameter, while the even grained anorthositic rocks have grain sizes which vary from about 1 mm to 4 mm. Plagioclase megacrysts up to 10 cm in size are known to occur. Melanocratic minerals are predominantly pyroxenes and amphiboles, although olivine and garnet have been described in this rock (Söhne, 1946; Bahnemann, 1972; Barton et al., 1979a). Discrete melanocratic units occur within the anorthositic and gabbroic rocks, and are often dyke or sill-like in form. Commonly, they are boudinaged along their strike. Also, they display a form of graded layering, where plagioclase megacrysts or aggregates grade in size across the thickness of the units (see Plates in Barton et al., 1979a). These structures have been interpreted as 'fining upward' cycles, and used to provide facing directions in these rocks (Barton et al., 1979a). Wherever they are observed, these directions appear to be consistent, although reversals in direction occur due to internal folding. Also, the metopyroxenite and serpentinites described earlier have been regarded as forming

an integral part of the Messina Layered Intrusion suite (Barton et al., 1979a). However, within the study area, no direct spatial association between these rock types was observed.

The rocks of the Messina Layered Intrusion vary in composition from more plagioclase-rich anorthosites to more melanocratic gabbros. Mineralogical compositions are presented below for two typical end-members in this range. An approximate mode for the anorthosite is as follows: 90 per cent plagioclase, 7 per cent clinopyroxene, 3 per cent quartz and accessory ore; and for the gabbro: 45 per cent plagioclase, 40 per cent hornblende, 10 per cent clinopyroxene, 5 per cent quartz and alteration minerals. Using the refractive index method on cleavage fragments (see p.327, Deer et al., 1966), compositions of the plagioclase were estimated. Typical values of the refractive index,  $n_a$ , varied from about 1,560 to 1,565 which suggests anorthite contents in the plagioclase from about 60 per cent to 70 per cent (labradorite to bytownite). The plagioclase is commonly sericitized, and typically forms cumulate-type equant grains. The clinopyroxene is typically highly altered and replaced by chlorite, and together with quartz, occurs as intercumulus-type material in the interstitial spaces between the plagioclase grains (Figure 25). A replacement texture occurs in some of the more gabbroic samples whereby the often chloritized clinopyroxene appears to replace hornblende and contains



Figure 25: Interstitial altered clinopyroxene between plagioclase in an anorthositic gneiss from the Farm Shangani (4 km west of the main Messina-Tshipise road - see Map 1 in rear pocket). Scale bar is about 0,5 mm.

optically continuous inclusions of the amphibole (Figure 26) probably by a reaction of the form:



Alteration is apparent in these rock-types and common alteration minerals include epidote, zoisite, chlorite and sericitic micas.

Whole-rock analyses of samples collected on Shangani, Veenen and Heuningfontein, although an integral part of the present study, are included in a joint publication (Barton *et al.*, 1979a, Table 1). The six samples from Farm Shangani were collected on a slightly oblique traverse across the width of the unit at approximately 100 m intervals in an attempt to show the compositional variation which is apparent in this region.



Figure 26: Clinopyroxene (cpx) replacing and containing optically continuous inclusions of hornblende (hnble) in a gabbroic gneiss from the Farm Shangani (4 km west of the main Messina-Tshipise road - see Map 1 in rear pocket). The scale bar is approximately 0,5 mm.

Samples 26-5-A and 26-5-F are positioned close to the margins of the unit and are the most gabbroic in composition. Samples 26-5-B, 26-5-C, 26-5-D and 26-5-E are spaced between and reveal more anorthositic compositions.  $\text{SiO}_2$ ,  $\text{Al}_2\text{O}_3$  and  $\text{CaO}$  are the most abundant constituents commonly making up over 90 of the rock by weight.  $\text{K}_2\text{O}$  usually comprises less than 1 per cent of the rock. Sr and Ba show wide variations.

Electron probe microanalyses of hornblende, clinopyroxene and plagioclase from these rocks are presented in Appendix 2. Use has been made of the mineral analytical data in geobarometer calculations discussed later.



### Discussion

The area studied does not lend itself well to the problem of recognizing and describing the differences between 'basement' and supracrustal components of the geology of the area. The isolated outcrops of the grey banded gneisses recognized as being basement are unfortunately found in regions of poor exposure, and contacts with the supracrustal gneisses were not observed. However, the basement gneisses were recognized as such by their obvious physical characteristics comparable to the Sand River Gneisses described in detail as being a basement to supracrustal cover units by Fripp (1981a-c). These gneisses are amongst the most ancient occurring on the Earth, and have provided whole-rock Rb-Sr isochrons of about 3 800 m.y. (Barton et al., 1978). Thus they can be compared with the Isua supracrustals and Amitsoq gneisses of the Archaean terrane in Greenland (Bridgewater et al., 1976). The mafic dykes may be the equivalents of the Ameralik dykes in Greenland, though two ages of these ancient deformed dykes are described in the Sand River Gneisses (Barton et al., 1977). It has not been possible to distinguish in the mapped area which of these two dyke events, at 3 570 and 3 060 m.y. respectively (see Table 1), is represented by the mafic dykes occurring in the basement outcrops in the study area (e.g. Figure 3).

The bulk of the area is underlain by supracrustal gneisses,

which are recognized as such due to their heterogeneous composition. The interbanding of units such as quartzite, banded magnetite quartzite, marble, calc-silicate gneiss and metapelitic garnet-cordierite-sillimanite gneiss suggests a stratigraphy which can only belong to a supracrustal sequence.

The quartzo-feldspathic gneisses form the largest volume of the supracrustal rocks exposed in the study area. The observations of cross-cutting quartzo-feldspathic dykes in the upper supracrustal units, and the intrusion of large masses into the basement gneisses are suggestive of a partial melting origin for these lithologies, and it is concluded that the ubiquitous distribution and abundance of quartzo-feldspathic units in the area reflect the considerable degree of anatexis that occurred during the metamorphism and tectonism in the region. The garnet-cordierite-sillimanite gneisses are always associated with the quartzo-feldspathic gneisses, and together with the high Al and Mg refractory corundum and sapphirine-bearing rocks ('restites') support the contention that anatexis has been widespread in these regions. Although these rocks are comprised of predominantly quartz and feldspar, considerable variations in the proportions of CaO, Na<sub>2</sub>O, K<sub>2</sub>O, Rb, Sr and Ba occur, revealing the relative mobilities of these components in these rocks under high grade metamorphic conditions and anatexis.

The composition of the Singelele-type granitoid gneiss may

be closely compared with average compositions of rhyolites and arkoses (Table 6) and can be seen to closely match the composition of an average rhyolite. Also, the analytical data of the Singelele samples obtained from within the study area (Table 2) when plotted in a Qz-Ab-Or ternary diagram (Figure 27) falls within the field of quartz-rich granites. Thus, although the rock may have experienced anatexis, it is highly probable that its origin was volcanic, being extruded contemporaneously with the sedimentation of the other supracrustal lithologies. A study of the Rb, Sr and Ba trace element patterns in this rock (McCarthy, 1977) has shown that considerable partial melting occurred during the peak of metamorphism that affected the Singelele gneiss, and that a partial melt fraction enriched in Rb and Ba was extracted and locally separated from a residual fraction richer in Sr. From samples collected at the type locality in the Singelele Hills near Messina (Figure 2) the partial melt fraction typically shows about 78 per cent  $\text{SiO}_2$  in its composition, while the residue shows about 72 per cent  $\text{SiO}_2$ . The Singelele samples from Farm Ostend have values which average close to 78 per cent  $\text{SiO}_2$ , and probably indicates that these outcrops in the study area are made up of mainly partially melted material. Thus the conclusion of Bahnmann (1973) and McCarthy (1977) that the Singelele granitoid owes its origin in part or locally to anatexis is supported, although no evidence could be

Table 6: Comparison of the Singelele-type granitoid gneiss composition with those of rhyolite and arkose

	1	2	3
SiO <sub>2</sub>	78,79	76,21	75,57
TiO <sub>2</sub>	0,12	0,07	0,42
Al <sub>2</sub> O <sub>3</sub>	11,21	12,58	11,38
Fe <sub>2</sub> O <sub>3</sub>	1,88	0,30	0,82
FeO	-	0,73	1,63
MnO	0,01	0,04	0,05
MgO	0,07	0,03	0,72
CaO	0,49	0,61	1,69
Na <sub>2</sub> O	3,19	4,05	2,45
K <sub>2</sub> O	4,63	4,72	3,35
P <sub>2</sub> O <sub>5</sub>	0,04	0,01	0,30
H <sub>2</sub> O+			1,06
H <sub>2</sub> O-	{ 0,17	{ 0,52	0,05
CO <sub>2</sub>			0,51
Total	100,59	99,87	100,00

- 1: average of 6 analyses of samples of Singelele-type granitoid gneiss (B76-85 to B76-90) - Farm Ostend (see Table 2, columns 5 to 10).
- 2: rhyolitic obsidian, Mono Craters, California (Carmichael et al., 1974, p.35).
- 3: average of three analyses of Torridonian arkose (Kennedy, 1951, p.258).

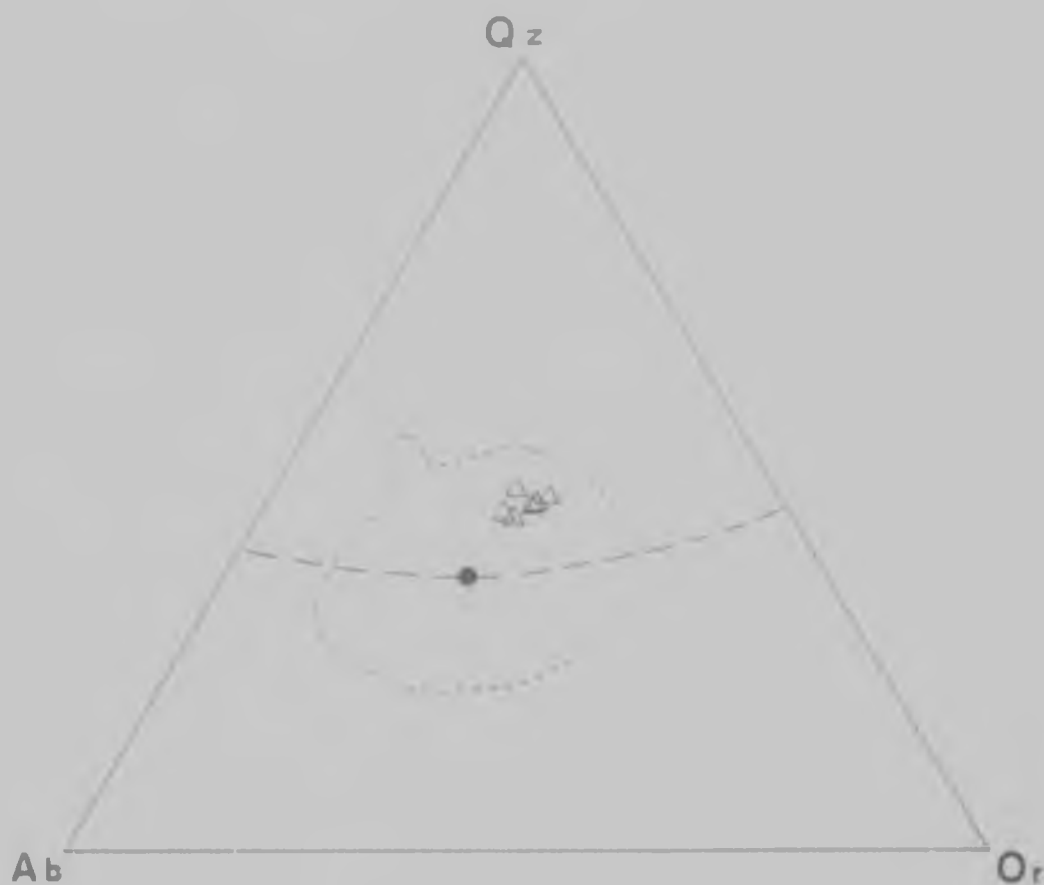


Figure 27: A quartz-albite-orthoclase (Qz-Ab-Or) ternary diagram showing the compositions (open triangles) of the Singelele-type granitoid gneiss sampled on the Farm Ostend (see Map 2 in rear pocket - data from Table 2). The dotted line outlines the region of anatectic granites, while the solid dot marks the temperature minimum on the dashed cotectic line (after Winkler, 1974).

found which supports Bahnemann's view that Singelele represents a remobilized melt from the other units in the stratigraphy, such as the anorthosite, quartzo-feldspathic gneiss, and garnet-cordierite-sillimanite gneiss. The Rb, Sr and Ba population of the Singelele samples are discrete from those of the other stratigraphic units, and are not dispersed in a differentiation trend. It may therefore be concluded that the Singelele-type granitoid represents a volcano-sedimentary unit of rhyolitic composition within the stratigraphic sequence, and not a later intrusive melt fraction as suggested by Bahnemann (1973). In addition, it has been shown that this rock has experienced all the structural deformation history that the other supracrustal units have undergone (Fripp et al., 1979) and hence this unit is at least as old as the other supracrustal rocks. As a readily distinguishable unit within the stratigraphy, the Singelele gneiss provides a useful marker horizon, as does the banded magnetite quartzite, and it may be assumed that these units each formed continuous horizons prior to tectonism.

The thinly banded calc-silicate and marble units confirm the supracrustal nature of the major part of stratigraphy in the study area, and it is important to notice the steady increase in abundance of these lithologies towards the south-east, to the point where they predominate in the region around Tshipise (Figure 2). This suggests a changing environment of deposition

for the supracrustals, where a suitable shallow water marine or shelf facies occupied the south-east region during sedimentation. However, the quartzite-banded magnetite quartzite-pyroxenitic amphibolite association in the north-west of the study area suggests a deeper water environment allowing the accumulation of cherts, thin shales, and volcanic material as the precursors of the present-day lithologies. The garnet-cordierite-sillimanite metapelitic gneisses may fall in an intermediate position between shelf and deep water facies, where shales, greywackes and turbidites would occur. In this way, it may be concluded that the supracrustal lithologies include a range of possible facies that occur in intercontinental basins or eugeosynclines.

The metapyroxenite and serpentinite are found mainly in a zone in the north-west of the study area. These units, lenses and boudins are commonly associated with the quartzites and pyroxenitic amphibolites, and appear to have belonged to a former single sheet-like or sill unit conformable with the stratigraphy. Thus it is suggested that an igneous origin is feasible for these lithologies, though no primary magmatic structures or textures were observed. However, no spacial relationship was seen between these rock types and those of the Messina Layered Intrusion, and it seems likely that they are unrelated. The gabbroic and anorthositic gneisses also form a conformable sill-like unit, and although these rock types may have been intruded





### CHAPTER 3: STRUCTURE

#### Introduction

The quality of the outcrop in the study area and the complex interlayering, infolding, and lensing of the stratigraphic units does not lend itself well to detailed structural mapping. The 1 : 25 000 scale of mapping is suitable for revealing only the larger scale structures. A scale of 1 : 2 000 similar to that used by the Geology Department of the Messina Copper Mines in their excellent surface mapping reveals the structural complexity of the region. Even more detailed mapping of individual outcrops and well-exposed areas has been invaluable in studying the structural features of the terrane (see Fripp, 1981a-c).

In this section, various large scale and small scale structural elements are discussed, and the field measurements of structural attitudes presented.

#### Large scale structure

Large scale structures are most obvious in the north-west of the area (see Map 1 in rear pocket). Towards the south-eastern portion of the area, the strata become progressively more attenuated in thickness and aligned to the regionally pervasive ENE trend of the Limpopo Mobile Belt as the Bosbokpoort Fault is approached (see Map 1 in rear pocket). South-east of

this fault, younger Jurassic sediments and some volcanics of the Karoo Supergroup occur which have very gentle dips, less than  $30^{\circ}$ , to the north. These sediments are fault bounded to their north, and lap off to the south onto the Precambrian gneisses which again occur near the village of Tshipise (Figure 2). The Precambrian rocks within the study area have all been folded to very steep dips, over  $60^{\circ}$ , and typically are sub-vertical to vertical in attitude.

Measurements were made of the orientation of the planes defined by the 'foliation' or mineral banding in the gneisses, and by bedding where recognized, such as in the quartzite, banded magnetite quartzite, calc-silicate gneiss and marble. The poles to these planes measured throughout the area have been plotted in an equal area stereographic projection, and display a non-random distribution (Figure 28). A great circle has been visually fitted to this distribution and represents a plane which strikes  $116^{\circ}$  and dips  $35^{\circ}$  N. The pole to this plane plunges  $55^{\circ}$  on a bearing of  $206^{\circ}$ , and is interpreted as the axis about which the above distribution has been dispersed, namely the overall fold axis for the area.

In addition, the above data have been divided into five selected areal domains (see Map 2 in rear pocket) on the basis that each contains an individual fold closure system. In this way, the fold axes for each of these domains were sought.

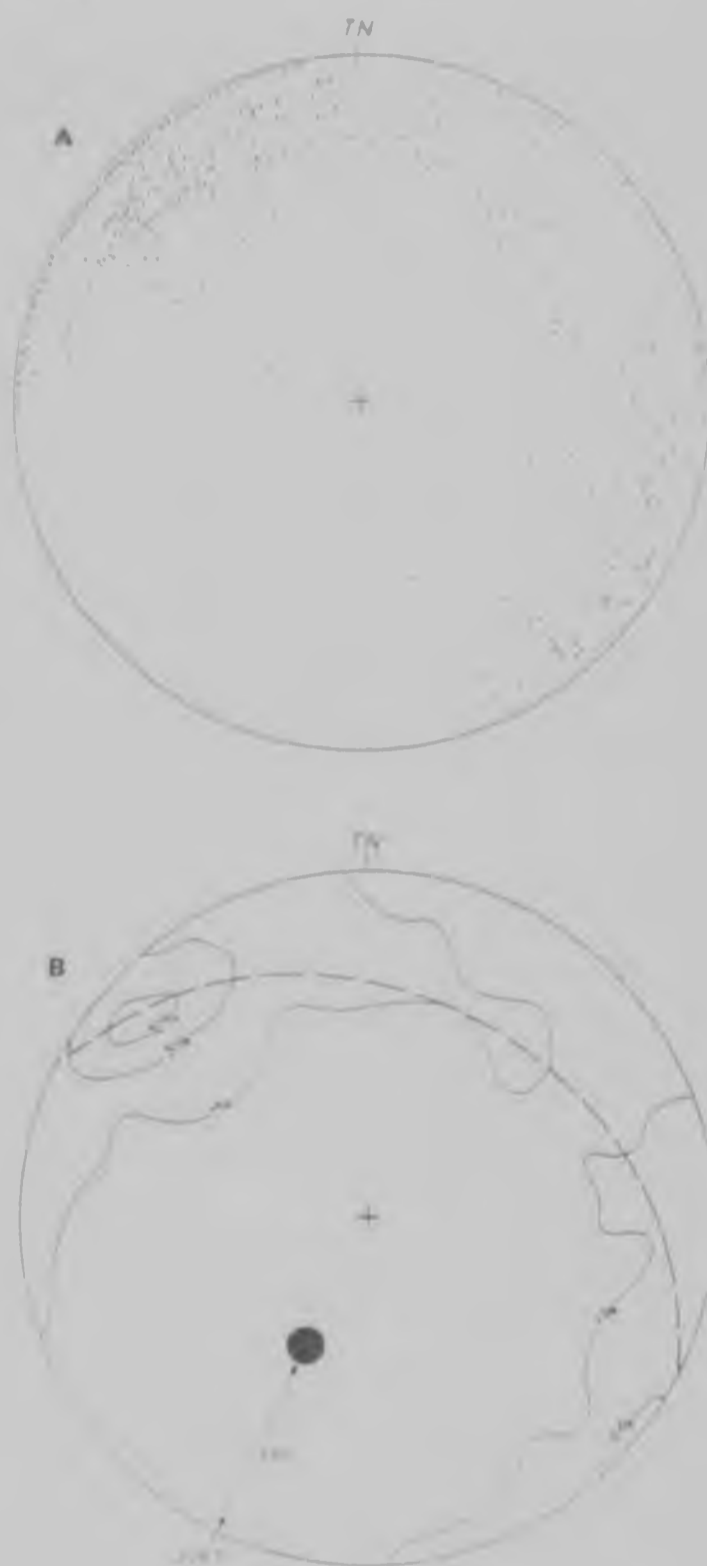


Figure 28: Equal area stereographic projection showing the orientation of bedding and mineral banding planes measured in the study area: A: poles to bedding and mineral banding planes (n=297); B: contoured data from A with contours at 1, 5 and 10 per cent intervals per 0,35 per cent area. Solid circle is a pole to the visually fitted great circle and plunges about  $55^{\circ}$  on a bearing of about  $210^{\circ}$ .

Domain I contains a fold closure in quartzites occurring in the eastern part of Farm Heuningfontein and the southwestern part of Farm Oorsprong (see Map 2 in rear pocket). A thin anorthosite unit on the western part of Farm Boulogne also clearly reveals this structure and is included in the domain. Two thin parallel bonded magnetite quartzite units not more than 1 m in thickness occur within pyroxenitic amphibolites folded around this closure. Owing to much boudinaging of these units, no small closures were observed linking these two units. The dip directions of the quartzites around this closure and the symmetry of a minor fold exposed on its eastern flank indicate that the structure is caused by a synform whose hinge line plunges moderately to the south-west. Expanding this domain to the south-west reveals the existence of a basin-like structure, elliptical in outcrop and about 3 km by 10 km in size. Poles to mineral banding and bedding planes were used to define a great circle (Figure 29) whose pole plunges  $80^{\circ}$  on an azimuth of  $173^{\circ}$ , and which probably reflects the fold axis of the synform within the domain.

Domain II contains a folded quartzite in the area around the junction of the Farms Heuningfontein, Oorsprong, Dover and Veenen (see Map 2 in rear pocket). In this area, a large serpentinite and metapyroxenite unit occurs, and this unit internally contains a folded quartzite unit. Close examination

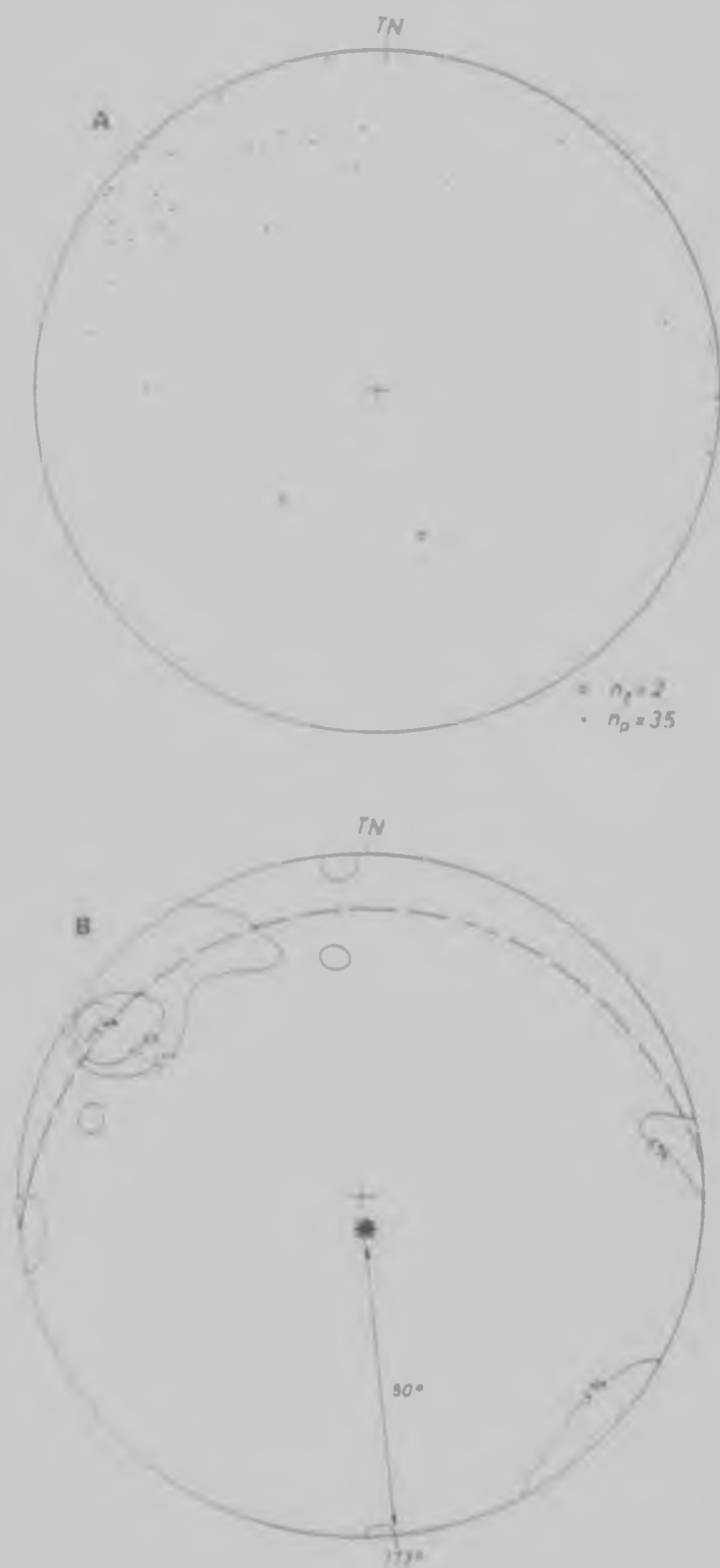


Figure 29: A: poles to bedding and mineral banding from Domain I (see Map 2 in rear pocket) plotted on an equal area stereographic projection ( $n_p=35$ ). Open circles are mineral lineation orientations (quartz rodding) in this domain ( $n_l=2$ ). B: contoured data from A with contours at 5, 10 and 15 per cent intervals per 1 per cent area. Star symbol is the pole to the visually fitted dashed great circle.

of this quartzite isolated within the serpentinite failed to reveal any fold closures within the quartzite, and this suggests that it does not represent an interference structure, but rather a boudin within the serpentinite. A 'foliation' within the serpentinite and metapyroxenite is accentuated by elongated orthopyroxene megacrysts, which follows the layering in the surrounding quartzites around the large scale fold closure. Poles to bedding and this 'foliation' cluster about a plane whose pole plunges about  $60^{\circ}$  on a bearing of about  $206^{\circ}$  (Figure 30). The fold displays an overall 'S'-type or left-lateral symmetry.

Domain III lies in the northern part of the Farm Oorsprong (see Map 2 in rear pocket) where the mineral banding of quartzofeldspathic and other supracrustal gneisses reveal a fold closure. The symmetry and orientation of small scale parasitic folds on this structure indicate that the closure is formed by the surface intersection of a southerly plunging antiform. Pole measurements in this domain are dispersed about a plane, whose pole plunges about  $60^{\circ}$  on a bearing of  $208^{\circ}$  (Figure 31).

Domain IV occurs in the north-west of Farm Randjesfontein (see Map 2 in rear pocket) and the closures in this area are clearly defined by a banded magnetite quartzite as well as by thicker quartzites. The banded magnetite quartzite reveals three fold closures in this region and suggests two stages of

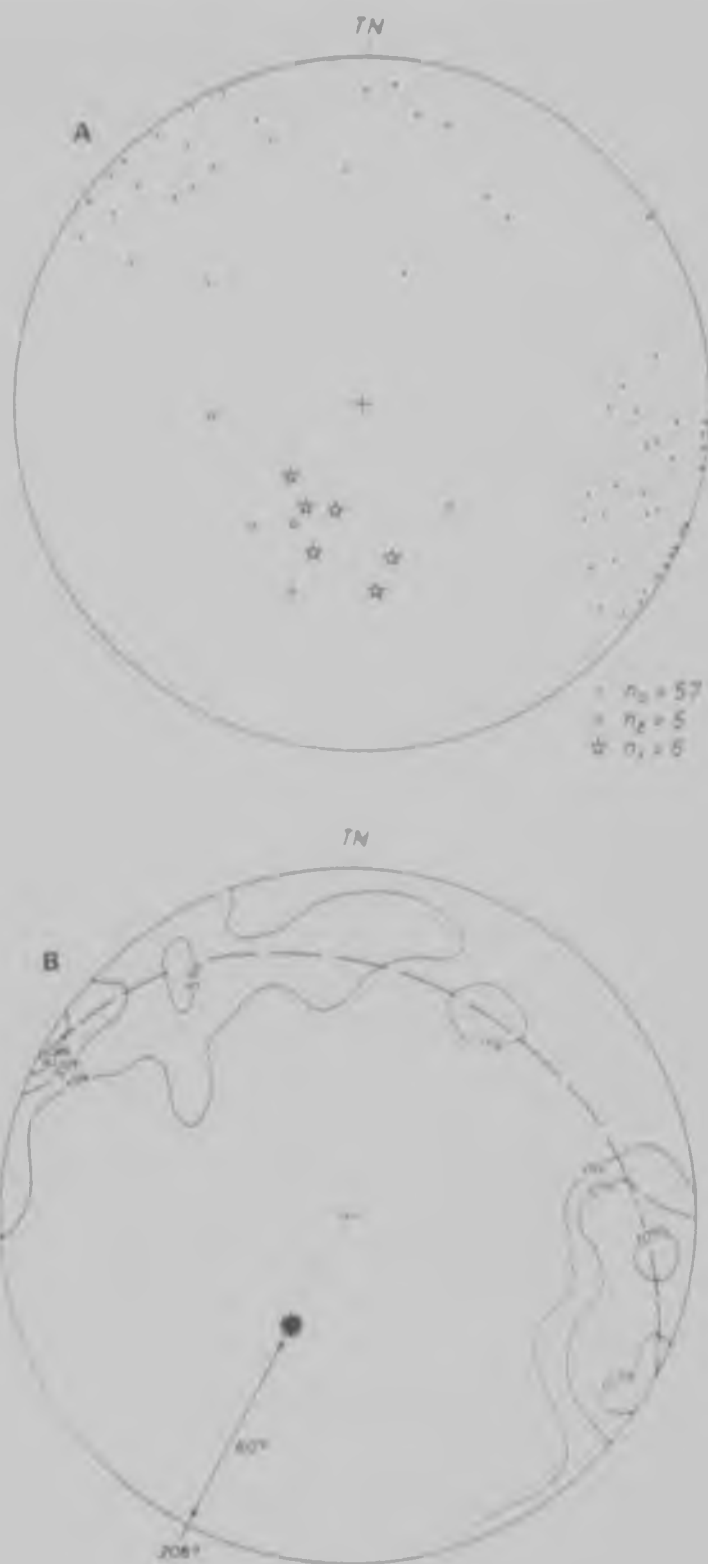


Figure 30: A: poles to bedding and mineral banding planes ( $n_p=57$ ), mineral lineations (open circles,  $n_l=5$ ) and minor fold hinges (stars,  $n_f=6$ ) from Domain II (see Map 2 in rear pocket) plotted on an equal area stereographic projection. B: contoured data from A per 1 per cent area. The star is the pole to the visually fitted dashed great circle.

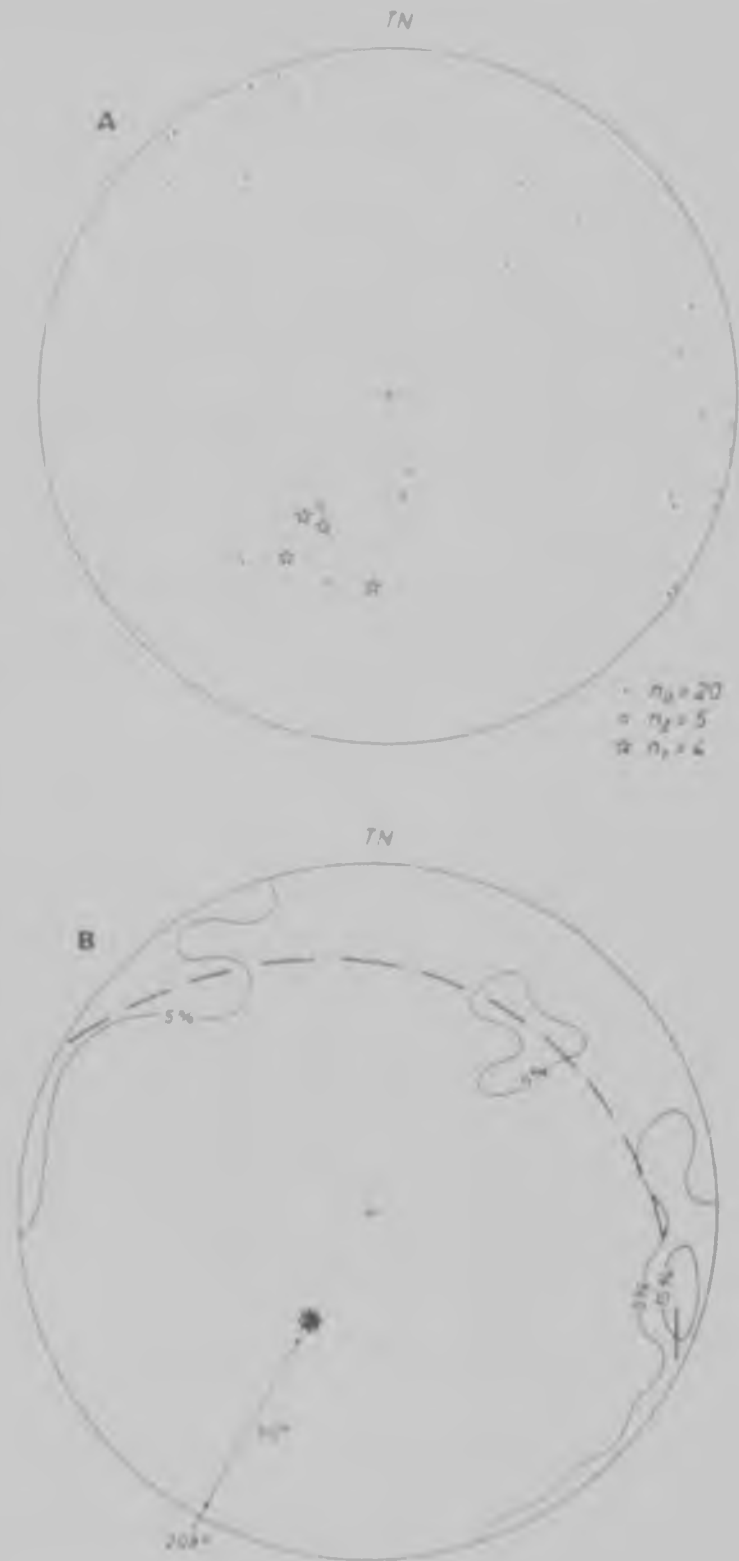


Figure 31: A: poles to bedding and mineral banding planes ( $n_p=20$ ), mineral lineations (open circles,  $n_l=5$ ) and minor fold hinges (stars,  $n_f=4$ ) from Domain III (see Map 2 in rear pocket) plotted on an equal area stereographic projection. B: contoured data from A per 1 per cent area. The star is the pole to the visually fitted dashed great circle.



fold closure producing a 'refolded fold'. However, measurements of bedding and 'foliation' plane orientations give poles which define a plane that has a pole plunging about  $50^{\circ}$  on a bearing of about  $230^{\circ}$  (Figure 32).

Domain V contains fold closures affecting conformable units of quartzite and anorthosite on the Farm Magdala (see Map 2 in rear pocket). These closures display a similar 'S'-type or left-lateral symmetry to those in Domain II. Measurements from this region define a plane whose pole plunges  $60^{\circ}$  on an azimuth of  $235^{\circ}$  (Figure 33). This indicates that these closures are produced by a synform-antiform pair which plunges to the south-west.

Further evidence for folding recognizable at the 1 : 25 000 scale of the mapping is provided by the rootless folds affecting the banded magnetite quartzite exposed in the southern part of Farm Chirundu (see Map 1 in rear pocket). This fold is characterized by an acute isoclinal interlimb angle of less than  $5^{\circ}$ , but appears to leave the bounding quartzites and other supracrustal rocks unaffected. It is thus an intrafolial fold, and may represent the earliest stage of folding in this terrane. Also, the infolded supracrustal rocks occurring along a central axis within the gabbroic and anorthositic gneisses in the north-west of the study area (see Map 1 in rear pocket) are themselves folded around the synform-antiform pair in Domain V, and again

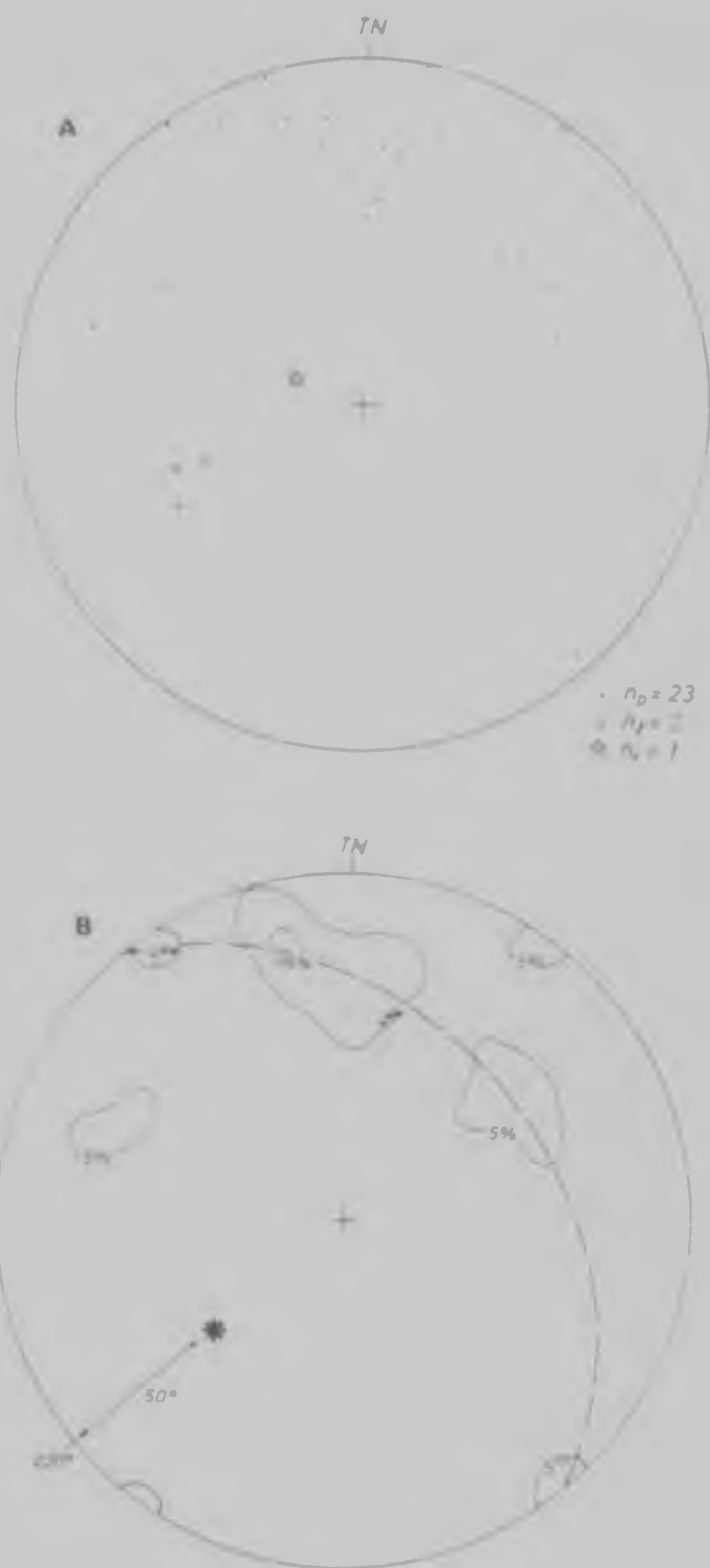


Figure 32: A: poles to bedding and mineral banding planes ( $n_p=23$ ), mineral lineations (open circles,  $n_l=3$ ) and a minor fold hinge (star) from Domain IV (see Map 2 in rear pocket) plotted on an equal area stereographic projection. B: contoured data from A per 1 per cent area. The star is the pole to the visually fitted dashed great circle.

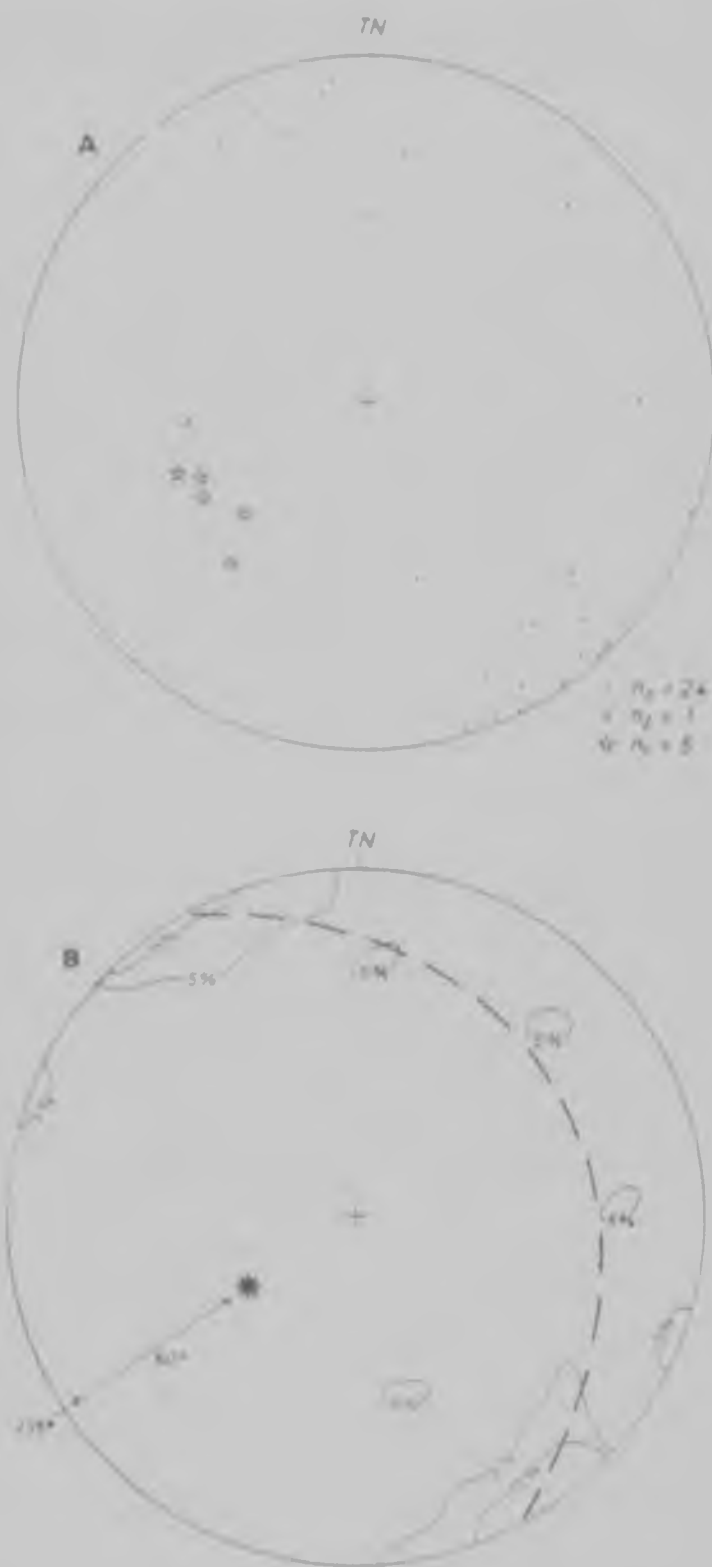


Figure 33: A: poles to bedding and mineral banding planes ( $n_p=24$ ), a mineral lineation (open circle) and minor fold hinges (stars,  $n_f=5$ ) in Domain V (see Map 2 in rear pocket) plotted on an equal area stereographic projection. B: contoured data from A per 1 per cent area. The star is the pole to the visually fitted great circle.

suggests at least two stages of fold closure in this region.

#### Small scale structures

The structures described in this section are those observed within the scale of the outcrops and are often less than a few metres in size. Consequently they cannot be represented at the scale of the mapping.

The exposures of the basement gneisses preserved on the Farms Oorsprong and Middelbult (see Map 1 in rear pocket) exhibit structural and physical features similar to those exposed in the bed of the Sand River on the Farm Veenen (Fripp, 1981a-c). The outcrops are typically eroded into smooth whale-backed pavements, and are thus immediately distinguishable from the other heterogeneous supracrustal gneisses which form dissected and irregular outcrops, and generally are poorly exposed. Tight isoclinal folding of the mineral banding, often only a few millimetres in thickness, occurs where these small folds are intrafolial and often do not appear to affect adjacent layers. Deformed mafic dykes transect the mineral banding of the grey gneisses, and only one age of dyke emplacement has been recognized in the outcrops within the study area on the basis of cross-cutting relationships. The dykes show cusped boundary structures which are convex inwards into the dyke, suggesting that they were deformed under conditions

where they had lower viscosities than the host basement gneisses. In addition, abundant leucocratic veins, which are often parallel to the mineral banding, occur up to a few centimetres in thickness. Larger pegmatitic masses of predominantly fabric-free feldspar grains up to 2 cm in diameter invade the grey basement gneisses.

Minor or parasitic folds are observed throughout the area, and can be used to determine orientation of larger scale folding by considering their orientation and symmetry. The hinge lines of these small folds plunge to the south-west, and give an average orientation which plunges about  $50^{\circ}$  on a bearing of  $225^{\circ}$  (Figure 34). This corresponds closely with those fold axes determined from the poles to bedding and mineral banding from the area as a whole and from the five selected Domains described earlier (Figures 28 - 33). Minor fold hinges measured in each of the Domains are also plotted in stereographic projections for each of these areas (Figures 29 - 33) and also show good correlations with those fold axes determined from the pole plots.

The metapyroxenite and serpentinite units reveal a layered structure in many outcrops where thin and parallel veins or layers of pyroxene up to a few centimetres in thickness occur within more massive serpentine. This layering is also preserved on a microscopic scale (Figure 24). Poikiloblastic megacrysts

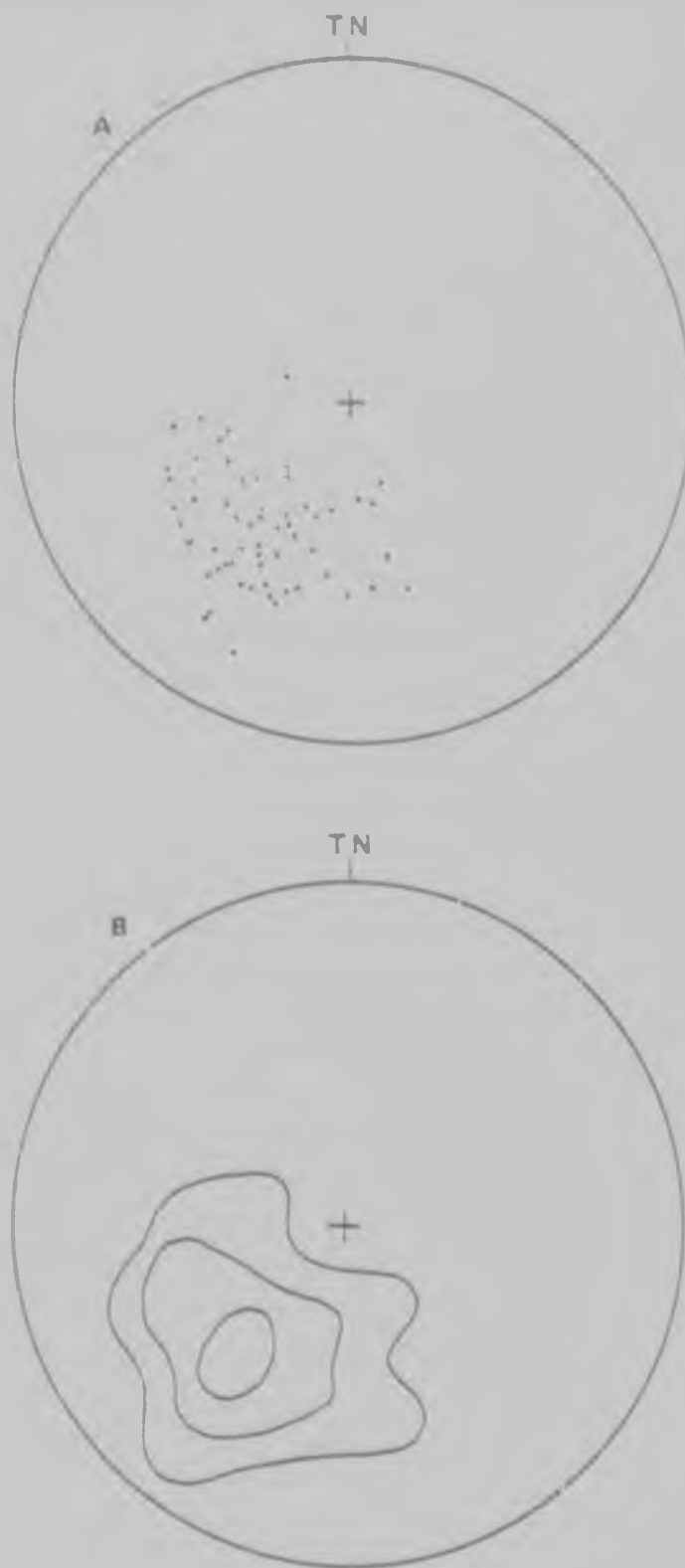


Figure 34: A: minor fold hinges and other linear structures such as mineral lineations ( $n=57$ ) plotted on an equal area stereographic projection. B: contoured data from A at 1, 5 and 10 per cent intervals per 2 per cent area. The maximum plunges about  $50^{\circ}$  on a bearing of about  $225^{\circ}$ .

of orthopyroxene are also present in many outcrops and are commonly ellipsoidal in shape probably reflecting the strain suffered by the rocks. Their longest orientations parallel the regional 'foliation' and thus produce a marked fabric in the rock.

Events of dyke development are widespread within the study area, and different ages are easily recognized by successive cross-cutting relationships. Dykes of melanocratic, leucocratic and pegmatitic material can be found transecting both the basement and supracrustal lithologies. A locality on the Farm Kopjesfontein shows two ages of leucocratic dykes which cross-cut a host rock transected by numerous small veins (Figure 35).



Figure 35: Two ages of leucocratic dyke cross-cutting a pyroxenitic amphibolite containing leucocratic veins from the Farm Kopjesfontein (4,5 km east of the main Messina-Tshipise road - see Map 1 in rear pocket). Note the xenolith of the host rock within the younger dyke.

Many mafic dyke types occur which include the less abundant deformed varieties which cut the basement gneisses, and younger diabase and dolerite varieties which are unmetamorphosed and free of any tectonic fabrics.

A post-tectonic dyke of possible Karoo age occurs on the Farm Kopjesfontein (4,5 km east of the main Messina-Tshipise road - see Map 1 in rear pocket) and preserves many interesting structures. Over a limited section of its length (about 250 m) it reaches a maximum thickness of over 40 m where it is distinctively and symmetrically zoned. Outer chill margins of fine grained basaltic rock between 1 and 2 m in thickness bound zones of coarser grained diabasic rock from 10 to 11 m in thickness. The centre of the dyke is filled with a breccia of fine grained diabasic rock which contains fragments of the wall rock quartzo-feldspathic gneisses. This central zone of breccia is up to 18 m in thickness, and suggests that this locality in the dyke represents a vent or diatreme structure.

Boudinage in this terrane is widespread due to the considerable along strike extension that has accompanied the deformation and attenuation which has affected these rocks. Some rock types are observed to boudinage more readily than others due to their higher viscosities at the time of deformation. These include the banded magnetite quartzite, metapyroxenite and serpentinite. The metapyroxenite and serpentinite form



small boudins along strike typically within the quartzite units in the north and west of the study area. The banded magnetite quartzite however, preserves early tight isoclinal folds within the individual boudins suggesting an earlier event during which this lithology behaved in a much more ductile fashion. Within the supracrustal gneisses, many small units are extensively and locally boudinaged making it impossible to trace them except over limited strike lengths. Thus many of the stratigraphic units in the supracrustal gneisses have lense-like forms.

Late mylonites of a few centimetres in thickness which cross-cut the mineral banding in the gneisses are locally present as for example on the Farm Oorsprong, although these structures are not traceable over strike lengths of more than a few metres. They are not folded, and usually contain abundant porphyroclasts of quartz and feldspar (Figure 36) making this rock type a blastomylonite.

Outcrops of Singelele gneiss on the Farm Ostend rarely show structures such as folds or boudinage, but have suffered a large degree of attenuation and flattening perpendicular to strike. However, thin mafic layers occur up to 1 or 2 cm in thickness which are cut by small shear zones (Figure 37). Displacements may be up to several centimetres, though the sense of movement varies from outcrop to outcrop. Mafic dykes are rarely seen to intrude this lithology.



Figure 36: A blastomylonite traversing a pyroxenitic amphibolite on the Farm Oorsprong (1,3 km east of the main Messina-Tshipise road - see Map 1 in rear pocket).

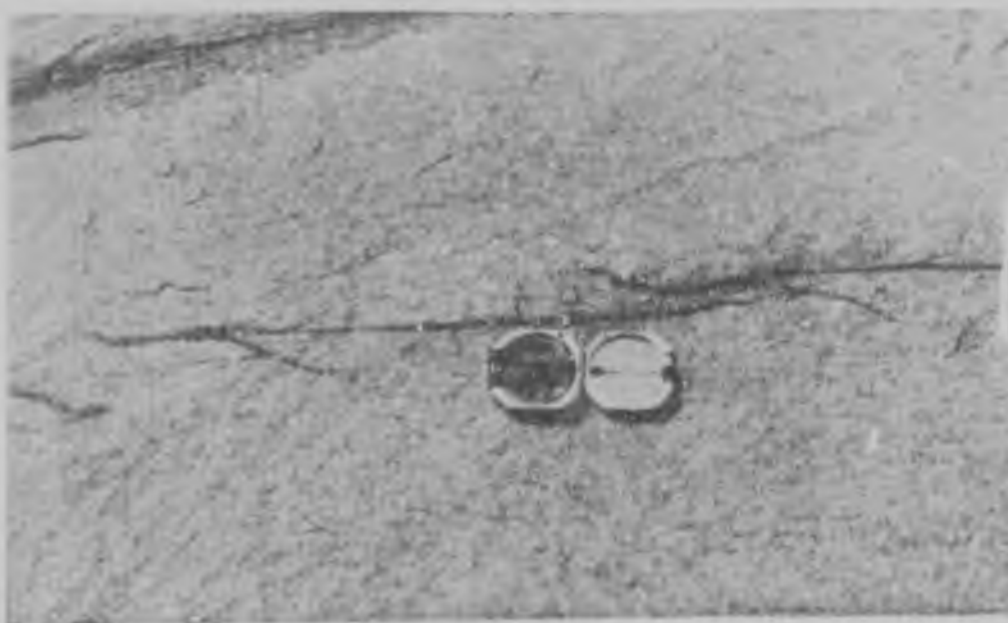


Figure 37: Shear zones deforming thin mafic layers within the Singelele-type granitoid gneiss on Farm Ostend (5,5 km east of the main Messina-Tshipise road - see Map 1 in rear pocket).

Jointing is well developed in the quartzite units in the area causing their outcrops to be blocky and dissected. Some localities reveal both tension and shear jointing sets, and typically the line of intersection of these joints is sub-vertical to vertical. This suggests that the maximum and minimum stress directions producing these joints lie in the horizontal plane. None of the observed joints are folded.

Both planar and linear mineral fabrics occur in the rocks due to deformed mineral grains of mainly sillimanite, amphibole, biotite and quartz. In many outcrops, the planar fabric or cleavage is very close in orientation to the gneissic 'foliation' defined by the mineral banding and causes difficulty in recognizing primary features such as compositional banding and bedding in these rocks.

Linear fabrics imposed by the alignment of prismatic mineral grains together with rodding and mullion structures generally plunge moderately to the south-west and correlate well with the hinge line orientations of both minor and large-scale folds in the area. Linear structure orientations are plotted together with fold hinges in a stereographic projection (Figure 34), and show a maximum which plunges about  $50^{\circ}$  on a bearing of about  $225^{\circ}$ . In addition, linear structures measured within each of the five selected Domains are also plotted in the individual stereographic projections for these Domains

(Figures 29 - 33) where they also show good correlations with the orientations of minor fold hinge lines.

### Faults

Two large regionally extensive faults occur within the study area and in fact mark the northern and southern boundaries of the area (see Map 1 in rear pocket). In the north, a major strike-slip fault called the Dowe-Tokwe Fault (Söhnge, 1946) has a displacement in a right-lateral sense (Figure 2). Outcrops of fault breccia occur, though outcrop is generally poor in this region. The southern boundary is marked by the Bosbokpoort Fault (Söhnge, 1946), which is bounded on its southern side by Karoo-age sediments. These sediments are correlated with those of the Stormberg Group (Söhnge, 1946) and lap off onto the Precambrian gneisses further south near Tshipise (Figure 2). Thus the Karoo sedimentation has occurred in yoked basins controlled by faults. Large vertical displacements are indicated for this fault due to the juxtaposition of the Jurassic age Karoo sediments against the Archaean gneisses. A fault of local extent also occurs centrally in the study area with a strike which is sub-parallel to the Dowe Tokwe Fault. Outcrops of highly silicified fault breccia occur on the Farms Randjesfontein, Trotsky and Middelbult (see Map 1 in rear pocket) and the fault appears to either terminate against the quartzite

units in the west of the area, or to change orientation to parallel the stratigraphy in this area. On Farm Oorsprong, the stratigraphy appears to have been displaced by right-lateral shear in the vicinity of this fault, suggesting that the fault has the same sense of movement as the Dowe-Tokwe Fault. A pivotal fault parallels the main Messina-Tshipise road on the Farms Dover and Magdala (see Map 1 in the rear pocket) and breccia is exposed in some of the road-cuttings. The eastern end of this fault displays a left-lateral displacement, marked by the thin anorthositic unit in this area, while the western end of the fault near the Sand River shows a right-lateral displacement (Fripp, 1981c).

#### Discussion

The study area contains only limited exposures of the grey basement gneisses similar to those occurring in the type area, in the bed of the Sand River on the Farm Veenen. These outcrops are not sufficiently definitive to prove any basement-cover relationships on structural evidence. However, the supracrustal gneisses within the study area show evidence for at least two and possibly even three phases of fold closure.

The two thin layers of banded magnetite quartzite occurring within a pyroxenitic amphibolite in the fold closure of Domain I (see Maps 1 and 2 in rear pocket) are probably the same unit

simply duplicated by tight isoclinal folding. However, fold closures connecting the two thin units are not observed mainly due to the poor exposure and significant along-strike extension and boudinaging which has accompanied deformation in this region. Thus, two events of fold closure are interpreted within Domain I. The first event is represented by the tight isoclinal folds which duplicate the banded magnetite quartzite, while the second event produces the large scale closure revealed at the mapping scale. This second closure has a fold axis which plunges to the south (Figure 29) at a steep angle. By extending this Domain in a south-westerly direction, a basin-like structure of elliptical shape is revealed which suggests a possible third event of folding (see Map 2 in rear pocket). The structural style of Domain I is schematically illustrated in Figure 38.

Domain II is significant in that the serpentinite body which is folded by a synform/antiform pair which plunges moderately to the south-west (Figure 30) contains a folded boudin of quartzite (see Map 2 in rear pocket). Thus the onset of flattening perpendicular to bedding, with attendant thinning and boudinaging of the units, preceded the folding which produced the fold closures in this domain. This may also suggest two episodes of deformation, or more likely, a system of progressive deformation whereby the effect of strain accumulation, probably by simple shear, has rotated the rocks

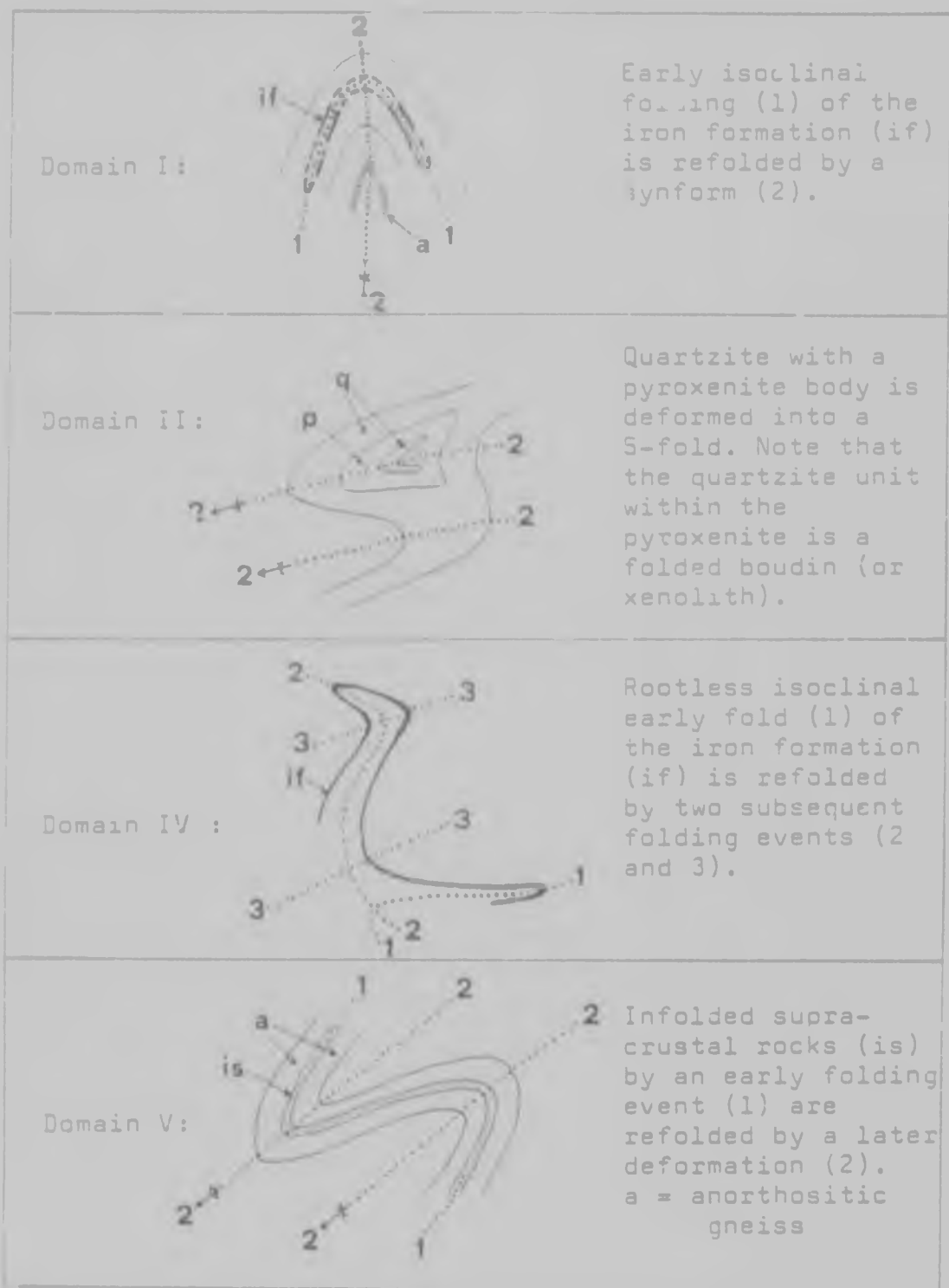


Figure 38: Schematic structural elements from selected domains within the study area (see Map 2 in rear pocket, and text for discussion).

from a field where buoyancy occurs to one where folding is characteristic. Figure 38 illustrates schematically the style of the deformation in this domain.

The banded magnetite quartzite in Domain IV (see Map 2 in rear pocket) may be regarded as displaying the geometry of a 'refolded fold', and thus again, either records two discrete events of fold closure, or a progressive deformation situation whereby successive strain increments are added at differing orientations. By considering the eastward extension of this

banded magnetite quartzite unit, a tight rootless isoclinal

intrafolial fold terminates the unit on the Farm Chirundu. This rootless isocline does not appear to fold the adjacent gneisses and quartzites and is interpreted as being an earlier closure than those described as producing the refolded fold on this unit in Domain IV on Farm Randjesfontein. Figure 38 shows schematically how a succession of three possible fold phases could have produced the outcrop pattern in this domain.

In addition, the banded magnetite quartzite units throughout the study area commonly display tight isoclinal folds which developed probably synchronously with the rootless intrafolial fold described on Farm Chirundu. Thus during the earlier part of the deformational history of these units, they behaved in a ductile fashion, probably due to the development of recumbent or nappe-like structures following their deposition and rapid



burial. Subsequent events have refolded these units in places, for example on Farm Randjesfontein, probably by simple shear, and more commonly boudinaged them into their present disposition.

Domain V provides clear evidence of at least two phases of folding (see Map 2 in rear pocket). The anorthosite contains infolded metasediments which can be observed in the Farm Boschrand, and also in the main Messina-Tshipise road cutting on the Farm Dover. However, the anorthosite with these infolded paragneisses are again folded into the synform-antiform pair of this domain, and is schematically illustrated in Figure 38.

From the above data, it appears that following any structural events which solely affected the basement gneisses prior to the deposition of the supracrustal rocks (see Fripp, 1981a-c) the deformational history of the supracrustal gneisses commenced with a phase of ductile isoclinal folding which in many outcrops is now manifest by intrafolial folds. This may be related to a process of rapid burial to great depth such as would be experienced in a large geosyncline on an unstable and probably thin cratonic platform. Later, the stress field induced further refolding, considerable flattening, attenuation and along strike boudinaging of the stratigraphy probably by a process of simple shear. The symmetry of folds

in the north-western portion of the study area suggests that this simple shear had a left-lateral sense of movement consequently producing the 'S'-shaped folds.

An interpretive map of the study area has been prepared at an approximate scale of 1 : 50 000 (see Map 2 in rear pocket) on which the trends of various fold axial traces are marked. Also, a NW-SE cross-section of the area has been constructed from this map, and is shown in Figure 39. The section line is marked on this map.



Figure 39: A schematic cross-section of the study area with a simplified and tentative stratigraphic column. See Map 2 in rear pocket for the location of the section line. The length of the cross-section is approximately 11 km with no vertical exaggeration.

## CHAPTER 4: THE MESSINA LAYERED INTRUSION

### Introduction

Anorthositic and gabbroic rocks are common in high-grade and poly-deformed Archaean terranes (Windley, 1973) and have been described in the Central Zone of the Limpopo Mobile Belt (Söhnge, 1946; Söhnge et al., 1948; Bahnemann, 1970, 1972; Hor et al., 1975; Barton et al., 1979a). They occur over a widespread region in the Limpopo belt (see Figure 1 of Barton et al., 1979a - in rear pocket). The presence of relict cumulate textures and phase layered magnetitites and chromitites has provided convincing evidence of an igneous origin for these rocks. Barton et al. (1979a) have argued that a tholeiitic magma may have been parental to these rocks in the Limpopo Mobile Belt on the basis of certain petrological trends revealed in a variety of Harker-type variation diagrams. Some workers (e.g. Bahnemann, 1970) have suggested that in part at least, some of the anorthosites may have been derived from the partial melting and fusion of calcareous sediments with the extraction of granitic anatectic liquids leaving an anorthositic residue. This section presents additional evidence to support the cumulate nature of these rocks and the argument that these rocks are the result of a fractionating magma.

### Geological setting

The anorthositic and gabbroic rocks occurring in the Central Zone of the Limpopo Mobile Belt have been grouped together with various metapyroxenite and serpentinite units as the Messina Layered Intrusion (Barton et al., 1979a). They form a generally conformable and sill-like suite of rocks within the basement-supracrustal sequences of Archaean age which underlie the Central Zone of the Limpopo Mobile Belt. Two age determinations have been obtained for these rocks. A whole-rock Pb-Pb isochron of about 3 270 m.y. is considered to reflect the time of emplacement (Barton, 1981) and a whole-rock Rb-Sr isochron of about 3 150 m.y. with an initial  $^{87}\text{Sr}/^{86}\text{Sr}$  ratio of about 0,703 (Barton et al., 1979a) is considered to reflect a high-grade metamorphism. The rocks show abundant evidence of being deformed (Barton et al., 1979a) and metamorphically recrystallised (Hor et al., 1975), although primary structures and textures have been recognized. These latter features include units up to a metre in thickness which show both compositional and grain-size grading with the composition changing from more anorthositic types with labradorite ( $\text{An}_{80}$ ) to more gabbroic compositions with andesine ( $\text{An}_{50}$ ) in which clinopyroxene and hornblende become more abundant. Crystals grade in size and suggest upward fining cycles. Megacrysts of plagioclase up to 10 cm in size occur

and have been regarded as cumulate crystals, and they generally occur in a matrix of smaller clinopyroxene, amphibole and plagioclase grains. These structures and textures have been described by Irton et al. (1979a, see their Plates 1 and 2), although Hor et al. (1975) describe textures which are essentially recrystallized. The magnetites are titaniferous and occur in thin bands and lenses which show lateral impersistence. They are coarsely crystalline with grains up to 4 mm in size and are distinct from the finely laminated banded magnetite quartzites which occur in the supracrustal successions. Söhnge et al. (1948) describe these chromitites with strike lengths of several kilometres from within anorthositic horizons. Söhnge et al. (1948) concluded that the magnetitites and chromitites represent phase layers within a fractionally crystallized magmatic and plutonic rock.

#### Compositional variation of a unit sampled on Farm Shangani

A traverse across strike of an anorthositic and gabbroic unit of the Messina Layered Intrusion was made on the Farm Shangani about 4 km west of the main Messina-Tshipise road - see Map 1 in rear pocket. Samples were collected for whole-rock and mineral analysis at approximately 100 m intervals along a farm road in this area. The observed physical and chemical data (Table 7) are presented in Figures 40 and 41 and

Table 7: Whole-rock analyses of gabbroic and anorthositic gneisses of the Massim Layered Intrusion and their C.I.P.W. norms.

	1	2	3	4	5	6	7	8
SiO <sub>2</sub>	51,70	48,31	48,55	48,43	47,80	48,94	53,32	51,52
TiO <sub>2</sub>	0,38	0,38	0,28	0,17	0,20	0,69	0,32	0,47
Al <sub>2</sub> O <sub>3</sub>	20,19	30,17	30,53	31,37	27,65	24,55	25,77	18,82
Fe <sub>2</sub> O <sub>3</sub>	7,09	2,95	2,48	1,58	2,76	6,19	3,53	7,61
MnO	0,14	0,05	0,04	0,04	0,04	0,07	0,04	0,10
MgO	5,53	1,10	0,93	0,53	2,37	3,56	1,71	6,90
CaO	11,36	14,89	14,48	15,14	16,37	13,99	9,80	11,10
Na <sub>2</sub> O	2,50	1,83	2,33	2,02	1,42	1,34	3,64	2,24
K <sub>2</sub> O	0,74	0,28	0,27	0,25	0,27	0,67	0,90	0,73
P <sub>2</sub> O <sub>5</sub>	0,03	0,03	0,05	-	-	0,02	0,04	0,09
LOI	0,66	0,67	0,73	0,94	0,54	0,61	1,42	0,57
Total	100,32	100,56	100,67	100,47	99,42	100,63	100,49	100,15
Rb ppm.	16	6	3	6	5	16	25	14
Sr ppm.	172	176	187	177	160	142	188	333
Ba ppm.	380,0	29,6	23,0	32,4	71,1	96,4	157,0	98,3
K/Rb	463	467	900	417	540	419	360	521
Rb/Sr	0,09	0,03	0,02	0,03	0,03	0,11	0,13	0,04
quartz	0,91	1,76	0,50	1,68	1,19	2,34	3,40	0,94
corundum	-	-	0,29	0,28	-	-	1,09	-
orthoclase	4,37	1,66	1,60	1,48	1,61	3,95	5,36	4,32
albite	21,15	15,48	19,71	17,6	12,14	11,31	31,02	18,96
anorthite	41,65	73,22	71,21	75,30	68,98	58,79	48,68	39,13
diopside	7,56	0,16	-	-	7,07	4,97	-	8,44
hedenbergite	4,25	0,16	-	-	3,50	3,45	-	4,00
enstatite	10,26	2,66	2,31	1,32	2,69	6,53	4,29	13,26
ferrosilite	7,01	3,28	3,01	1,96	1,62	5,51	4,42	7,64
magnetite	2,06	0,83	0,72	0,47	0,81	1,79	1,04	2,20
ilmenite	0,72	0,72	0,53	0,32	0,38	1,31	0,61	0,89
apatite	0,07	0,07	0,12	0,02	0,02	0,05	0,09	0,21
%An	66	83	78	81	85	84	61	64

1 to 6: anorthositic and gabbroic gneiss (26-5-A to 26-5-F) (samples collected at equal intervals across strike).

7: anorthositic gneiss (18-6-B) - Form Veenan.

8: gabbroic gneiss (30-1-20) - Form Heuningfontein.

Analyst: P.C. Horrocks  
LOI - loss on ignition  
Total Fe as Fe<sub>2</sub>O<sub>3</sub>

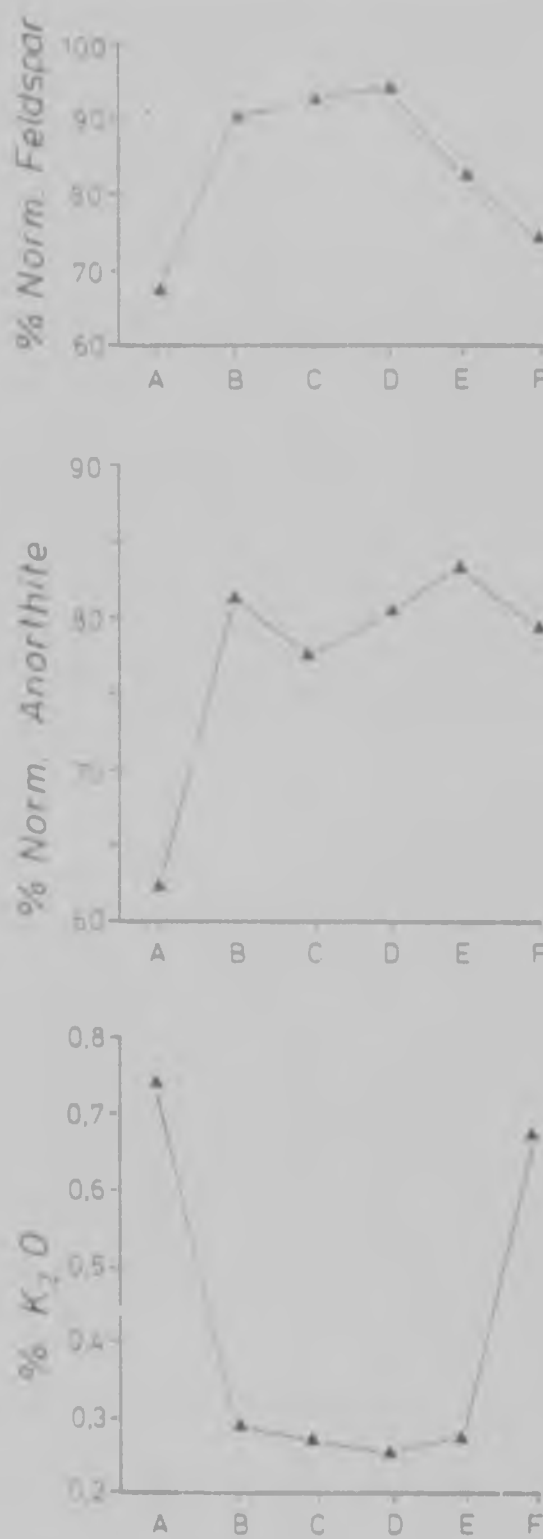


Figure 40: Variation diagrams for per cent normative total feldspar, per cent normative anorthite, and per cent K<sub>2</sub>O for samples 26-5-A to 26-5-F of anorthositic and gabbroic gneiss from Farm Shangani (see Map 2 in rear pocket). Geochemical data are from Table 7.



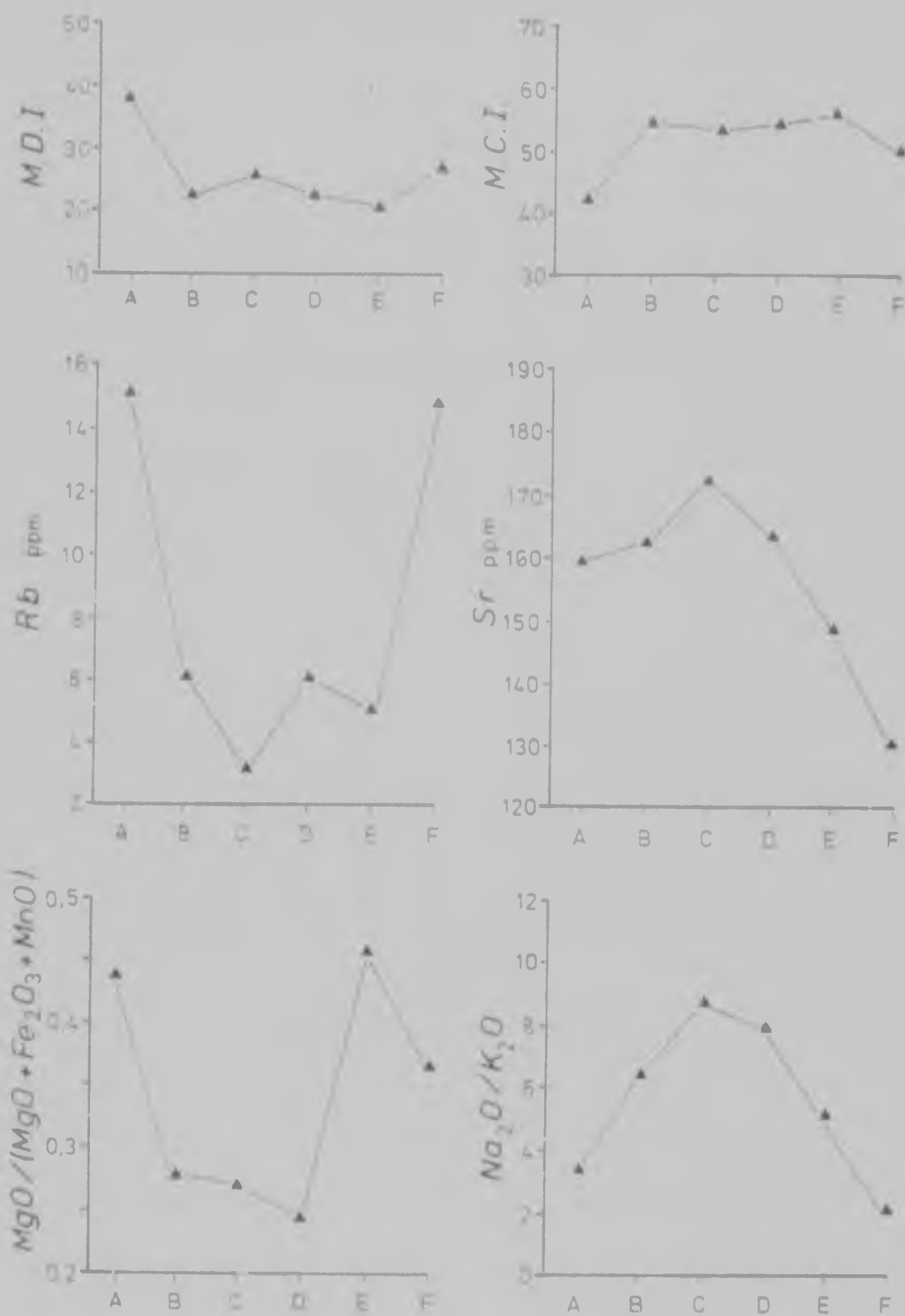


Figure 41: Variation diagrams for modified differentiation and crystallization indices (M.D.I. and M.C.I. respectively), Rb, Sr,  $\text{MgO}/(\text{MgO} + \text{Fe}_2\text{O}_3 + \text{MnO})$ , and  $\text{Na}_2\text{O}/\text{K}_2\text{O}$  for the samples of anorthositic and gabbroic gneiss from Farm Shangani as described in Figure 40.

reveal the compositional symmetry of this unit. Marginal melanocratic varieties occur adjacent to the unit's north-western and south-eastern boundaries and are enriched in  $K_2O$ , Rb and MgO with respect to the more leucocratic central portion of the unit. The central portion shows enrichment in normative anorthite, normative total feldspar proportion,  $Na_2O$  and Sr compared with the outer zones (Figures 40 and 41) and may be explained by magmatic differentiation. The modified differentiation and crystallization indices of von Gruenewaldt (1973) are also plotted in Figure 41 and indicate that the earliest crystallized portion of the unit (i.e. that with the higher crystallization and lower differentiation indices) is the central variety. Here, the plagioclase also shows higher anorthite contents, of about  $An_{80}$ , compared with the marginal gabbros where anorthite contents of about  $An_{50}$  are typical. Electron probe microanalyses of plagioclase from these samples (see Table 2.21, Appendix 2) correlate well with the normative values. These data indicate that plagioclase was a primary cumulate phase during the fractionation of the original magma of these rocks.

#### Pearce diagrams

The availability of seventy-five whole rock geochemical analyses of anorthositic and gabbroic gneisses of the Messina Layered Intrusion occurring in the Central Zone of the Limpopo

Mobile Belt has enabled the use of Pearce-type petrological diagrams (Pearce, 1970) to illustrate cumulate trends in these rocks. The data is available from several sources (Van Zyl, 1950; Hor et al., 1975; Barton et al., 1979a; T.S. McCarthy, unpublished data) and these data have been used to plot a ternary An-Ab-Or diagram (Figure 42) of normative weight per cent values. A clear trend is indicated which varies from labradoritic compositions in the anorthositic rocks to those with significant albite and orthoclase from the more gabbroic varieties.

In the Pearce diagrams (Figures 43 and 44),  $K_2O$  has been used to normalize the Pearce ratios since it does not form a constituent of the cumulate phase under consideration and by inspection was found to vary by only small amounts in the analyses available. Thus  $Al_2O_3/K_2O$ ,  $CaO/K_2O$  (Figure 43) and  $Na_2O/K_2O$  (Figure 44) were plotted against  $SiO_2/K_2O$  in each case since  $Al_2O_3$ ,  $CaO$ ,  $Na_2O$  and  $SiO_2$  are constituent oxides of plagioclase. In all cases, good positive linear relationships exist, particularly for those data points with  $SiO_2/K_2O$  ratios of more than 70. Straight line regression curves were fitted to the plots in Figure 43 for those points with the  $SiO_2/K_2O$  ratio of more than 70 and correlation coefficients of better than 0.98 were obtained in both cases. The  $Na_2O/K_2O$  plot (Figure 44) shows a greater degree of scatter probably due to



Figure 42: An Anorthite-Albite-Orthoclase (An-Ab-Or) ternary diagram showing 75 feldspar compositions (normative weight per cent) from anorthositic and gabbroic gneisses of the Messina Layered Intrusion in the Central Zone of the Limpopo Mobile Belt (data from: Van Zyl, 1950; Hor et al., 1975; Barton et al., 1979a; and T.S. McCarthy, unpublished data).

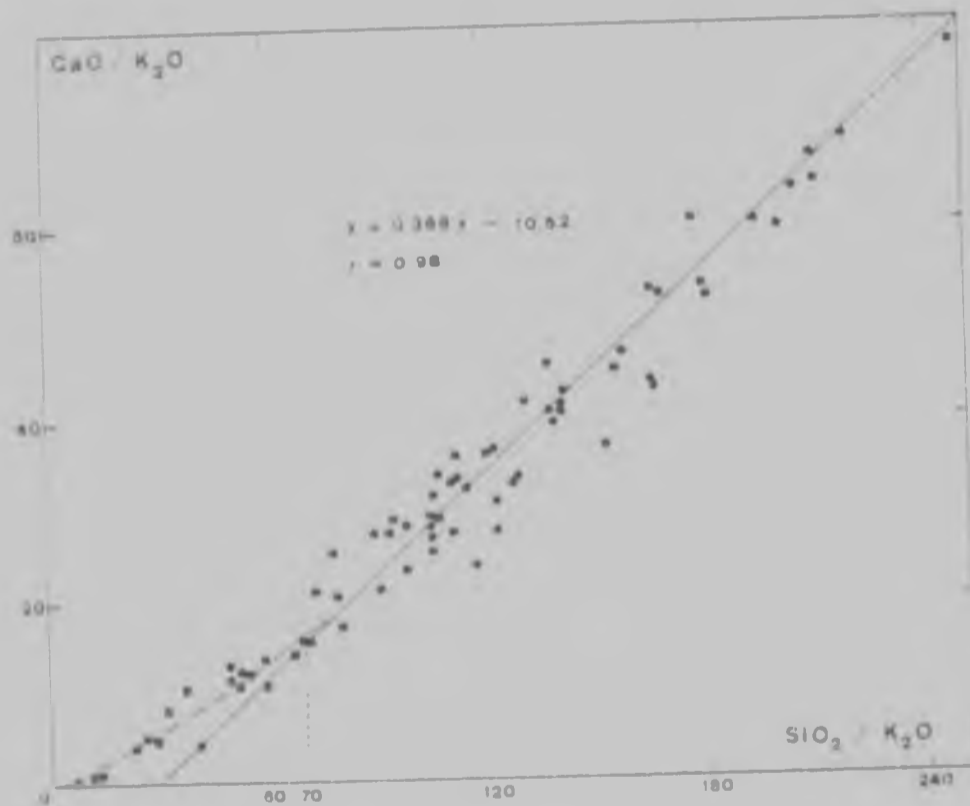
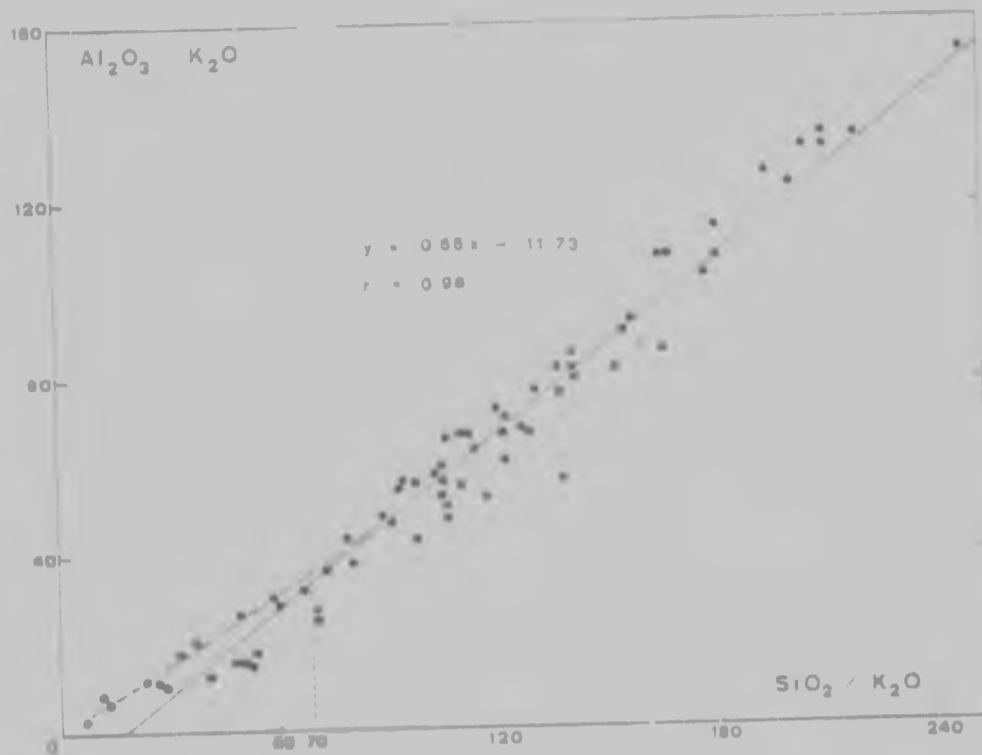


Figure 43: Pearce diagrams for the anorthositic and gabbroic gneisses of the Messina Layered Intrusion. Straight line regression equations and correlation coefficients are calculated for data with SiO<sub>2</sub>/K<sub>2</sub>O ratios greater than 70.

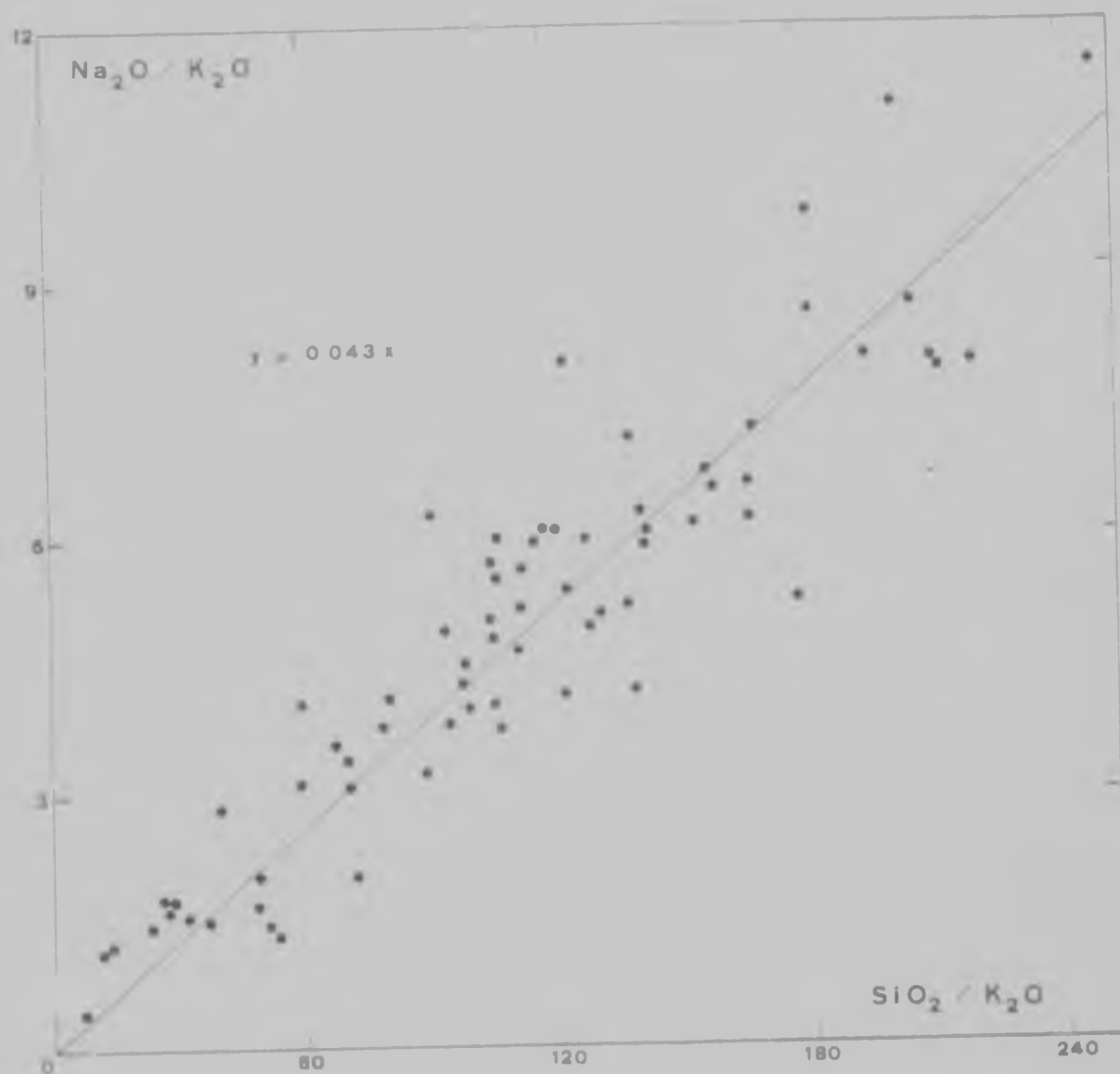


Figure 44: Pearce diagram for the anorthositic and gabbroic gneisses of the Messina Layered Intrusion. The straight line is visually fitted and constrained to pass through the origin.

the increased mobility of Na under the metamorphic and anatexis conditions which these rocks have experienced during their post emplacement history (Horrocks, 1980). A straight line was visually fitted to these data and constrained to pass through the origin. With the removal of a plagioclase cumulate from a pristine magma, the residual liquid would become depleted in those components which make up the plagioclase, and later cumulate crystals would be consequently also depleted in these components. Thus the relationship between the first formed cumulates, later cumulates and the evolution of the magmatic liquid should be linear with respect to those components of the cumulate phase (Figure 45). In this way, the slopes of these Pearce plots may be used to determine the proportions of the various components in the cumulate phase, and hence its composition in a solid solution series. The slopes obtained from the Pearce diagrams (Figures 43 and 44) are as follows:

from  $\text{Na}_2\text{O}/\text{K}_2\text{O}$  versus  $\text{SiO}_2/\text{K}_2\text{O}$  :  $m_{\text{Na}} = 0,043$

from  $\text{CaO}/\text{K}_2\text{O}$  versus  $\text{SiO}_2/\text{K}_2\text{O}$  :  $m_{\text{Ca}} = 0,368$

from  $\text{Al}_2\text{O}_3/\text{K}_2\text{O}$  versus  $\text{SiO}_2/\text{K}_2\text{O}$  :  $m_{\text{Al}} = 0,654$

and from  $\text{SiO}_2/\text{K}_2\text{O}$  versus  $\text{SiO}_2/\text{K}_2\text{O}$  :  $m_{\text{Si}} = 1,000$  (trivial)

These data express the proportions of these constituent oxides in weight percentages, and may be converted to molecular proportions as follows:

$$m'_x = \frac{m_x}{\text{molec. weight}_x} \cdot 10^5$$

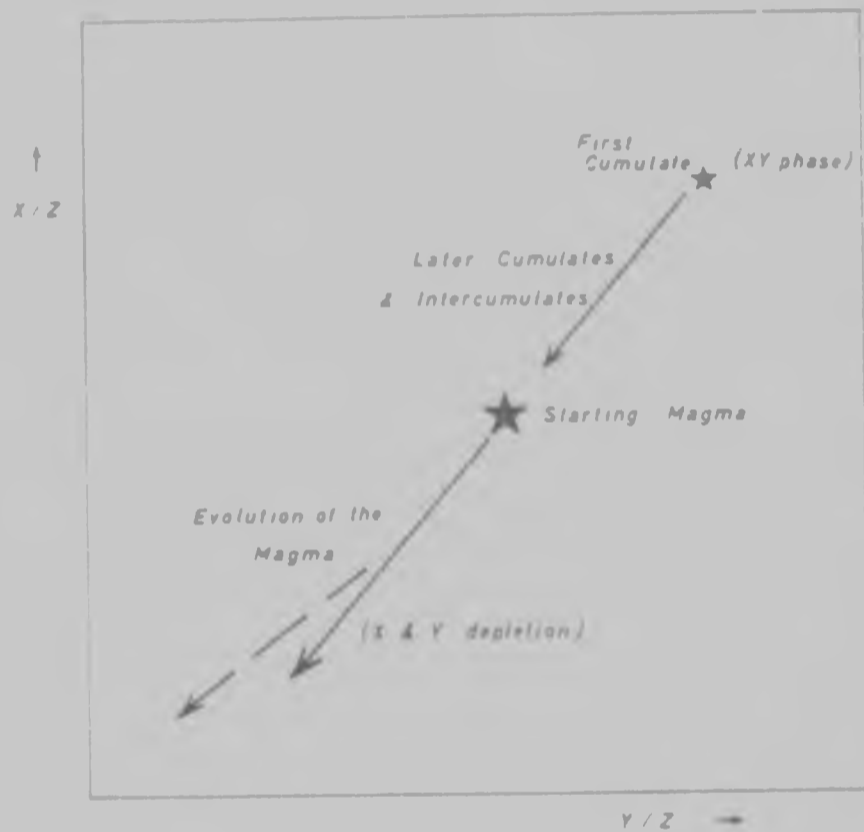


Figure 45: Schematic Pearce diagram showing the linear relationship produced during fractionation between cumulates and the evolving magma.



where the factor  $10^5/69$  is used to normalize the values so that the value for Na is equal to 1. Thus:

$$\begin{aligned} m'_{\text{Na}} &= 1,0 \\ m'_{\text{Ca}} &= 9,5 \\ m'_{\text{Al}} &= 9,3 \\ m'_{\text{Si}} &= 24,1 \end{aligned}$$

These values represent the molecular proportions of the constituent oxides ( $\text{Na}_2\text{O}$ ,  $\text{CaO}$ ,  $\text{Al}_2\text{O}_3$  and  $\text{SiO}_2$ ) in the cumulus phase, plagioclase, and from these values, it is possible to subtract two molecules of albite to consume the Na:



leaving:

$$\begin{aligned} m'_{\text{Na}} &= 0 \\ m'_{\text{Ca}} &= 9,5 \\ m'_{\text{Al}} &= 8,3 \\ m'_{\text{Si}} &= 18,1 \end{aligned}$$

If 8,3 molecules of anorthite are then subtracted to consume the  $\text{Al}_2\text{O}_3$ :



the remainder is:

$$\begin{aligned} m'_{\text{Na}} &= 0 \\ m'_{\text{Ca}} &= 1,2 \\ m'_{\text{Al}} &= 0 \\ m'_{\text{Si}} &= 1,5 \end{aligned}$$

This remaining CaO and SiO<sub>2</sub> forms a minor proportion, and may be accounted for by the intercumulus clinopyroxene, hornblende and quartz which occurs in these rocks. Also, values with SiO<sub>2</sub>/K<sub>2</sub>O ratios of less than seventy appear to follow a line of less slope in Figure 43, which may signify the entrance of other cumulate phases, notably clinopyroxene and/or hornblende, during fractionation or the mixing with intercumulus phases.

Plagioclase consisting of two parts albite and 8,3 parts anorthite (on a molecular basis) has a composition of An<sub>81</sub> and it is thus suggested that this represents the composition of the primary cumulate plagioclase which fractionated from the parental magma. Electron probe microanalyses of feldspars from samples of these anorthositic and gabbroic gneisses (see Table 2.21 - Appendix 2) support this result, since plagioclase from anorthositic gneiss and thus probably an earlier cumulate, have in fact compositions of about An<sub>80</sub> while compositions from the more gabbroic varieties, and thus later cumulus/intercumulus mixtures, vary down to about An<sub>50</sub>. These lower anorthite proportions may also be due to subsequent metamorphic effects such as the growth of metamorphic hornblende, or a re-equilibration of Ca between plagioclase and the mafic minerals.

#### Rb, Sr and K<sub>2</sub>O relationships

The variation between Rb and K<sub>2</sub>O and between Rb and Sr

ore shown in Figures 46 and 47 respectively, using data from Barton et al. (1979a) for various anorthositic and gabbroic varieties. Linear trends are revealed between these components using logarithmic scales. The data reveal that these rocks have closely similar compositions to other anorthositic rocks reported around the world (see Duchesne and Demaiffe, 1978) and are enriched in  $K_2O$  relative to Rb when compared to the main trend of Shaw (1968) which describes the K-Rb fractionation in average magmatic rocks. Duchesne and Demaiffe (1978) concluded that this overall trend of K/Rb relationships in anorthosites and related rocks can be simply explained by fractional crystallization of liquids with variable K/Rb ratios, rather than by fractional crystallization of a unique liquid.

The linear trend with logarithmic axes between Rb and Sr also suggests that fractionation may explain the distribution of the data. Thus, the Raleigh fractionation law:

$$\frac{C_L}{C_0} = F^{D-1}$$

may be used to model the relationship revealed by these data. The Sr varies from about 100 ppm to over 300 ppm but the bulk of the data (about 80 per cent) range between about 150 ppm and 200 ppm (see Figure 47). Rb shows a wide variation from less than 2 ppm to about 50 ppm for the samples analysed (Figure 47). Assuming that a particular sample consists of

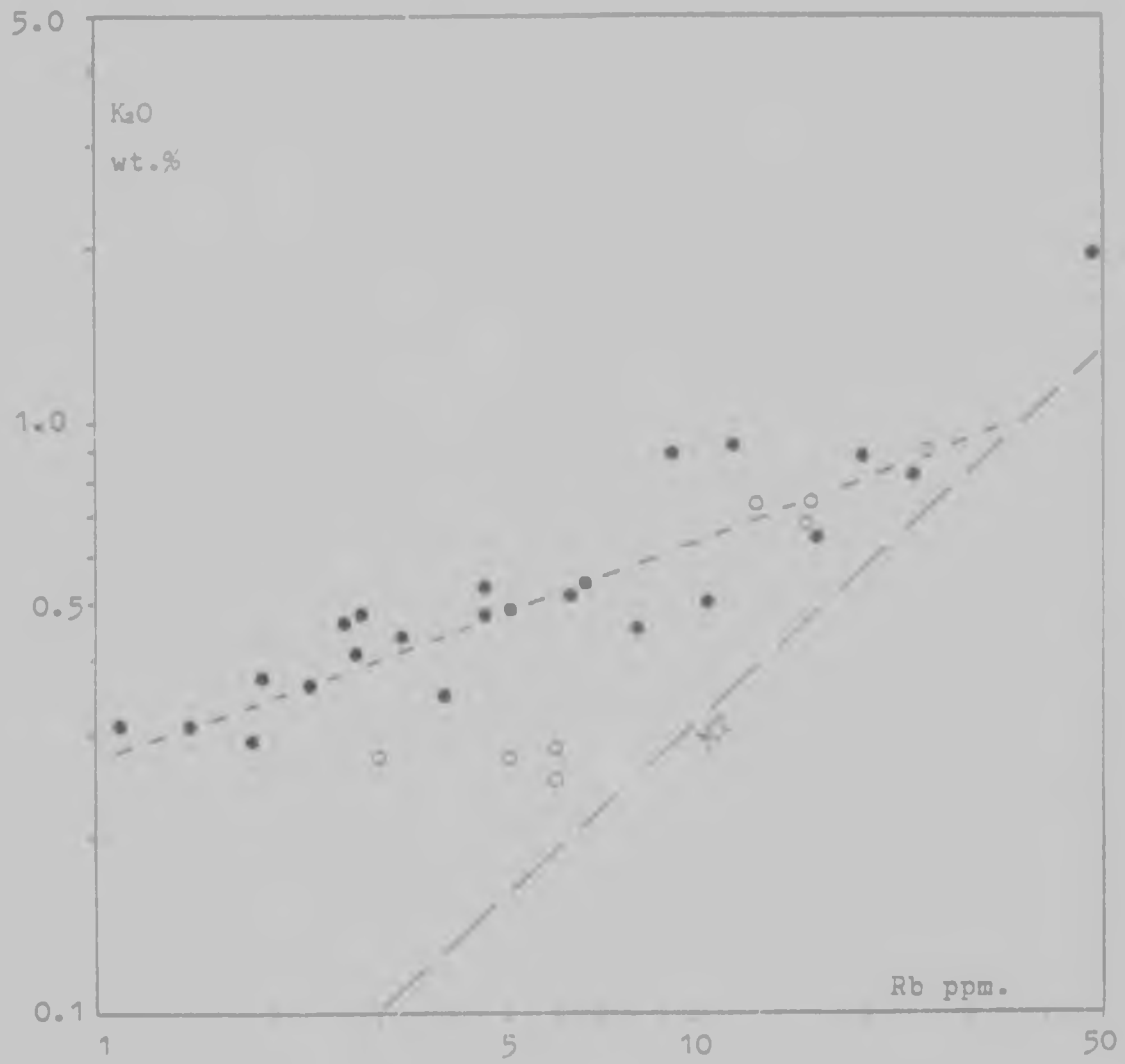


Figure 46:  $K_2O$  versus Rb diagram for the anorthositic and gabbroic gneisses of the Messina Layered Intrusion (data sources: solid circles, Barton *et al.*, 1979a; open circles, Table 7 in this study). MT is the main trend of Shaw (1968) describing the K-Rb fractionation in average magmatic rocks.

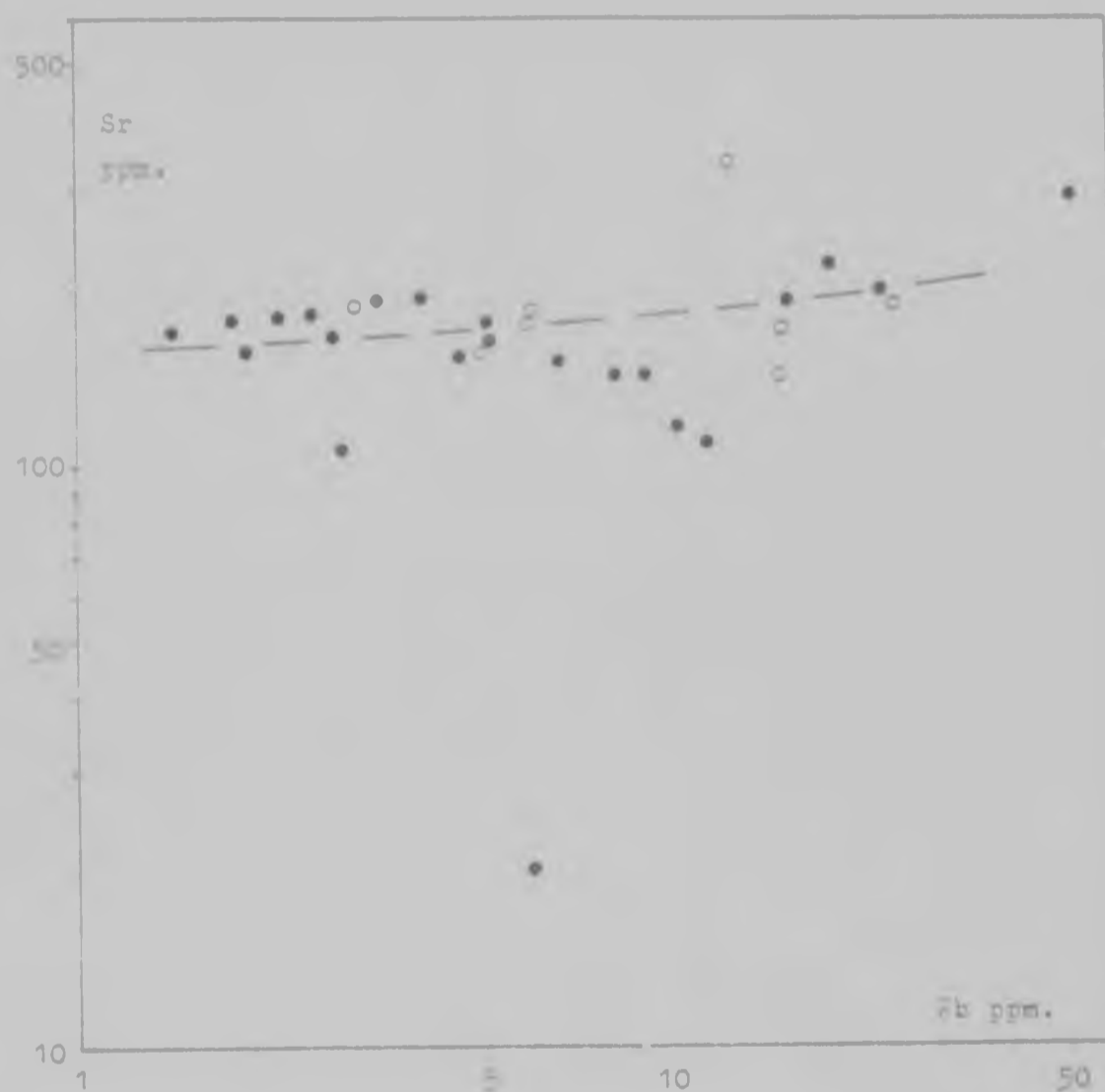


Figure 47: Sr versus Rb diagram for the anorthositic and gabbroic gneisses of the Messina Layered Intrusion (see Figure 46 for data sources).

about 75 per cent cumulate and 25 per cent interstitial liquid, then a parental magma with about 100 ppm Sr and a solid phase, such as plagioclase cumulus with about 200 ppm Sr would generate a sample with about 175 ppm Sr. This value closely correlates with those values determined in samples presented in Table 7 and the data given by Barton et al. (1979a). 200 ppm Sr is a typical value for plagioclase, and thus suggests that the parental magma to the Messina Layered Intrusion contained Sr to the order of about 100 ppm. The distribution coefficient for Rb between plagioclase and a liquid is about 0,1, thus a parental liquid with about 100 ppm Rb would fractionate plagioclase cumulates with about 10 ppm Rb. Thus a sample consisting of 75 per cent cumulate and 25 per cent interstitial liquid would contain about 33 ppm Rb. Then Raleigh 's law becomes:

$$\frac{100}{33} = \frac{0,1-1,0}{F}$$

and the value of F which satisfies this relationship is about 0,3, or about 70 per cent fractionation. Thus a parental magma which contains 100 ppm Rb is not unreasonable for the Messina Layered Intrusion. However, typical tholeiites contain about 5 ppm Rb, and hence the contention of Barton et al. (1979a) that the parental magma for the intrusion was tholeiitic is not entirely supported by this evidence. If the parental liquid contained only 50 ppm Rb (thus about 10

times more than average tholeiitic liquids), and a F value of about 0,28, (taking  $C_0 = 175$  ppm Sr, and  $D = 1,5$ ) would yield a  $C_L$  value of 30 ppm Sr.

Alternatively, by considering the tectonic and metamorphic history experienced by these rocks, the admixture of anatectites in these rocks is a distinct possibility. If a cumulate plagioclase rock with 10 ppm Rb is mixed with a 200 ppm liquid for a typical anatectite in the proportion 75 per cent to 25 per cent, then a sample with about 58 ppm Rb would result. Also, a magmatic liquid with 100 ppm Rb, when mixed with this anatectite in the same proportions, would yield a liquid with 125 ppm Rb, which in turn would fractionate cumulates with about 12,5 ppm Rb. All these values are consistent with the observed analytical data.

#### Discussion

The data presented here support the argument that the anorthositic and gabbroic rocks of the Messina Layered Intrusion are in fact of plutonic igneous origin. Pearce diagrams reveal a clear trend of plagioclase fractionation where the composition of the plagioclase cumulate was about  $An_{80}$ . The gabbros form later differentiates with the inclusion of clinopyroxene and hornblende phases. Rb and Sr values are not consistent with those of typical tholeiitic parental liquids but show enrichment

of Rb in amounts exceeding 50 ppm. Sr contents of about 100 ppm are suggested for the parental magma. Raleigh's fractionation law indicates that about 70 per cent fractionation has occurred in these rocks. A tholeiitic parental liquid has been suggested for the Messina Layered Intrusion on the basis of Harker-type variation diagrams (see Table 2 and Figure 5 of Barton et al., 1979a, in rear pocket).



of Rb in amounts exceeding 50 ppm. Sr contents of about 100 ppm are suggested for the parental magma. Raleigh's fractionation law indicates that about 70 per cent fractionation has occurred in these rocks. A tholeiitic parental liquid has been suggested for the Messina Layered Intrusion on the basis of Harker-type variation diagrams (see Table 2 and Figure 5 of Barton et al., 1979a, in rear pocket).

## CHAPTER 5: METAMORPHISM

### Introduction

The availability of over 300 electron probe microanalyses of minerals made from samples collected in the study area (see Appendix 2) has allowed the application of certain experimental data together with various thermodynamic techniques in order to evaluate the physical parameters of the metamorphism which has affected the supracrustal paragneisses of the region. These include the temperature and pressure of metamorphism, and the activity of water. A metamorphic study of the basement gneisses is presented in a complementary study (Fripp, 1981a-c). An attempt has been made to reconstruct the pressure-temperature field for these lithologies, and the PT pathway experienced by these rocks.

Various topics are considered below which utilize the mineral geochemical data (Appendix 2) obtained during this study.

### Solubility of aluminium in orthopyroxene

It has been suggested that the solubility of  $Al_2O_3$  in enstatite is in part dependent on the metamorphic grade (Anastasiou and Seifert, 1972). Orthopyroxenes analysed in this study contain about 1 per cent  $Al_2O_3$  (Appendix 2, Tables 2.16 - 2.20) in the pyroxenitic amphibolites (opx+cpx+plag+hbl+qz+ore+gar), about 3 per cent  $Al_2O_3$  (Appendix 2,

Tables 2.13 - 2.15) in the garnet-bearing symplectites (gar+opx+plag), and up to 7 per cent  $\text{Al}_2\text{O}_3$  (Appendix 2, Tables 2.7 - 2.12) in the sapphirine-bearing varieties of the garnet-cordierite-sillimanite gneiss (gar+cord+sapph+sp+cor+plag+opx+biot+sil!). These values are not particularly high when one considers that from the experimental data, well over 7 per cent  $\text{Al}_2\text{O}_3$  can be accommodated in enstatite at temperatures around  $1000^\circ\text{C}$  and at pressures of about 5 kbar. Using the curves of Anastasiou and Seifert (1972, p.283) the variation of 1 to 7 per cent  $\text{Al}_2\text{O}_3$  along a 5 kbar isobaric curve (experimental data) gives a temperature range from about  $800^\circ\text{C}$  to  $1000^\circ\text{C}$  respectively, although temperatures below  $900^\circ\text{C}$  were out of the experimental range.

It seems unlikely that metamorphic temperatures are solely responsible for this range in  $\text{Al}_2\text{O}_3$  contents. It appears that host rock compositions, and the Fe content of the orthopyroxene (Holdaway, 1976) may effect more control on the Al content of the pyroxenes. In the sapphirine rocks, free corundum and sillimanite occur, and it is logical that these peraluminous lithologies should have orthopyroxenes with the highest  $\text{Al}_2\text{O}_3$  contents. The pyroxenitic amphibolites have hydrous phases in their mineralogy, and it is also possible that a high water partial pressure may play a rôle in suppressing Al from the enstatite molecule.

Aluminium and titanium in hornblende

It has been shown that the  $Al^{6+}$  and Ti contents of hornblende may be related to metamorphic conditions (Raase, 1974). The hornblendes studied by Raase were derived from regional metamorphic terranes varying from greenschist to granulite grade, and have enabled a curve to be defined which separates low-pressure from high-pressure hornblendes on the basis of their  $Al^{6+}$  and Si contents. The data collected during this study (Figure 48) fall mainly within the low-pressure field (less than 5 kbar) defined by Raase (1974), although the gedrite analysis and an analysis of a hornblende from a metapyroxenite occur in the high-pressure field. It thus appears that host-rock composition (i.e. mineral paragenesis) is a major factor controlling the composition of hornblende, and not simply metamorphic conditions. The gedrite from the peraluminous sapphirine bearing rock shows the highest Al content, and from textural evidence, probably formed at a later stage in the metamorphism after the peak of high grade conditions. Thus, according to Raase's diagram, it should plot in lower pressure regions compared to the other hornblendes from the pyroxenitic amphibolites which coexist with metamorphic orthopyroxene.

The distribution of Ti in hornblendes from different metamorphic grades has also been compiled by Raase (1974),

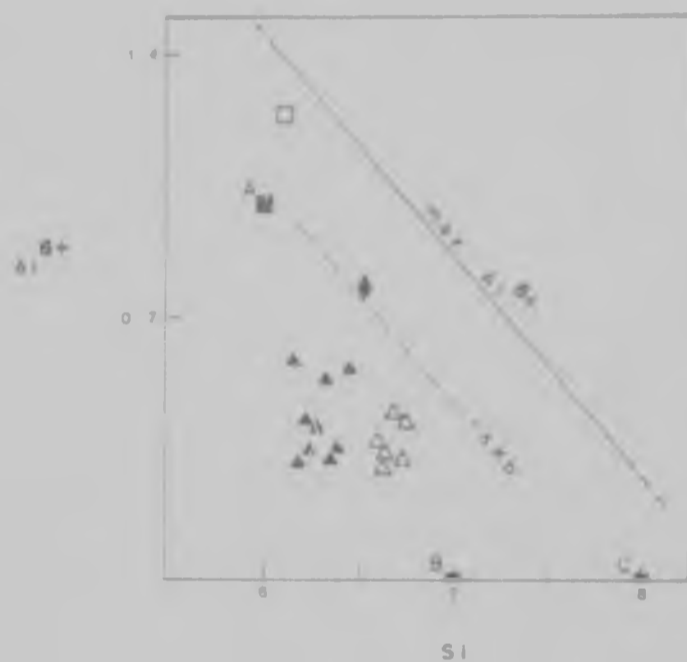


Figure 48:  $Al^{6+}$  versus Si (ions) diagram for hornblendes analysed from the study area. The 5 kbar line is after Raase (1974) and separates low pressure (below) from high pressure (above) hornblendes. A, pargasite; B, edenite; C, actinolite; solid triangles, pyroxenitic amphibolites; solid diamond, metapyroxenite; open square, gedrite from the sapphirine bearing rock (sample no.2-8-12); open triangles, gabbroic and anorthositic gneisses of the Messina Layered Intrusion. All data are taken from Appendix 2.

who suggests that Ti contents increase with increasing metamorphic grade (Figure 49). The data obtained in this study are distributed over all the metamorphic grades of Raase's compilation, with the hornblendes from the pyroxenitic amphibolites having the highest Ti contents which correlate with other hornblendes occurring within hornblende granulite facies terranes. The data from anorthositic and gabbroic samples of the Messina Layered Intrusion correlate with lower amphibolite facies hornblendes, while the metapyroxenite and sapphirine-bearing samples yield hornblende compositions which correlation with greenschist-amphibolite transition varieties. These data again suggest a host-rock composition control on the composition of metamorphic hornblendes. As in the case of Al, therefore, the Ti contents of hornblendes are not good indicators of either P or T.

#### Parameters of metamorphism

Pressure, temperature and water activity are three equilibrium parameters which may be readily calculated for appropriate metamorphic mineral assemblages using standard thermodynamics principles (e.g. Wood and Fraser, 1976). The application and results obtained from data presented in this study (Appendix 2) of various geobarometers, geothermometers and other techniques are described in Appendix 3. The equilibria utilized are as follows:

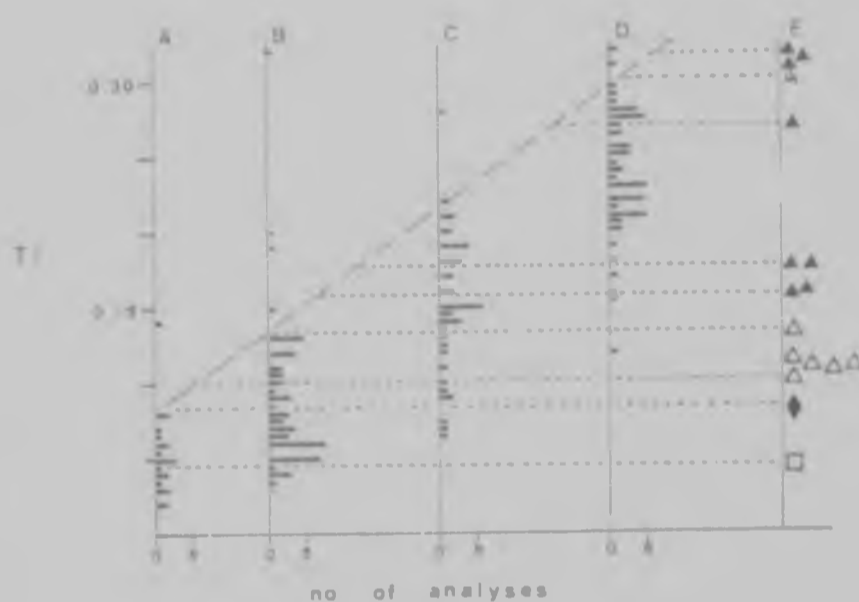


Figure 49: Ti contents of hornblendes from different metamorphic grades, and for samples analysed in this study. Histograms A, B, C and D after Raase (1974) with: A, greenschist-amphibolite transition; B, lower grade amphibolite facies; C, higher grade amphibolite facies; D, hornblende granulite facies; and E, data from this study (Appendix 2) in which the symbols are as given in Figure 48.

- (1)  $\text{Mg}_2\text{Si}_2\text{O}_6$  opx solid solution =  $\text{Mg}_2\text{Si}_2\text{O}_6$  cpx solid solution
- (2)  $\text{CaMgSi}_2\text{O}_6$  cpx +  $\text{Mg}_2\text{Si}_2\text{O}_6$  opx =  $\text{CaMgSi}_2\text{O}_6$  opx +  $\text{Mg}_2\text{Si}_2\text{O}_6$  cpx
- (3)  $\text{Mg}_2\text{Si}_2\text{O}_6$  opx +  $\text{MgAl}_2\text{SiO}_6$  opx =  $\text{Mg}_3\text{Al}_2\text{Si}_3\text{O}_{12}$  pyrope
- (4)  $\frac{1}{3}\text{Ca}_3\text{Al}_2\text{Si}_3\text{O}_{12}$  garnet +  $\text{Mg}_2\text{Si}_2\text{O}_6$  opx =  
 $\frac{1}{3}\text{Mg}_3\text{Al}_2\text{Si}_3\text{O}_{12}$  garnet +  $\text{CaMgAl}_2\text{O}_6$  opx
- (5)  $\text{Mg}_2\text{Si}_2\text{O}_6$  opx +  $\text{CaAl}_2\text{Si}_2\text{O}_8$  plag =  
 $(\frac{2}{3}\text{Mg}_3\text{Al}_2\text{Si}_3\text{O}_{12} + \frac{1}{3}\text{Ca}_3\text{Al}_2\text{Si}_3\text{O}_{12})$  garnet solid soln.  
+  $2\text{SiO}_2$  qz
- (6)  $\frac{1}{3}\text{Mg}_3\text{Al}_2\text{Si}_3\text{O}_{12}$  pyrope +  $\text{CaFeSi}_2\text{O}_6$  hedenbergite =  
 $\frac{1}{3}\text{Fe}_3\text{Al}_2\text{Si}_3\text{O}_{12}$  almandine +  $\text{CaMgSi}_2\text{O}_6$  diopside
- (7)  $\text{Fe}_3\text{Al}_2\text{Si}_3\text{O}_{12}$  almandine +  $\text{KMg}_3\text{AlSi}_3\text{O}_{10}(\text{OH})_2$  phlogopite =  
 $\text{Mg}_3\text{Al}_2\text{Si}_3\text{O}_{12}$  pyrope +  $\text{KFe}_3\text{AlSi}_3\text{O}_{10}(\text{OH})_2$  annite
- (8)  $3(\text{Mg,Fe})_2\text{Al}_4\text{Si}_5\text{O}_{18}$  cord =  $2(\text{Mg,Fe})_3\text{Al}_2\text{Si}_3\text{O}_{12}$  garnet +  
 $4\text{Al}_2\text{SiO}_5$  sill +  $5\text{SiO}_2$  qz
- (9)  $\text{CaAl}_2\text{Si}_2\text{O}_8$  anorthite =  $\text{CaAl}_2\text{SiO}_6$  Ca-Tschermak +  $\text{SiO}_2$  qz
- (10)  $\text{Ca}_2\text{Mg}_5\text{Si}_8\text{O}_{22}(\text{OH})_2$  tremolite =  $2\text{CaMgSi}_2\text{O}_6$  diopside +  
 $3\text{MgSiO}_6$  enstatite +  $\text{SiO}_2$  qz +  $\text{H}_2\text{O}$  vapour



Pressures can be determined from equilibria (3), (4), (5), (8) and (9) (Wood and Banno, 1973; Wood, 1974, 1977; Powell, 1978; Wells, 1979). Temperatures may be calculated from equilibria (1), (2), (4), (6), (7), (8) and (9) (Currie, 1971; Hensen and Green, 1971, 1972, 1973; Wood and Banno, 1973; Råheim and Green, 1974; Thompson, 1976; Holdaway and Lee, 1977; Wells, 1977; Wood, 1977; Ferry and Spear, 1978; Powell, 1978; Ellis and Green, 1979; Wells, 1979) although equilibrium (9) in effect generates a P-T curve (Wood, 1977). Water activity may be determined from equilibrium (10) (Fisher and Zen, 1971; S.W. Richardson, pers. comm.). Thermodynamic data on mineral phases are tabulated by Robie et al. (1978) and Helgeson et al. (1978), while the thermodynamic principles used in generating these methods are discussed by Wood and Fraser (1976). Results from using these techniques are tabulated in Appendix 3, and presented graphically in the following sections according to lithology or rock-types.

#### Garnet-cordierite-sillimanite gneiss

Analyses of feldspar, garnet, cordierite and biotite have been made from these metapelitic rocks and are presented in Appendix 2 (Tables 2.2 - 2.6). Two samples (21-7-F and 21-7-G) were collected on the Farm Boschrand (see Map 2 in rear pocket) and petrographic observations indicate that the above minerals form typical reaction textures according to

the following possible equilibria:



The Fe-Mg solid-solution properties of garnet, cordierite and biotite have been studied to determine their dependence on metamorphic conditions (e.g. for garnets, see Keesmann *et al.*, (1971) and various geothermometers and geobarometers have been derived. Mineral analyses obtained in this study show biotites of intermediate Fe-Mg composition, garnets which are richer in almandine than pyrope, and cordierites with more magnesian than iron-rich compositions. However, the garnets display a compositional zoning from more pyrope-rich cores to more almandine-rich rims, and this zonation is discussed in more detail later.

The pressure and temperature determinations using these data are given in Appendix 3 (Tables 3.7, 3.8 and 3.9) and are graphically presented in Figures 50-51 and summarized in Table 8. Fe-Mg partitioning between coexisting garnet and biotite has yielded geothermometers (Thompson, 1976; Ferry and Spear, 1978). Ferry and Spear's thermometer gives higher temperatures by about 50°C, although 50°C is a realistic error in these determinations, and both techniques suggest temperatures between 700°C and 800°C for the equilibration of garnet and

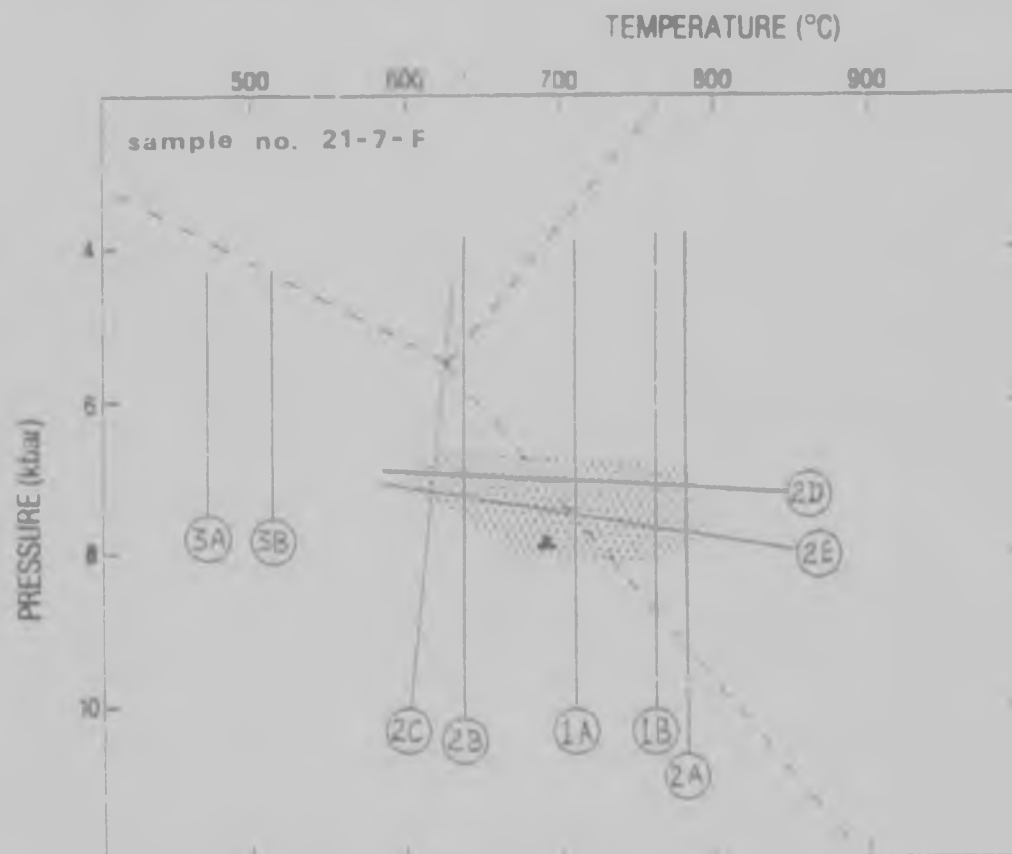


Figure 50: Pressure-temperature diagram for sample no. 21-7-F of garnet-cordierite-sillimanite gneiss (Farm Boschrand - see Map 2 in rear pocket) showing the results of the geothermometer and geobarometer calculations (see Appendix 3, Tables 3.7 to 3.9). The curves are as follows:

- 1A: garnet-biotite thermometer of Thompson (1976);
- 1B: garnet-biotite thermometer of Ferry and Spear (1978);
- 2A: garnet-cordierite thermometer of Currie (1971);
- 2B: garnet-cordierite thermometer of Thompson (1976);
- 2C: garnet-cordierite thermometer of Wells (1979);
- 2D: garnet-cordierite barometer of Wells (1979) for Fe end-members;
- 2E: garnet-cordierite barometer of Wells (1979) for Mg end-members
- 3A: two feldspar thermometer of Stomer and Whitney (1977) using; sanidine-albite solid solution; and
- 3B: two-feldspar thermometer of Stomer and Whitney (1977) using microcline-albite solid solution.

Solid triangle is the garnet-cordierite intersection point using the method of Holdaway and Lee (1977). Only results using garnet-rim compositions have been shown in this diagram, while the alumino-silicate stability fields are taken from Richardson *et al.* (1969). The stippled area is the preferred field for coexisting garnet, biotite and cordierite.

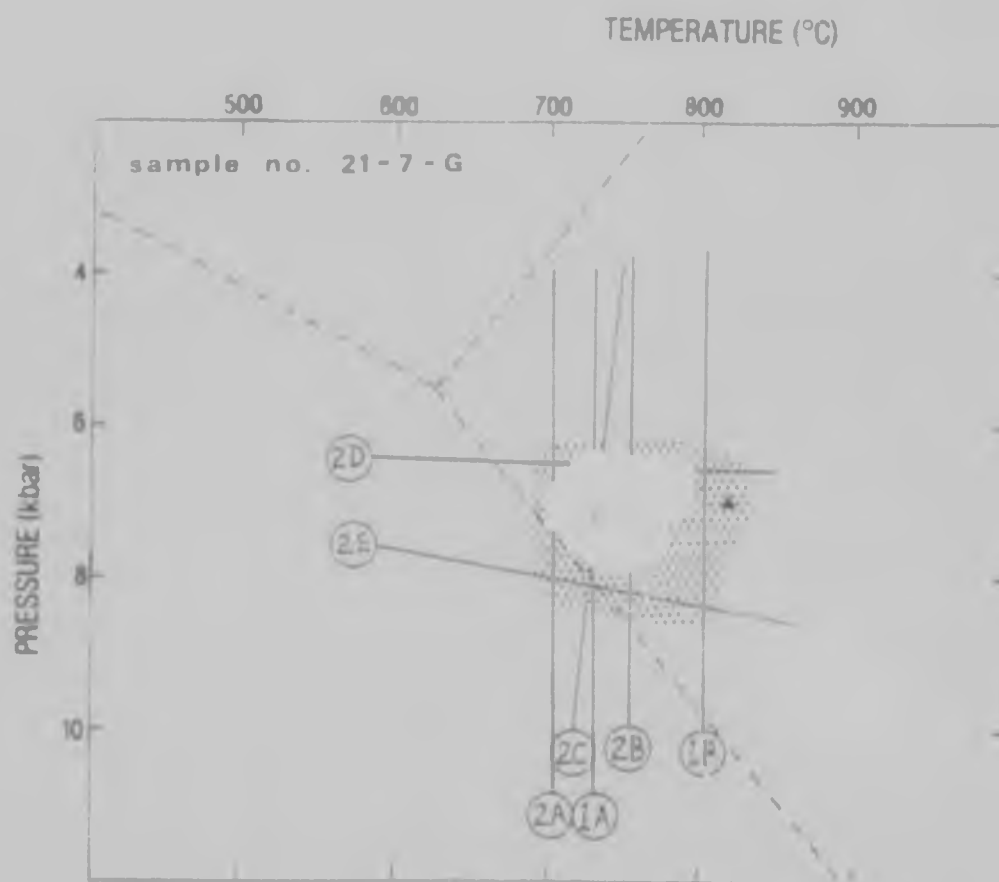


Figure 51 : Pressure-temperature diagram for sample no.21-7-G of garnet-cordierite-sillimanite gneiss (Farm Boschrand - see Map 2 in rear pocket) showing the results of the geothermometer and geobarometer calculations (see Appendix 3, Tables 3.7 and 3.8). Curves and symbols are as designated in Figure 50. Only results using garnet-rim compositions have been shown in this diagram. The stippled area is the preferred field for coexisting garnet, biotite and cordierite.

Table 8: Summary and range of pressure (kbar) and temperature (°C) results for garnet-cordierite-sillimanite gneiss (samples 21-7-F and 21-7-G from Farm Boschrand - see Map 2 in rear pocket).

	Data source (Appendix 3)	Coexisting minerals	21-7-F	21-7-G	
				garnet core	garnet rim
T1	Table 3.7	garnet+biotite	708	852	734
T2	Table 3.7	garnet+biotite	764	989	802
T3	Table 3.8	garnet+cordierite	783	647	705
T4	Table 3.8	garnet+cordierite	638	880	755
T5	Table 3.8	garnet+cordierite	-	850	-
T6	Table 3.8	garnet+cordierite	690	870	815
P6	Table 3.8	garnet+cordierite	7,9	6,8	7,0
T7	Table 3.8	garnet+cordierite	613 - 633	847 - 872	727 - 749
P7	Table 3.8	garnet+cordierite	6,8 - 7,8	6,2 - 9,0	6,4 - 8,4

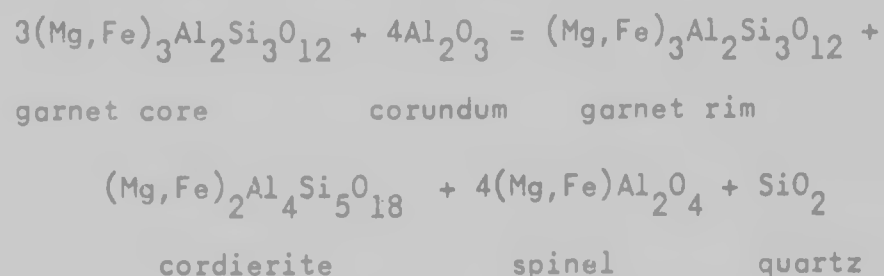
- T1: Thompson (1976)
- T2: Ferry and Spear (1978)
- T3: Currie (1971)
- T4: Thompson (1976)
- T5: Hensen and Green (1973)
- T6 and P6: Holdaway and Lee (1977)
- T7 and P7: Wells (1979)

biotite in these lithologies. The Fe-Mg partitioning between coexisting garnet and cordierite has also allowed derivation of thermometers and barometers (Currie, 1971; Thompson, 1976; Holdaway and Lee, 1977; Wells, 1979). Good consistency between these methods suggest temperatures between 600°C and 800°C at pressures between 6,5 kbar and 8,0 kbar for the stable equilibrium between coexisting garnet and cordierite. Thus the high-grade metamorphism affecting the garnet-cordierite-sillimanite gneiss and which stabilized biotite, garnet and cordierite was characterized by pressure and temperature conditions indicated by the shaded areas of Figures 50-51, namely temperatures between 600°C and 800°C, and pressures between 6,5 kbar and 8,5 kbar.

#### Sapphirine-bearing rocks

The textural and petrographic evidence of the sapphirine-bearing varieties of the garnet-cordierite-sillimanite gneisses suggests a complex sequence of reactions involving garnet, cordierite, sapphirine, spinel and corundum (see Chapter 2). Early formed garnet (more pyrope-rich ?) and corundum, formed during the peak of metamorphism, are separated by 'canals' of cordierite, sapphirine and spinel (see Figures 6 and 7) suggesting that sapphirine formed during later retrogression in the metamorphism. Mineral chemical data are presented in Appendix 2 (Tables 2.7 - 2.12). The garnet porphyroblasts

are concentrically zoned and are approximately Fe-Mg solid solutions in which Ca and Mn comprise less than 2 per cent of the octahedrally coordinated cations as in the garnets occurring in the garnet-cordierite-sillimanite gneisses. The centres of the porphyroblasts approach  $\text{Alm}_{49}\text{Py}_{50}\text{Gross}_1$  compositions, while steeper gradients towards more iron-rich compositions occur around the margins where compositions of  $\text{Alm}_{55}\text{Py}_{44}\text{Gross}_1$  are typically obtained. The grossular content appears to be relatively constant from core to margin, while spessartine contents are relatively negligible. The cordierite shows minimal zoning, and has Fe/Fe+Mg ratios of about 0.1. The spinel composition approaches  $\text{Spinel}_{55}\text{Hercynite}_{45}$  while the orthopyroxene is bronzite with  $\text{Al}_2\text{O}_3$  contents of about 7 per cent. Typical coexisting minerals from these rocks are plotted in a  $\text{MgO}+\text{FeO} - \text{SiO}_2 - \text{Al}_2\text{O}_3$  ternary diagram (Figure 52). The upper stability limits of pyrope have been studied by Schreyer (1968) and of almandine-pyrope compositions by Keessmann *et al.* (1971) and their data suggest that the garnet cores were stable at temperatures exceeding  $800^\circ\text{C}$  and pressures in excess of 8 kbar. The zonation in the garnet, and the 'rims' of spinel, sapphirine and cordierite separating garnet and corundum suggest a reaction of the following form:



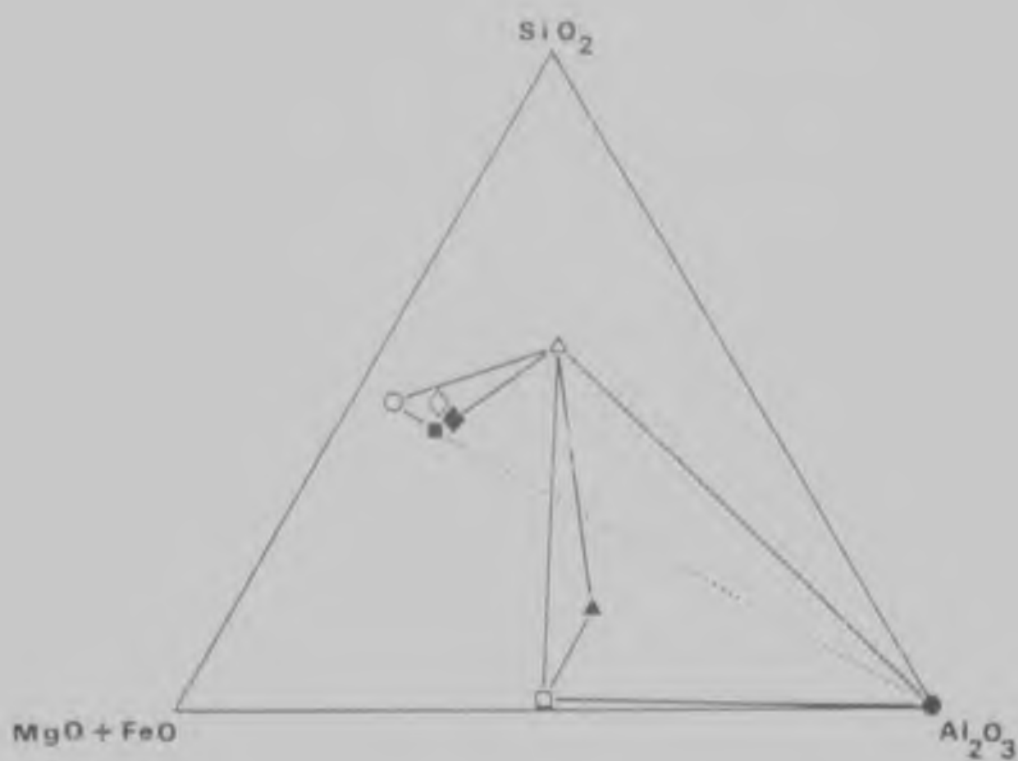
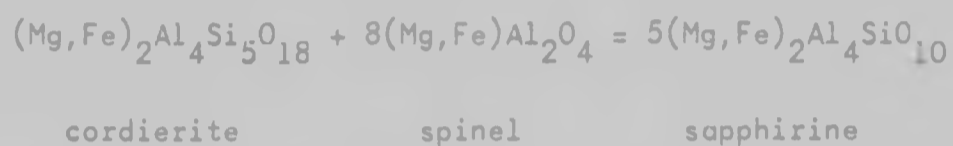


Figure 52: A MgO+FeO - SiO<sub>2</sub> - Al<sub>2</sub>O<sub>3</sub> ternary diagram showing the compositions of minerals from the sapphirine bearing variety of the garnet-cordierite-sillimanite gneiss. Solid square, garnet; open triangle, cordierite; solid triangle, sapphirine; open square, spinel; solid circle, corundum; solid diamond, biotite; open diamond, gedrite; open circle, orthopyroxene. Tie lines join coexisting phases, while the dotted line joins earlier formed garnet+corundum, now no longer in equilibrium.



where the garnet on the right-hand side of this reaction becomes more iron-rich in the presence of the magnesian phases of spinel and cordierite. The observation of sapphirine occurring along spinel-cordierite boundaries suggests that the sapphirine-forming reaction was as follows:



This reaction is similar to that proposed by Seifert (1974, eqn.9), which produced orthopyroxene (Figure 53), according to the reaction:



This reaction occurs between 3 and 4 kbar and between 765°C and 1200°C (Figure 53). The invariant point of cordierite+enstatite+sapphirine+spinel+chlorite+H<sub>2</sub>O is situated at 765°C and 3,8 kbar.

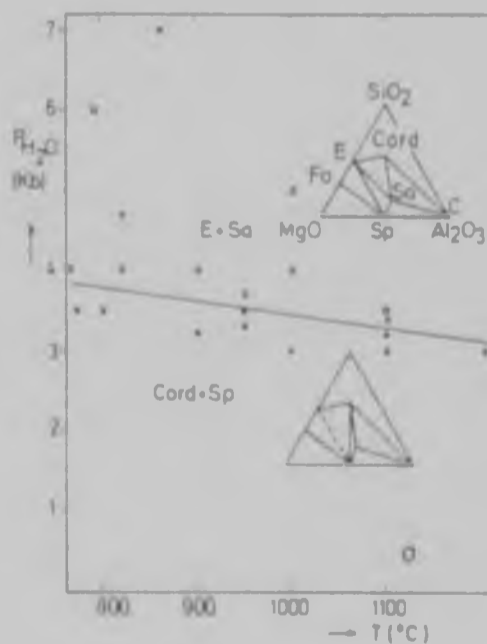


Figure 53: Experimental data for the reaction cord+sp = en+sa (from Seifert, 1974)

The bronzite occurring in these lithologies was not observed to be directly related to the garnet-cordierite-sapphirine-spinel-corundum assemblage, and it occurs in only small amounts in coexistence with garnet, cordierite and plagioclase (Figure 8). Its presence may be limited by the availability of  $Al_2O_3$ , since in  $Al_2O_3$  deficient compositions, hypersthene + sapphirine + cordierite + spinel assemblages would be stable (Seifert, 1974), while in  $Al_2O_3$ -rich environments, sapphirine replaces hypersthene to produce sapphirine + cordierite + spinel + corundum + sillimanite assemblages. The bronzitic orthopyroxene has an  $Al_2O_3$  content greater than 7.5 per cent, and the work of Anasiasiu and Seifert (1972) suggests that the Al-enstatite solvus occurs at temperatures over  $1000^{\circ}C$  and at pressures less than 5 kbar.

The reaction of garnet with corundum described earlier produces quartz during this metamorphism, but no free quartz was observed in the sapphirine-bearing rocks under study. This may be accounted for by considering the abundant quartz-rich veins and pegmatites which 'soak' the surrounding terrane and which resulted during the extensive anatexis which has affected the region. Consideration of the whole-rock compositions of the sapphirine rock (Table 3) and its host (garnet-cordierite-sillimanite gneiss) shows that the sapphirine rock is relatively depleted in  $SiO_2$ , CaO,  $Na_2O$  and

$K_2O$ , while enriched in  $MgO$ ,  $FeO$  and  $Al_2O_3$ . This supports the view that these sapphirine-bearing assemblages represent metamorphic residues after the extraction of minimum melt granitic liquids (Clifford *et al.*, 1975; Lal *et al.*, 1978) and are not due to magnesium or aluminium metasomatism (e.g. Robertson, 1977).

The lack of published thermodynamic data on sapphirine precludes the direct calculation of P-T curves for the sapphirine-producing reactions. However, other thermometers and barometers can be applied to certain phases in these assemblages, notably for coexisting garnet and cordierite, and garnet and phlogopitic biotite. Also, the presence of orthopyroxene allows the application of coexisting garnet and orthopyroxene methods. The results of these determinations are tabulated in Appendix 3 (Tables 3.3, 3.4, 3.7 and 3.8) for sample nos. 2-8-12 and 11-8, and are presented graphically in Figures 54-55 and summarized in Table 9. P-T curves for coexisting garnet and phlogopite geothermometry are presented in Figures 54-55. However, for sample no. 2-8-12, two sets of analytical data from two different laboratories are available (see Appendix 2 - Tables 2.8 and 2.9) and these sets of data yield distinctly different results (Figure 54). Those obtained using data from the Cape Town laboratory suggest temperatures from  $600^{\circ}C$  to  $650^{\circ}C$  while the Witwatersrand laboratory data

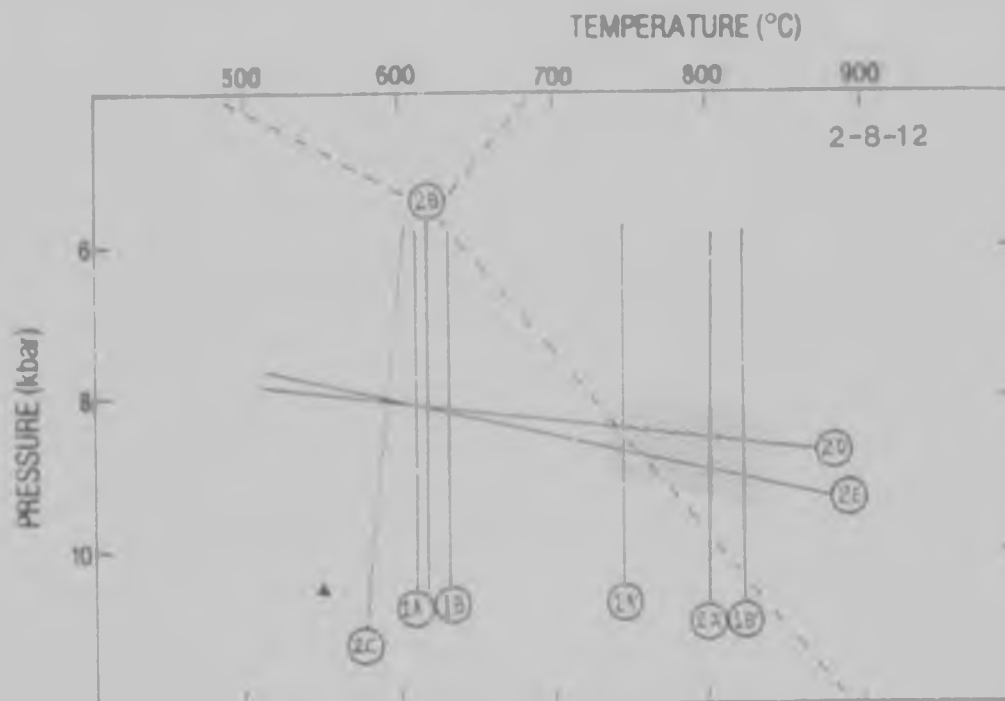


Figure 54: Pressure-temperature diagram for sample no. 2-8-12 of sapphirine bearing rock (Farm Randjesfontein - see Map 2 in rear pocket) showing the results of the geothermometer and geobarometer calculations (see Appendix 3, Tables 3.3, 3.4, 3.7 and 3.8). The curves are as follows:

- 1A: garnet-biotite thermometer of Thompson (1976) - UCT laboratory;
- 1A': garnet-biotite thermometer of Thompson (1976) - WITS laboratory;
- 1B: garnet-biotite thermometer of Ferry and Spear (1978) - UCT;
- 1B': garnet-biotite thermometer of Ferry and Spear (1978) - WITS;
- 2A: garnet-cordierite thermometer of Currie (1971);
- 2B: garnet-cordierite thermometer of Thompson (1976);
- 2C: garnet-cordierite thermometer of Wells (1979);
- 2D: garnet-cordierite barometer of Wells (1979) for Fe end-members;
- 2E: garnet-cordierite barometer of Wells (1979) for Mg end-members.

Solid triangle is the garnet-cordierite intersection point using the method of Holdaway and Lee (1977). Only results using garnet-rim compositions have been shown in this diagram, while the aluminosilicate stability fields are taken from Richardson *et al.* (1969). Stippled area is the preferred field for coexisting garnet, biotite and cordierite.

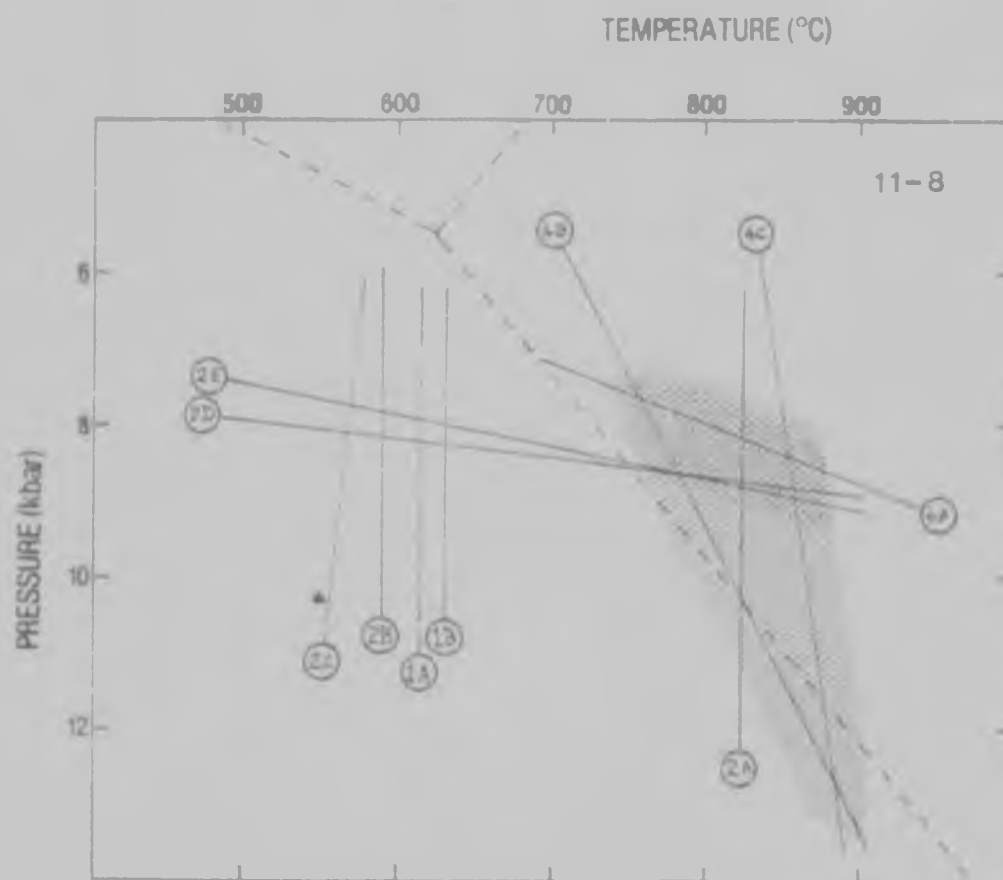


Figure 55 : Pressure-temperature diagram for sample no.11-8 of sapphirine bearing rock (Farm Randjesfontein - see Map 2 in rear pocket) showing the results of geothermometer and geobarometer calculations (see Appendix 3, Tables 3.3, 3.4, 3.7 and 3.8). The curves are as designated in Figure 54 , and, in addition, the following:

- 4A: coexisting garnet and orthopyroxene (Wood and Banno, 1973);
- 4B: coexisting garnet and orthopyroxene (Wood, 1974); and
- 4C: coexisting garnet and orthopyroxene (Powell, 1978).

The ruled area is the preferred field of coexisting garnet and orthopyroxene. The stippled area is the preferred field for coexisting garnet, biotite and cordierite.

Table 9: Summary and range of pressure (kbar) and temperature ( $^{\circ}\text{C}$ ) results for sapphirine-bearing rock (samples 2-8-12 and 11-8 from Farm Randjesfontein - see Map 2 in rear pocket).

	Data source (Appendix 3)	Coexisting minerals	2-8-12	11-8	
				garnet core	garnet rim
P1	Table 3.3	orthopyroxene+garnet	-	4,1 - 6,4	5,7 - 8,8
P2	Table 3.3	orthopyroxene+garnet	-	0 - 13,7	0 - 13,6
T3	Table 3.4	orthopyroxene+garnet	-	928 - 979	820 - 861
T4	Table 3.7	garnet+biotite	615 - 748	704	615
T5	Table 3.7	garnet+biotite	633 - 824	759	633
T6	Table 3.8	garnet+cordierite	802	755	824
T7	Table 3.8	garnet+cordierite	616	675	591
T8	Table 3.8	garnet+cordierite	550	630	550
P8	Table 3.8	garnet+cordierite	10,5	9,8	10,3
T9	Table 3.8	garnet+cordierite	592 - 611	649 - 670	568 - 587
P9	Table 3.8	garnet+cordierite	7,8 - 8,9	7,6 - 9,2	7,5 - 8,8

P1: Wood and Banna (1973)

P2: Wood (1974)

T3: Powell (1978)

T4: Thompson (1976)

T5: Ferry and Spear (1978)

T6: Currie (1971)

T7: Thompson (1976)

T8 and P8: Holdaway and Lee (1977)

T9 and P9: Wells (1979)

suggest temperatures from 750°C to 525°C. However, the results with the lower temperatures fall in the field of kyanite (after Richardson et al., 1969), and since no kyanite has been recognized in any rock-types within the study area, should be regarded with caution. Coexisting garnet and cordierite yields both thermometers and barometers, and are shown in Figures 54-55. The thermometers of Thompson (1976) and Wells (1979) agree with the temperatures for garnet-phlogopite pairs using the Cape Town data, but not with the higher temperatures using the data obtained with the ARL-SEMQ instrument. However, the garnet-cordierite thermometer of Currie (1971) is consistent with the higher temperatures close to 800°C obtained from the higher temperature garnet-phlogopite thermometric data. Garnet-cordierite barometers of Wells (1979) are shown for Fe and Mg end-members and indicate pressures of about 8 kbar in both samples (Figures 54-55). P-T curves for coexisting garnet and orthopyroxene define a large field (Figure 55) with temperatures from 750°C to 880°C and pressures from 7,5 kbar to 13 kbar, the latter yielded by sample no.11-8 only.

In summary, intersection of the above curves defines three fields in P-T space. Coexisting garnet, phlogopite and cordierite suggests two fields depending on the data source: from 575°C to 640°C and from 7,5 to 8,5 kbar (Cape

own data - Cambridge Microscan 5), and from 740°C to 850°C and 7,5 kbar to 9,0 kbar (ARL-SEM, Wits instrument). In sample no. 11-8, coexisting garnet and orthopyroxene defines a field ranging from 750°C to 850°C and from 8 kbar to 12 kbar (Figure 55 - ruled area). It is suggested that the P-T conditions which are most consistent for the entire assemblage of garnet-rim + cordierite + phlogopite + orthopyroxene (and probably also sapphirine + spinel) for the equilibrating phase of the metamorphism lie within 750°C and 850°C and close to 8 kbar.

#### Garnet-orthopyroxene-plagioclase symplectite

The garnet-hypersthene-plagioclase rock (samples 2-8-10A and 2-8-10B) occurs on the Farm Randjesfontein (see Map 2 in rear pocket) and contains distinctive symplectitic corona textures. Garnet porphyroblasts are rimmed by an intergrowth of myrmekitic hypersthene in a plagioclase host (Figure 10; see also Horrocks, 1980, Fig.2). Leyreloup *et al.* (1975) ascribed this texture to a retrograde transition from high-temperature high-pressure to high-temperature intermediate-pressure granulite facies metamorphism probably due to uplift of the lower crust with erosion. The texture is produced by the reaction:

garnet (+ diopside-augite) + quartz = hypersthene + plagioclase



in the case of garnets rich in almandine ( $\text{FeO}/\text{MgO} > 1$ ), which is true for garnets of this lithology in the area under study. Garnets which are particularly rich in grossular, such as in mafic granulites, are probably subject to the following reaction:



In the Southern Marginal Zone of the Limpopo Mobile Belt south of the Soutpansberg mountains (Figure 1), a similar texture has been described (Van Reenen and Du Toit, 1978) from 'cordierite-garnet-hypersthene-biotite granulites', which may be correlative with the garnet-cordierite-sillimanite gneisses occurring in the study area. However, an important difference exists between the assemblage in the Southern Marginal Zone and the symplectite assemblage described from the study area, in that the hypersthene is hosted in plagioclase, whereas the samples of Van Reenen and Du Toit show hypersthene hosted in cordierite. Although hypersthene-cordierite-biotite symplectites do occur in the study area (Figure 9) mainly in rocks which are also sapphirine bearing, it appears that the samples of Van Reenen and Du Toit (1978) contained sufficient MgO and FeO to produce cordierite rather than plagioclase, perhaps due to the enrichment of these components during anatexis. Also, the garnet is less calcic in the samples from the Southern Marginal Zone suggesting a more pelitic composition. Thus, Van Reenen and Du Toit (1978) considered

the following reaction:



to have produced their symplectites. Alternatively, the presence of cordierite over plagioclase south of the Soutpansberg in this corona-forming reaction may suggest different metamorphic conditions prevailed in the two regions, whereby cordierite has not reacted and equilibrated with phases such as spinel and sapphirine to take up MgO and FeO. The assemblages from Farm Randjesfontein in the study area contain no free quartz, and the garnets appear to show relatively little compositional zoning. Thus quartz may have been entirely consumed during these reactions, or may have been lost during anatexis of the region. In places within the samples, no garnet remains, and only spherical 'knots' of myrmekitic hypersthene in plagioclase occur suggesting the complete replacement of the garnet.

Calculations of the pressure and temperature conditions for these mineral assemblages are tabulated in Appendix 3 (Tables 3.3, 3.4, 3.5, and 3.7) and are presented graphically in Figures 56a-d and summarized in Table 10. The use of different sets of analytical data reveals inconsistencies between these different methods (see Figures 56a-d) which may be due to either defective analytical data, or data from locations within mineral grains which are not in equilibrium. The latter explanation is preferred, since although severe

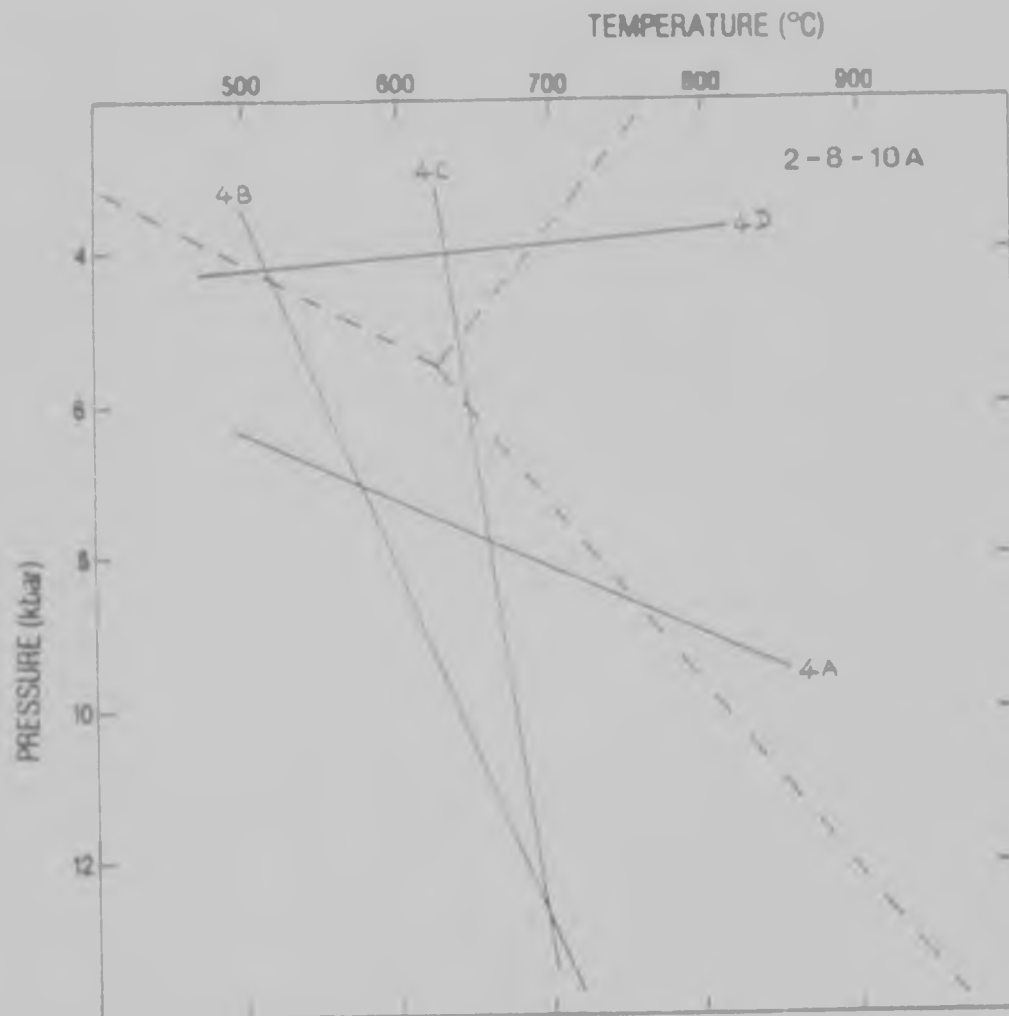


Figure 56a: Pressure-temperature diagram for sample no. 2-8-10A of garnet-orthopyroxene-plagioclase symplectite (Farm Randjesfontein - see Map 2 in rear pocket) showing the results of the geothermometer and geobarometer calculations (Appendix 3, Tables 3.3, 3.4, 3.5 and 3.7). The curves are as follows: 4A: garnet-orthopyroxene barometer of Wood and Banno (1973); 4B: garnet-orthopyroxene barometer of Wood (1974); 4C: garnet-orthopyroxene thermometer of Powell (1978); and 4D: garnet-orthopyroxene barometer of Powell (1978). Alumino-silicate stability fields are taken from Richardson *et. al.* (1969).

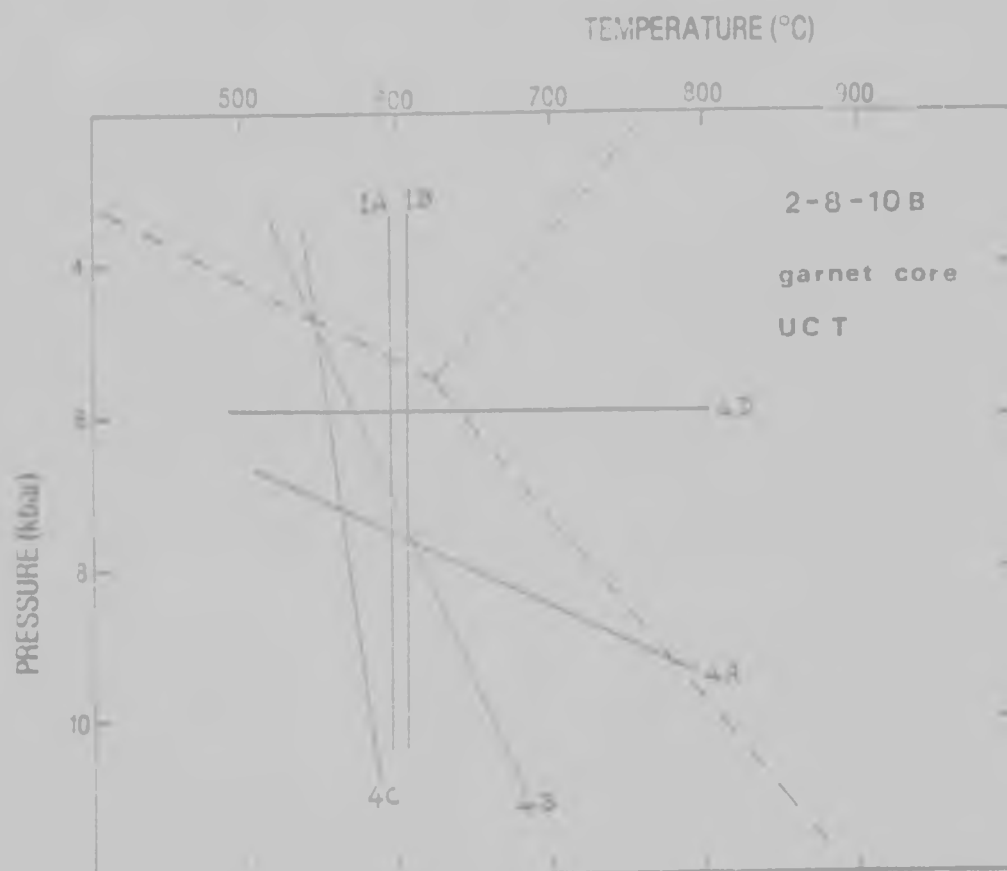


Figure 56b: Pressure-temperature diagram for sample no. 2-8-10B of garnet-orthopyroxene-plagioclase symplectite (Farm Randjesfontein - see Map 2 in rear pocket) showing the results of the geothermometer and geobarometer calculations (Appendix 3, Tables 3.3, 3.4, 3.5 and 3.7). The curves are designated as in Figure 56a and in addition the following:  
 1A: garnet-biotite thermometer of Thompson (1976); and  
 1B: garnet-biotite thermometer of Ferry and Spear (1978).  
 Only results using garnet-core compositions are shown in this diagram, and which were obtained from the UCT laboratory (Appendix 2, Table 2.14).

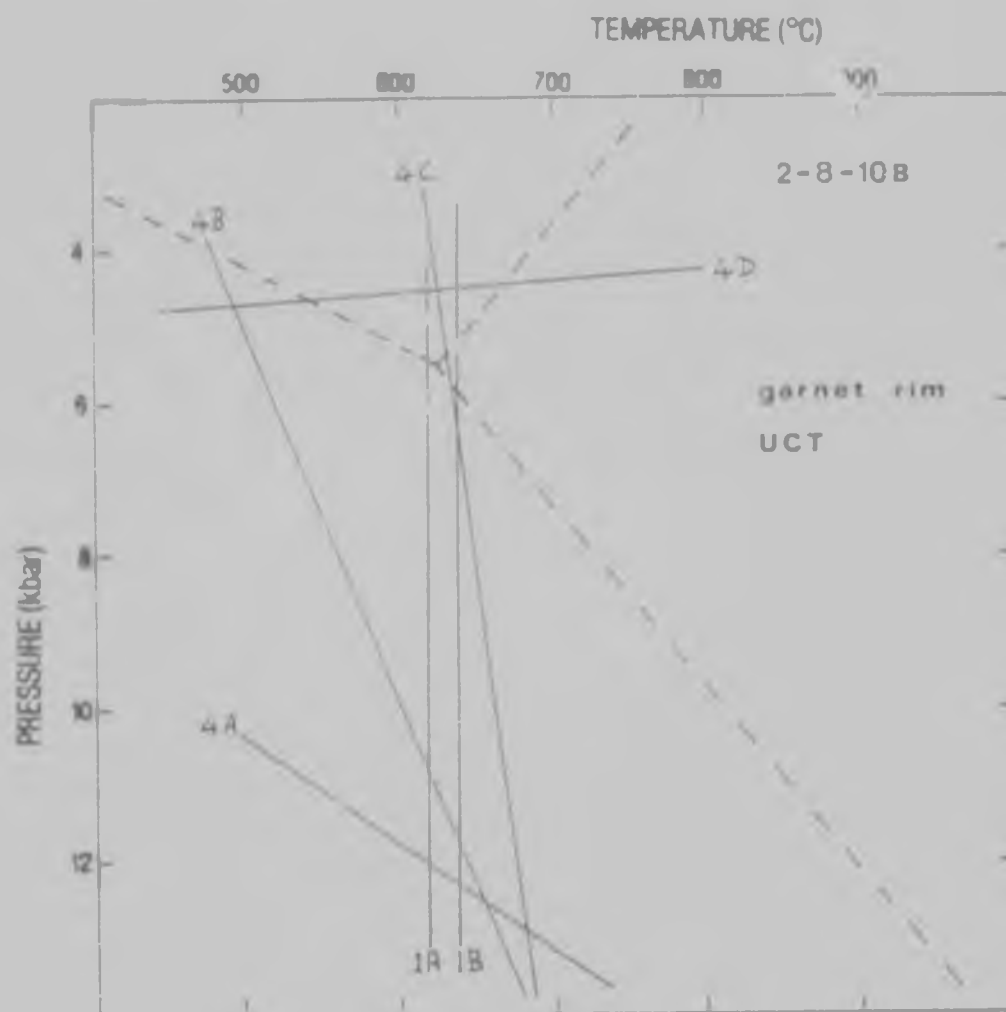


Figure 56c: Pressure-temperature diagram for sample no. 2-8-10B of garnet-orthopyroxene-plagioclase symplectite (Farm Randjesfontein - see Map 2 in rear pocket) showing the results of the geothermometer and geobarometer calculations (Appendix 3, Tables 3.3, 3.4, 3.5 and 3.7). The curves are as designated in Figures 56a and 56b. Only results using garnet-rim compositions are shown in this diagram, and which were obtained from the UCT laboratory (Appendix 2, Table 2.14).

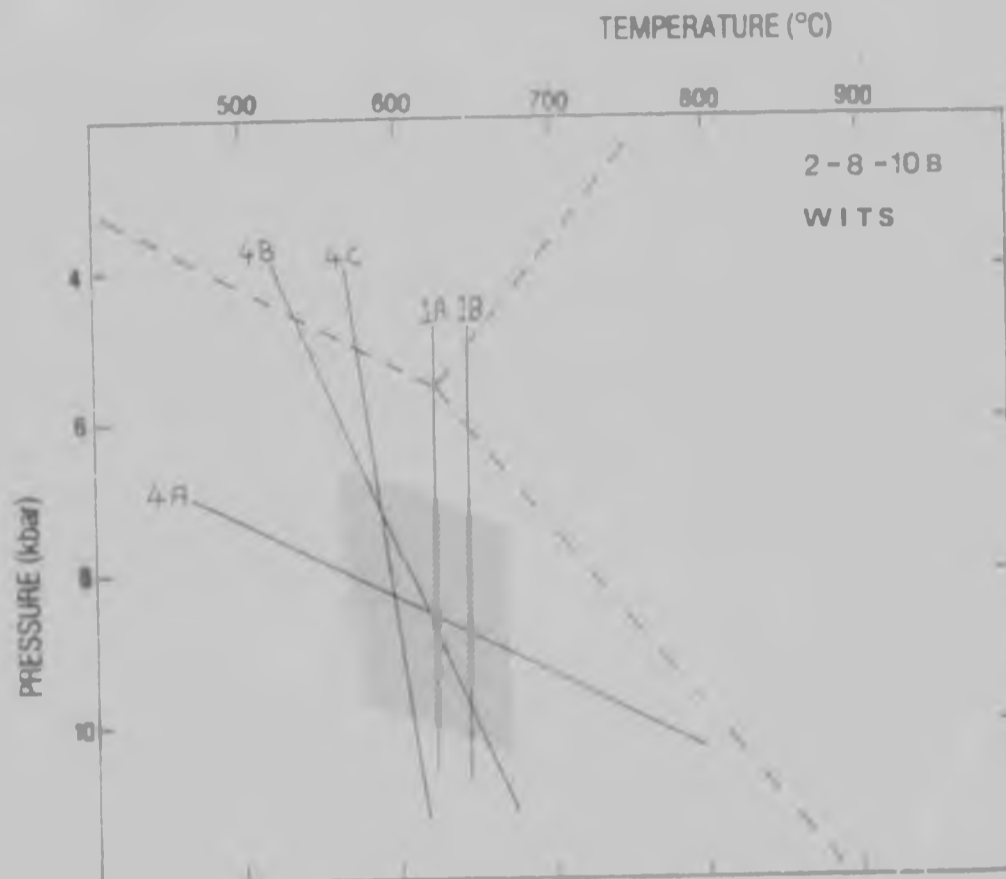


Figure 56d: Pressure-temperature diagram for sample no. 2-8-10B of garnet-orthopyroxene-plagioclase symplectite (Farm Randjesfontein - see Map 2 in rear pocket) showing the results of the geothermometer and geobarometer calculations (Appendix 3, Tables 3.3, 3.4, 3.5 and 3.7). The curves are as designated in Figures 56a and 56b. Only results using the data from the WITS laboratory (Appendix 2, Table 2.15) are shown in this diagram. The ruled area is the preferred field of coexisting garnet, biotite and orthopyroxene.

Table 10: Summary and range of pressure (kbar) and temperature ( $^{\circ}\text{C}$ ) results for garnet-orthopyroxene-plagioclase symplectite (samples 2-8-10A and 2-f-10B from Farm Randjesfontein - see Map 2 in rear pocket).

	Data source (Appendix 3)	Coexisting minerals	2-8-10A	2-8-10B	
				garnet core	garnet rim
P1	Table 3.3	garnet+orthopyroxene	6,4 - 9,9	6,6 - 11,3	10,4 - 16,1
P2	Table 3.3	garnet+orthopyroxene	3,5 - 22,3	2,6 - 21,6	5,0 - 24,6
T3	Table 3.4	garnet+orthopyroxene	634 - 678	540 - 609	623 - 665
P4	Table 3.5	garnet+orthopyroxene	3,4 - 4,2	5,9	4,1 - 4,7
T5	Table 3.7	garnet+biotite	-	593 - 625	620
T6	Table 3.7	garnet+biotite	-	603 - 646	639

P1: Wood and Banno (1973)

P2: Wood (1974)

T3: Powell (1978)

P4: Wells (1979)

T5: Thompson (1976)

T6: Ferry and Spear (1978)

inconsistencies appear with the results for sample no.2-8-10A (Figure 56a) consistent intersections of the different P-T curves occur with the application of the data obtained from the same laboratory for sample no.2-8-10B where only garnet-core compositions are used. Here, a P-T field from about 550°C to 600°C and from about 6,0 kbar to 7,5 kbar is suggested for equilibrium between phlogopite, garnet-cores and hypersthene (see Figure 56b). However, data from the same laboratory (UCT - Cambridge Microscan 5) and for the same sample (no. 2-8-10B) but using only garnet-rim compositions (Figure 56c) again yields large inconsistencies between the different techniques. While temperatures are constrained to lie between about 600°C and 700°C, the barometers give results ranging from less than 5 kbar to over 12 kbar. Thus, disequilibrium compositions rather than faulty data appear to produce these inconsistencies. The most reliable data, from analytical quality and equilibrium composition stand-points, give the results shown in Figure 56d using data from the WITS laboratory (ARL-SEMQ) for sample no.2-8-10B. A field from about 575°C to 650°C and from 7 kbar to 9 kbar is indicated.

#### Garnet zonation in the pelitic rock-types

Studies of zoning in garnets have been made to determine histories of metamorphism in both regional and contact metamorphic terranes (Kretz, 1973; Tracey et al., 1975;



Thompson *et al.*, 1977; Berg, 1977). Zoning has also been recognized in garnets from the garnet-cordierite-sillimanite gneiss and its sapphirine-bearing varieties within the study area, and to a lesser extent, in the garnet-orthopyroxene-plagioclase symplectites. To illustrate these compositional variations, over 150 microanalyses were completed on individual garnet porphyroblasts from the above rock-types (see Appendix 2, Tables 2.4, 2.10 and 2.15), and all garnet analyses obtained in this study with the exception of those obtained from mafic rock-types (167 analyses) are plotted in three Ca+Mn - Fe<sup>2+</sup> - Mg ternary diagrams for each of the above pelitic lithologies (Figures 57 - 59). Obvious compositional variation trends are revealed for the garnet-cordierite-sillimanite gneiss (Figure 57) and sapphirine-bearing rock-type garnets (Figure 58) while the garnets from the symplectite show a relatively poor zonation (Figure 59). Compositions vary from about Alm<sub>54</sub>Py<sub>43</sub>Gr<sub>3</sub> cores to Alm<sub>67</sub>Py<sub>28</sub>Gr<sub>5</sub> rims in the garnet-cordierite-sillimanite gneiss (Figure 57) for a garnet porphyroblast about 1 cm in diameter, and few garnets exceed this dimension, while many are smaller. The sapphirine-bearing variety (Figure 58) show more magnesian-rich cores of about Alm<sub>41</sub>Py<sub>57</sub>Gr<sub>2</sub> with rims of about Alm<sub>53</sub>Py<sub>43</sub>Gr<sub>4</sub>. Spessartine forms negligible amounts, usually not more than 1 or 2 per cent, and Mn is grouped with Ca in the ternary diagrams for clarity. Thus

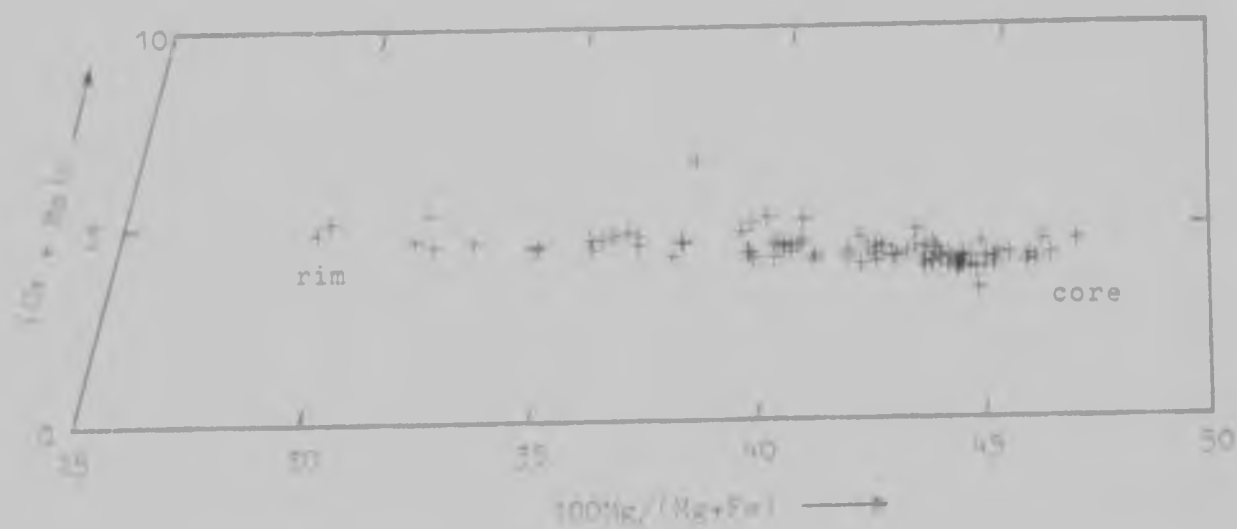


Figure 57:  $\text{Ca+Mn} - \text{Fe}^{2+} - \text{Mg}$  ternary diagram showing the compositional variation of garnet from the core to rim of a garnet porphyroblast from a garnet-cordierite-sillimanite gneiss (sample no.21-7-G, Farm Boschrand - see Map 2 in rear pocket). Data from Appendix 2, Table 2.4.

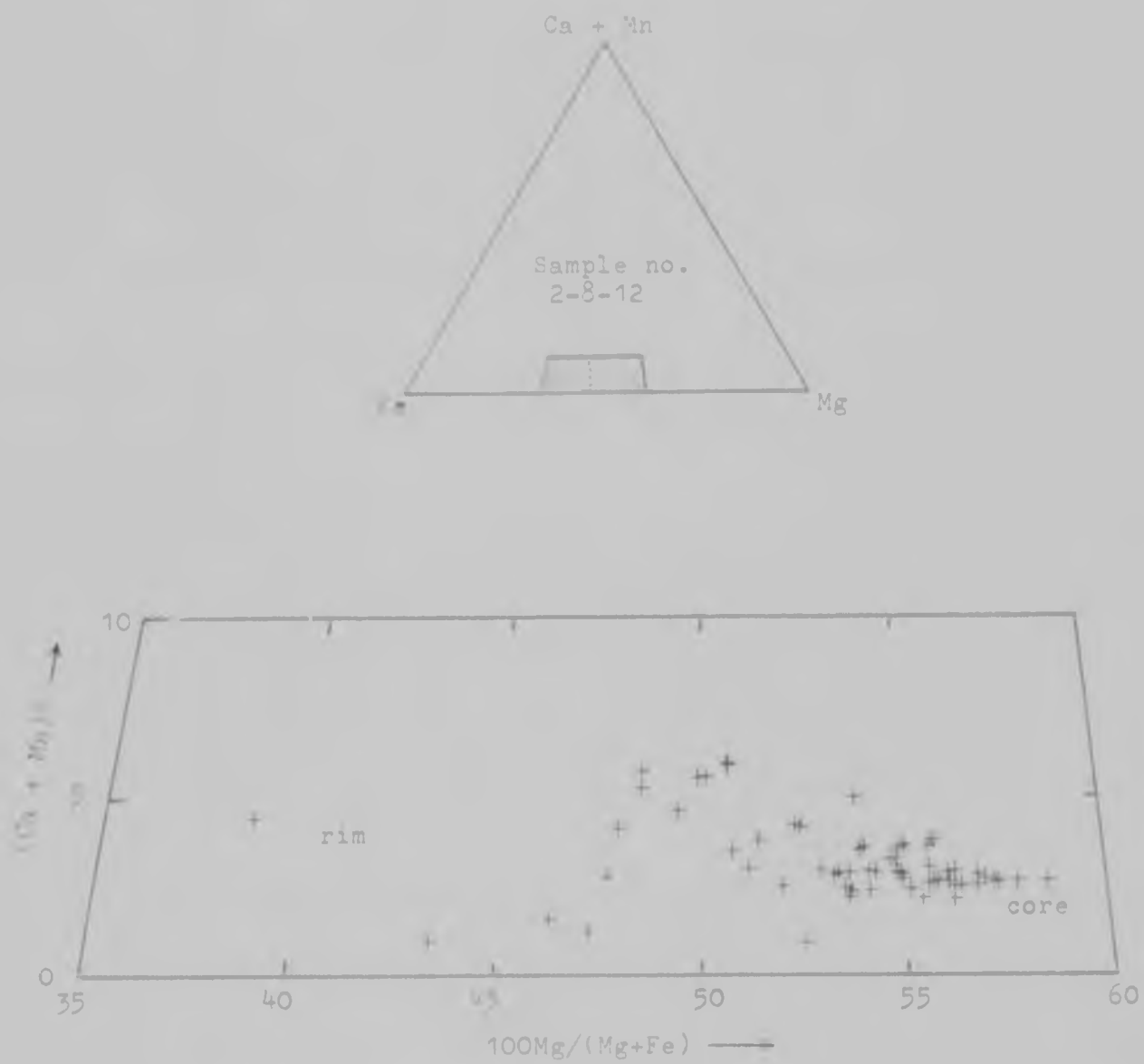


Figure 58: Ca+Mn - Fe<sup>2+</sup> - Mg ternary diagram showing the compositional variation of garnet from the core to rim of a garnet porphyroblast from a sapphirine bearing rock (sample no.2-8-12, Farm Randjesfontein - see Map 2 in rear pocket). Data from Appendix 2, Table 2.10.

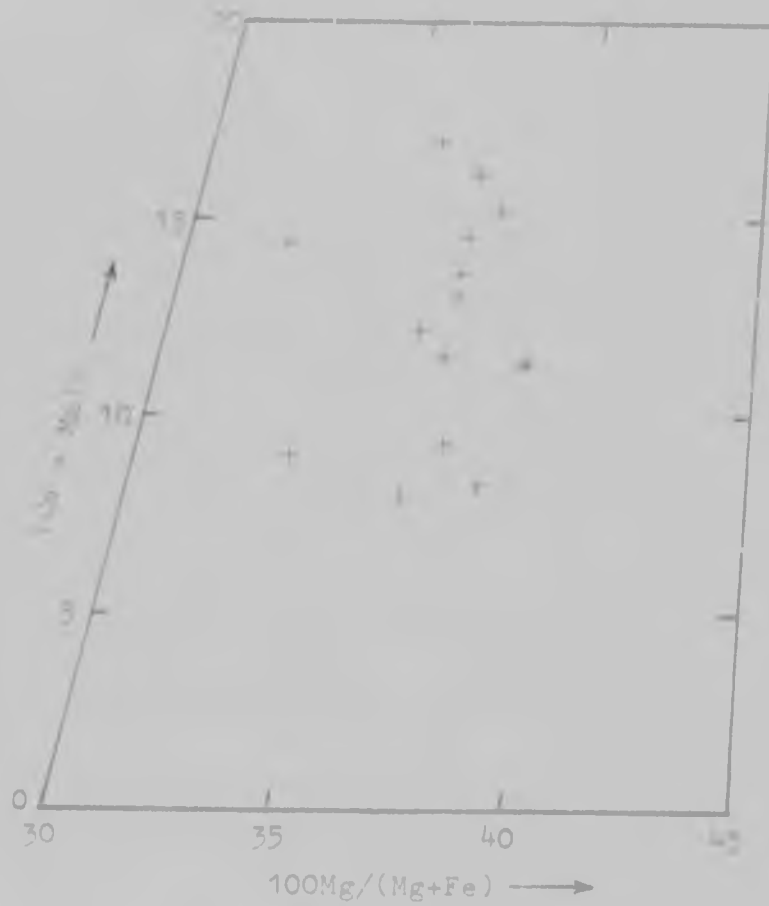


Figure 57: Ca+Mn - Fe<sup>2+</sup> - Mg ternary diagram showing the compositional variation of garnet from a garnet-orthopyroxene-plagioclase symplectite (sample no. 2-8-10B, Farm Randjesfontein - see Map 2 in rear pocket). Data from Appendix 2, Table 2.15.

these garnets form near perfect Mg-Fe solid solutions and are ideal for the application of the various geothermometers and geobarometers that have been developed for Mg-Fe systems. The garnet compositions in the symplectite (Figure 59) do not show an obvious trend, but scatter about an approximate composition of  $\text{Alm}_{53}\text{Py}_{35}\text{Gr}_{12}$  and are thus much more calcic than the garnets occurring in the previous two varieties. Also, this symplectite is plagioclase-bearing in contrast to other symplectites described from the Limpopo Mobile Belt (Van Reenen and Du Toit, 1978) which contain cordierite, again illustrating the more calcic nature of these symplectites occurring in the study region.

Figures 60 and 61 illustrate the garnet porphyroblasts studied from the garnet-cordierite-sillimanite gneiss and sapphirine-bearing rock respectively, while Figures 62 and 63 show the locations of the electron probe microanalyses. In the case of the garnet-cordierite-sillimanite gneiss (sample no.21-7-G, Figures 60 and 62), several cordierite analyses were obtained from areas immediately surrounding the garnet, and several biotites were also analysed, occurring both as inclusions within the garnet and as small grains outside the garnet. No phlogopites were observed within the garnet from the sapphirine-bearing rock (sample no.2-8-12, Figures 61 and 63) that were suitable for analysis, but cordierites,

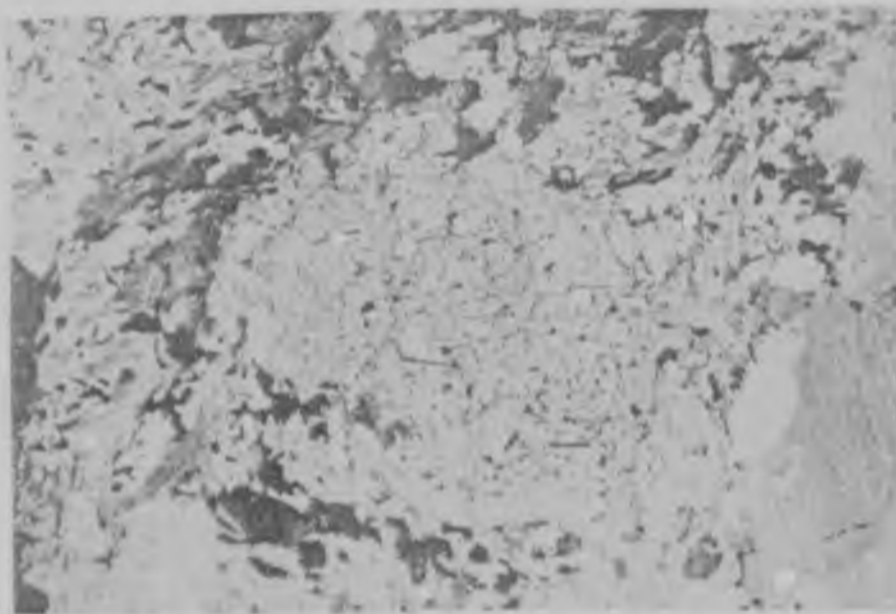


Figure 60: Photomicrograph of the garnet porphyroblast from a garnet-cordierite-sillimanite gneiss (sample no.21-7-G, Farm Boschrand - see Map 2 in rear pocket) used in the study of garnet zonation. The garnet has a diameter of about 1 cm.

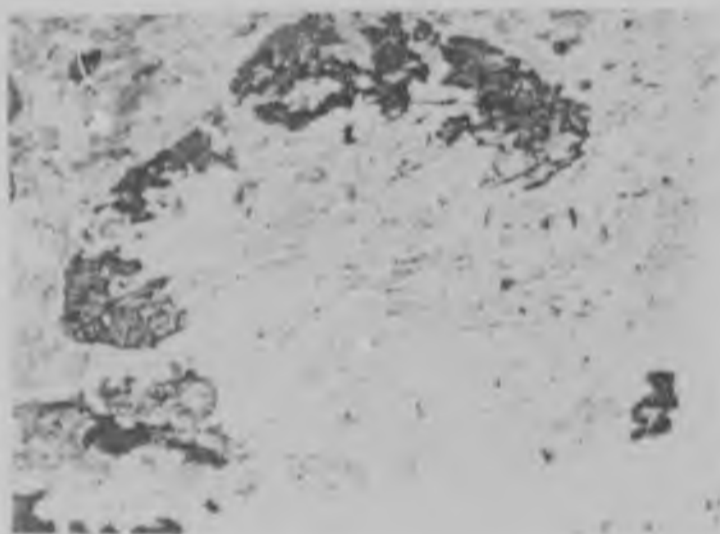


Figure 61: Photomicrograph of the garnet porphyroblast from the sapphirine bearing rock (sample no.2-8-12, Farm Randjesfontein - see Map 2 in rear pocket) used in the study of garnet zonation. The garnet has a diameter of about 1 cm.



Figure 62: Schematic representation of the garnet porphyroblast from a garnet-cordierite-sillimanite gneiss shown in Figure 60 showing the locations of the electron probe microanalyses made on the garnet and adjacent minerals, including the biotite fragments. The arrowed location is the nearest to the geometrical centre of the grain - see text for discussion.

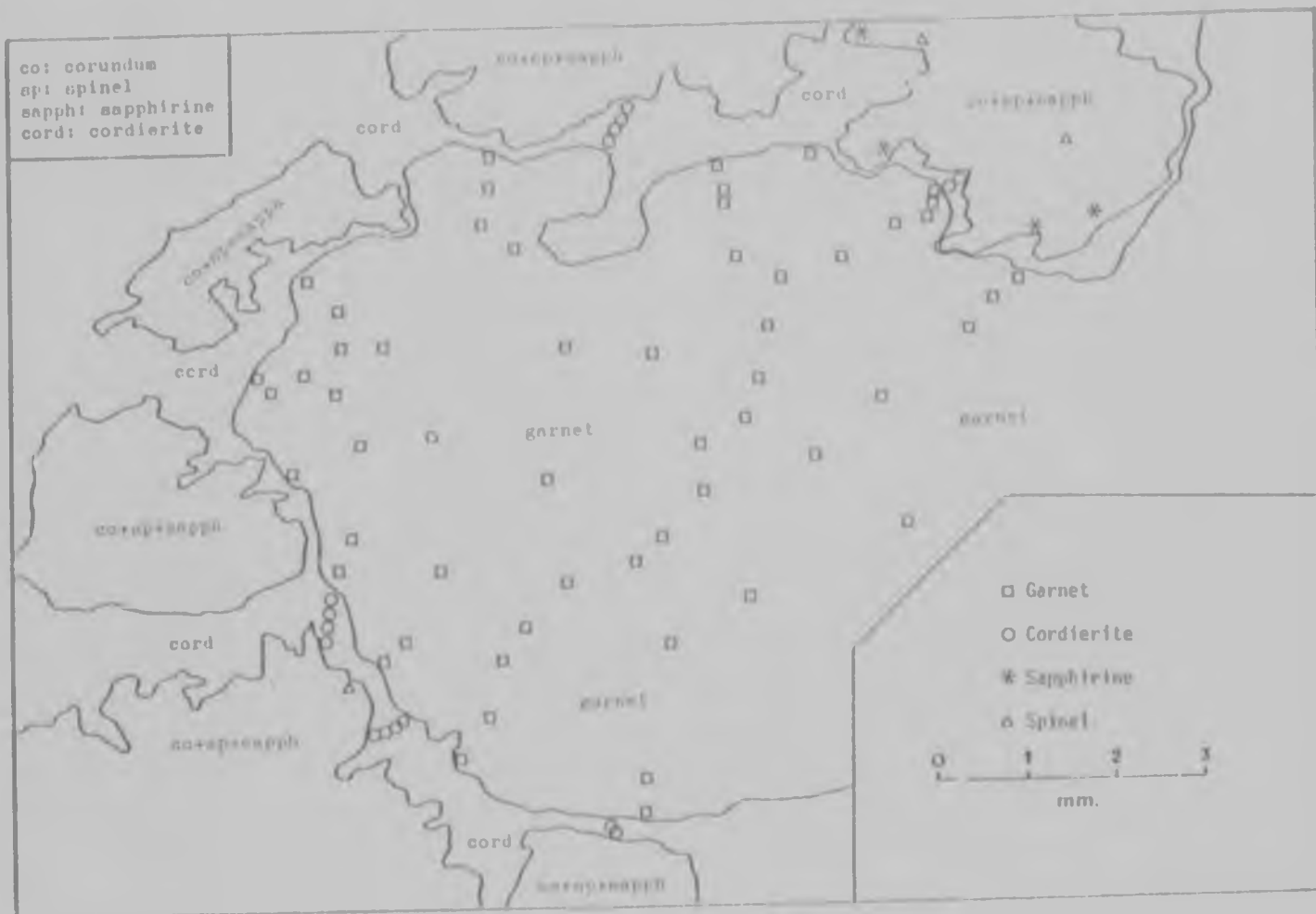


Figure 63: Schematic representation of the garnet porphyroblast from the sapphirine bearing rock shown in Figure 61 showing the locations of the electron probe microanalyses made on the garnet and adjacent minerals.



sapphirines and spinels were analysed from the regions immediately adjacent to the garnet. Small corundum inclusions occur within the garnet from the sapphirine-bearing rock, but are in all cases 'armoured' from the garnet by a rim of cordierite. Mole fraction data calculated from the structural formulae of these analyses have been plotted and contoured (Figures 64-66) and show similar compositional distributions for both the garnet-cordierite-sillimanite gneiss and the sapphirine-bearing variety. Figure 64 shows the distribution of ferrous iron in the M1 octahedrally coordinated site in the garnet molecule ( $X_{Fe}^{M1}$ ), and a broad plateau of values for this mole fraction between 0,525 and 0,575 is revealed which covers about 80 per cent of the garnet area. Steep gradients then occur around the grain margins, with values approaching 0,675 adjacent to the grain boundaries. These highest  $X_{Fe}^{M1}$  values are only achieved where the garnet borders against cordierite+biotite+sillimanite assemblages, while where the garnet borders against quartz grains, values of only about 0,575 are typical. Thus, compositional profiles are dependent on adjacent assemblages on a microscopic scale, and the relevant mineral reactions between these phases. Figures 65-66 show similar patterns for the garnet porphyroblast examined from a sapphirine-bearing variety (sample no.2-8-12) with broad compositional plateaux covering most of the grain, and steep

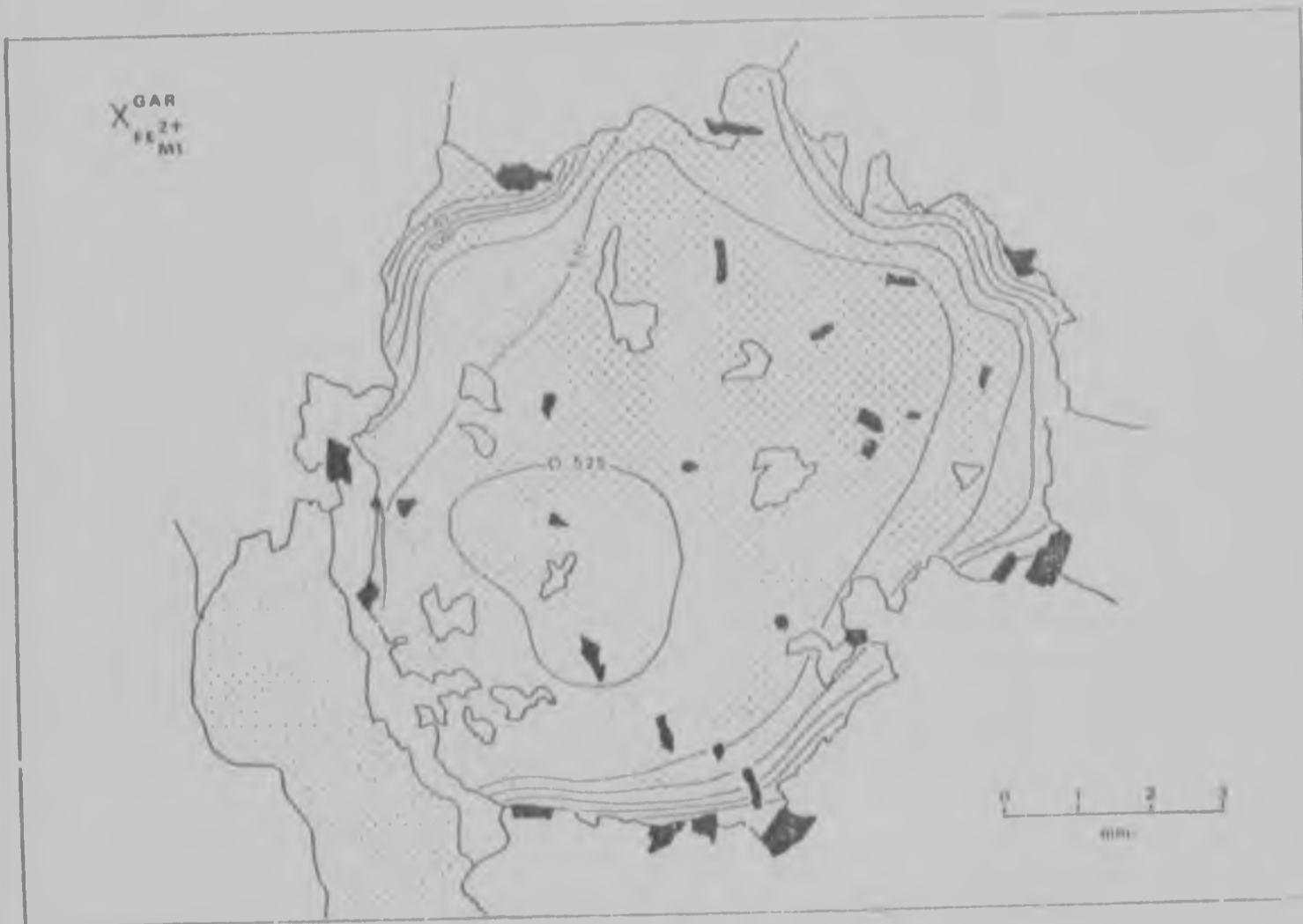


Figure 64: Schematic diagram of the garnet porphyroblast from a garnet-cordierite-sillimanite gneiss illustrated in Figures 60 and 62, showing the compositional contours of the mole fraction of ferrous iron in the M1 octahedrally coordinated site of the garnet molecule.

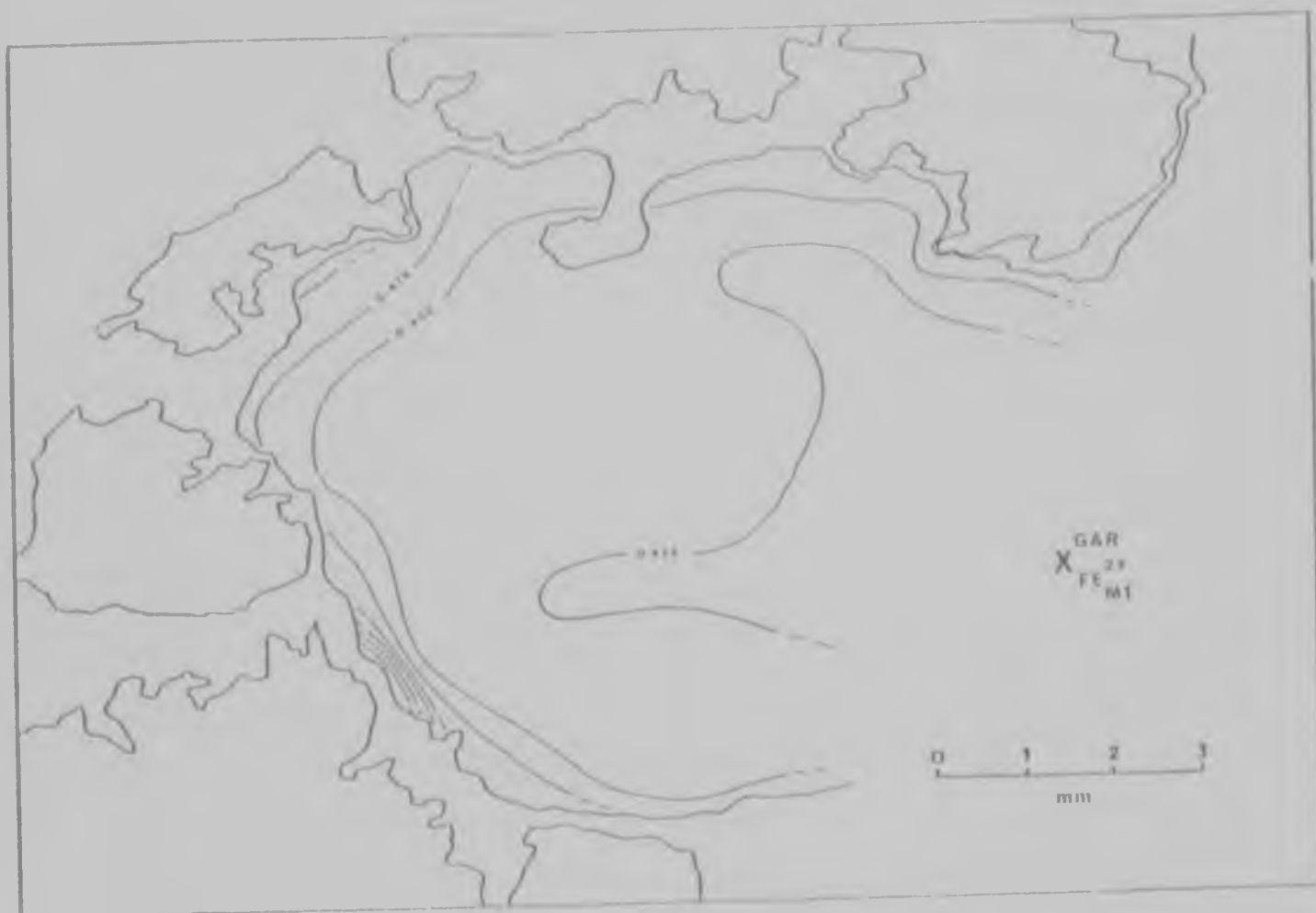


Figure 65: Schematic diagram of the garnet porphyroblast from the sapphirine-bearing rock illustrated in Figures 61 and 63 showing the compositional contours of the mole fraction of ferrous iron in the M1 octahedrally coordinated site of the garnet molecule.

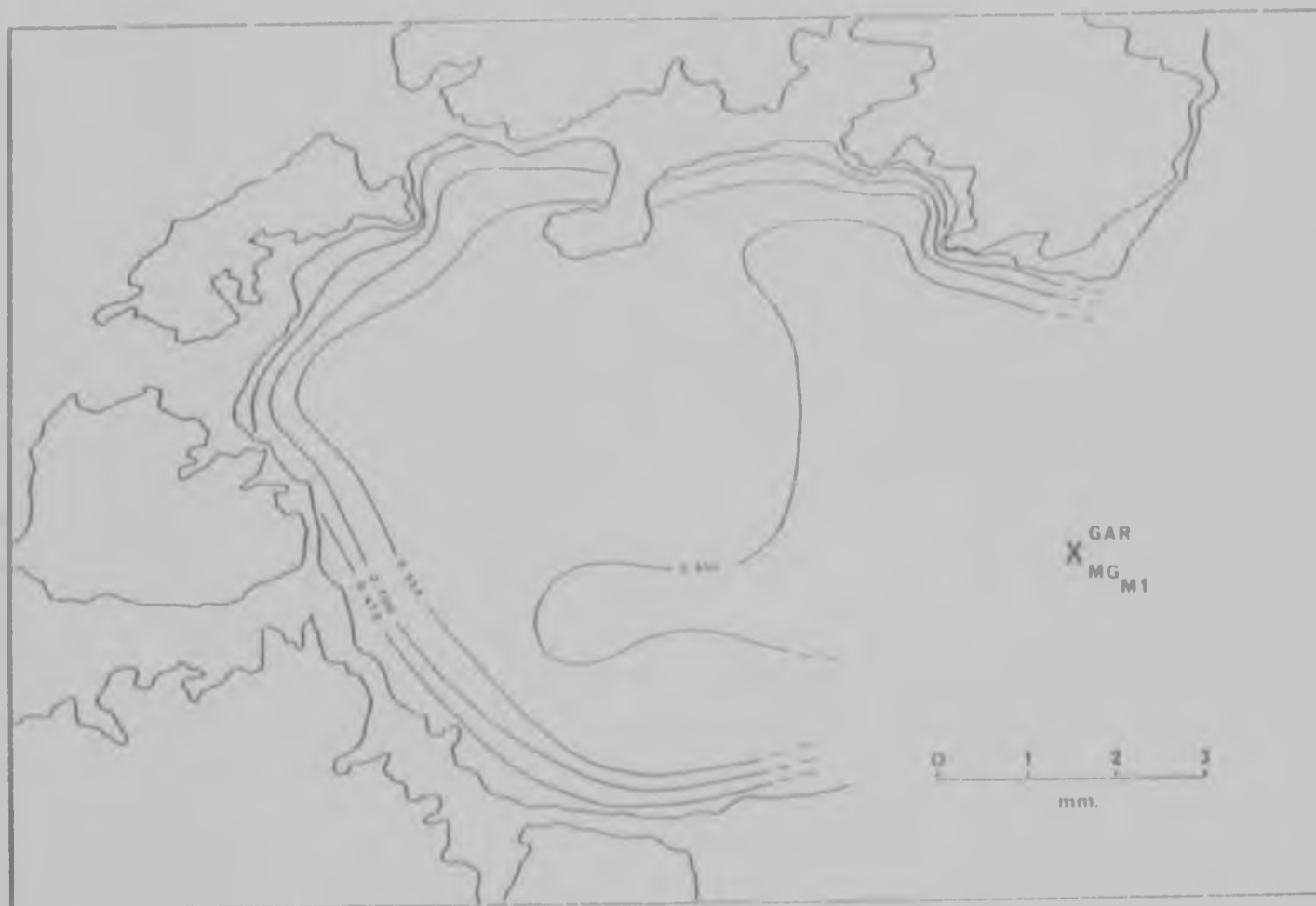


Figure 66: Schematic diagram of the garnet porphyroblast from the sapphirine bearing rock illustrated in Figures 61 and 63 showing the compositional contours of the mole fraction of magnesium in the M1 octahedrally coordinated site of the garnet molecule.

gradients around the grain margin. Contours of  $X_{Fe}$  and  $X_{Mg}$  for the M1 site (Figures 65 and 66 respectively) display almost 'mirror-image' patterns illustrating the binary Fe-Mg solid-solution character of these garnets. Core values of  $X_{Fe}=0,425$  and  $X_{Mg}=0,550$  are typical, while rim values of  $X_{Fe}=0,500$  and  $X_{Mg}=0,475$  are characteristic.

The data for the garnet studied in the garnet-cordierite-sillimanite gneiss (Figures 62 and 64) have also been plotted against the radius of the grain (Figure 67) whereby the positions of the individual analysis points were measured on a radius passing from the arrowed analysis point which is closest to the geometrical centre of the garnet section (Figure 62) out to the grain margin. Then the radius position of the analysis point was normalized to a value between 0 and 1, such that at 0 the analysis point lies at this centre point, and at 1 the point lies on the grain boundary. Different mole fraction populations are plotted in Figure 67 and show clear trends varying from core (radius = 0) to margin (radius = 1) which are extracted and plotted in Figure 68. The iron and magnesium mole fractions for the garnet show 'mirror-images' with almost constant values from the core to a radius value of about 0,75, while steeper opposed gradients appear towards the margins. This reflects the binary solid-solution between Mg and Fe in these garnets. However, a large scatter



Figure 67: Diagram showing the variation of mole fraction compositional data with increasing radius from the garnet porphyroblast from a garnet-cordierite-sillimanite gneiss illustrated in Figures 60 and 62. The centre of the garnet is at radius = 0, while the garnet rim is at radius = 1. For values of radius greater than 1, cordierite+biotite+sillimanite+quartz assemblages occur. Symbols are as follows: +, mole fraction of ferrous iron in the M1 site of garnet; x, mole fraction of magnesium in the M1 site of garnet; open triangles, mole fraction of calcium in the M1 site of garnet; open diamonds, mole fraction of ferrous iron in the biotite molecule; and open squares, mole fraction of ferrous iron in the cordierite molecule.

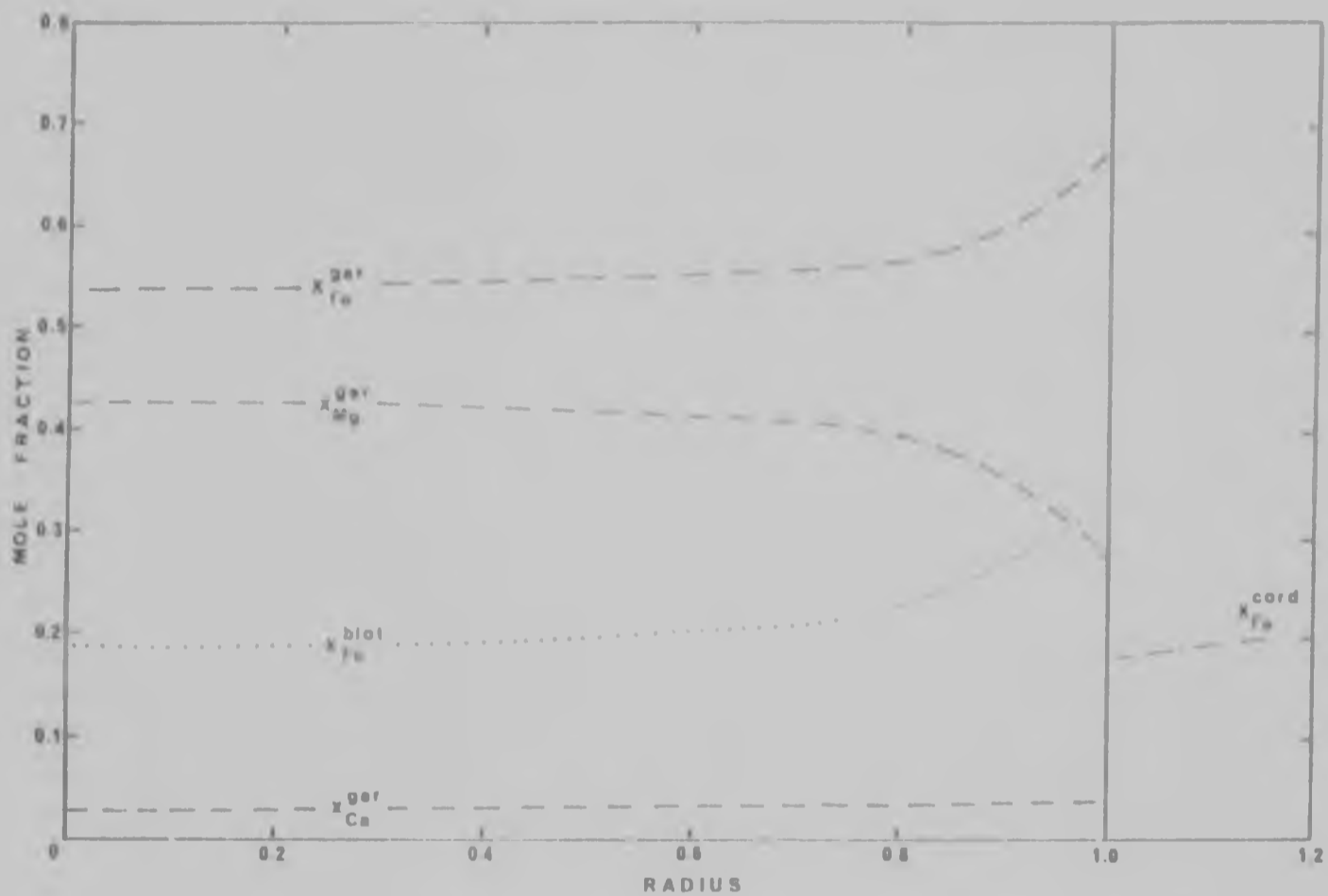


Figure 68: Schematic representation of the compositional variation trends with radius of the data shown in Figure 67, from a garnet porphyroblast from a garnet-cordierite-sillimanite gneiss (sample no. 21-7-G, Form Boschrand - see Map 2 in rear pocket). See text for discussion on the selection of the curves.

In the data appears towards the margin (radius = 1) due to the fact that the zoning is not concentric about the grain centre, but deflected near the grain margins depending on the adjacent mineral assemblage (see Figure 64). The curves extracted in Figure 68 ignore those data points taken from regions in the garnet adjacent to quartz grains (lower  $X_{Fe}^{gar}$  and higher  $X_{Mg}^{gar}$  values) and use the data from points adjacent to bounding cordierite-bearing assemblages. This is valid since the mineral equilibria calibrated by various geothermometers and geobarometers involve these assemblages.  $X_{Ca}^{gar}$  values show almost no variation from core to rim, while  $X_{Fe}^{biot}$  values follow a similar trend to that for  $X_{Fe}^{gar}$ .  $X_{Fe}^{biot}$  values for analysis points outside the garnet (i.e. biotite flakes within cordierite) show a large scatter (see Figure 67 for radius values greater than 1). Cordierite values outside the garnet show little variation with distance from the garnet margin (see Figures 67 and 68).

The availability of these compositional data from a single grain enables the application of garnet-biotite geothermometers within the grain, and garnet-cordierite geothermometers and geobarometers at the grain boundary. Thus a temperature profile may be constructed from the core to margin of this garnet grain (Figure 69). Temperatures for garnet-biotite pairs within the garnet were determined



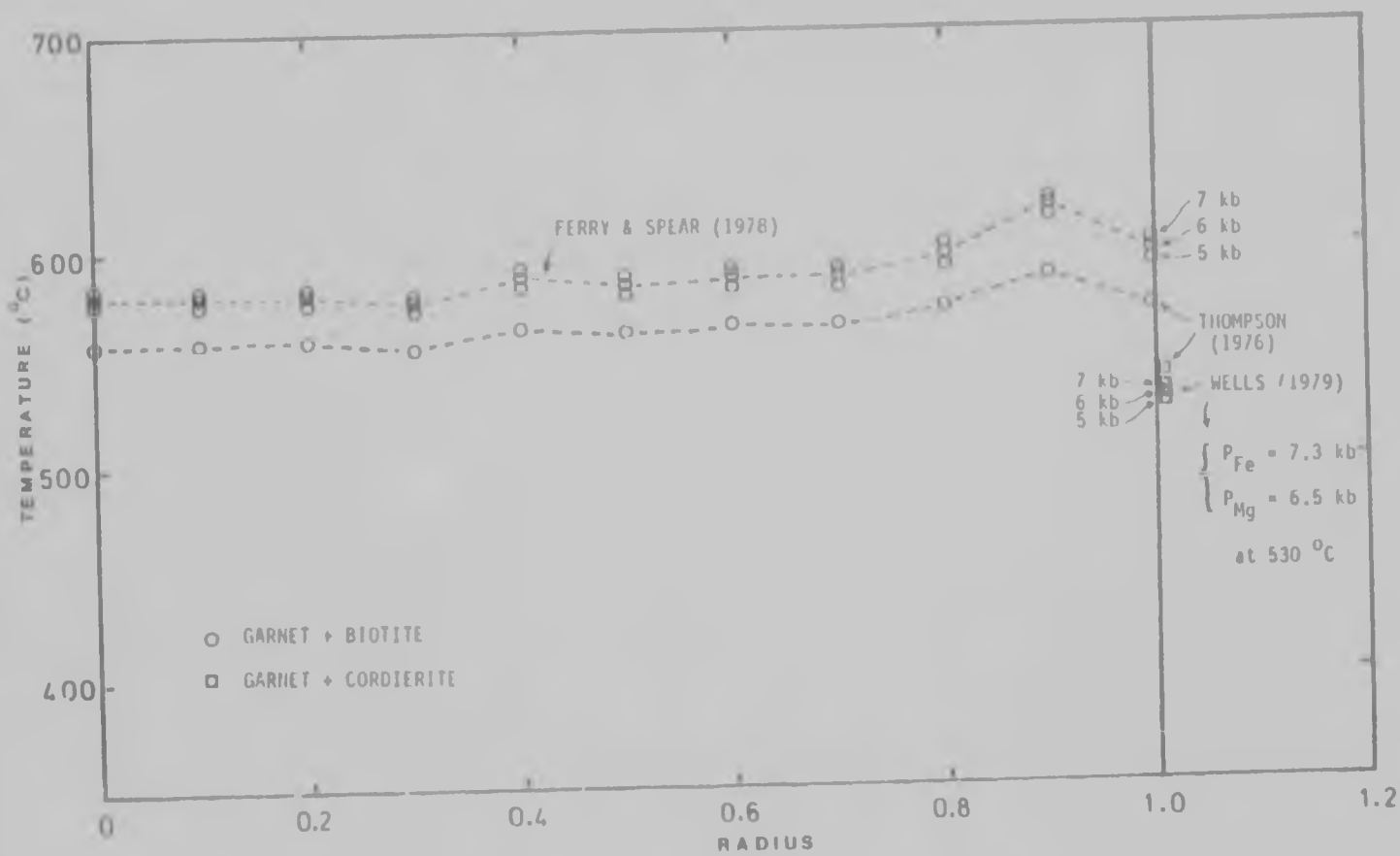


Figure 69: Results of temperature and pressure calculations with increasing radius of the garnet porphyroblast illustrated in Figures 60 and 62, obtained by using the mole fraction data shown in Figures 67 and 68.

using the methods of Thompson (1976) and Ferry and Spear (1978) taking mole fraction data directly from Figure 68. The data used in obtaining these values have all been recalculated to include an estimation of ferric iron in the garnet only (see Appendix 2). The temperatures obtained by these methods show little variation from core to rim. Thompson's temperatures vary around  $560^{\circ}\text{C}$ , while Ferry and Spear's technique gives values about  $20^{\circ}\text{C}$  to  $30^{\circ}\text{C}$  higher for pressures from 5 kbar to 7 kbar. These variations are all significantly less than the errors in the methods themselves (about  $\pm 50^{\circ}\text{C}$ ) and demonstrate an excellent consistency between these techniques. Garnet-cordierite coexistence at the grain boundary allows temperatures (Thompson, 1976; Wells, 1979) and pressures (Wells, 1979) to be determined. Thompson's method gives about  $540^{\circ}\text{C}$ , and Wells' method gives about  $530^{\circ}\text{C}$  for pressures from 5 kbar to 7 kbar. Pressure determinations after Wells for a temperature of  $530^{\circ}\text{C}$  yield values of 7,3 kbar (Fe system) and 6,5 kbar (Mg system), and again very good correlations and consistency are obtained between the different techniques (see Figure 69).

These results indicate that the metamorphic event producing the zoned garnet was characterized by singular values of pressure and temperature. Thus, the gradual compositional variation from core to rim (as opposed to discrete overgrowths)

is not a result of changing metamorphic conditions during the growth of the garnet, but appears to be related to the distribution coefficients, and the availability of elements during the nucleation and growth of the mineral at a fixed temperature. Instead of retrograde conditions producing garnet with successively more iron-rich compositions, it appears that the availability of magnesium is reduced during the growth of the phase, probably suggesting that the solid-solid partition coefficient for Mg in garnet is greater than that for Fe. A study of the kinetics of garnet nucleation and growth by Kretz (1973) suggested that the growth of garnet may be represented by a function that is proportional to the surface area of the grain (as opposed to the radius or volume), and thus growth rates should not directly influence the composition of the garnet, since diffusion of elements must be constant at all points on the surface of a developing mineral phase at a particular time during the metamorphism.

#### Pyroxenitic amphibolites

The mafic granulites which occur interbedded mainly with the quartzites contain suitable assemblages for the application of several geothermometers and geobarometers (opx+cpx+plag+qz<sup>+</sup>gar). The results obtained using these methods are plotted as P-T curves in Figures 70a-d and summarized in Table 11 for sample nos. 27, X21395 and X21399 from the Farm Artonvilla, a

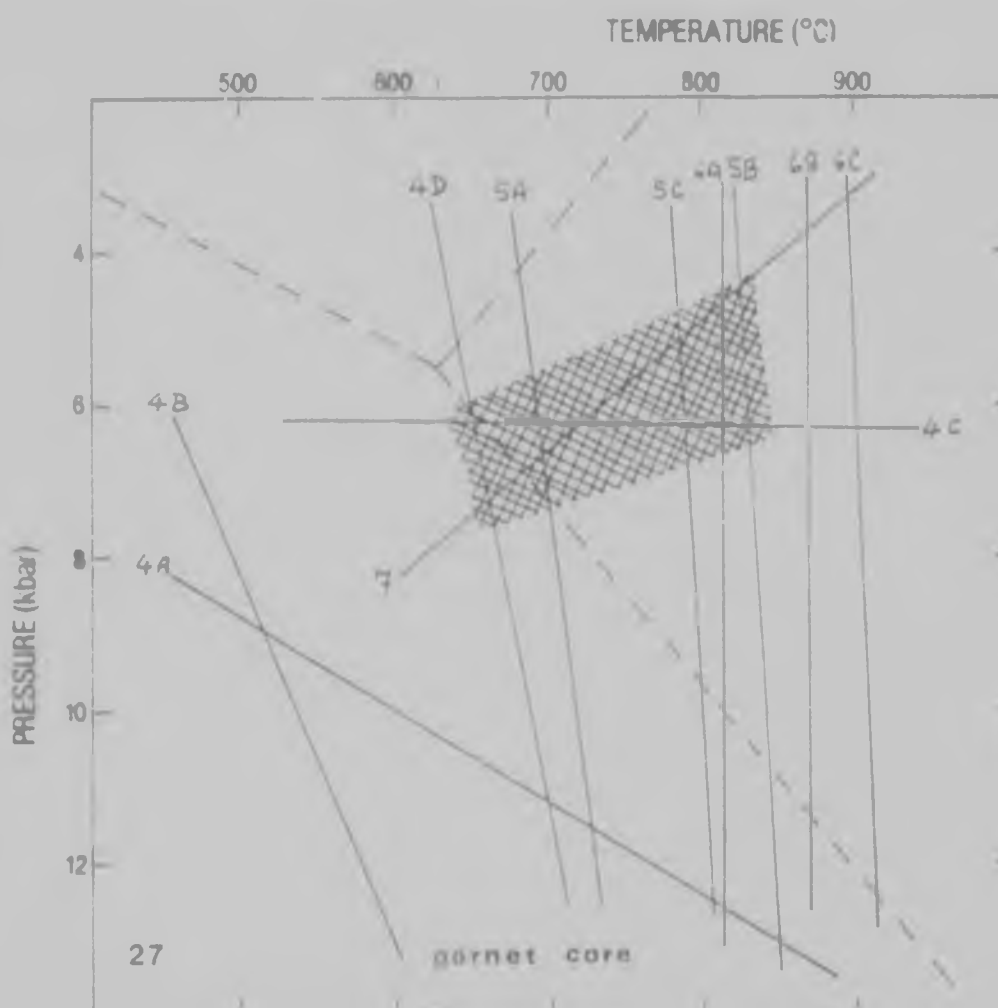


Figure 70a: Pressure-temperature diagram for sample no. 27 of pyroxenitic amphibolite (Farm Artonvilla - see Horrocks, 1975) showing the results of the geothermometer and geobarometer calculations (Appendix 3, Tables 3.1 - 3.6 and 3.14). The curves are as follows:

- 4A: garnet-orthopyroxene barometer of Wood and Banno (1973);
- 4B: garnet-orthopyroxene barometer of Wood (1974);
- 4C: garnet-orthopyroxene thermometer of Powell (1978);
- 4D: garnet-orthopyroxene barometer of Wells (1979);
- 5A: garnet-clinopyroxene thermometer of Raheim and Green (1974);
- 5B: garnet-clinopyroxene thermometer of Ellis and Green (1979);
- 5C: garnet-clinopyroxene thermometer of Wells (1979);
- 6A: orthopyroxene-clinopyroxene thermometer of Wood and Banno (1973);
- 6B: orthopyroxene-clinopyroxene thermometer of Wells (1977);
- 6C: orthopyroxene-clinopyroxene thermometer of Powell (1978); and
- 7: coexisting plagioclase+clinopyroxene+quartz (see Appendix 3, Table 3.14).

Only results using garnet-core compositions are shown in this diagram. The  $\alpha$  umino-silicate stability fields are taken from Richardson *et.al.* (1969). The shaded area is the preferred field for coexisting orthopyroxene, clinopyroxene, plagioclase, garnet and quartz.

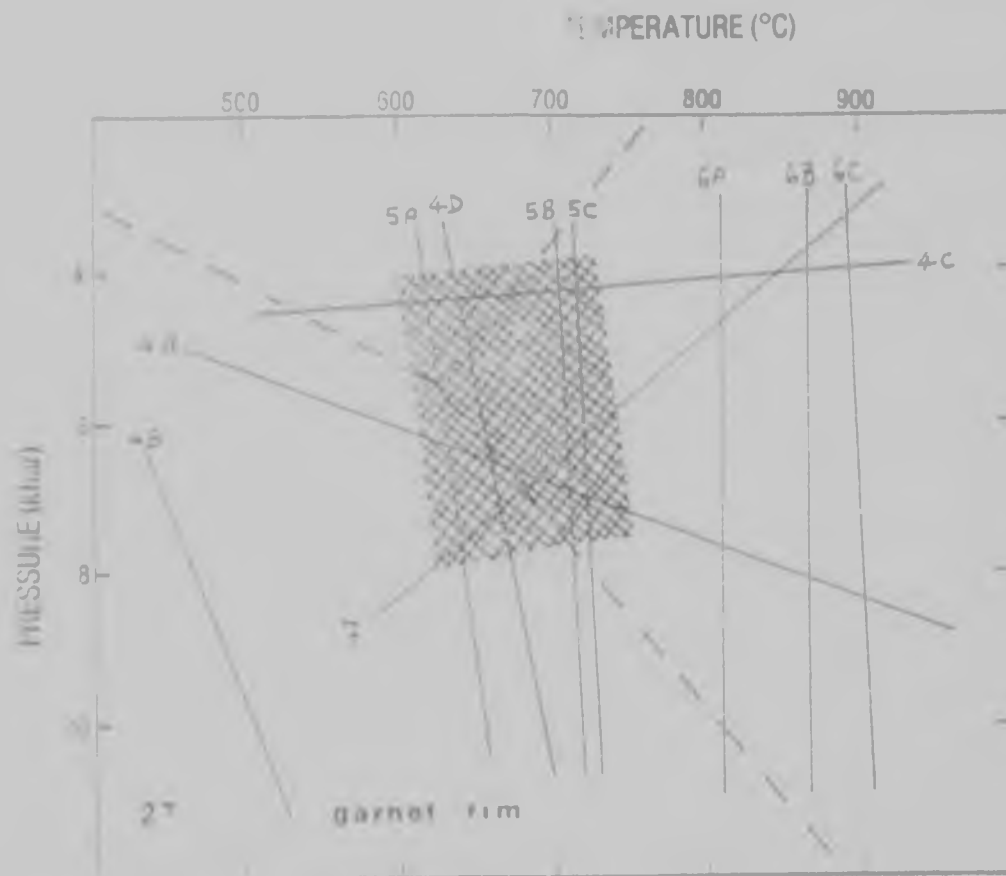


Figure 70b: Pressure temperature diagram for sample no.27 of pyroxenitic amphibolite (Farm Artonvilla - see Horrocks, 1975) showing the results of the geothermometer and geobarometer calculations (Appendix 3, Tables 3.1 - 3.6 and 3.14). The curves are as designated in Figure 70a. Only results using garnet-rim compositions are shown in this diagram, for curves 4A-4D and 5A-5C. The shaded area is the preferred field for coexisting orthopyroxene, clinopyroxene, plagioclase, garnet and quartz.

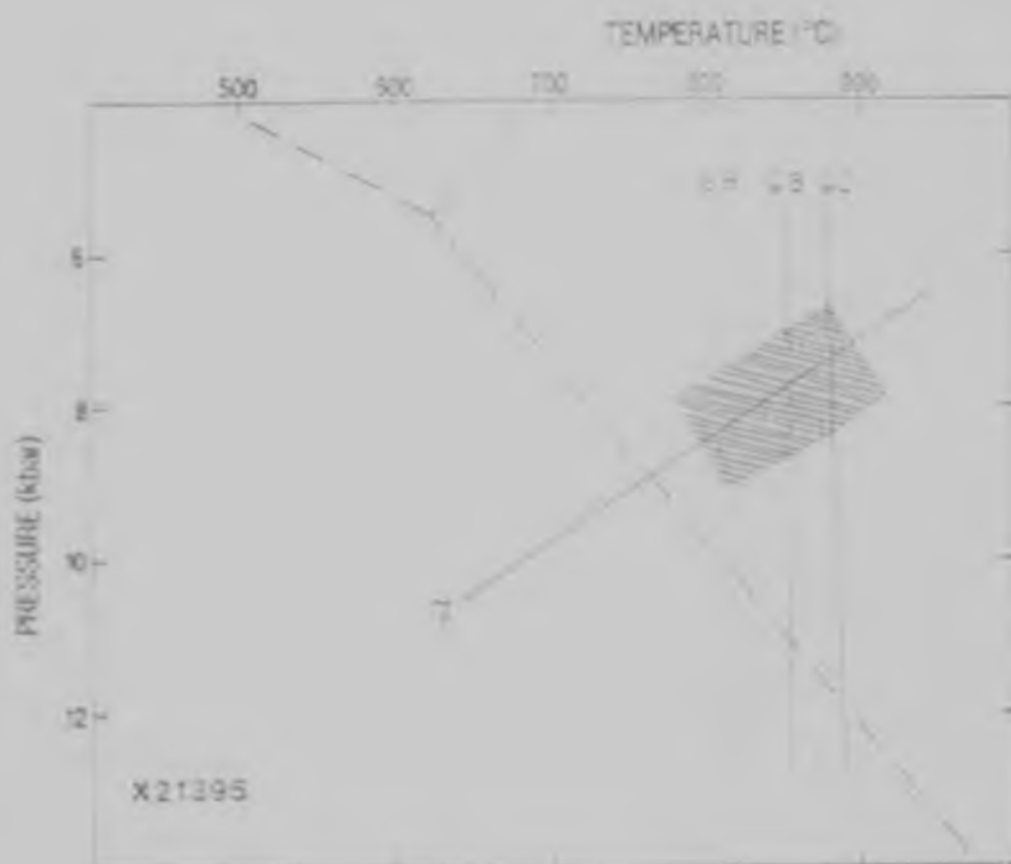


Figure 70c: Pressure-temperature diagram for sample no. X21395 of pyroxenitic omphacite (Farm Antonville - see Horrocks, 1975) showing the results of the geothermometer and geobarometer calculations (Appendix 3, Tables 3.1, 3.2 and 3.14). The curves are as designated in Figure 70a.

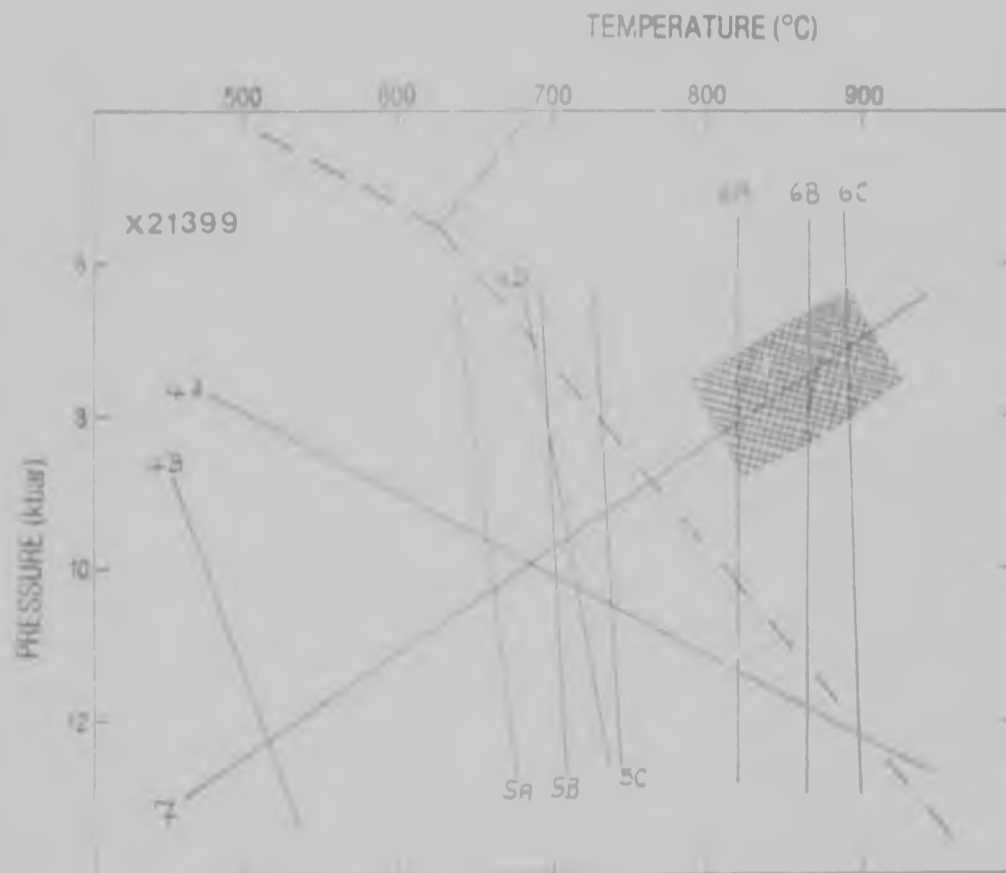


Figure 70d: Pressure-temperature diagram for sample no. X21399 of pyroxenitic amphibolite (Farm Artonvilla - see Horrocks, 1975) showing the results of the geothermometer and geobarometer calculations (Appendix 3, Tables 3.1 - 3.6 and 3.14). The curves are as designated in Figure 70a.

Table 11: Summary and range of pressure (kbar) and temperature (°C) results for pyroxenite amphibolite (samples 27, X21395 and X21399 from Farm Artonvilla - see Horrocks, 1975).

	Data source (Appendix 3)	Coexisting minerals	27	X21395	X21399
T1	Table 3.1	orthopyroxene+clinopyroxene	804 - 814	798 - 837	809 - 821
T2	Table 3.1	orthopyroxene+clinopyroxene	857 - 871	838 - 898	850 - 867
T3	Table 3.2	orthopyroxene+clinopyroxene	891 - 967	868 - 896	879 - 896
P4	Table 3.3	garnet+orthopyroxene	5,3 - 27,7	-	7,9 - 12,2
P5	Table 3.3	garnet+orthopyroxene	8,0 - 48,3	-	11,1 - 33,4
T6	Table 3.4	garnet+orthopyroxene	632 - 710	-	664 - 716
P7	Table 3.5	garnet+orthopyroxene	4,0 - 6,2	-	-
T8	Table 3.6	garnet+clinopyroxene	618 - 718	-	623 - 663
T9	Table 3.6	garnet+clinopyroxene	701 - 840	-	686 - 703
T10	Table 3.6	garnet+clinopyroxene	717 - 799	-	723 - 739
P11	Table 3.14	plagioclase+clinopyroxene+quartz	1,0 - 8,3	7,1 - 11,1	6,8 - 10,9

T1: Wood and Banno (1973)      P7: Wells (1979)  
 T2: Wells (1977)                T8: Raheim and Green (1974)  
 T3: Powell (1978)                T9: Ellis and Green (1979)  
 P4: Wood and Banno (1973)    T10: Wells (1979)  
 P5: Wood (1974)                 P11: see Appendix 3  
 T6: Powell (1978)



portion of which was mapped earlier by the author (Horrocks, 1975). Only samples 27 and X21399 contain garnet, and in the case of sample no.27, the garnet occurs in a micro-vein of quartz and not in direct coexistence with any pyroxene, so the methods relying on coexisting garnet and pyroxene will produce results that must be regarded with caution for this sample (Figures 70a,b). The garnet in sample X21399, however, coexists with clinopyroxene, orthopyroxene and plagioclase.

Temperature estimates using the methods of Wood and Banno (1973), Wells (1977) and Powell (1978) have been made for all three samples and give between 800°C and 900°C (see Table 11 and Figures 70a-d). Coexisting garnet and clinopyroxene has been used to derive a geothermometer by three studies: Råheim and Green (1974), Ellis and Green (1979) and Wells (1979). Using this approach in the case of sample 27, data from garnet core compositions (Figure 70a) and from garnet rim compositions (Figure 70b) yield two sets of results: garnet core data give temperatures from 680°C to 820°C (Figure 70a) while garnet rim data yield values from about 610°C to 720°C (Figure 70b). Results from data on sample X21399 (Figure 70d) using a garnet (small and unzoned) in direct coexistence with clinopyroxene, are between 630°C and 740°C and correlate with the results from sample 27 using garnet rim values. Coexisting garnet and orthopyroxene has produced both a geothermometer

(Powell, 1978) and geobarometers (Wood and Banno, 1973; Wood, 1974; and Powell, 1978). These curves are consistent with the garnet-clinopyroxene curves in all the samples with the exception of that determined using Wood's (1974) equation which is inconsistent with any other method. The methods of Wood and Banno (1973) and Wood (1974) place much reliance on the accurate determination of aluminium site occupancy data in both tetrahedrally and octahedrally coordinated positions. O'Hara and Yarwood (1978) have made a detailed comparison of these methods and shown large discrepancies in the pressure estimates. It is thus apparent that until a better understanding of aluminium solution in pyroxene and garnet is obtained, these methods are not reliable. However, Powell (1978) calibrates his geothermometer and geobarometer using only the solution of Mg, Fe<sup>++</sup> and Ca in octahedrally coordinated sites in both pyroxene and garnet. These data are more readily obtained with greater reliability, and Powell's methods appear to show greater consistency in this study. Thus, fields in P-T space where garnet+orthopyroxene+clinopyroxene are stable for the different samples may be defined, and are shaded in Figures 70a-d. For sample 27 temperatures from about 650°C to 800°C and pressures from about 5 kbar to 7 kbar are suggested using garnet core compositions, while garnet rim compositions yield 600°C to

700°C and 4 kbar to 8 kbar based on intersections between the different curves. This high pressure of up to 8 kbar can only be supported by reliance on Wood and Banno's (1973) geobarometer. For sample X21399 (Figure 70d), a field from 650°C to 750°C at about 10 kbar is defined, where the high pressure estimate again depends on Wood and Banno's method. By rejecting pressure estimates from the methods of Wood and Banno (1973) and Wood (1974), and placing greater credence to the temperature results from sample X21399, allows the derivation of a P-T field for coexisting orthopyroxene, clinopyroxene and garnet from 650°C to 750°C, and from 4 kbar to 6 kbar, which encompasses the greatest consistency between the most reliable methods. Coexisting plagioclase, clinopyroxene and quartz also allow the calculation of a P-T curve (see Appendix 3, Table 3.14) for the reaction anorthite = clinopyroxene+quartz, and results of this determination are plotted in Figures 70a-d. Since no plagioclase analysis is available for sample X21399, the plagioclase data from X21395 was used to derive a curve for X21399 (Figure 70d). For these two samples (Figures 70a and 70d), the curves intersect with the orthopyroxene-clinopyroxene temperature lines to suggest a field of stability of orthopyroxene+clinopyroxene+plagioclase+quartz which clearly show petrographic evidence of mutual coexistence and equilibrium from 800°C to 900°C and

from 7 kbar to 9 kbar. Data for sample 27 (Figures 70a and 70b) suggest similar temperatures but at lower pressures of about 4 kbar. Owing to the obvious later stage anatexis (quartz veining), the results from samples X21395 and X21399 are preferred for their consistency.

In summary, P-T conditions interpreted from the data in Figures 70a-d suggest the orthopyroxene+clinopyroxene+plagioclase+quartz assemblage equilibrated at about 850°C and 8 kbar, while garnetiferous assemblages (cpx+cpx+gar) equilibrated at about 700°C and 5 kbar, indicating that a metamorphic transition to lower grades initiated the growth of garnet.

#### Intrusive rocks

Intrusive rocks, including serpentinites, metapyroxenites, and the gabbros and anorthosites of the Messina Layered Intrusion exhibit all of the deformations experienced by the supracrustal rocks (Hor et al., 1975; Barton et al., 1979a) and contain metamorphic phases such as garnet (McLean, 1976) and sapphirine+kornerupine (Schreyer and Abraham, 1976). Thus mineral analytical data from these rocks may be used to estimate metamorphic parameters. Coexisting orthopyroxene and clinopyroxene in the metapyroxenite allows temperature estimates (Figure 71a) to be made using the methods of Wood and Banno (1973), Wells (1977) and Powell (1978). Results

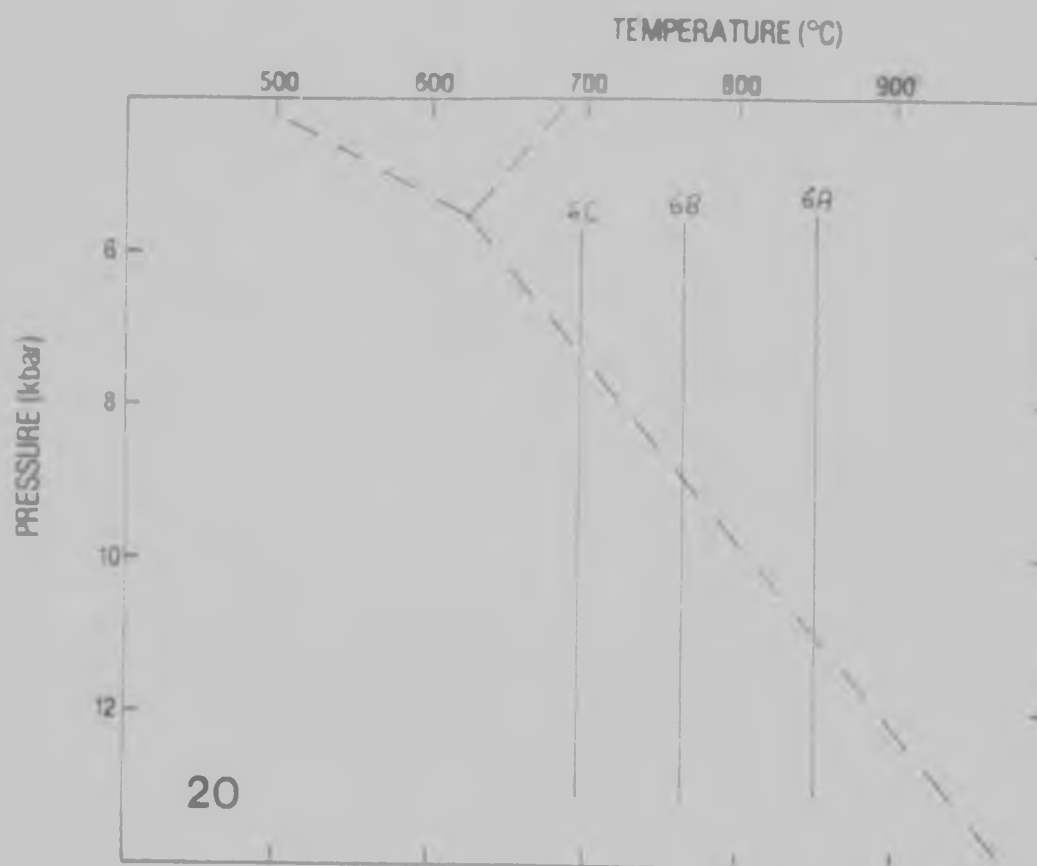


Figure 71a: Pressure-temperature diagram of sample no.20 of metapyroxenite (Farm Artonvilla - see Horrocks, 1975) showing the results of the geothermometer calculations (Appendix 3, Tables 3.1 and 3.2). The curves are as follows:  
 6A: orthopyroxene-clinopyroxene thermometer of Wood and Banno (1973);  
 6B: orthopyroxene-clinopyroxene thermometer of Wells (1977); and  
 6C: orthopyroxene-clinopyroxene thermometer of Powell (1978).  
 The aluminosilicate stability fields are taken from Richardson *et al.* (1969).

vary from about 700°C to 850°C depending on the method, and are in general agreement with temperature estimates made from the pyroxenitic amphibolite samples. Analytical data for coexisting plagioclase and clinopyroxene (+ quartz) in the gabbroic anorthosites enables the application of the anorthite = clinopyroxene+quartz technique to produce a P-T curve (see Appendix 3) for samples 26-5-A and 26-5-E which are shown in Figure 71b. These results for the metapyroxenite and gabbroic anorthosite do not uniquely define a P-T field. However, Barton et al. (1979a) proposed that these lithologies both formed part of the Messina Layered Intrusion, and are thus genetically related, both in time and space. Although direct spatial relationships between these rock-types could not be shown within the study area, intersection of the P-T curves given in Figures 71a and 71b suggest a P-T field of 700°C to 850°C and from about 7 kbar to 9 kbar. This field is in close agreement with fields defined by other lithologies.

#### Water activity

Suitable assemblages such as hornblende+orthopyroxene+clinopyroxene+quartz enable the estimation of water activities in lithologies such as pyroxenitic amphibolite and metapyroxenite. Utilization of hydrothermal equilibrium data has allowed water activities of these rocks to be calculated (Appendix 3 - Table 3.16), and they vary between 0 and 1. At 0, no water is present

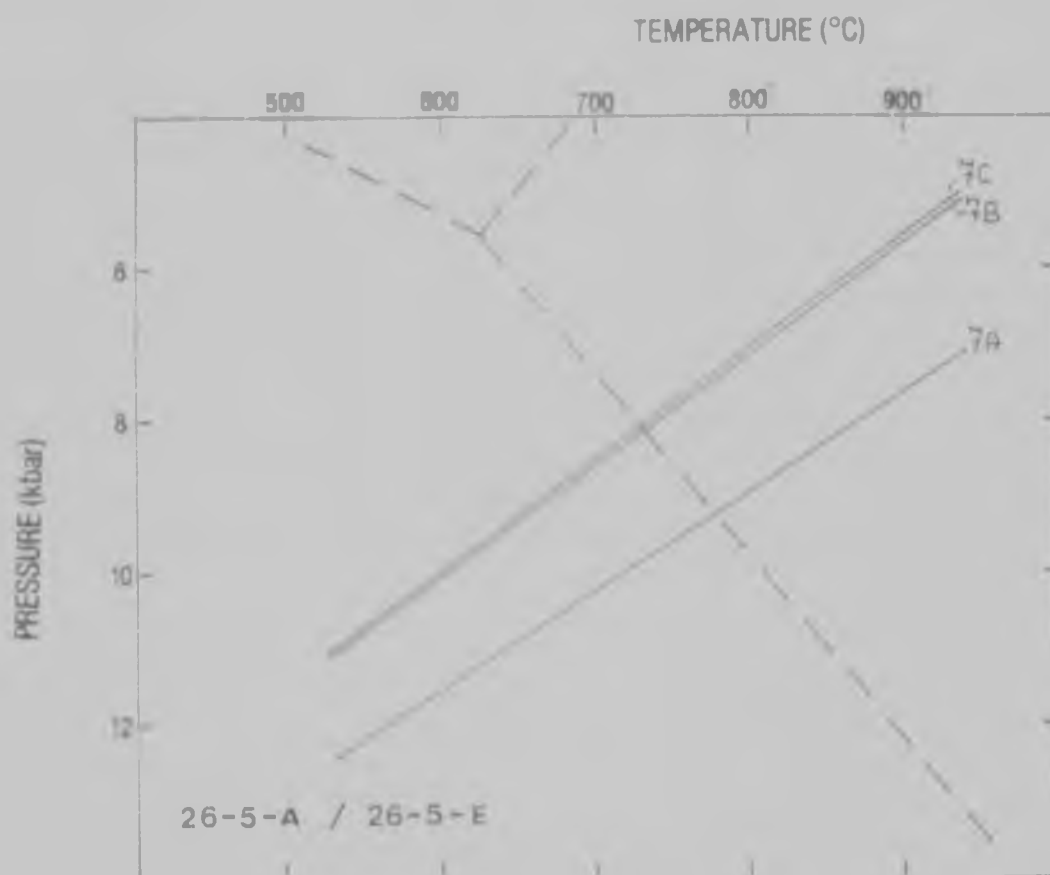


Figure 71b: Pressure-temperature diagram for samples of gabbroic gneiss from the Messina Layered Intrusion (sample nos. 26-5-A and 26-5-E, Farm Shangani - see Map 2 in rear pocket) showing the results of the thermodynamic calculation for coexisting plagioclase, clinopyroxene and quartz (Appendix 3, Table 3.14).

The curves are as follows:

- 7A: sample no.26-5-A using data from the UCT laboratory (Appendix 2, Table 2.22);
- 7B: sample no.26-5-E using UCT data (Appendix 2, Table 2.22); and
- 7C: sample no.26-5-A using data from the WITS laboratory (Appendix 2, Table 2.23).

in the fluid phase occurring with the other solid mineral phases, while at 1, water is the only fluid phase present in the system. Values determined in this study are all low, typically less than 0,1 and commonly less than 0,01. Thus water comprised from 1 per cent to 10 per cent of the fluids present during the stabilization of these assemblages. Typical values at about 800°C and 8 kbar for the pyroxenitic amphibolites vary from 1 per cent to 4 per cent, while for the metapyroxenite, about 5 per cent is typical. Touret (1971) made a similar study of migmatites and granulites in the basement of southern Norway, and recognized a sudden decrease in water partial pressure (at about 700°C - 800°C and 6 kbar to 8 kbar - about 20 to 30 km depth) in a transition from amphibolites (Telemark area) to granulites (Bamble area). While all rocks contain late, water-rich and NaCl-bearing fluid inclusions in quartz, it was noted that only granulite facies rock contains inclusions rich in CO<sub>2</sub>. Thus the fluid phase during granulite metamorphism appears to be composed almost exclusively of CO<sub>2</sub>. Touret (1971) concluded that the provenance of these fluids is most likely juvenile (degassing of the mantle) and related to the synorogenic emplacement of mafic intrusives. These arguments are supported by the low water activities obtained for the granulites observed in the study area.



### The P-T field - a synthesis

The data and results obtained from this study, and other workers (Chinner and Sweatman, 1968; Van Reenen and Du Toit, 1978; Fripp, 1981c) have been compiled in Figures 72 and 73 which shows the P-T fields for the different lithologies examined within the study region. Except for fields C and D (see Figure 72), a broad path from granulite facies at about 9 kbar and nearly 900°C to amphibolite facies at about 4 kbar and 650°C is defined. The assemblages which record the highest pressures and temperatures occur in the pyroxenitic amphibolites, and consist of orthopyroxene, clinopyroxene, plagioclase and quartz. This assemblage is typical of true mafic granulites (De Waard, 1965; Winkler, 1974). However results obtained from these lithologies using garnet show the lowest temperatures and pressures in the pathway. Clearly, the garnet appears to have formed at a later stage in the metamorphism and these are not therefore eclogitic assemblages. Thus, the reaction studied by Green and Ringwood (1967) and which Winkler (1974) also used to subdivide the regional granulite facies of metamorphism for mafic assemblages:

$$\text{orthopyroxene} + \text{plagioclase} = \text{clinopyroxene} + \text{garnet} + \text{quartz}$$

must have moved to the left-hand side at an early stage during the metamorphism producing this field. Also, the presence of plagioclase precludes the garnet-bearing assemblage from

### The P-T field - a synthesis

The data and results obtained from this study, and other workers (Chinner and Sweatman, 1968; Van Reenen and Du Toit, 1978; Fripp, 1981c) have been compiled in Figures 72 and 73 which shows the P-T fields for the different lithologies examined within the study region. Except for fields C and D (see Figure 72), a broad path from granulite facies at about 9 kbar and nearly 900°C to amphibolite facies at about 4 kbar and 650°C is defined. The assemblages which record the highest pressures and temperatures occur in the pyroxenitic amphibolites, and consist of orthopyroxene, clinopyroxene, plagioclase and quartz. This assemblage is typical of true mafic granulites (De Waard, 1965; Winkler, 1974). However results obtained from these lithologies using garnet show the lowest temperatures and pressures in the pathway. Clearly, the garnet appears to have formed at a later stage in the metamorphism and these are not therefore eclogitic assemblages. Thus, the reaction studied by Green and Ringwood (1967) and which Winkler (1974) also used to subdivide the regional granulite facies of metamorphism for mafic assemblages:

$$\text{orthopyroxene} + \text{plagioclase} = \text{clinopyroxene} + \text{garnet} + \text{quartz}$$

must have moved to the left-hand side at an early stage during the metamorphism producing this field. Also, the presence of plagioclase precludes the garnet-bearing assemblage from

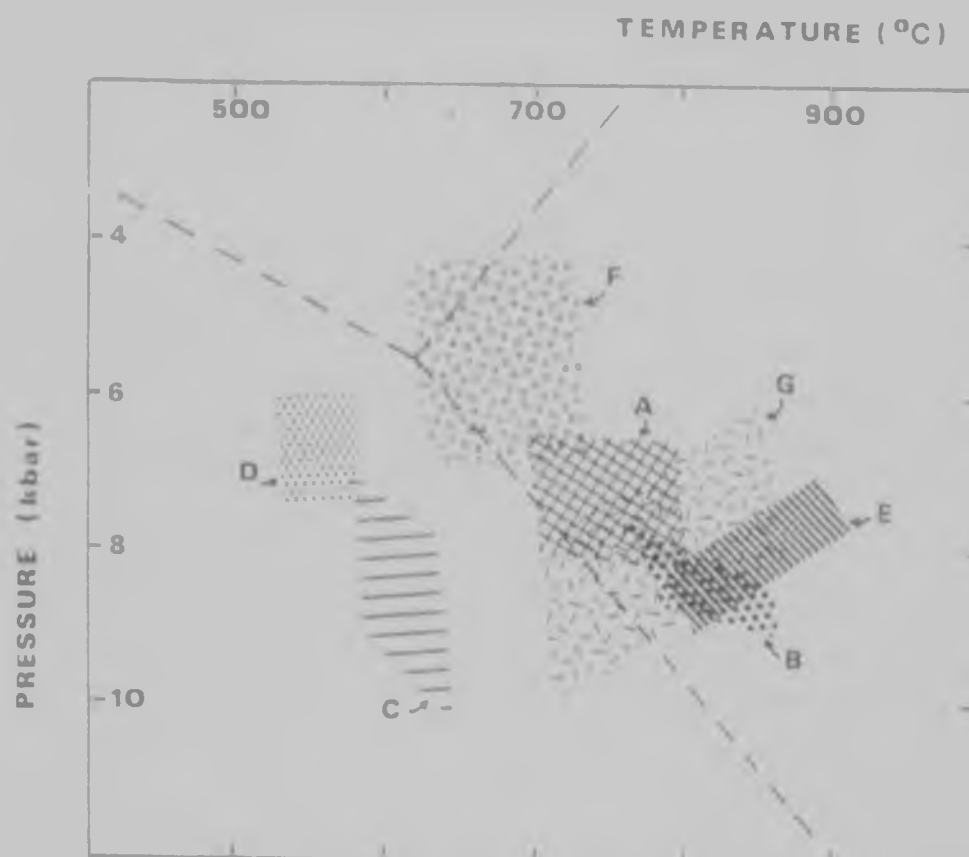


Figure 72: P-T fields for the lithologies examined in the study area:

- A: garnet-cordierite-sillimanite gneiss (gar+biot+cord - Figures 50-51);
- B: sapphirine bearing rock (gar+biot+cord+opx - Figures 54-55);
- C: garnet-orthopyroxene-plagioclase symplectite (gar+biot+opx - Figures 56a-d);
- D: data from zoned garnet study from sample no.21-7-G (garnet-cordierite-sillimanite gneiss, gar+biot+cord - Figure 69);
- E: pyroxenitic amphibolite (opx+cpx+plag+qz - Figures 70 a-d);
- F: pyroxenitic amphibolite (opx+cpx+gar - Figures 70 a-d); and
- G: metapyroxenite and gabbroic gneiss of the Messina Layered Intrusion (opx+cpx+plag+qz - Figures 71 a,b).

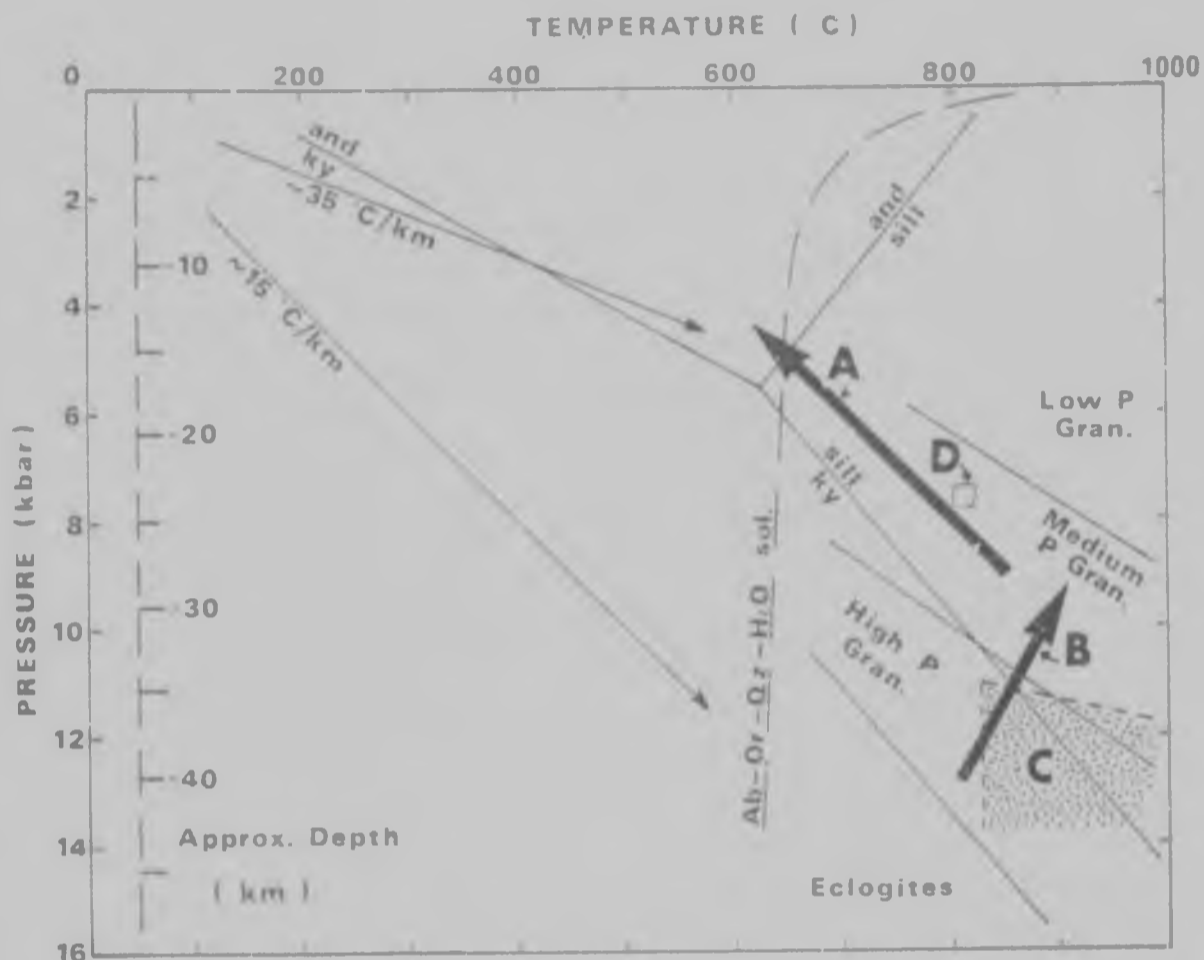


Figure 73: The P-T field for the high-grade metamorphism affecting the Central Zone of the Limpopo Mobile Belt.

- A: pathway for lithologies determined from this study;  
 B: pathway determined from basement units (Fripp, 1981c);  
 C: stability field of enstatite+kyanite+quartz assemblage described from near Beit Bridge, Zimbabwe (Chinner and Sweatman, 1968); and  
 D: result for coexisting garnet+biotite+cordierite+orthopyroxene from the Southern Marginal Zone of the Limpopo Mobile Belt (Van Reenen and Du Toit, 1978).

Geothermal gradients are calculated for crustal rocks, and the approximate depth scale is estimated assuming about 3,3 kbar/km. The  $Ab-Or-Qz-H_2O$  solidus is after Luth *et.al.* (1964), the stability fields of the aluminosilicates is after Richardson *et.al.* (1969), and the subdivision of the granulite field is after Green and Ringwood (1967).

being a high-pressure or eclogitic group. The garnet may have formed during a prograding reaction of the above type (i.e. the reaction moving to the right-hand side but has generally either been consumed, or has been partially consumed where preserved in samples from the study area). Classical kelyphitic coronas of plagioclase about garnet are typical in hornblende-rich varieties of these mafic granulites (see Figures 13 and 14) and illustrate this consumption of garnet:

$$\text{hornblende} + \text{garnet} + \text{quartz} = \text{clinopyroxene} + \text{plagioclase} + \text{H}_2\text{O}.$$

This has been described by De Waard (1965) as one of the reactions accounting for the disappearance of hydrous phases, such as amphibole, and the characteristic appearance of orthopyroxene, if the garnet is an almandine-pyrope solution with little or no grossular, and which is diagnostic of the entrance into granulite facies metamorphism. However, the garnets occurring in these mafic granulites all typically contain up to about 20 per cent grossular, suggesting that clinopyroxene, and not orthopyroxene, appears on the right-hand side of the above reaction. A similar reaction has also been recognized in eclogitic rocks for high to intermediate pressure granulite transitions (Leyreloup *et al.*, 1975) and which produces these kelyphitic textures. Their reaction has the following generalized form:



where, in the case of the samples from the study area, the kelyphitoid is predominantly hornblende, and the kelyphite is predominantly the coronas of plagioclase (see Figure 13).

The P-T fields of the garnet-cordierite-sillimanite gneiss (A of Figure 72), sapphirine-bearing rock (B of Figure 72) and the intrusive rocks (G of Figure 72) correlate closely with those of the pyroxenitic amphibolites (E and F of Figure 72) generally falling between the 'opx+cpx+plag+qz' and 'opx+cpx+gar' areas reflecting pressures of 7 to 8 kbar and temperatures between 700°C and 850°C. These results suggest a continuous progression of reactions equilibrating at successively lower temperatures and pressures following the peak in the metamorphic path. This path occurs within the sillimanite field defined by Richardson et al. (1969) and follows closely along the sillimanite-kyanite transition boundary. This is notable since no kyanite was recognized in any of the samples collected within the study area. However, former kyanite has been reported to occur further north in Zimbabwe in the neighbourhood of Beitbridge (Chinner and Sweatman, 1968). Van Reenen and Du Toit (1978) also point out the need for careful identification to distinguish between kyanite and sillimanite. Abundant needles of sillimanite are characteristic of the pelitic lithologies, and some localities such as on the Farm Randjesfontein (see

Map 1 in rear pocket) show massive monominerallic sillimanite rocks, which suggest that the metamorphism affecting the study area drove all kyanite to sillimanite during a high to low pressure or low to high temperature transition. Chinner and Sweatman (1968) favoured the former and have suggested at least two stages of metamorphic recrystallization, where an earlier high pressure stage produced an enstatite+kyanite+quartz assemblage. A later retrogression caused kyanite to transform to sillimanite, together with the production of cordierite and the consumption of quartz. This reaction may account for the lack of quartz, and the relatively minor amounts of orthopyroxene found in the symplectites. However, the P-T field for the garnet-orthopyroxene-plagioclase symplectite, and that determined from the study on the garnet zoning in the garnet-cordierite-sillimanite gneiss sample no. 21-7-G, fall well within the kyanite field as defined by Richardson et al. (1969), and it appears that the temperatures deduced for these assemblages are too low (see C and D of Figure 72). Their pressure values are consistent with those obtained for the other pelitic units such as garnet-cordierite-sillimanite gneiss and sapphirine bearing rock, and higher temperatures would allow them to overlap with other fields defining the pathway described previously. This inconsistency in temperature is unlikely to be real since

other data from samples 21-7-F and 21-7-G give results which fall within the above mentioned pathway (see Figures 50, 51 and Field A of Figure 72) and may be caused by compositional irregularities, such as the lack of free quartz (e.g. in the symplectite), Na and H<sub>2</sub>O activities, or high Ti contents in biotite, which could cause deviations in the results. Hensen and Green (1973) show that in silica-deficient assemblages more iron-rich sapphirine remains stable to very low temperatures, and thus the presence of this mineral in these undersaturated lithologies is not uniquely diagnostic of particular temperature regimes (see Seifert, 1974). Also, lines in P-T space of Al<sub>2</sub>O<sub>3</sub> solubility in enstatite (after Anastasiou and Seifert, 1972) suggest much higher temperatures approaching 1 000°C than the other thermodynamic data. This is again influenced by rock compositional factors (3,3 per cent Al<sub>2</sub>O<sub>3</sub> in the symplectite, and 7,5 per cent Al<sub>2</sub>O<sub>3</sub> in the sapphirine-bearing rock). Also, Anastasiou and Seifert's data are based on pure magnesian end-members, while Fe causes a drastic temperature lowering effect on the stability of enstatite (Holdaway, 1976). However, all the results from calculations using coexisting garnet and cordierite data fall within the garnet-cordierite stability field defined by Hensen and Green (1971, 1972, 1973).

Thus, it appears that the 'low temperature' results generating Fields C and D in Figure 72 (garnet-orthopyroxene-



plagioclase symplectite and zoned garnet data respectively) are misleading and spurious. The symplectite is a silica-deficient assemblage which contains garnet with appreciable grossular (Ca) content. Thus disequilibrium conditions probably exist which do not allow the application of thermodynamic calibrations based on Fe-Mg systems only. The biotite compositions in the study of the zoned garnet from sample 21-7-G contain up to nearly 5 per cent  $TiO_2$  (see Appendix 2 - Table 2.6, analyses nos. 5 and 19). Both Thompson (1976) and Ferry and Spear (1978) point out that such large  $TiO_2$  contents are not considered by their geothermometers, and probably explain the low temperatures achieved for these samples in this study.

## CHAPTER 6: CONCLUSIONS

The Precambrian lithologies in the study area consist of a basement of grey banded granodioritic gneisses metamorphosed about 3 800 m.y. ago and intruded by ancient tholeiitic dykes about 3 570 m.y. ago (Barton et al., 1977). Subsequently, a geosynclinal-type series of supracrustal rocks or 'cover' were deposited at least partly on a thin sialic crust, and consisted of shallow water marine or shelf facies in the south-east characterized by carbonates (now marbles), cherts and calc-silicates. Transitional facies with shales, greywackes and turbidites (now the metapelitic garnet-cordierite-sillimanite gneiss) and the rhyolitic and/or arkosic precursor of the Singelele Gneiss occur in the central portion of the study area. Towards the north-west of the area, deeper water facies are present and probably represent cherts, mafic shales and/or volcanics (probably continental basalts) and banded ironstones, which now form the quartzite-banded magnetite quartzite-pyroxenitic amphibolite association. In this way, it may be concluded that the supracrustal lithologies include a range of possible facies that occur in intercontinental basins or eugeosynclines. Anorthositic and gabbroic gneisses of the Messina Layered Intrusion, and probably also metapyroxenites and serpentinites intruded the above lithologies at about 3 270 m.y. ago (Barton, 1981). Unmetamorphosed and undeformed

mafic dykes intruded the area about 2 200 m.y. ago (Barton, 1979).

Subsequent to any structural events solely affecting the basement gneisses prior to the deposition of the supracrustal rocks, the deformational history of the supracrustal gneisses appears to have commenced with a phase of ductile isoclinal folding, which in many outcrops is now manifest by intrafolial folds. This may be related to a process of rapid burial to great depth such as would be experienced in a large geosyncline on an unstable and probably thin sialic platform. Later, the stress field induced further refolding, considerable flattening, attenuation and along-strike boudinaging of the stratigraphy probably by a process of simple shear. The asymmetry of folds in the north-western portion of the study area suggests that this simple shear had a left-lateral sense of movement consequently producing 'S'-shaped folds.

The data presented in this study support the view that the anorthositic and gabbroic rocks of the Messina Layered Intrusion are of plutonic igneous origin. Pearce diagrams reveal a clear trend of plagioclase fractionation where the composition of the plagioclase cumulate was about  $An_{80}$ . The gabbros formed later differentiates with the crystallization of clinopyroxene and hornblende. The hornblende may have been metamorphically produced. Rb and Sr data suggest that

the tholeiitic parental liquid was anomalously enriched in Rb probably in amounts exceeding 50 ppm, while Sr contents of about 100 ppm are suggested for the parental liquid. Raleigh's fractionation law indicates that about 70 per cent fractionation occurred in these rocks.

The P-T fields for the different units examined in the study area define a broad region in P-T space from about 9 kbar at 900°C to about 4 kbar at 650°C for the high-grade metamorphism. The assemblages which record the highest metamorphic conditions occur in the pyroxenitic amphibolites and consist of  $opx+cpx+plag+qz$ . Garnet-bearing assemblages in both the mafic and pelitic lithologies record lower conditions, and are probably generated by a metamorphism within the medium pressure granulite field. This contrasts with the view of Bahnemann (1972) who considered two metamorphic events: an earlier granulite facies metamorphism, and a later amphibolite facies metamorphism at about 2 600 m.y. (remobilization of the Singelele Gneiss).

An earlier high pressure granulite phase of the metamorphism has been reported by other studies (Chinner and Sweatman, 1968; Fripp, 1981c) where conditions attained pressures in excess of 12 kbar at temperatures above 800°C. Figure 73 shows a compilation of available data in order to deduce an overall metamorphic pathway for the units under study. The pathway apparent from this study of supracrustal lithologies is shown

by arrow A from about 9 kbar at 900°C to about 4 kbar at 650°C. A complementary study to this which considers the basement lithologies of the Sand River Gneisses (Fripp, 1981c) has shown another pathway (arrow B, Figure 73) derived from using  $\text{opx}+\text{cpx}+\text{plag}+\text{qz}$  assemblages in the more anhydrous Sand River Gneisses and various deformed amphibolitic dykes which transect them. These data suggest a transition from high pressure granulites to intermediate pressure granulites, as defined by Green and Ringwood (1967) from about 13 kbar at 800°C to 10 kbar at 900°C. This pathway makes a direct transition from the kyanite to sillimanite field, and is in close correlation with the field of  $\text{en}+\text{ky}+\text{qz}$  stability suggested by Chinner and Sweatman (1968) for the early high-pressure phase of the metamorphism (field C, Figure 73). The result given by Van Reenen and Du Toit (1978) for a  $\text{cord}+\text{gar}+\text{opx}+\text{biot}$  assemblage occurring in the Southern Marginal Zone of the Limpopo Mobile Belt is in close agreement with results from similar assemblages examined in this study (point D, Figure 73) and all fall within Green and Ringwood's (1967) field of medium pressure granulites. All these results are within the field of melting for hydrous granitic compositions (after Luth *et al.*, 1964).

Thus, a P-T pathway for these regions forms a loop from high-pressure high-temperature to lower pressure high-

temperature conditions which encompass average crustal geothermal gradients ranging from about  $15^{\circ}\text{C}/\text{km}$  for the early high pressure event, to about  $35^{\circ}\text{C}/\text{km}$  for the later medium pressure event. These geotherms are typical for rocks that have undergone Archaean high-grade metamorphism and tectonism, and have been reported and discussed by several workers (Burke and Kidd, 1978; Drury, 1978; Bickle, 1978; England, 1979). By assuming a relationship of about 3,3 kbar/km for silicic crustal rocks, approximate depths may be estimated for the high-grade metamorphism. The early high-pressure phase suggests burial to about 40 km while subsequent uplift by either tectonic or erosional means to depths of about 15 km, or pressures of about 4 kbar, produced medium pressure granulites at fairly constant temperatures. A similar P-T loop has been proposed by O'Hara (1977) for granulites and migmatites belonging to the Scourie Gneiss Complex of north-western Scotland (Figure 74). An initial high-grade 'peak' of metamorphism was followed by a slower fall off in grade whereby pressure decreases faster than temperature. During the peak, the rocks were subjected to burial into the deep regions of the lower crust, where zones of melting and depleted residues after anatexis have been suggested (Moorbath, 1975; see Figure 75).

O'Hara (1977) was able to correlate events along his

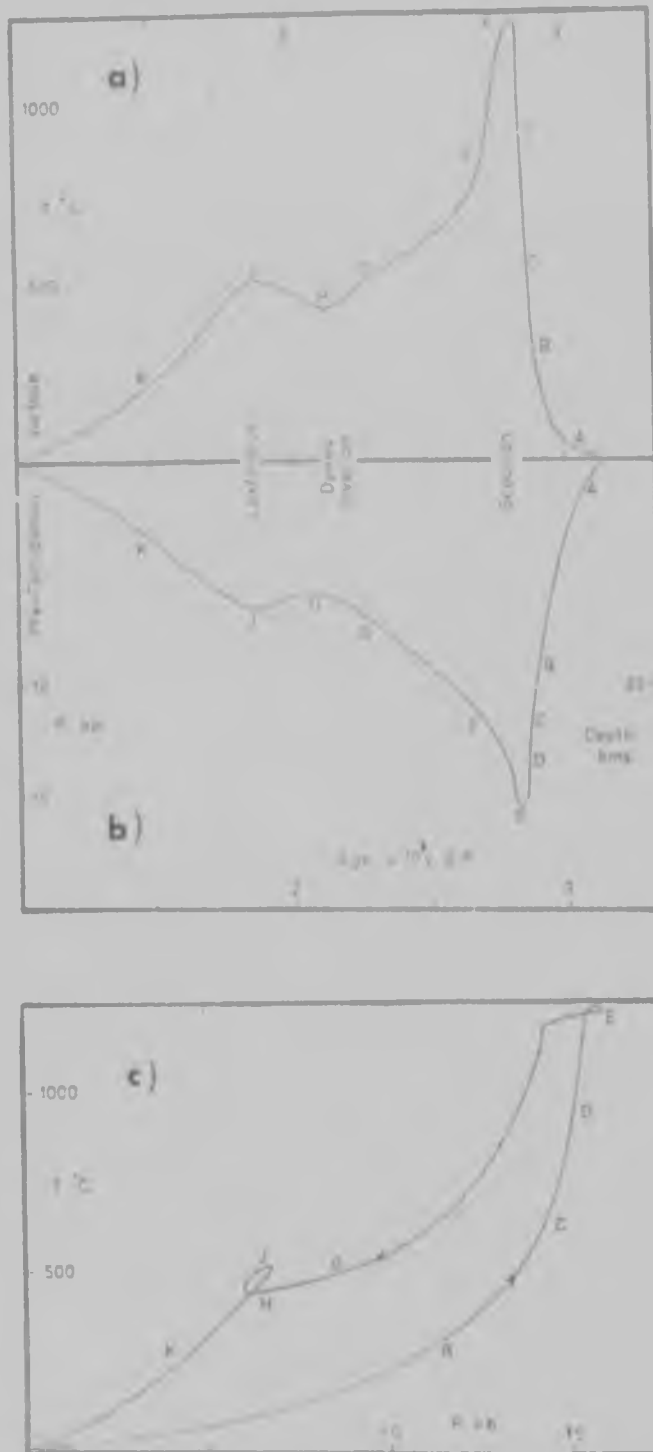


Figure 74: Metamorphic conditions with time for the Scourie Gneiss Complex in north-western Scotland (after O'Hara, 1977): a) temperature-time diagram; b) pressure-time diagram; and c) P-T loop for the high-grade metamorphism.

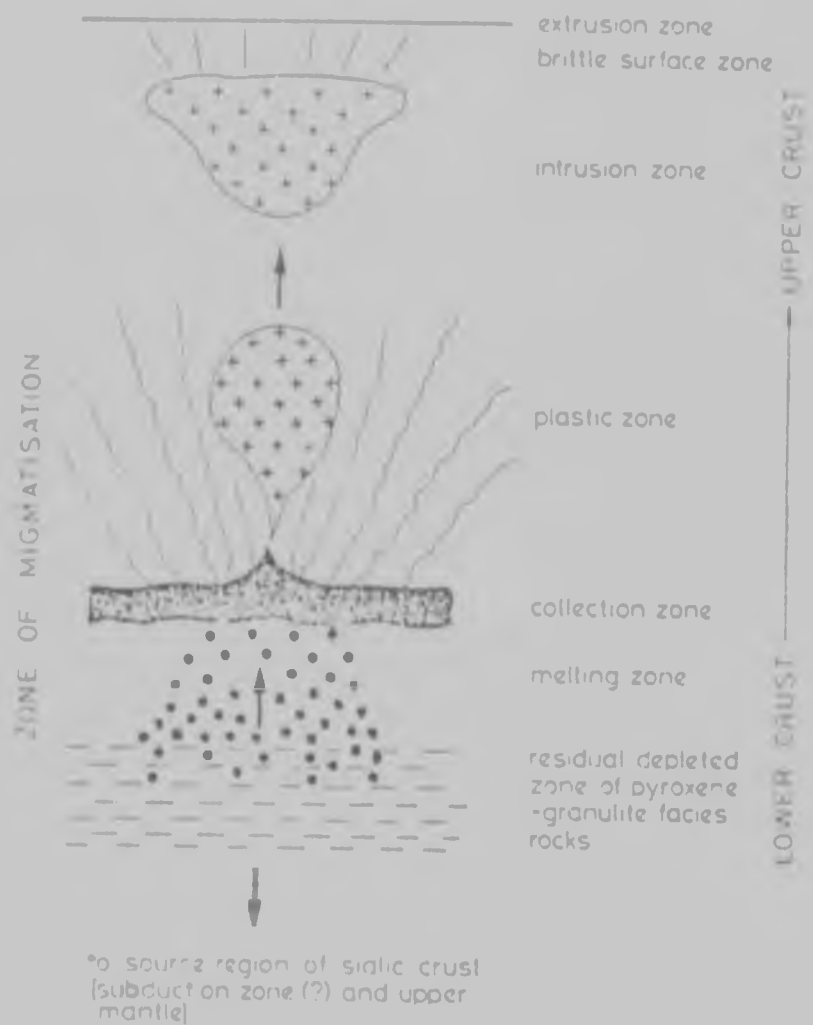


Figure 75: Schematic diagram of geochemical differentiation and production of compositional layering within a 30 - 40 km thick portion of silicic crust, with the formation of granitic diapirs (after Moorbath, 1975).



P-T loop for the Scourie rocks with geochronologically defined events (Figure 74) and thus suggest a P-T-time path for the metamorphism. The availability of geochronological data for the Limpopo Mobile Belt allows a similar P-T-time path (Figure 76) to be suggested for the study area. The supracrustal lithologies were deposited sometime between the intrusion of about 3 570 m.y. old mafic dykes (Barton et al., 1977) and the intrusion of the Messina Layered Intrusion (Barton, 1981) at about 3 270 m.y. ago. The resetting of the Rb-Sr isotopic ratios in the Messina Layered Intrusion at about 3 150 m.y. ago probably reflects the 'peak' of the high-grade metamorphism. Thus, the lithologies experienced burial to depths of about 40 km over a period of about 200 to 300 m.y. During the subsequent excavation of the units and lowering pressures, anatexis proceeded. The intrusion of the Bulai Gneiss (or remobilization) occurred about 2 700 m.y. ago (Barton et al., 1979b) and the Singelele Gneiss has yielded metamorphic ages at about 2 600 m.y. ago (Barton et al., 1979b). The intrusion of a fabric-free and undeformed mafic dyke about 2 200 m.y. ago (Barton, 1979) implies that the high-grade metamorphism had ended by that time. Thus, the units experienced uplift from about 40 km to nearly 15 km of depth in a period of about 900 m.y. i.e. an uplift rate of about 0,03 mm/yr. This rate is very slow when compared with

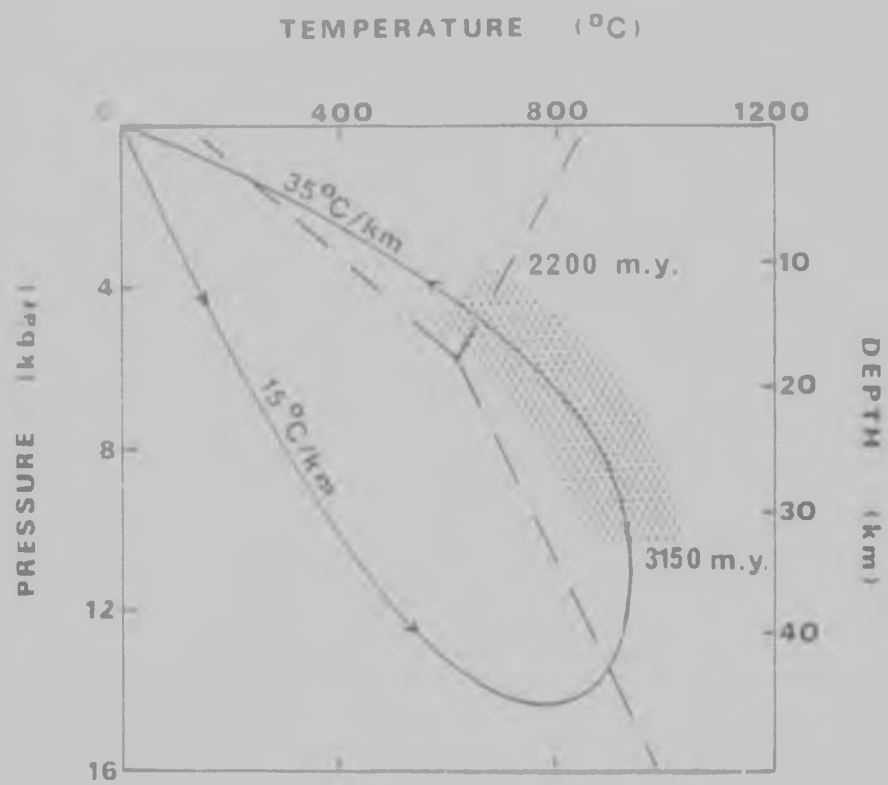


Figure 76: Schematic pressure-temperature diagram showing a P-T loop with time for the high-grade metamorphism affecting the Central Zone of the Limpopo Mobile Belt. The stippled area represents that portion of the loop obtained from this study. Higher pressure portions of the loop are based on data from Chinner and Sweatman (1968) and Fripp (1981). See text for a discussion of the ages.

uplift rates for modern mountain belts (e.g. about 1mm/yr for the Alps), but uplift rates may have been highly variable during the history of the excavation of the Limpopo rocks. The metamorphic, tectonic and geochronological events affecting the supracrustal units in the study area are summarized in Table 12.

Table 12: Summary of the metamorphic, tectonic and geochronological events affecting the supracrustal units in the area under study

Event	Age (m.y.)	Metamorphic conditions
Intrusion of dolerite dykes and the end of high-grade metamorphism	2 200	-
Waning (retrograding) metamorphism, deformation and orotexis	2 600 - 2 400	600°C-800°C 4 kbar - 9 kbar
Intrusion of Stockford-age dykes, now deformed and metamorphosed	3 060	-
Peak of high-grade metamorphism and deformation	3 150	800°C-900°C 9 kbar - 13 kbar
Intrusion of the Messina Layered Intrusion	3 270	-
Formation of the supracrustal lithologies	3 570 - 3 270	-

1: see Table 1 for geochronological data; and  
2: see Figure 73 for metamorphic conditions.

## APPENDIX 1: ANALYTICAL TECHNIQUES

### Whole-rock analysis

Whole-rock analysis in this study was undertaken using X-ray fluorescence techniques in the Department of Geology, University of the Witwatersrand. The large grain size of many of the rock-types analyzed meant that samples exceeding 5 kg in weight were collected with care being taken to avoid cross-cutting veins and gmatites. Both crushed chips and powders from these samples were thoroughly mixed during the sample preparation to ensure representative samples. The major and minor elements were analysed using the fusion method of Norrish and Hutton (1969), while sodium and trace elements were determined on whole-rock pellets. In the case of trace element determination, mass absorption corrections were applied whereby a calculated value was used for Ba using the Tables of Birks (1963), and the Compton peak method for Rb and Sr (Reynolds, 1967). Information pertaining to the accuracy and precision of the analytical method is given by McCarthy (1976). For a more complete description of the analytical method and instrumental conditions, the reader is referred to McCarthy (1977).

### Electron probe microanalysis

Mineral analyses (presented in Appendix 2) were obtained

from two laboratories: the Department of Geochemistry at the University of Cape Town (UCT) which uses a Cambridge Microscan 5 instrument, and the Department of Geology at the University of the Witwatersrand (WITS) which uses an ARL-SEMQ instrument. Both laboratories utilize similar procedures. The WITS laboratory operates with a 15 kV accelerating potential which generates a focused electron beam between 3 and 5 microns in diameter and produces a specimen current of 0,05 micro-amps on brass. On-line data reduction makes use of correction factors tabulated by Albee and Ray (1970). Both natural and synthetic standards were used (see Table 1.1 for those used in the WITS laboratory) and relative errors on all elements are routinely within 2 per cent. For further more detailed description of the analytical technique, see Davies (in prep.).

Table 1.1: Mineral standards used during electron-probe micro-analysis at the Department of Geology, University of the Witwatersrand

Element	pyroxene amphiboles micas	garnets cordierites	spinel sapphirines	plagioclases
Si	Wakefield diopside	spessartine	spessartine	Hakoni anorthite
Ti	Obergarten ilmenite	Obergarten ilmenite	Obergarten ilmenite	Obergarten ilmenite
Al	ferric glass (syn.)	spessartine	spinel (syn.)	Hakoni anorthite
Fe <sup>2+</sup>	ferric glass (syn.)	ferric glass (syn.)	grunerite	ferric glass (syn.)
Mn	rhodonite	spessartine	spinel (syn.)	-
Mg	Wakefield diopside	Wakefield diopside	spinel (syn.)	-
Ca	Wakefield diopside	Wakefield diopside	spinel (syn.)	Hakoni anorthite
Na	Hawk oligoclase	Hawk oligoclase	-	Hawk oligoclase
K	sanidine	sanidine	sanidine	sanidine

(syn.) = synthetic

APPENDIX 2: ELECTRON PROBE ANALYTICAL DATAIntroduction

Over 300 mineral analyses have been obtained in this study of feldspars, micas, amphiboles, pyroxenes, garnets, cordierites, sapphirines, and spinels. Two instruments were used to obtain these data: a Cambridge Microscan 5 in the Department of Geochemistry at the University of Cape Town, and an ARL-SEMQ in the Department of Geology at the University of the Witwatersrand. Good consistency was obtained between these two instruments.

The data are presented in computer generated Tables according to the rock-type and instrument. Rock types that were selected for study include the garnet-cordierite-sillimanite gneiss together with the sapphirine and symplectite varieties, pyroxenitic amphibolite, metapyroxenite and gabbroic and anorthositic gneiss from the Messina Layered Intrusion. The Tables also present certain compositional, mole fraction and activity parameters pertinent to certain minerals as outlined in the succeeding sections. Ferric iron is estimated for amphibole, pyroxene and garnet, and recalculated analyses for these minerals are included in the Tables adjacent to the ferric-free versions. A summary chart is included and precedes the Tables. This chart provides a key to the Tables, and should be consulted to determine rock-type, number of analyses



and other details concerning the data.

### Feldspar

Feldspars are recalculated into a structural formula on the basis of 32 oxygens per molecule:



In addition, the weight percentages of two feldspar end-members are given in the Tables. These are for albite and anorthite, and are calculated as follows:

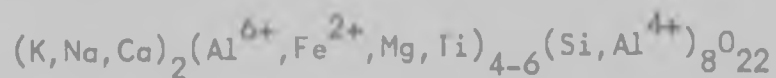
$$X_{Ab} = \frac{262.231xNa}{262.231xNa + 278.34xK + 278.2xCa}$$

$$X_{An} = \frac{278.2xCa}{262.231xNa + 278.34xK + 278.2xCa}$$

These values are only calculated for feldspar analyses and are labelled 'X-ANORTHIT' for  $X_{An}$  and 'X-ALBITE' for  $X_{Ab}$  in the Tables. Other parameters are not calculated and appear as zeros.

### Mica

Biotite and phlogopite are recalculated on the basis of 22 oxygens according to the following formula:



neglecting  $2H_2O$  not determined by the microprobe technique.

Two ionic ratios are calculated and labelled in the Tables as follows:

$$\begin{aligned} \text{'X-FE'} &= \frac{\text{Fe}^{++}}{\text{Fe}^{++} + \text{Mg}} \\ \text{'MG/FE'} &= \frac{\text{Mg}}{\text{Fe}^{++}} \end{aligned}$$

No other parameters are calculated, causing zeros to appear in the Tables.

#### Amphibole

Calcic amphiboles (hornblendes) predominate in the study area with the exception of the sapphirine and corundum bearing enclaves within the garnet-cordierite-sillimanite gneiss where gedrite occurs. The microprobe analyses are recalculated on the basis of 13 oxygens neglecting 1H<sub>2</sub>O:



However, all analyses presented in the Tables are recalculated a second time where an estimate of ferric iron is considered. Powell (1975) found that on average 14 per cent of FeO is required to be converted to Fe<sub>2</sub>O<sub>3</sub> to attain charge balance in calcic amphiboles (i.e. hornblendes) while about 4 per cent FeO is required in the case of calcic-poor amphiboles (e.g. cummingtonite). The value of 14 per cent is applied in calculating the ferric content of amphiboles presented in the Tables.

In addition, the activity of tremolite ('A-TREMOLIT') is calculated and presented in the Tables for all amphibole

analyses. Site occupancies are filled according to the following rules (S. Richardson, pers. comm.):

1. The tetrahedral site is filled to total 8 ions by adding enough Al to Si.
2. The M2 site contains any excess Al after filling the tetrahedral site above, and also Ti and any Fe<sup>+++</sup> (if estimated). Then this site is filled to total 2 ions by Fe<sup>++</sup> and Mg such that these ions occur in the same proportions to each other as they do in the whole analysis (ideal solution model with random mixing).
3. The M1 and M3 sites contain the remainder of the Fe<sup>++</sup> and Mg and should total between 3 and 4 ions.
4. The M4 site is filled with Co and Mn, and then enough Na to total 2 ions.
5. The A site is filled with the remaining Na plus any K. In addition, a vacant site ( $\square$ ) is filled with enough ions to make this A site total 1 ion.

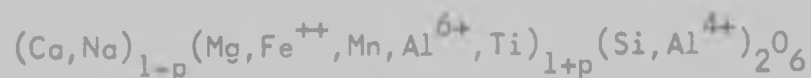
Then the activity of tremolite is given by:

$$'A\text{-TREMOLIT}' = (x_{\square}^A) \cdot (x_{Ca}^{M4})^2 \cdot (x_{Mg}^{M1M2M3})^5 \cdot (x_{Si}^{Tet})^8$$

No other parameters are calculated for amphibole analyses.

### Pyroxene

Pyroxenes are recalculated on the basis of 6 oxygens according to the following formula:



where 'p' approximates 1 in orthopyroxenes, and is close to zero in clinopyroxenes. Ferric iron is also estimated for all pyroxenes in the Tables and is given in a second accompanying analysis. The ferric estimate is based on the stoichiometric charge balance method of Ryburn et al. (1975). The pyroxene structural formula is first calculated to a cation total of approximately 4 with all Fe as Fe<sup>++</sup>. Then, Fe<sup>+++</sup> is determined by the equation:

$$\text{Fe}^{+++} = \text{Ideal cation charge} - \text{calculated charge}$$

which in pyroxenes is equivalent to:

$$\text{Fe}^{+++} = 4 - 2\text{Si} - 2\text{Ti} - \text{Al} - \text{Cr} + \text{Na} + \text{K}$$

Then:

$$\text{Fe}^{++} = \text{Fe}^{\text{total}} - \text{Fe}^{+++}$$

The following compositional parameters are calculated for all pyroxene analyses:  $\text{Fe}^{++}/(\text{Fe}^{++} + \text{Mg})$ ,  $\text{FeO}/\text{MgO}$ ,  $2 \cdot (X_{\text{Al}}^{\text{OPX}})$ ,  $X_{\text{Al}}^{\text{Tet}}$ ,  $X_{\text{Al}}^{\text{M1}}$ ,  $X_{\text{Mg}}^{\text{M1}}$ ,  $X_{\text{Mg}}^{\text{M2}}$ ,  $X_{\text{Fe}}^{\text{M2}}$ ,  $X_{\text{Ca}}^{\text{M2}}$  and the activity of enstatite in the pyroxene. All of these calculations are made after the pyroxene sites have been filled according to the scheme of Wood and Banno (1973);

1. Enough Al is added to Si to fill the tetrahedral site to 2 ions.
2. M1 contains any Al remaining from above, plus Cr, Ti and any Fe<sup>+++</sup> (if estimated).

3. M2 contains Ca, Na and Mn.
4. Then, both M1 and M2 sites are filled to total 1 ion by  $\text{Fe}^{++}$  and Mg such that:

$$\left[ \frac{\text{Mg}}{\text{Mg} + \text{Fe}^{++}} \right]_{\text{M1}} = \left[ \frac{\text{Mg}}{\text{Mg} + \text{Fe}^{++}} \right]_{\text{M2}} = \left[ \frac{\text{Mg}}{\text{Mg} + \text{Fe}^{++}} \right]_{\text{mineral}}$$

(Wood and Banno, 1973, eqn.25) which assures the ideal solution model with random distribution of Mg and  $\text{Fe}^{++}$  over the M1 and M2 sites. The activity of enstatite ('A-ENSTATIT') is modified after eqn. 24 of Wood and Banno (1973) as follows:

$${}^{\text{A}}\text{Mg}_2\text{Si}_2\text{O}_6 = x_{\text{Mg}}^{\text{M1}} \cdot x_{\text{Mg}}^{\text{M2}} \cdot (x_{\text{Si}}^{\text{Tet}})^2$$

#### Garnet

Garnets are recalculated on the basis of 24 oxygens with the following formula:



Ferric estimates are made by the charge balance method of Ryburn et al. (1975) in a similar way to that for pyroxenes:

$$\text{Fe}^{+++} = \text{Ideal cation charge} - \text{calculated charge}$$

which in garnet is equivalent to:

$$\text{Fe}^{+++} = 16 - 2\text{Si} - 2\text{Ti} - \text{Al} - \text{Cr}$$

on the basis of 24 oxygens per structural formula.

The following ratios are calculated and presented in the Tables for each garnet recalculation:

$$'X-Fe' = \frac{Fe^{++}}{Fe^{++} + Mg}$$

$$'FeO/MgO' = \frac{FeO}{MgO} \text{ (wt.\%)}$$

$$'Fe/Mg' = \frac{Fe^{++}}{Mg} \text{ (ions)}$$

$$'Mg/Fe' = \frac{Mg}{Fe^{++}} \text{ (ions)}$$

In addition, three mole fractions for divalent cations in the M1 site are calculated:

$$'X-A-M1' = \frac{A}{Mg + Fe^{++} + Mn + Ca} \text{ (ions)}$$

where A is Mg, Fe<sup>++</sup> or Ca.

#### Cordierite

Cordierites are recalculated into structural formulae on the basis of 18 oxygens:



Only one ratio is presented for cordierites:

$$'X-Fe' = \frac{Fe^{++}}{Fe^{++} + Mg}$$

#### Sapphirine

Sapphirines are recalculated on the basis of 10 oxygens after the formula of Schreyer and Seifert (1969):



No compositional parameters are calculated for sapphirine analyses listed in the tables.

### Spinel

Spinel is recalculated into structural formulae on the basis of 32 oxygens:



No parameters are presented in the Tables.

### Outline chart

Table 2.1 provides a key to the computer printed data tables (Tables 2.2 - 2.23). It should be consulted to determine the following information for each data Table: sample number, locality (also given on Map 2 in rear pocket), rock type, analytical laboratory, mineral types analysed, and the numbers of analyses.

The analytical laboratories have the following abbreviations:

UCT, Cambridge Microscan 5 instrument at the Department of Geochemistry, University of Cape Town;

WITS, ARL-SEM instrument at the Department of Geology, University of the Witwatersrand.

Table 2.1: Outline chart to data tables

Table number	Sequence number	Form locality (Map ' in rear pocket)	Rock type	Laboratory	Feldspar	Mica	Amphibole	Pyroxene	Garnet	Cordierite	Sapphirine	Spinel	
2.2	21-7-F	Boschrand	garnet-cordierite- sillimanite gneiss	UCT	2	1	-	-	1	1	-	-	
2.3	21-7-G		ditto	UCT	-	2	-	-	4	1	-	-	
2.4	21-7-G		ditto	WITS	-	-	-	-	86	-	-	-	
2.5	21-7-G		ditto	WITS	-	-	-	-	-	12	-	-	
2.6	21-7-G		ditto	WITS	-	19	-	-	-	-	-	-	
2.7	8-7-B	Rona,	sapphirine-bearing rock	UCT	-	1	-	-	-	2	2	3	
2.8	2-8-12		ditto	UCT	-	1	1	-	1	1	1	1	
2.9	2-8-12		ditto	WITS	-	1	-	-	1	-	5	6	
2.10	2-8-12		ditto	WITS	-	-	-	-	55	-	-	-	
2.11	2-8-12		ditto	WITS	-	-	-	-	-	19	-	-	
2.12	11-G		ditto	UCT	-	3	-	1	4	3	3	2	
2.13	2-8-10A	Rondjefuntein	garnet-orthopyroxene- plagioclase symplec- tite	UCT	1	-	-	1	1	-	-	-	
2.14	2-8-10B		ditto	UCT	1	1	-	1	2	-	-	-	
2.15	2-8-10B		ditto	WITS	-	3	-	4	12	-	-	-	
2.16	27	Artonville (see Morrocks, 1975)	pyroxenitic amphibolite	UCT	1	-	1	2	1	-	-	-	
2.17	27		ditto	WITS	1	-	1	2	2	-	-	-	
2.18	X21395		ditto	UCT	1	-	1	3	-	-	-	-	
2.19	X21395		ditto	WITS	-	-	4	7	-	-	-	-	
2.20	X21399		ditto	UCT	-	-	2	2	1	-	-	-	
2.21	20	Artonville	metopyroxenite	WITS	-	-	1	5	-	-	-	-	
2.22	26-5-A	Shangani	gabbro	UCT	1	-	1	1	-	-	-	-	
	26-5-C		anorthosite	UCT	1	-	-	-	-	-	-	-	
	26-5-E		gabbro	UCT	1	-	1	1	-	-	-	-	
2.23	26-5-A		gabbroic anorthosite	WITS	-	-	4	2	-	-	-	-	
TOTAL (324 analyses)						10	32	17	32	171	39	11	12

UCT: University of Cape Town (Cambridge Microscan 5)  
WITS: University of the Witwatersrand (ARI-SEM)









TABLE 3\*

	1	2	3	4	5
SIU2	38.78	38.84	39.02	39.41	39.41
SIU3	0.01	0.0	0.02	0.01	0.01
AL2O3	21.21	21.62	21.75	21.74	21.74
CR2O3	0.0	0.0	0.0	0.0	0.0
FE2O3	0.0	0.0	0.0	0.0	0.0
FE3	29.90	27.97	27.04	26.82	26.71
FMU	9.65	0.49	0.48	0.49	0.49
AGU	7.85	9.41	10.05	10.38	10.38
CA7	1.13	1.11	1.11	1.13	1.13
MA3	0.0	0.0	0.0	0.0	0.0
K-O	0.0	0.0	0.0	0.0	0.0
TOTAL WIR	99.51	99.46	99.34	99.73	99.72
NO OXYGENS	24.	24.	24.	24.	24.
SI	6.065	6.017	6.012	6.041	6.043
FE	6.001	6.014	6.010	6.041	6.030
AL	3.902	3.947	3.949	3.929	3.954
CR	0.0	0.0	0.0	0.0	0.0
FE2O3	0.0	0.0	0.0	0.0	0.0
FE3	3.944	3.604	3.491	3.413	3.425
FMU	0.087	0.064	0.063	0.064	0.050
MC	1.830	2.172	2.308	2.362	2.582
CA	0.189	0.184	0.183	0.185	0.176
VA	0.0	0.0	0.0	0.0	0.0
K	0.0	0.0	0.0	0.0	0.0
TOTAL IONS	15.984	16.003	16.010	16.994	15.952
X-FE	0.5813	0.6252	0.6020	0.5910	0.5523
FE2O3	3.8059	2.9724	2.9555	2.9545	2.2074
FMU	2.1374	1.6580	1.5126	1.447	1.2387
MGUFE	0.4672	0.5995	0.6611	0.6049	0.8073
2-X-AL-LPX	0.0	0.0	0.0	0.0	0.0
X-AL-TC1	0.0	0.0	0.0	0.0	0.0
X-AL-41	0.0	0.0	0.0	0.0	0.0
X-MG-41	0.3011	0.3594	0.3818	0.3721	0.4293
X-FE-41	0.6495	0.5995	0.5775	0.5665	0.5337
X-CA-41	0.0315	0.0305	0.0303	0.0309	0.0293
X-MG-M2	0.0	0.0	0.0	0.0	0.0
X-FE-42	0.0	0.0	0.0	0.0	0.0
X-CL-M2	0.0	0.0	0.0	0.0	0.0
A-L-STABILITY	0.0	0.0	0.0	0.0	0.0
A-TEMOLIT	0.0	0.0	0.0	0.0	0.0
A-ANDRIT	0.0	0.0	0.0	0.0	0.0
X-AL-ITE	0.0	0.0	0.0	0.0	0.0



TABLE 2.15 (continued)

	10	11	12	13	14	15
TI	10.47	39.47	39.25	31.11	34.80	34.02
AL	0.01	0.01	0.01	0.02	0.01	0.01
ALC	11.52	21.02	22.01	22.03	1.56	2.45
CH2	0.0	0.0	0.0	0.0	0.0	0.0
FE	0.0	0.0	0.0	0.0	0.0	0.0
FEF	25.57	0.43	0.43	0.40	26.87	27.27
MMJ	11.42	0.38	0.38	0.42	3.5	0.42
MO	11.23	10.84	10.84	10.84	0.09	9.82
CA	1.08	1.24	1.24	1.29	1.49	1.43
KA2	0.0	0.0	0.0	0.0	0.0	0.0
K2O	0.0	0.0	0.0	0.0	0.0	0.0
TOTAL	100.00	100.00	99.96	99.83	99.34	99.51
NO OXYGENS	24	24	24	24	24	24
TI	5.008	6.002	5.993	5.981	5.997	6.026
AL	0.001	0.001	0.001	0.002	0.001	0.001
ALC	3.934	3.930	3.962	3.972	1.927	3.906
CH2	0.0	0.0	0.0	0.0	0.0	0.0
FE	0.0	0.0	0.0	0.0	0.0	0.0
FEF	3.304	3.252	3.338	3.367	3.473	3.523
MMJ	0.034	0.054	0.049	0.052	0.059	0.064
MO	2.548	2.478	2.476	2.425	2.321	2.261
CA	0.176	0.176	0.203	0.211	0.245	0.237
KA	0.0	0.0	0.0	0.0	0.0	0.0
K	0.0	0.0	0.0	0.0	0.0	0.0
TOTAL	16.024	16.002	16.025	16.023	16.031	16.019
X-FE	0.546	0.5610	0.5739	0.5811	0.5993	0.6091
FE3/MO	2.3108	2.2771	2.4004	2.4718	2.5657	2.7770
FE/MO	1.4567	1.2778	1.3470	1.3671	1.4054	1.5584
MO/FE	0.7712	0.7826	0.7424	0.7209	0.6885	0.6417
Z-X-AL-CPX	0.0	0.0	0.0	0.0	0.0	0.0
X-AL-TIT	0.0	0.0	0.0	0.0	0.0	0.0
X-AL-MI	0.0	0.0	0.0	0.0	0.0	0.0
X-MG-MI	0.4189	0.4223	0.4084	0.4077	0.3907	0.3716
X-FE-MI	0.5432	0.5396	0.5501	0.5558	0.5495	0.5750
X-CA-MI	0.0270	0.0292	0.0334	0.0349	0.0402	0.0389
X-MG-M2	0.0	0.0	0.0	0.0	0.0	0.0
X-FE-M2	0.0	0.0	0.0	0.0	0.0	0.0
X-CA-M2	0.0	0.0	0.0	0.0	0.0	0.0
A-ENSTIATIT	0.0	0.0	0.0	0.0	0.0	0.0
A-THEMLIT	0.0	0.0	0.0	0.0	0.0	0.0
X-ANGRTMIF	0.0	0.0	0.0	0.0	0.0	0.0
X-ALEITH	0.0	0.0	0.0	0.0	0.0	0.0

TABLE 24 (cont.)

	16	17	18	19	20
Al <sub>2</sub> O <sub>3</sub>	38.45	38.39	38.42	38.61	39.50
SiO <sub>2</sub>	0.0	0.0	0.01	0.02	0.0
FeO	21.69	21.54	21.40	21.73	21.75
MgO	0.0	0.0	0.0	0.0	0.0
CaO	28.16	27.94	27.97	28.24	-0.00
K <sub>2</sub> O	0.55	0.55	0.53	0.44	0.43
Na <sub>2</sub> O	8.97	9.36	9.03	9.46	10.57
Total	1.25	1.17	1.29	1.21	1.10
Loss on Ignition	0.0	0.0	0.0	0.0	0.0
Total	99.73	99.95	99.23	99.25	99.82
Major Elements	28.0	28.0	24.0	24.0	24.0
Si	5.972	5.976	6.001	6.037	6.042
Al	0.0	0.0	0.001	0.002	0.001
Fe	3.971	3.954	3.930	3.915	3.922
Mg	0.0	0.0	0.0	0.0	0.0
Ca	3.743	3.644	3.641	3.628	3.667
Fe <sup>++</sup>	0.072	0.073	0.070	0.071	0.071
Fe <sup>+++</sup>	2.072	2.172	2.096	2.273	2.409
Ca	0.208	0.195	0.215	0.198	0.190
Na	0.0	0.0	0.0	0.0	0.0
K	0.0	0.0	0.0	0.0	0.0
Total	16.043	16.041	16.040	15.985	15.997
X-Fe	0.6422	0.6218	0.6348	0.6065	0.6340
Fe <sup>++</sup> /Mg	3.2125	2.9300	3.0977	3.7240	2.6507
Fe <sup>++</sup> /Ca	1.8030	1.6442	1.7674	1.5786	1.4011
Mg/Fe	3.4546	3.5970	3.5638	3.5542	3.7837
X-Al <sub>2</sub> O <sub>3</sub>	0.0	0.0	0.0	0.0	0.0
X-Al <sub>2</sub> SiO <sub>5</sub>	0.0	0.0	0.0	0.0	0.0
X-Al <sub>2</sub> Si <sub>2</sub> O <sub>7</sub>	0.0	0.0	0.0	0.0	0.0
X-Mg <sub>2</sub> SiO <sub>4</sub>	0.3404	0.3573	0.3444	0.3787	0.3994
X-Fe <sub>2</sub> SiO <sub>4</sub>	0.6137	0.5984	0.6047	0.5780	0.5500
X-Ca <sub>2</sub> SiO <sub>4</sub>	0.0241	0.0321	0.0351	0.3320	0.0315
X-Mg <sub>2</sub> SiO <sub>4</sub>	0.0	0.0	0.0	0.0	0.0
X-Fe <sub>2</sub> SiO <sub>4</sub>	0.0	0.0	0.0	0.0	0.0
X-Ca <sub>2</sub> SiO <sub>4</sub>	0.0	0.0	0.0	0.0	0.0
X-Enstatite	0.0	0.0	0.0	0.0	0.0
X-Thornhillite	0.0	0.0	0.0	0.0	0.0
X-Anorthite	0.0	0.0	0.0	0.0	0.0
X-Albite	0.0	0.0	0.0	0.0	0.0

TABLE 2 4 (cont.)

	21	22	23	24	25
ALC	39.14	39.03	39.02	39.99	39.43
ALD	0.02	0.01	0.02	0.01	0.02
ALM	21.02	21.90	21.08	21.08	21.08
ALN	0.0	0.0	0.0	0.0	0.0
ALP	0.0	0.0	0.0	0.0	0.0
ALQ	25.89	25.42	25.22	25.38	25.37
ALR	0.42	0.43	0.32	0.4	0.37
ALS	10.02	11.00	11.17	11.22	11.24
ALT	1.25	1.09	1.10	1.07	1.08
ALU	0.0	0.0	0.0	0.0	0.0
ALV	0.0	0.0	0.0	0.0	0.0
TOTAL	99.37	99.32	99.44	99.37	99.31
NO. OBSERVATIONS	24	24	24	24	24
AL	5.017	5.900	5.975	5.973	5.927
ALD	0.022	0.001	0.022	0.00	0.022
ALM	3.929	3.260	3.956	3.967	3.943
ALN	0.0	0.0	0.0	0.0	0.0
ALP	0.0	0.0	0.0	0.0	0.0
ALQ	3.362	3.263	3.233	3.262	3.233
ALR	0.055	0.056	0.051	0.053	0.050
ALS	2.447	2.517	2.549	2.570	2.590
ALT	0.206	0.179	0.180	0.175	0.177
ALU	0.0	0.0	0.0	0.0	0.0
ALV	0.0	0.0	0.0	0.0	0.0
TOTAL	16.017	16.008	16.012	16.023	16.000
ALC	0.576	0.5048	0.5591	0.5594	0.5588
ALD	2.445	2.3123	2.2600	2.2520	2.2571
ALM	1.3740	1.2970	1.2682	1.2694	1.2646
ALN	0.7278	0.7592	0.7715	0.7973	0.7885
ALP	0.0	0.0	0.0	0.0	0.0
ALQ	0.0	0.0	0.0	0.0	0.0
ALR	0.0	0.0	0.0	0.0	0.0
ALS	0.4031	0.4182	0.4239	0.4240	0.4247
ALT	0.5537	0.5464	0.5376	0.5382	0.5380
ALU	0.0339	0.0396	0.0300	0.0291	0.0293
ALV	0.0	0.0	0.0	0.0	0.0
TOTAL	6.033	6.039	6.030	6.030	6.030
ALC	0.0	0.0	0.0	0.0	0.0
ALD	0.0	0.0	0.0	0.0	0.0
ALM	0.0	0.0	0.0	0.0	0.0
ALN	0.0	0.0	0.0	0.0	0.0
ALP	0.0	0.0	0.0	0.0	0.0
ALQ	0.0	0.0	0.0	0.0	0.0
ALR	0.0	0.0	0.0	0.0	0.0
ALS	0.0	0.0	0.0	0.0	0.0
ALT	0.0	0.0	0.0	0.0	0.0
ALU	0.0	0.0	0.0	0.0	0.0
ALV	0.0	0.0	0.0	0.0	0.0
TOTAL	0.0	0.0	0.0	0.0	0.0



TABLE 2 (cont.)

	26	27	28	29	30
SI	39.35	38.93	78.97	13.10	38.16
TI	0.01	0.0	0.02	0.03	0.01
AL	21.97	21.91	21.75	21.80	21.38
CR	0.0	0.0	0.0	0.0	0.0
FE	0.18	0.0	0.0	0.0	0.0
MN	25.28	-0.09	26.58	27.35	27.87
CA	0.38	0.39	0.42	0.46	0.53
MG	11.26	10.51	10.12	9.74	9.03
NA	1.10	1.11	1.26	1.15	1.16
K	0.0	0.0	0.0	0.0	0.0
TOTAL	99.52	98.73	99.13	73.71	98.11
NO OXIGENS	24.	24.	24.	24.	24.
SI	6.010	6.011	6.016	5.989	6.004
TI	0.001	0.0	0.002	0.001	0.001
AL	3.954	3.989	3.958	3.987	3.960
CR	0.0	0.0	0.0	0.0	0.0
FE	0.021	0.011	0.004	0.007	0.003
MN	3.251	3.353	3.329	3.565	3.667
CA	0.049	0.051	0.055	0.061	0.071
MG	2.503	2.419	2.328	2.262	2.113
NA	0.180	0.184	0.208	0.192	0.196
K	0.0	0.0	0.0	0.0	0.0
TOTAL	16.011	15.998	16.001	15.937	16.015
FEU/400	0.5575	0.5009	0.558	0.5119	0.6329
FE/4C	2.2602	2.4702	2.6243	2.3080	3.0864
MG/FE	1.2601	1.3802	1.4727	1.5753	1.7370
CA/FE	0.7684	0.7214	0.6790	0.6846	0.6574
X-AL-CPX	0.0	0.0	0.0	0.0	0.0
X-AL-TEI	0.0	0.0	0.0	0.0	0.0
X-AL-41	0.0	0.0	0.0	0.0	0.0
X-MG-41	0.4256	0.4027	0.3807	0.3721	0.3499
X-FE-41	0.5375	0.5582	0.5695	0.5843	0.6061
X-CA-41	0.0298	0.0306	0.0346	0.0315	0.0323
X-MG-M2	0.0	0.0	0.0	0.0	0.0
X-FL-M2	0.0	0.0	0.0	0.0	0.0
X-CA-42	0.0	0.0	0.0	0.0	0.0
A-TRILITE	0.0	0.0	0.0	0.0	0.0
A-TRIMITE	0.0	0.0	0.0	0.0	0.0
X-AL-41	0.0	0.0	0.0	0.0	0.0
X-AL-41	0.0	0.0	0.0	0.0	0.0

TOTAL 24 Levels

	31	32	33	34	35
TI	27.91	37.28	33.93	33.27	34.37
AL	0.02	0.01	0.02	0.01	0.00
FE	21.30	21.92	21.84	21.25	21.21
CU	0.00	0.00	0.00	0.00	0.00
FL	0.21	0.00	0.00	0.00	0.00
MNO	30.71	26.37	27.17	30.47	31.12
W/C	0.62	0.44	0.47	0.55	0.61
CA	7.15	10.30	9.94	9.78	7.93
NA	1.20	1.12	1.22	1.21	1.11
K2O	0.00	0.00	0.00	0.00	0.00
TOTAL #1x	98.92	99.44	93.91	93.53	98.34
NO OXYGENS	24	24	24	24	24
TI	5.99	6.03	5.98	6.07	6.02
AL	0.02	0.01	0.02	0.01	0.00
FE	3.97	3.97	3.96	3.93	3.92
CU	0.00	0.00	0.00	0.00	0.00
FL	0.02	0.00	0.00	0.00	0.00
MNO	4.06	3.38	3.52	3.75	3.95
W/C	0.84	0.57	0.73	0.71	0.81
CA	1.68	2.35	2.30	2.53	1.85
NA	0.20	0.18	0.20	0.20	0.18
K	0.00	0.00	0.00	0.00	0.00
TOTAL #LNS	16.012	15.988	16.006	15.026	16.018
X-FE	0.70	0.59	0.60	0.64	0.68
F-D/M	4.95	2.56	2.72	3.25	3.79
FE/ML	2.41	1.43	1.53	1.81	2.13
MG/FE	0.41	0.00	0.65	0.51	0.62
X-AL-CPX	0.00	0.00	0.00	0.00	0.00
X-AL-TEI	0.00	0.00	0.00	0.00	0.00
X-AL-41	0.00	0.00	0.00	0.00	0.00
X-MG-VI	0.21	0.39	0.37	0.33	0.30
X-FE-41	0.67	0.56	0.57	0.67	0.65
X-CA-41	0.03	0.03	0.03	0.03	0.03
X-MG-42	0.00	0.00	0.00	0.00	0.00
X-FE-42	0.00	0.00	0.00	0.00	0.00
X-CA-42	0.00	0.00	0.00	0.00	0.00
A-ENSTATT	0.00	0.00	0.00	0.00	0.00
A-THE4JLIT	0.00	0.00	0.00	0.00	0.00
X-ANDRTMIF	0.00	0.00	0.00	0.00	0.00
X-ALRIFL	0.00	0.00	0.00	0.00	0.00

TABLE 2.4 (cont.)

	36	37	38	39	40	
SI02	38.43	39.30	39.07	39.67	38.81	38.81
TI02	0.03	0.02	0.02	0.02	0.02	0.02
AL2O3	21.99	21.98	22.11	22.11	22.08	22.08
CH2O3	0.0	0.0	0.0	0.0	0.0	0.0
FE2O3	0.0	0.0	0.0	0.0	0.0	0.0
FE3	1.95	1.80	1.41	1.41	1.41	1.41
WNO	23.82	24.06	24.85	24.85	26.24	26.24
MNO	0.40	0.35	0.37	0.37	0.41	0.41
MGO	11.75	11.50	11.54	11.54	11.25	11.25
CAO	1.32	1.33	1.23	1.23	1.28	1.28
NA2O	0.0	0.0	0.0	0.0	0.0	0.0
K2O	0.0	0.0	0.0	0.0	0.0	0.0
TOTAL	99.68	99.17	100.00	100.60	100.11	100.25
NO. OF	24	24	24	24	24	24
TI	5.868	5.898	5.337	5.317	5.27	5.907
AL	0.003	0.002	0.002	0.002	0.002	0.002
CH	3.577	3.991	3.961	3.968	3.975	3.968
CP	0.0	0.0	0.0	0.0	0.0	0.0
FE	0.224	0.208	0.160	0.160	0.20	0.065
FE3	3.042	3.307	3.148	3.148	3.351	3.71
W	0.052	0.047	0.047	0.047	0.053	0.053
M	2.674	2.639	2.605	2.605	2.554	2.554
CA	0.216	0.219	0.200	0.200	0.211	0.210
NA	0.0	0.0	0.0	0.0	0.0	0.0
K	0.0	0.0	0.0	0.0	0.0	0.0
TOTAL	16.112	16.104	16.021	16.027	16.023	16.029
X-FE	0.456	0.5562	0.5595	0.5172	0.5667	0.5542
FE/MGO	2.1782	2.2330	2.2614	2.1536	2.3302	2.2143
FE/MG	1.2212	1.2531	1.2702	1.2086	1.3077	1.2430
MG/FE	0.8159	0.7980	0.7813	0.8274	0.7667	0.8066
Z-X-AL-CPX	0.0	0.0	0.0	0.0	0.0	0.0
X-AL-TET	0.0	0.0	0.0	0.0	0.0	0.0
X-AL-TA	0.0	0.0	0.0	0.0	0.0	0.0
X-MG-41	0.308	0.4248	0.4228	0.4311	0.4148	0.4293
X-FE-41	0.5261	0.5123	0.5371	0.5247	0.5424	0.5293
X-CA-41	0.348	0.0353	0.0324	0.0333	0.0342	0.0351
X-MG-42	0.0	0.0	0.0	0.0	0.0	0.0
X-FE-42	0.0	0.0	0.0	0.0	0.0	0.0
X-CA-42	0.0	0.0	0.0	0.0	0.0	0.0
A-ENSATIT	0.0	0.0	0.0	0.0	0.0	0.0
A-TMELIT	0.0	0.0	0.0	0.0	0.0	0.0
X-ANC4TIT	0.0	0.0	0.0	0.0	0.0	0.0
X-ALIT	0.0	0.0	0.0	0.0	0.0	0.0



TABLE 2 (cont.)

	47	48	49	50
SI 12	30.23	30.53	30.69	30.42
TI 12	0.0	0.0	0.01	0.01
MLZG3	21.91	21.91	22.14	21.67
CRZG3	0.0	0.0	0.0	0.0
FEZG3	0.0	1.97	0.0	0.0
FMJ	26.78	26.23	27.02	26.58
AMJ	0.47	0.36	0.40	0.35
AMJ	11.16	11.57	11.64	11.25
CA 1	1.16	1.21	1.14	1.22
CA 2	0.0	0.0	0.0	0.0
NA 1	0.0	0.0	0.0	0.0
NA 2	0.0	0.0	0.0	0.0
TOTAL M1	59.97	100.16	100.04	99.64
MC EXPENSE	24.	24.	24.	24.
TI	5.911	5.885	5.905	5.912
AL	3.963	3.945	3.883	3.931
CR	0.0	0.0	0.0	0.0
FE 1	3.436	0.214	3.122	3.421
FE 2	0.56	3.206	3.052	0.051
MG	2.857	0.056	2.661	2.893
CA	0.191	2.641	2.637	2.893
NA	0.0	0.199	3.186	0.201
K	0.0	0.0	0.0	0.0
TOTAL JUNS	16.108	16.036	16.033	16.121
X-FE	0.5735	0.5599	0.5564	0.5493
FE/MJD	2.1996	2.2671	2.2354	2.3419
FE/WG	1.1406	1.2722	1.2544	1.3142
4G/FE	0.7426	0.7860	0.7972	0.7805
2+X-AL-CPX	0.0	0.0	0.0	0.0
X-AL-FET	0.0	0.0	0.0	0.0
X-AL-41	0.0	0.0	0.0	0.0
X-MG-41	0.4093	0.4228	0.4260	0.4148
X-FE-41	0.512	0.5179	0.5251	0.5181
X-CA-41	0.0306	0.0358	0.0360	0.0321
X-4G-42	0.0	0.0	0.0	0.0
X-FE-42	0.0	0.0	0.0	0.0
X-CA-42	0.0	0.0	0.0	0.0
A-ENSTATITE	0.0	0.0	0.0	0.0
A-TREASILET	0.0	0.0	0.0	0.0
X-ANURITE	0.0	0.0	0.0	0.0
X-ALBITE	0.0	0.0	0.0	0.0

TABLE 2 (cont.)

	51	53	56	55
JI 12	38.05	37.04	37.83	37.94
JI 32	0.01	0.01	0.01	0.01
AL 20	21.80	21.24	21.81	21.70
AL 33	0.0	0.0	0.0	0.0
FE 2	0.0	0.0	0.0	0.0
FE 3	26.41	27.43	26.98	27.01
FL 3	0.32	0.47	0.45	0.42
4N 3	11.16	10.32	10.65	10.72
4G 0	1.17	1.15	1.19	1.23
CA 3	0.0	0.0	0.0	0.0
NA 2	0.0	0.0	0.0	0.0
K 3	0.0	0.0	0.0	0.0
TOTAL #13	99.20	99.14	99.14	99.29
NO URGENS	24.	24.	24.	24.
JI	5.852	5.904	5.878	5.889
TI	0.001	0.001	0.001	0.001
AL	3.980	3.972	3.934	3.982
CH	0.0	0.0	0.0	0.0
FE 1	0.0	0.0	0.0	0.0
FE 2	3.171	3.467	3.233	3.233
4N	0.050	0.051	0.051	0.055
4G	2.520	2.522	2.465	2.468
CA	0.194	0.192	0.191	0.205
NA	0.0	0.0	0.0	0.0
K	0.0	0.0	0.0	0.0
TOTAL IONS	16.117	16.109	16.036	16.119
X-FE	0.5708	0.5788	0.5629	0.5857
FE 3/4	2.3623	2.4492	2.2945	2.5192
FE 1/2	1.3254	1.3744	1.2876	1.4139
WG/FE	0.7244	0.7276	0.7766	0.7373
X-AL-EPH	0.0	0.0	0.0	0.0
X-AL-TLT	0.0	0.0	0.0	0.0
X-AL-MI	0.0	0.0	0.0	0.0
X-MG-M1	0.4132	0.4047	0.4194	0.3970
X-FE-M1	0.5477	0.5562	0.5401	0.5614
X-CA-M1	0.0311	0.0309	0.0320	0.0328
X-MG-M2	0.0	0.0	0.0	0.0
X-FE-42	0.0	0.0	0.0	0.0
X-CA-M2	0.0	0.0	0.0	0.0
A-ENSTATIT	0.0	0.0	0.0	0.0
A-TREASIT	0.0	0.0	0.0	0.0
X-ANCRITHE	0.0	0.0	0.0	0.0
X-ALEITE	0.0	0.0	0.0	0.0

TABLE 4-4 cont-1

	56	57	58	59	60
SI	38.38	38.54	38.29	37.70	36.15
TI	0.01	0.0	0.01	0.0	0.01
AL	21.76	21.96	21.78	21.82	21.81
CR	0.0	0.0	0.0	0.0	0.0
FE	1.93	1.76	1.70	1.70	0.0
MN	25.25	24.79	24.64	25.49	25.24
MG	0.41	0.40	0.34	0.42	0.41
CA	10.97	11.34	11.29	10.94	10.85
NA	1.18	1.15	1.14	1.08	1.11
K	0.0	0.0	0.0	0.0	0.0
TOTAL	55.60	99.76	99.19	99.45	99.10
NO	24	24	24	24	24
SI	5.916	5.888	5.892	5.875	5.913
TI	0.001	0.0	0.001	0.001	0.001
AL	3.953	3.995	3.951	3.970	3.981
CR	0.0	0.0	0.0	0.0	0.0
FE	0.212	0.202	0.197	0.234	0.191
MN	3.468	3.167	3.170	3.453	3.460
MG	0.054	0.052	0.044	0.055	0.051
CA	2.520	2.582	2.589	2.541	2.503
NA	0.195	0.188	0.189	0.179	0.184
K	0.0	0.0	0.0	0.0	0.0
TOTAL	16.106	16.034	16.033	16.039	16.096
X-FE	0.5791	0.5509	0.5505	0.5761	0.5805
FE/MG	1.3781	1.2266	1.245	1.214	1.227
MG/FE	0.7267	0.8152	0.8166	0.8359	0.7256
X-AL-CPX	0.0	0.0	0.0	0.0	0.0
X-AL-TET	0.0	0.0	0.0	0.0	0.0
X-AL-41	0.0	0.0	0.0	0.0	0.0
X-MG-41	0.4041	0.4311	0.4321	0.4379	0.4307
X-FE-41	0.5501	0.5288	0.5291	0.543	0.5579
X-CA-41	0.0313	0.0314	0.0314	0.0314	0.0297
X-MG-42	0.0	0.0	0.0	0.0	0.0
X-FE-42	0.0	0.0	0.0	0.0	0.0
X-CA-42	0.0	0.0	0.0	0.0	0.0
A-ENSIFALIT	0.0	0.0	0.0	0.0	0.0
A-THEMILIT	0.0	0.0	0.0	0.0	0.0
X-ANGRTTIT	0.0	0.0	0.0	0.0	0.0
X-ALBITE	0.0	0.0	0.0	0.0	0.0

TABLE 2 (cont.)

	61	62	63	64	65
SIJ2	39.11	39.88	38.54	38.42	38.43
TIJ2	0.0	0.01	0.01	0.0	0.03
AL2C1	22.23	21.90	22.04	21.78	21.97
CR2C3	0.0	0.0	0.0	0.0	0.0
FE2C3	0.0	1.04	0.0	0.0	1.02
FE3	1.02	28.89	27.72	27.84	28.37
MNU	0.41	0.47	0.49	0.57	0.50
M3C	10.86	10.12	9.45	9.21	9.95
CA	1.18	1.22	1.25	1.19	1.20
MA2C	0.0	0.0	0.0	0.0	0.0
K2C	0.0	0.0	0.0	0.0	0.0
TOTAL MIX	100.75	100.41	100.76	100.67	100.55
	24.	24.	24.	24.	24.
NO CRYSTALS					
AI	5.934	5.946	5.910	5.954	5.937
TI	0.0	0.001	0.001	0.0	0.003
AL	3.917	3.956	3.984	3.979	3.991
CA	0.0	0.0	0.0	0.0	0.0
FE**	0.116	0.118	0.145	0.141	0.119
FE**	2.292	3.439	3.555	3.073	3.650
MNU	0.053	0.061	0.064	0.075	0.065
M3C	2.456	2.307	2.160	1.895	2.052
CA	0.192	0.200	0.205	0.197	0.200
MA	0.0	0.0	0.0	0.0	0.0
K	0.0	0.0	0.0	0.0	0.0
TOTAL ICNS	16.019	16.020	16.024	16.013	16.020
A-FE	0.5728	0.5885	0.6221	0.5758	0.6474
FE/MNU	2.4733	2.6568	2.9333	3.0150	3.1093
FE/M3C	1.3406	1.4009	1.6461	2.0347	1.7785
MG/FE	6.7466	0.6767	0.6075	0.1707	0.5447
	0.0	0.0	0.0	0.0	0.0
X-AL-CPA	0.0	0.0	0.0	0.0	0.0
X-AL-TE F	0.0	0.0	0.0	0.0	0.0
X-AL-M1	0.0	0.0	0.0	0.0	0.0
X-MU-M1	0.4098	0.3440	0.3609	0.3998	0.3435
X-FE-M1	0.5894	0.5726	0.5941	0.5457	0.600
X-CA-M1	0.0314	0.0326	0.0343	0.0323	0.0343
X-MG-M2	0.0	0.0	0.0	0.0	0.0
X-FE-M2	0.0	0.0	0.0	0.0	0.0
X-CA-M2	0.0	0.0	0.0	0.0	0.0
A-ENSTALIT	0.0	0.0	0.0	0.0	0.0
A-TREMLIT	0.0	0.0	0.0	0.0	0.0
X-ANCIPTIT	0.0	0.0	0.0	0.0	0.0
X-ALBITE	0.0	0.0	0.0	0.0	0.0



TABLE 2-4. CONT'D.

	66	67	68	69	70
SI	34.85	38.74	39.33	33.80	39.00
TI	0.03	0.02	0.02	0.01	0.01
AL	21.88	22.02	21.48	21.43	21.75
CR	0.0	0.0	0.0	0.0	0.0
FE	27.59	27.00	26.88	23.54	27.67
MN	0.44	0.39	0.40	0.51	0.44
MG	9.90	10.49	11.14	9.60	10.24
CA	1.52	1.37	1.26	1.19	1.31
NA	0.0	0.0	0.0	0.0	0.0
K	0.0	0.0	0.0	0.0	0.0
TOTAL	100.01	100.14	100.92	100.20	100.63
NO OXYGENS	24.	24.	24.	24.	24.
SI	5.967	5.977	5.952	5.919	5.953
TI	0.002	0.002	0.002	0.001	0.001
AL	3.962	3.971	3.932	3.903	3.931
CR	0.0	0.0	0.0	0.0	0.0
FE	3.544	3.464	3.336	3.335	3.441
MN	0.057	0.051	0.051	0.071	0.057
MG	2.266	2.392	2.513	2.087	2.335
CA	0.250	0.225	0.206	0.186	0.211
NA	0.0	0.0	0.0	0.0	0.0
K	0.0	0.0	0.0	0.0	0.0
TOTAL	16.049	16.064	16.021	16.003	16.019
X-FL	0.0100	0.5817	0.5640	0.5587	0.5026
FE/MG	2.7869	2.4783	2.3029	3.4395	2.7021
FE/MG	1.8639	1.3908	1.2934	1.302	1.5164
X-G/FE	0.6354	0.7190	0.7731	0.5181	0.5595
2-X-AL	0.0	0.0	0.0	0.0	0.0
X-AL-TL	0.0	0.0	0.0	0.0	0.0
X-AL-M1	0.0	0.0	0.0	0.0	0.0
X-MG-41	0.3704	0.3991	0.4175	0.3189	0.3758
X-FL-41	0.5793	0.5550	0.5400	0.6299	0.5760
X-CA-41	0.0409	0.0375	0.0340	0.0322	0.0345
X-MG-M2	0.0	0.0	0.0	0.0	0.0
X-FE-M2	0.0	0.0	0.0	0.0	0.0
X-CA-M2	0.0	0.0	0.0	0.0	0.0
A-THE-41	0.0	0.0	0.0	0.0	0.0
A-THE-41	0.0	0.0	0.0	0.0	0.0
A-ANG-41	0.0	0.0	0.0	0.0	0.0
X-ALBITE	0.0	0.0	0.0	0.0	0.0

TABLE 24 (cont.)

	71	72	73	74	75	76
TIU-	39.90	39.41	39.07	39.25	39.10	39.80
TIJ2	0.01	0.02	0.02	0.01	0.01	0.01
AL201	22.30	22.16	22.24	22.96	22.06	22.44
CR203	0.0	0.0	0.0	0.0	0.0	0.0
FE203	0.0	0.0	0.0	0.0	0.0	0.0
FEJ	25.21	25.04	26.29	26.47	25.43	25.92
MNJ	0.37	0.41	0.38	0.39	0.39	0.37
MGJ	11.18	11.19	11.06	10.63	11.02	11.33
CAJ	1.14	1.15	1.14	1.15	1.15	1.15
NAJU	0.0	0.0	0.0	0.0	0.0	0.0
KLO	0.0	0.0	0.0	0.0	0.0	0.0
TOTAL MEV	111.11	100.67	100.26	99.87	103.93	101.07
MEV GARGENS	24.	24.	24.	24.	24.	24.
SI	6.006	5.974	5.952	5.929	5.912	5.984
TI	0.001	0.002	0.002	0.001	0.001	0.001
AL	3.957	3.960	3.935	4.011	4.000	3.981
CR	0.0	0.0	0.0	0.0	0.0	0.0
FE	0.021	0.086	0.094	0.0	0.031	0.0
FE***	3.275	3.246	3.350	3.430	3.290	3.262
MN	0.047	0.053	0.043	0.051	0.040	0.047
MG	2.505	2.524	2.507	2.452	2.473	2.552
CA	0.184	0.186	0.186	0.193	0.182	0.185
NA	0.0	0.0	0.0	0.0	0.0	0.0
K	0.0	0.0	0.0	0.0	0.0	0.0
TOTAL ICNS	16.011	16.043	16.047	16.040	16.022	16.003
X-FE	0.5081	0.5690	0.5715	0.5331	0.5736	0.5582
FE/MG	2.3444	2.3530	2.3770	2.4225	2.3771	2.3511
MG/FE	1.3156	1.3204	1.3339	1.2987	1.3222	1.2631
MG/FE	1.7601	0.7573	0.7417	0.7150	0.7423	0.7313
2-A-AL-CPX	0.0	0.0	0.0	0.0	0.0	0.0
X-AL-TET	0.0	0.0	0.0	0.0	0.0	0.0
X-AL-41	0.0	0.0	0.0	0.0	0.0	0.0
X-MG-41	0.4168	0.4141	0.4119	0.4003	0.4091	0.4247
X-FE-41	0.5464	0.5467	0.5495	0.5597	0.5503	0.5385
X-CA-41	0.0304	0.0306	0.0305	0.0314	0.0321	0.0301
X-MG-MC	0.0	0.0	0.0	0.0	0.0	0.0
X-FE-42	0.0	0.0	0.0	0.0	0.0	0.0
X-CA-42	0.0	0.0	0.0	0.0	0.0	0.0
A-TREMLIT	0.0	0.0	0.0	0.0	0.0	0.0
A-TREMLIT	0.0	0.0	0.0	0.0	0.0	0.0
X-ANCRIMII	0.0	0.0	0.0	0.0	0.0	0.0
X-ALEITE	0.0	0.0	0.0	0.0	0.0	0.0

Table 4. cont. 1.

	76	77	78	79	80
SI02	39.37	38.53	38.07	37.59	37.71
TI02	0.01	0.01	0.01	0.01	0.02
AL03	21.93	21.99	21.84	21.79	21.67
CR03	0.0	0.0	0.0	0.0	0.0
FE03	0.0	1.25	1.73	0.63	0.87
FE04	26.43	25.66	25.69	23.90	26.05
VM0	0.40	0.41	0.46	0.51	0.44
VM1	11.26	10.70	10.46	9.47	9.91
CA0	1.16	1.17	1.18	1.15	1.32
MA0	0.0	0.0	0.0	0.0	0.0
K0	0.0	0.0	0.0	0.0	0.0
TOTAL AIR	100.60	99.71	98.27	97.99	99.14
NO. OXYGENS	24.	24.	24.	24.	24.
J	5.960	5.913	5.902	5.896	5.892
TI	0.001	0.001	0.001	0.001	0.002
AL	3.918	3.979	3.992	3.991	3.992
CR	0.0	0.0	0.0	0.0	0.0
FE	0.0	0.144	0.201	0.0	0.0
FE03	0.0	0.0	0.0	0.0	0.0
FE04	26.358	3.293	3.317	3.285	3.702
VM	0.051	0.053	0.060	0.068	0.063
VM1	2.245	2.447	2.437	2.380	2.238
CA	0.189	0.192	0.196	0.193	0.221
MA	0.0	0.0	0.0	0.0	0.0
K	0.0	0.0	0.0	0.0	0.0
TOTAL ICNS	18.655	16.072	16.191	15.999	16.110
X-FE	0.5684	0.5841	0.5936	0.5959	0.5983
FE03	2.3472	2.5028	2.6052	3.1502	2.7480
FE04	1.3172	1.4045	1.4619	1.4923	1.6443
MG/FE	0.7592	0.7120	0.6840	0.5819	0.6045
X-AL-CPW	0.0	0.0	0.0	0.0	0.0
X-AL-TL	0.0	0.0	0.0	0.0	0.0
X-AL-MI	0.0	0.0	0.0	0.0	0.0
X-MG-MI	0.4167	0.3992	0.3894	0.3201	0.3595
X-FE-MI	0.5452	0.5607	0.5693	0.6377	0.5948
X-CA-MI	0.0307	0.0314	0.0316	0.0312	0.0355
X-MG-M2	0.0	0.0	0.0	0.0	0.0
X-FE-M2	0.0	0.0	0.0	0.0	0.0
X-CA-M2	0.0	0.0	0.0	0.0	0.0
A-INSTITUTE	0.0	0.0	0.0	0.0	0.0
A-TREMLIT	0.0	0.0	0.0	0.0	0.0
X-ANORIT	0.0	0.0	0.0	0.0	0.0
X-ALBITE	0.0	0.0	0.0	0.0	0.0

TABLE 24 (cont.)

	81	82	83	84	85
TOTAL	59.18	59.36	59.06	59.11	59.52
NO OXYGENS	24.	24.	24.	24.	24.
Si	5.710	5.885	5.918	5.895	5.957
Ti	0.001	0.004	0.0	0.002	0.001
Al	3.995	3.980	3.978	3.961	3.956
Ca	0.0	0.0	0.0	0.0	0.0
Fe	0.0	0.241	0.0	0.0	0.0
Mg	3.508	3.414	3.623	3.702	4.145
Mn	0.051	0.050	0.058	0.065	0.081
Na	2.427	2.314	2.319	2.294	1.651
K	0.198	0.204	0.135	0.203	0.217
TOTAL	16.031	16.040	16.093	16.122	16.064
X-FE	0.5711	0.5973	0.6097	0.6174	0.7097
FE/MG	2.5756	2.6426	2.7838	2.8751	3.3564
FE/MG	1.4434	1.5878	1.5627	1.6131	1.8447
MG/FE	0.6719	0.6743	0.6401	0.6198	0.6091
X-AL-CPX	0.0	0.0	0.0	0.0	0.0
X-AL-FET	0.0	0.0	0.0	0.0	0.0
X-AL-VI	0.0	0.0	0.0	0.0	0.0
X-MG-M	0.3925	0.3701	0.3743	0.3663	0.2760
X-PE-M	0.5673	0.5876	0.5848	0.5910	0.6746
X-CA-M	0.0220	0.0328	0.0315	0.0324	0.0354
X-MG-M2	0.0	0.0	0.0	0.0	0.0
X-FE-M2	0.0	0.0	0.0	0.0	0.0
X-CA-M2	0.0	0.0	0.0	0.0	0.0
A-EMSA-TIT	0.0	0.0	0.0	0.0	0.0
A-TRE-AL-TIT	0.0	0.0	0.0	0.0	0.0
X-ANG-TIT	0.0	0.0	0.0	0.0	0.0
X-ALBITE	0.0	0.0	0.0	0.0	0.0





















TABLE 6.10

	1	2	3	4	5
TI D2	39.01	40.50	40.10	40.21	39.66
AL 2C 2	0.01	0.01	0.03	0.01	0.02
CR 2U 2	22.60	22.90	22.71	22.50	22.36
FE 2L 2	0.0	0.0	0.0	0.0	0.0
FE 2J	0.0	0.59	0.88	0.72	0.0
MNO	23.16	22.19	20.90	21.04	21.03
MGO	0.07	0.04	0.04	0.02	0.04
CAO	12.26	13.77	14.73	14.92	15.11
NA 2J	2.05	1.52	0.92	0.91	0.95
K 2J	0.0	0.0	0.0	0.0	0.0
TOTAL MIX	100.40	101.51	100.31	99.85	99.37
NO OXYGENS	24.	24.	24.	24.	24.
SI	5.955	5.975	5.946	5.984	5.902
TI	0.001	0.001	0.003	0.001	0.002
AL	1.006	3.983	3.970	3.949	3.943
CR	0.0	0.0	0.0	0.0	0.0
FE	0.081	0.066	0.038	0.081	0.023
FL	2.973	2.732	2.592	2.550	2.631
MN	0.009	0.005	0.005	0.003	0.005
MG	2.747	3.027	3.255	3.309	3.369
CA	0.330	0.240	0.146	0.145	0.152
NA	0.0	0.0	0.0	0.0	0.0
K	0.0	0.0	0.0	0.0	0.0
TOTAL IONS	16.041	16.033	16.010	15.040	16.004
X-FE	0.5214	0.4807	0.4432	0.4447	0.4385
FE/4M	1.7113	1.5492	1.4190	1.4263	1.3918
FE/MG	1.0594	0.9255	0.7363	0.8009	0.7810
MG/FE	0.9130	1.0805	1.2558	1.2489	1.2804
X-AL-LPX	0.0	0.0	0.0	0.0	0.0
X-AL-TLT	0.0	0.0	0.0	0.0	0.0
X-AL-MI	0.0	0.0	0.0	0.0	0.0
X-MG-MI	0.4519	0.4984	0.5427	0.5419	0.5471
X-FE-MI	0.4923	0.4612	0.4321	0.4339	0.4273
X-CA-MI	0.0543	0.0396	0.0244	0.0239	0.0247
X-MG-M2	0.0	0.0	0.0	0.0	0.0
X-FE-42	0.0	0.0	0.0	0.0	0.0
X-CA-42	0.0	0.0	0.0	0.0	0.0
A-ENSTATITE	0.0	0.0	0.0	0.0	0.0
A-THEMULITE	0.0	0.0	0.0	0.0	0.0
A-TRIPHYLITE	0.0	0.0	0.0	0.0	0.0
X-ALBITE	0.0	0.0	0.0	0.0	0.0

TABLE 2 (cont.)

	6	7	8	9	10
SiO2	40.58	40.55	40.44	40.65	40.63
TiO2	0.02	0.02	0.00	0.01	0.01
Al2O3	22.62	22.62	22.60	22.91	22.67
CaO	0.00	0.00	0.00	0.00	0.00
FeO	0.00	0.00	0.00	0.00	0.00
MgO	20.47	20.47	21.84	21.32	21.45
MnO	0.02	0.02	0.03	0.04	0.01
K2O	15.15	14.93	14.22	14.54	14.80
Na2O	1.05	1.05	1.05	1.13	1.13
Sum	0.00	0.00	0.00	0.00	0.00
TOTAL Wt	100.49	100.55	100.64	101.07	100.75
NO OXYGENS	44	24	24	24	24
Si	5.984	5.984	5.995	5.983	5.982
Ti	0.002	0.002	0.000	0.001	0.001
Al	3.932	3.932	3.960	3.978	3.945
Ca	0.000	0.000	0.000	0.000	0.000
Fe	0.000	0.000	0.000	0.000	0.000
Mg	2.600	2.654	2.757	2.670	2.688
Mn	0.003	0.008	0.004	0.003	0.001
K	3.334	3.297	3.138	3.192	3.252
Na	0.166	0.150	0.167	0.189	0.175
Sum	0.000	0.000	0.000	0.000	0.000
TOTAL CGS	16.036	16.030	16.045	16.022	16.010
X-FE	0.4281	0.4467	0.4674	0.4554	0.4485
FE/MG	1.3894	1.4187	1.5640	1.4904	1.4493
MG/FE	1.2825	0.8074	0.8777	0.9364	0.8133
X-AL-CPX	0.00	0.00	0.00	0.00	0.00
X-AL-TFT	0.00	0.00	0.00	0.00	0.00
X-AL-M1	0.00	0.00	0.00	0.00	0.00
X-MG-M1	0.5464	0.5348	0.5176	0.5172	0.5310
X-FE-M1	0.4260	0.4351	0.4543	0.4403	0.4308
X-CA-M1	0.0272	0.0247	0.0275	0.0210	0.0294
X-MG-M2	0.00	0.00	0.00	0.00	0.00
X-FE-M2	0.00	0.00	0.00	0.00	0.00
X-CA-M2	0.00	0.00	0.00	0.00	0.00
A-ENSURE II	0.00	0.00	0.00	0.00	0.00
A-TRENTH II	0.00	0.00	0.00	0.00	0.00
A-ANDRTH II	0.00	0.00	0.00	0.00	0.00
A-ALBITE	0.00	0.00	0.00	0.00	0.00

TABLE 2 (cont.)

	11	12	13	14	15
SiO2	40.22	40.58	39.75	39.77	39.15
Al2O3	0.02	0.04	0.02	0.01	0.01
Fe2O3	22.86	23.16	23.05	23.26	23.38
FeO	0.0	0.0	0.0	0.0	0.0
MnO	21.44	21.00	20.42	21.44	20.40
MgO	3.04	0.03	0.05	0.03	0.03
CaO	14.84	14.88	14.86	14.94	14.73
Na2O	1.05	0.97	0.89	0.91	0.70
K2O	0.0	0.0	0.0	0.0	0.0
TOTAL	100.56	101.18	100.25	100.50	100.32
NO OXIGENS	24	24	24	24	24
Si	5.953	5.954	5.893	5.878	5.814
Ti	0.002	0.004	0.002	0.001	0.001
Al	3.990	4.011	4.029	4.030	4.093
CR	0.0	0.0	0.0	0.0	0.0
Fe	0.056	0.057	0.135	0.131	0.20
Fe**	2.554	2.577	2.532	2.532	2.534
Mn	0.005	0.004	0.006	0.005	0.004
Mg	3.274	3.254	3.281	3.310	3.274
Ca	0.167	0.153	0.141	0.144	0.121
Na	0.0	0.0	0.0	0.0	0.0
K	0.0	0.0	0.0	0.0	0.0
TOTAL IONS	16.048	16.010	16.023	16.015	16.034
Al-AL	0.477	0.4474	0.4354	0.4313	0.4373
Fe-Fe	1.487	1.4115	1.3742	1.3330	1.330
Mg-Mg	3.2107	3.254	3.281	3.310	3.2773
Ca-Ca	1.2234	1.2750	1.2967	1.3167	1.2865
X-AL-CPX	0.0	0.0	0.0	0.0	0.0
X-AL-TET	0.0	0.0	0.0	0.0	0.0
X-AL-41	0.0	0.0	0.0	0.0	0.0
X-MG-41	0.5307	0.5435	0.5500	0.5407	0.5503
X-FE-41	3.4351	3.4305	3.4246	3.442	3.428
X-CA-41	0.6273	0.6252	0.6237	0.6235	0.6204
X-MG-M2	0.0	0.0	0.0	0.0	0.0
X-FE-42	0.0	0.0	0.0	0.0	0.0
X-CA-42	0.0	0.0	0.0	0.0	0.0
A-ENSTAI II	0.0	0.0	0.0	0.0	0.0
A-TREMIL II	0.0	0.0	0.0	0.0	0.0
X-ANORT II	0.0	0.0	0.0	0.0	0.0
X-ALEITE	0.0	0.0	0.0	0.0	0.0



TABLE 2.10 (cont.)

	10	17	18	19	20
SI	39.73	39.29	39.88	33.24	40.19
TI	0.01	0.02	0.01	0.01	0.01
AL	22.93	23.05	23.06	23.09	23.28
CR	0.0	0.0	0.0	0.0	0.0
FE	0.0	1.27	0.98	2.175	0.75
MN	21.68	22.25	22.21	22.21	20.01
Mg	0.02	0.03	0.04	0.05	0.02
CA	14.10	13.55	12.44	13.24	14.35
NA	0.79	0.89	1.97	1.03	1.05
K	0.0	0.0	0.0	0.0	0.0
TOTAL MIX	99.07	100.35	96.59	100.73	101.04
NO OXYGENS	24.	24.	24.	24.	24.
SI	5.926	5.872	5.872	5.875	5.922
TI	0.001	0.002	0.001	0.001	0.001
AL	4.034	4.073	4.106	4.085	4.051
CR	0.0	0.0	0.0	0.0	0.0
FE	0.080	0.143	0.111	0.102	0.073
MN	2.705	2.781	2.805	2.783	2.733
Mg	0.003	0.004	0.005	0.005	0.003
CA	3.136	3.027	2.800	3.762	3.156
NA	0.126	0.143	0.319	0.169	0.166
K	0.0	0.0	0.0	0.0	0.0
TOTAL IONS	16.013	16.024	16.019	16.081	16.021
X-FE	0.4704	0.4780	0.5008	0.5019	0.4963
FE/MG	1.5830	1.6324	1.7851	1.7945	1.7429
MG/FE	0.8883	0.9216	1.0018	1.0071	0.8758
WGT/FE	1.1257	1.0650	0.9982	1.0330	1.1550
Zr-AL-CPH	0.0	0.0	0.0	0.0	0.0
X-AL-TE	0.0	0.0	0.0	0.0	0.0
X-AL-MI	0.0	0.0	0.0	0.0	0.0
X-MG-AL	0.5183	0.5076	0.4723	0.4940	0.5210
X-FE-AL	0.4604	0.4678	0.4731	0.4873	0.4511
X-CA-AL	0.0209	0.0234	0.0528	0.0276	0.0274
X-MG-M2	0.0	0.0	0.0	0.0	0.0
X-FE-M2	0.0	0.0	0.0	0.0	0.0
X-CA-M2	0.0	0.0	0.0	0.0	0.0
A-EMSAITIT	0.0	0.0	0.0	0.0	0.0
A-TREMILIT	0.0	0.0	0.0	0.0	0.0
X-ANCIPTIT	0.0	0.0	0.0	0.0	0.0
X-ALEITE	0.0	0.0	0.0	0.0	0.0

TABLE 2 (continued)

	21	22	23	24	25
SI-2	40.21	40.70	40.66	40.72	39.47
AL-203	0.03	0.01	0.02	0.03	0.00
PR-203	23.02	22.71	23.02	22.93	22.22
FE-203	0.00	0.00	0.00	0.00	0.00
FE-203	0.00	0.00	0.00	0.00	0.00
FE-203	21.53	21.56	21.35	21.15	27.52
FM-203	0.03	0.02	0.03	0.04	0.09
MO-203	14.49	14.22	14.03	14.20	9.84
CA-203	1.05	1.30	1.04	1.02	1.53
NA-203	0.00	0.00	0.00	0.00	0.00
K-203	0.00	0.00	0.00	0.00	0.00
TOTAL MIN	100.06	100.51	101.04	101.27	100.67
NO OXYGENS	24.	24.	24.	24.	24.
SI	5.551	6.022	5.978	5.995	6.010
TI	0.003	0.001	0.002	0.003	0.000
AL	4.016	3.961	3.990	3.980	3.988
PR	0.00	0.00	0.00	0.00	0.00
FE	0.00	0.00	0.00	0.00	0.00
FM	2.702	2.668	2.605	2.750	3.504
AN	0.004	0.003	0.004	0.005	0.012
MO	3.191	3.136	3.208	3.116	2.233
CA	0.166	0.206	0.164	0.161	0.250
NA	0.00	0.00	0.00	0.00	0.00
K	0.00	0.00	0.00	0.00	0.00
TOTAL IONS	16.019	15.790	16.006	16.011	15.956
X-FE	0.4581	0.4604	0.4503	0.4589	0.4108
FE/AL	1.2066	1.5162	1.4597	1.5001	0.7987
FE/MO	0.8217	0.8532	0.8191	0.8725	1.5654
MG/FE	1.1828	1.1721	1.2036	1.1332	0.6372
2-X-AL-LPX	0.00	0.00	0.00	0.00	0.00
X-AL-TE	0.00	0.00	0.00	0.00	0.00
X-AL-41	0.00	0.00	0.00	0.00	0.00
X-MO-41	0.5333	0.5216	0.5344	0.5165	0.3719
X-FE-41	0.4382	0.4444	0.4377	0.4559	0.5047
X-CA-41	0.0278	0.0342	0.0273	0.0267	0.0416
X-MO-42	0.00	0.00	0.00	0.00	0.00
X-FE-42	0.00	0.00	0.00	0.00	0.00
X-CA-42	0.00	0.00	0.00	0.00	0.00
A-ENSTALIT	0.00	0.00	0.00	0.00	0.00
A-TREAJLIT	0.00	0.00	0.00	0.00	0.00
X-ANGREMIT	0.00	0.00	0.00	0.00	0.00
W-ALEITE	0.00	0.00	0.00	0.00	0.00

TABLE 2 (cont.)

	26	27	28	29	30
ALD2	0.33	40.09	40.55	40.83	41.31
ALD2C	0.0	0.01	0.01	0.02	0.03
CR2U	22.64	22.40	22.52	22.55	23.05
FE2U	0.0	0.0	0.0	0.0	0.0
FE2	0.0	0.0	0.0	0.0	0.0
FE1	23.61	22.35	23.79	22.5	21.92
WNG	0.07	0.04	0.04	0.0	0.03
BUO	12.40	13.32	12.48	13.32	14.51
CAJ	1.85	1.37	1.49	1.25	0.87
CAZ	0.0	0.0	0.0	0.0	0.0
K2C	0.0	0.0	0.0	0.0	0.0
TOTAL MIA	108.32	99.58	100.84	100.72	101.74
NO OXYGENS	24.	24.	28.	24.	24.
SI	6.030	6.019	6.048	6.050	6.033
SI	0.0	0.001	0.001	0.002	0.003
AL	3.951	3.965	3.960	3.961	3.966
EM	0.0	0.0	0.0	0.0	0.0
FE1A	0.052	0.005	0.043	0.007	0.081
FE1B	2.878	2.806	2.965	2.794	2.677
FE1C	0.009	0.005	0.005	0.003	0.004
FE1D	2.763	2.980	2.771	2.753	3.158
FE1E	0.303	0.220	0.238	0.191	0.136
CA	0.0	0.0	0.0	0.0	0.0
CA	0.0	0.0	0.0	0.0	0.0
TOTAL IUNS	15.974	15.997	15.993	15.967	15.980
X-PE	0.5101	0.4950	0.5204	0.5301	0.4623
FEC/MAX	1.8556	1.6779	1.8338	1.8558	1.5107
FLAMU	1.0413	0.9418	1.0352	1.0453	0.8477
MG/CFE	3.9003	1.0620	0.3348	0.0572	1.1752
X-AL-CP*	0.0	0.0	0.0	0.0	0.0
X-AL-TET	0.0	0.0	0.0	0.0	0.0
X-AL-41	0.0	0.0	0.0	0.0	0.0
X-MG-41	0.4632	0.4957	0.4602	0.4961	0.5285
X-PE-41	0.634	0.669	0.694	0.693	0.481
X-CA-41	0.0509	0.0367	0.0395	0.0333	0.0228
X-MG-M2	0.0	0.0	0.0	0.0	0.0
X-PE-M-	0.0	0.0	0.0	0.0	0.0
X-CA-42	0.0	0.0	0.0	0.0	0.0
A-INSTAITY	0.0	0.0	0.0	0.0	0.0
A-TREMOLITE	0.0	0.0	0.0	0.0	0.0
X-ANORTHITE	0.0	0.0	0.0	0.0	0.0
X-ALBITE	0.0	0.0	0.0	0.0	0.0



TABLE 2 (cont.)

	36	37	58	59	40
1-2	39.41	40.07	39.50	40.44	40.50
1-02	0.01	0.01	0.0	0.0	0.0
AL4CC	22.46	22.38	22.37	22.67	22.75
AR203	0.0	0.0	0.0	0.0	0.0
FE2O3	0.0	0.63	0.57	0.0	0.34
VEN	21.54	22.01	22.50	21.52	20.97
WNO	0.04	0.07	0.0	0.0	0.04
WGO	13.92	13.92	12.71	14.45	14.65
WCO	0.87	1.03	2.11	1.33	1.39
WZC	0.0	0.0	0.0	0.0	0.0
WZC	0.0	0.0	0.0	0.0	0.0
TOTAL MIX	59.18	100.12	99.10	100.43	100.31
NO EXGENS	24.	24.	24.	24.	24.
FE	5.946	5.982	5.965	5.993	5.955
TI	0.001	0.001	0.0	0.001	0.001
AL	3.995	3.939	3.983	3.961	3.970
AR	0.0	0.0	0.0	0.0	0.0
FE2O3	0.112	0.071	0.007	0.0	0.038
VEN	2.830	2.748	2.728	2.697	2.596
WNO	0.005	0.009	0.012	0.001	0.005
WGO	3.131	3.097	2.861	3.111	3.229
WCO	0.141	0.165	0.341	0.231	0.220
WZC	0.0	0.0	0.0	0.0	0.0
WZC	0.0	0.0	0.0	0.0	0.0
TOTAL TUNLS	16.056	16.012	15.011	16.015	16.010
X-FE	0.4741	0.4701	0.4932	0.4553	0.4454
FE/MINO	1.6067	1.5812	1.7362	1.4893	1.4314
VE/MG	0.9016	0.8873	0.9731	0.8357	0.8033
WC/FE	1.1091	1.1270	1.1274	1.1938	1.2285
J-X-A-CPR	0.0	0.0	0.0	0.0	0.0
X-AL-FET	0.0	0.0	0.0	0.0	0.0
X-AL-72	0.0	0.0	0.0	0.0	0.0
X-MG-41	0.5133	0.5146	0.4718	0.5257	0.5339
X-FL-41	0.4628	0.4566	0.4622	0.4393	0.4257
X-CA-41	0.0230	0.0271	0.0563	0.0348	0.0364
X-MG-42	0.0	0.0	0.0	0.0	0.0
X-FL-42	0.0	0.0	0.0	0.0	0.0
X-CA-42	0.0	0.0	0.0	0.0	0.0
A-ENSTAI II	0.0	0.0	0.0	0.0	0.0
A-TRENOLI II	0.0	0.0	0.0	0.0	0.0
X-ANCRIF II	0.0	0.0	0.0	0.0	0.0
X-ALBITE	0.0	0.0	0.0	0.0	0.0

TABLE 2 (cont.)

	43	44	45
SI	39.86	39.95	40.30
TI	0.01	0.01	0.02
AL	22.64	22.57	22.76
CR	0.00	0.00	0.00
FE	0.00	0.00	1.00
MN	21.27	21.80	22.23
MG	0.05	0.05	0.04
CA	14.06	13.54	14.62
NA	1.29	1.53	0.58
K	0.00	0.00	0.00
TOTAL	99.91	100.00	100.00
CHXGENS	24.	24.	24.
SI	5.959	5.763	5.957
TI	0.001	0.001	0.001
AL	3.930	3.971	3.982
CR	0.00	0.00	0.00
FE	0.00	0.00	0.091
MN	2.750	1.945	2.655
MG	0.006	0.006	0.006
CA	3.132	3.021	3.223
NA	0.207	0.245	0.155
K	0.00	0.00	0.00
TOTAL	16.045	16.051	16.057
IONS	16.	16.017	16.019
X-FE	0.4672	0.4951	0.4602
FE/MG	1.5667	0.789	1.5145
MG/FE	0.6781	0.7422	0.6617
2-X-AL-CPX	1.1384	1.0614	1.1728
X-AL-TL	0.00	0.00	0.00
X-AL-M1	0.00	0.00	0.00
X-MG-V1	0.5139	0.4939	0.5257
X-FE-M1	0.4512	0.4052	0.4482
X-CA-V1	0.0339	0.0400	0.0253
X-MG-M2	0.00	0.00	0.00
X-FE-M2	0.00	0.00	0.00
X-CA-M2	0.00	0.00	0.00
1-ENSTATT	0.00	0.00	0.00
A-TREMLIT	0.00	0.00	0.00
X-ANCRIT	0.00	0.00	0.00
X-ALEITE	0.00	0.00	0.00

TABLE 2 (cont.)

	46	47	48	49	50
SI	40.04	40.20	40.54	40.23	40.45
TI	0.01	0.0	0.01	0.01	0.01
AL	22.87	22.63	22.74	22.75	22.84
CR	0.0	0.0	0.0	0.0	0.0
FE	0.97	0.32	0.60	0.07	0.97
MN	20.50	21.13	20.81	20.73	20.57
MG	0.01	0.05	0.03	0.01	0.07
CA	14.83	13.86	14.97	13.22	15.65
NA	1.02	1.82	0.96	0.90	0.94
K	0.0	0.0	0.0	0.0	0.0
TOTAL	100.21	99.98	100.60	100.37	100.57
MC	24.	24.	24.	24.	24.
SI	5.94	5.98	5.96	5.95	5.98
TI	0.001	0.0	0.001	0.001	0.001
AL	4.002	3.977	3.955	3.970	3.965
CR	0.0	0.0	0.0	0.0	0.0
FE	0.108	0.036	0.000	0.118	0.07
MN	2.653	2.671	2.637	2.623	2.633
MG	0.001	0.006	0.004	0.001	0.005
CA	3.281	3.080	3.234	3.257	3.435
NA	0.172	0.291	0.152	0.152	0.148
K	0.0	0.0	0.0	0.0	0.0
TOTAL	11.954	16.018	16.033	16.050	16.034
X-FE	1.4471	0.4045	0.4245	0.4385	0.4139
FE/4MO	1.4410	1.5455	1.4252	1.3722	1.3144
FE/MG	0.8085	0.8673	0.8003	0.7913	0.7703
MG/FE	1.2366	1.1531	1.2495	1.2799	1.3859
X-AL-CR	0.0	0.0	0.0	0.0	0.0
X-AL-FE	0.0	0.0	0.0	0.0	0.0
X-AL-MN	0.0	0.0	0.0	0.0	0.0
X-MG-MN	0.5372	0.5092	0.5112	0.5173	0.5008
X-AL-MN	0.4344	0.4416	0.4332	0.4275	0.4136
X-AL-AL	0.0281	0.0481	0.0250	0.0348	0.0242
X-MU-AL	0.0	0.0	0.0	0.0	0.0
X-FE-MN	0.0	0.0	0.0	0.0	0.0
X-CA-MN	0.0	0.0	0.0	0.0	0.0
A-ENSTALIT	0.0	0.0	0.0	0.0	0.0
A-TREMILIT	0.0	0.0	0.0	0.0	0.0
X-ANDRIMIT	0.0	0.0	0.0	0.0	0.0
X-ALBITE	0.0	0.0	0.0	0.0	0.0

TABLE 2 (cont.)

	51	52	53	54	55
SI/2	16.95	39.43	39.91	39.13	38.06
TI/2	0.01	0.02	0.01	0.01	0.02
AL2O3	22.98	22.32	22.71	21.69	21.97
CR2O3	0.0	0.0	0.0	0.0	0.0
FE2O3	0.70	1.30	0.19	0.80	0.77
MNO	0.04	19.95	20.94	18.54	19.81
MGO	15.56	14.88	14.22	12.23	14.01
CaO	0.97	1.00	1.18	1.92	1.27
NA2O	0.0	0.0	0.0	0.0	0.0
K2O	0.0	0.0	0.0	0.0	0.0
TOTAL #18	101.21	98.90	99.16	97.41	97.19
NO OXYGENS	24.	24.	24.	24.	24.
SI	5.922	5.942	5.979	5.957	5.873
TI	0.001	0.002	0.001	0.001	0.002
AL	3.902	3.953	4.013	3.994	3.976
CR	0.0	0.0	0.0	0.0	0.0
FE	0.060	0.147	0.021	0.041	0.031
FE**	2.531	2.507	2.666	2.920	2.816
PE**	0.005	0.0	0.003	0.000	0.000
AN	2.351	3.331	3.176	2.847	3.222
AO	0.152	0.161	0.190	0.321	0.210
CA	0.0	0.0	0.0	0.0	0.0
NA	0.0	0.0	0.0	0.0	0.0
K	0.0	0.0	0.0	0.0	0.0
TOTAL IJNS	16.050	16.074	16.011	16.047	16.041
X-FE	0.274	0.434	0.545	0.5064	0.4664
FE/MGO	1.1303	1.4194	1.4727	1.9283	1.5575
CE/MG	0.7465	0.7365	0.8264	1.0260	0.8740
MG/FE	1.3395	1.2555	1.2004	0.9747	1.1442
Z-X-AL-CP*	0.0	0.0	0.0	0.0	0.0
X-AL-ICT	0.0	0.0	0.0	0.0	0.0
X-AL-MI	0.0	0.0	0.0	0.0	0.0
X-MG-MI	0.5570	0.5221	0.3201	0.4603	0.5153
X-FE-MI	0.4164	0.4178	0.4400	0.4780	0.4203
X-CA-MI	0.0250	0.0262	0.0315	0.0527	0.0336
X-MG-MZ	0.0	0.0	0.0	0.0	0.0
X-FE-42	0.0	0.0	0.0	0.0	0.0
X-CA-42	0.0	0.0	0.0	0.0	0.0
A-ENSIAI II	0.0	0.0	0.0	0.0	0.0
A-TREMJI II	0.0	0.0	0.0	0.0	0.0
X-ANCI TH I	0.0	0.0	0.0	0.0	0.0
X-ALEITE	0.0	0.0	0.0	0.0	0.0















TABLE 24

	feldspar	biotite	orthopyroxene	Garnet (R1B)	Garnet core		
SiO2	40.34	28.12	51.31	38.70	33.77	12.72	0.0
TiO2	0.0	3.09	0.12	0.02	0.00	0.00	0.0
Al2O3	34.87	17.54	3.33	22.85	17.35	11.38	0.0
Cr2O3	0.0	0.0	0.0	0.0	0.0	0.0	0.0
Fe2O3	0.0	0.0	1.07	0.0	0.0	0.0	0.0
MnO	0.29	0.0	22.36	25.84	15.62	18.72	0.0
MgO	0.0	11.29	0.11	0.30	0.51	2.42	0.0
CaO	0.0	0.0	22.03	9.21	7.89	2.33	0.0
Na2O	17.55	0.0	0.17	2.66	5.71	3.70	0.0
K2O	0.02	0.0	0.0	0.0	0.0	0.0	0.0
TOTAL OX	100.67	96.87	100.50	100.76	100.89	100.88	0.0
MG OXYGENS	32	32	6	24	24	24	0.0
Si	2.476	5.456	1.904	5.975	5.334	2.923	0.0
Ti	0.0	0.333	0.003	0.002	0.005	0.005	0.0
Al	7.519	2.959	0.146	4.061	4.040	4.333	0.0
Cr	0.0	0.0	0.0	0.0	0.0	0.0	0.0
Fe++	0.0	0.0	0.030	0.0	0.0	0.0	0.0
Fe++	0.0	0.0	0.694	3.342	3.253	1.479	0.0
Fe++	0.0	0.0	0.003	0.051	0.070	1.370	0.0
Mg	0.0	1.221	1.218	2.102	1.943	1.777	0.0
Ca	3.439	0.0	0.007	0.437	0.375	1.234	0.0
Na	0.587	0.0	0.0	0.0	0.0	0.0	0.0
K	0.005	1.832	0.0	0.0	0.0	0.0	0.0
TOTAL IONS	20.051	15.581	4.015	16.031	15.084	16.016	0.0
X-Fe	0.0	0.2021	0.3628	0.0202	0.6682	0.1332	0.0
Fe/Mg	0.0	0.0	1.0148	2.3142	3.2750	1.8712	0.0
Fe/Mg	0.0	0.0	0.0	1.6338	1.8103	1.2738	0.0
Mg/Fe	0.0	2.8158	0.0	0.6115	1.5524	1.1108	0.0
X-Al-GP*	0.0	0.0	0.0663	0.0	0.0	0.0	0.0
X-Al-TCT	0.0	0.0	0.0481	0.0	0.0	0.0	0.0
X-Al-M1	0.0	0.0	0.0495	0.0	0.0	0.0	0.0
X-Mg-M1	0.0	0.0	0.5847	0.3888	0.3054	1.0034	0.0
X-Fe-M1	0.0	0.0	0.0	0.5724	0.3773	3.4320	0.0
X-Ca-M1	0.0	0.0	0.0	0.0724	0.0525	0.0000	0.0
X-Mg-M2	0.0	0.0	0.6307	0.0	0.0	0.0	0.0
X-Fe-M2	0.0	0.0	0.3591	0.0	0.0	0.0	0.0
X-Ca-M2	0.0	0.0	0.0068	0.0	0.0	0.0	0.0
X-Enstatite	0.0	0.0	0.3345	0.0	0.0	0.0	0.0
X-Tremolite	0.0	0.0	0.0	0.0	0.0	0.0	0.0
X-Anorthite	0.0	0.0	0.0	0.0	0.0	0.0	0.0
X-Albite	0.1344	0.0	0.0	0.0	0.0	0.0	0.0





TABLE 2 is (cont.)

	Garnet 1	Garnet 2	Garnet 3	Garnet 4	Garnet 5
SiO2	39.27	39.08	37.06	38.27	37.64
TiO2	0.03	0.05	0.02	0.03	3.95
Al2O3	21.85	21.73	21.20	21.89	15.68
Cr2O3	0.0	0.0	0.0	0.0	0.0
Fe2O3	0.0	0.0	0.0	0.0	0.0
FEO	25.95	24.96	20.85	25.72	12.19
MnO	0.54	0.53	0.53	0.54	0.03
MgO	8.52	8.49	8.95	8.58	16.39
CaO	4.32	5.11	3.51	4.32	0.0
Na2O	0.0	0.0	0.0	0.0	0.0
K2O	0.0	0.0	0.0	0.0	8.36
TOTAL WT%	100.52	99.99	100.72	100.61	94.60
NO OXYGENS	24.	24.	24.	24.	24.
Si	6.008	6.008	5.933	6.004	5.556
Ti	0.003	0.006	0.002	0.003	0.429
Al	3.946	3.936	3.976	3.946	2.726
Cr	0.0	0.0	0.0	0.0	0.0
Fe	0.029	0.034	0.032	0.029	0.0
Fe++	3.289	3.173	3.941	3.289	1.505
Fe+++	0.070	0.059	0.033	0.070	0.004
Mn	1.955	1.944	2.079	1.955	3.539
Mg	0.708	0.741	0.849	0.708	0.0
Ca	0.0	0.0	0.0	0.0	0.086
Na	0.0	0.0	0.0	0.0	1.574
K	0.0	0.0	0.0	0.0	0.0
TOTAL IONS	16.014	16.017	16.076	16.005	12.426
X-Fe	0.6293	0.6226	0.6203	0.6272	0.2983
FeO/MgO	1.0245	2.9399	2.9106	2.9382	0.0
Fe/Mg	1.6272	1.6438	1.6333	1.6225	0.0
Mg/Fe	0.5892	0.6061	0.6122	0.5944	2.3521
2-X-AL-OPR	0.0	0.0	0.0	0.0	0.0
X-AL-TEF	0.0	0.0	0.0	0.0	0.0
X-AL-41	0.0	0.0	0.0	0.0	0.0
X-MG-41	0.3231	0.3207	0.3182	0.3246	0.0
X-Fe-41	0.5484	0.5291	0.5224	0.5462	0.0
X-CA-M1	0.1170	0.1388	0.0753	0.1175	0.0
X-MG-M2	0.0	0.0	0.0	0.0	0.0
X-Fe-42	0.0	0.0	0.0	0.0	0.0
X-CA-42	0.0	0.0	0.0	0.0	0.0
A-ENSTATT	0.0	0.0	0.0	0.0	0.0
A-THEMLIT	0.0	0.0	0.0	0.0	0.0
X-ANJHMIT	0.0	0.0	0.0	0.0	0.0
X-ALBITE	0.0	0.0	0.0	0.0	0.0

TABLE 4.15 (cont.)

	Garnet 5	Garnet 6	Garnet 7	Garnet 8	Garnet 9
SiO2	38.02	38.83	38.77	38.71	37.90
TiO2	0.03	0.02	0.01	0.02	0.02
Al2O3	21.37	21.65	21.74	21.32	21.47
Cr2O3	0.0	0.0	0.0	0.0	0.0
FeO	0.83	0.34	0.25	0.39	1.14
MnO	26.45	26.06	26.41	26.16	24.19
MgO	0.52	0.27	0.48	0.41	0.67
CaO	7.22	8.7	8.4	7.33	3.0
Na2O	4.71	4.18	3.85	3.78	5.43
K2O	0.0	0.0	0.0	0.0	0.0
TOTAL Wt	99.13	99.71	99.47	99.38	98.51
NO. CRYSTALS	24	24	24	24	24
Si	5.570	6.000	5.997	5.993	5.944
Ti	0.004	0.002	0.001	0.002	0.004
Al	3.542	3.944	3.967	3.903	3.970
Cr	0.0	0.0	0.0	0.0	0.0
Fe	0.098	0.039	0.029	0.040	0.136
Mn	3.572	3.367	3.447	3.341	3.702
Mg	0.066	0.035	0.061	0.063	0.064
Ca	1.685	1.927	2.285	2.087	1.882
Na	0.791	0.692	0.439	0.524	0.870
K	0.0	0.0	0.0	0.0	0.0
TOTAL IONS	16.045	16.007	16.014	16.013	16.067
X-Fe	0.6789	0.6360	0.6275	0.6141	0.6769
Fe/Mg	3.7673	3.1130	2.9771	2.9371	3.1241
MUITE	2.1141	1.7463	1.6848	1.6041	1.7591
X-AL-OPK	0.0	0.0	0.0	0.0	0.0
X-AL-TLT	0.0	0.0	0.0	0.0	0.0
X-MU-MI	0.0	0.0	0.0	0.0	0.0
X-AL-MI	0.2701	0.3201	0.3384	0.3400	0.3014
X-AL-MI	0.5316	0.5591	0.5702	0.5659	0.5771
X-AL-MI	0.1295	0.1149	0.1013	0.1025	0.1229
X-MG-M2	0.0	0.0	0.0	0.0	0.0
X-AL-M2	0.0	0.0	0.0	0.0	0.0
X-AL-M2	0.0	0.0	0.0	0.0	0.0
A-ENSTAIIT	0.0	0.0	0.0	0.0	0.0
A-INEALIT	0.0	0.0	0.0	0.0	0.0
X-ANORIT	0.0	0.0	0.0	0.0	0.0
X-ALBITE	0.0	0.0	0.0	0.0	0.0



TABLE 2.14

	feldspar	hornblende	orthopyroxene	clinopyroxene	Magnet	
SiO <sub>2</sub>	46.29	42.54	49.12	43.12	17.03	17.03
TiO <sub>2</sub>	0.01	1.34	0.10	0.10	0.07	0.07
Al <sub>2</sub> O <sub>3</sub>	24.83	11.57	1.02	1.02	21.84	21.84
Cr <sub>2</sub> O <sub>3</sub>	0.0	0.0	0.0	0.0	0.0	0.0
Fe <sub>2</sub> O <sub>3</sub>	0.0	3.24	0.84	0.84	0.0	0.0
FeO	20.80	17.89	33.72	18.18	27.73	27.73
MnO	0.30	0.14	0.54	0.34	0.0	0.0
MgO	0.02	8.20	13.65	10.60	0.0	0.0
CaO	17.74	11.21	1.04	1.04	0.0	0.0
Na <sub>2</sub> O	1.21	1.11	0.0	0.0	0.0	0.0
K <sub>2</sub> O	0.04	1.01	0.01	0.01	0.0	0.0
TOTAL wt%	100.00	98.24	99.20	99.18	100.00	100.00
wt%	32.	23.	6.	6.	24.	24.
MO OXYGENS						
Si	6.480	6.427	1.961	1.981	3.914	3.914
Ti	0.001	0.152	0.003	0.003	0.003	0.003
Al	7.522	2.077	0.048	0.048	0.012	0.012
Cr	0.0	0.0	0.0	0.0	0.0	0.0
Fe <sup>3+</sup>	0.0	0.0	0.0	0.0	0.0	0.0
Fe <sup>2+</sup>	0.0	0.368	0.025	0.025	0.002	0.002
Mn	0.046	2.260	1.095	0.57	0.002	0.002
Mg	0.0	0.018	0.018	0.003	0.014	0.014
Ca	0.005	1.946	0.810	0.809	0.933	0.933
Na	2.482	1.915	0.044	0.485	1.524	1.524
K	0.009	0.325	0.0	0.12	0.0	0.0
TOTAL IONS	13.577	15.467	4.013	4.001	15.072	15.072
X-FE	0.0	0.0	0.5909	0.4288	0.0	0.0
FE/CA	0.0	0.0	2.4703	1.3779	0.0	0.0
MG/FE	0.0	0.0	0.0	0.0	0.0	0.0
2-X-AL-CPX	0.0	0.0	0.0206	0.0200	0.0	0.0
X-AL-TEY	0.0	0.0	0.0197	0.0095	0.0	0.0
X-AL-MI	0.0	0.0	0.0087	0.0095	0.0	0.0
X-MG-MI	0.0	0.0	0.4142	0.5552	0.0	0.0
X-FE-MI	0.0	0.0	0.0	0.0	0.0	0.0
X-LA-MI	0.0	0.0	0.0	0.0	0.0	0.0
X-MG-M2	0.0	0.0	0.3928	0.0537	0.0	0.0
X-FE-M2	0.0	0.0	0.5445	0.0403	0.0	0.0
X-CA-M2	0.0	0.0	0.0445	0.0403	0.0	0.0
X-ENSAT II	0.0	0.0	0.1564	0.0202	0.0	0.0
X-TREOL II	0.0	0.006349	0.0	0.0	0.0	0.0
X-ANORTHIT	0.0	0.0	0.0	0.0	0.0	0.0
X-ALBIT	0.1040	0.0	0.0	0.0	0.0	0.0

TABLE 2.18

	feldspar	hornblende	orthopyroxene	clinopyroxene	Garnet core	
SiO2	44.70	42.41	48.65	50.55	54.37	0.0
TiO2	0.05	1.40	0.13	0.13	0.00	0.0
Al2O3	32.44	10.64	1.04	1.50	0.00	0.0
Cr2O3	0.0	0.0	0.0	0.0	0.0	0.0
FeO	0.0	3.29	1.11	1.13	1.07	0.0
MnO	0.02	21.13	34.87	13.83	20.77	0.0
MgO	0.0	0.12	0.61	0.27	0.87	0.0
CaO	0.0	3.52	13.16	0.94	4.07	0.0
Na2O	18.67	11.63	0.82	1.30	0.89	0.0
K2O	0.0	1.01	0.0	0.31	0.00	0.0
TOTAL WT%	92.08	97.93	93.17	97.09	100.00	0.0
NO JAGGENS	23.	23.	0.	0.	0.	0.
Si	5.426	6.497	1.947	1.953	5.433	0.0
Ti	0.007	0.161	0.004	0.006	0.000	0.0
Al	7.431	1.922	0.049	0.072	3.775	0.0
Cr	0.0	0.0	0.0	0.0	0.0	0.0
Fe	0.0	0.376	0.334	0.335	0.127	0.0
Mn	0.006	2.309	1.124	0.427	3.758	0.0
Mg	0.023	0.015	0.021	0.009	0.084	0.0
Mg	0.0	1.929	0.786	0.522	3.057	0.0
Ca	0.0	1.894	0.035	0.873	3.562	0.0
Na	5.771	1.509	0.0	0.003	0.007	0.0
K	0.355	0.300	0.0	0.0	0.0	0.0
TOTAL IONS	20.025	15.603	4.017	4.304	15.023	0.0
X-FE	0.0	0.0	0.5874	0.4180	0.7336	0.0
Fe/Al	0.0	0.0	2.5584	1.2715	2.2790	0.0
Fe/Mg	0.0	0.0	0.0	0.0	3.0332	0.0
Mg/Fe	0.0	0.0	0.0	0.0	0.2712	0.0
2-X-AL-OPX	0.0	0.0	0.0210	0.0321	0.0	0.0
X-AL-TET	0.0	0.0	0.0254	0.0237	0.0	0.0
X-AL-MI	0.0	0.0	-0.0017	0.0249	0.0	0.0
X-MG-MI	0.0	0.0	0.1950	0.5640	0.1312	0.0
X-FE-MI	0.0	0.0	0.0	0.0	0.0057	0.0
X-CR-MI	0.0	0.0	0.0	0.0	0.0074	0.0
X-MG-M2	0.0	0.0	0.1874	0.0502	0.0	0.0
X-FE-M2	0.0	0.0	0.5562	0.3362	0.0	0.0
X-CR-M2	0.0	0.0	0.0352	0.0816	0.0	0.0
A-ENSIFIT	0.0	0.0	0.1458	0.0870	0.0	0.0
A-TREMOLIT	0.0	0.008380	0.0	0.0	0.0	0.0
X-ANJMTIT	0.0	0.0	0.0	0.0	0.0	0.0
X-ALBIT	0.0	0.0	0.0	0.0	0.0	0.0



TABLE 218

	Feldspar	hornblende	orthopyroxene	clinopyroxene 1	clinopyroxene 2	
Al <sub>2</sub> O <sub>3</sub>	55.55	40.50	49.51	50.04	50.07	0.0
FeO	0.0	2.29	0.10	0.24	0.22	0.0
Al <sub>2</sub> SiO <sub>5</sub>	28.58	12.25	0.96	0.41	0.69	0.0
SiO <sub>2</sub>	0.0	0.0	0.0	0.0	0.0	0.0
TiO <sub>2</sub>	0.0	0.0	1.11	0.69	1.10	0.0
CaO	0.0	3.09	31.23	14.47	14.51	0.0
MgO	0.25	17.08	0.0	0.0	0.0	0.0
MnO	0.0	0.11	0.52	0.22	0.31	0.0
FeO	0.0	0.50	0.0	0.0	0.0	0.0
TiO <sub>2</sub>	0.0	0.55	15.17	10.81	10.84	0.0
CaO	10.28	11.43	0.79	0.77	0.77	0.0
MgO	5.37	1.43	0.0	0.37	0.17	0.0
FeO	0.38	1.57	0.0	0.01	0.0	0.0
TOTAL	100.37	98.62	99.37	99.34	99.58	0.0
AL CALCIUMS	32.0	23.0	54.0	54.0	54.0	0.0
Si	15.971	6.223	1.358	1.021	1.021	0.0
Al	0.0	0.203	0.003	0.007	0.007	0.0
Al	0.048	3.203	0.045	0.101	0.074	0.0
Cr	0.0	0.0	0.0	0.0	0.0	0.0
Fe	0.0	0.352	0.033	0.0	0.0	0.0
Fe	0.0	0.0	1.030	0.3	0.427	0.0
Fe	0.0	2.182	0.007	0.007	0.010	0.0
Mn	0.0	0.017	0.017	0.019	0.021	0.0
Mg	0.0	1.930	0.392	0.851	0.817	0.0
Ca	1.973	1.854	0.033	0.851	0.817	0.0
Na	1.859	0.420	0.0	0.023	0.024	0.0
K	0.052	0.303	0.0	0.000	0.0	0.0
TOTAL IONS	15.581	15.857	4.016	4.024	4.005	0.0
X-Fe	0.0	0.0	0.5361	0.4200	0.4201	0.0
Fe/Mg	0.0	2.1246	2.0510	1.3392	1.3391	0.0
Fe/Mg	0.0	0.0	0.0	0.0	0.0	0.0
Mg/Fe	0.0	0.0	0.0	0.0	0.0	0.0
X-AL-UPR	0.0	0.0	0.0193	0.0495	0.0495	0.0
X-AL-TEY	0.0	0.0	0.0209	0.0361	0.0361	0.0
X-AL-MI	0.0	0.0	0.0030	0.00375	0.00375	0.0
X-MG-MI	0.0	0.0	0.4485	0.5462	0.5462	0.0
X-Fe-MI	0.0	0.0	0.0	0.0	0.0	0.0
X-CR-MI	0.0	0.0	0.0	0.0	0.0	0.0
X-MG-M2	0.0	0.0	0.4407	0.615	0.625	0.0
X-Fe-M2	0.0	0.0	0.5012	0.662	0.673	0.0
X-CA-M2	0.0	0.0	0.0335	0.0852	0.0852	0.0
A-ENSTAIIT	0.0	0.0	0.1883	0.00312	0.00312	0.0
A-TREMOLIT	0.0	0.003760	0.0	0.0	0.0	0.0
A-ANURITHI	0.0	0.0	0.0	0.0	0.0	0.0
X-ALBITE	0.5109	0.0	0.0	0.0	0.0	0.0
	0.4615	0.0	0.0	0.0	0.0	0.0









TABLE 2.20

	hornblende	hornblende	orthopyroxene	clinopyroxene	garnet
SiO <sub>2</sub>	40.86	41.16	50.29	50.72	37.74
TiO <sub>2</sub>	1.52	1.53	0.04	0.15	0.04
Al <sub>2</sub> O <sub>3</sub>	13.51	12.42	1.58	0.09	21.94
CR <sub>2</sub> O <sub>3</sub>	0.0	0.0	0.0	0.0	0.0
FE <sub>2</sub> O <sub>3</sub>	0.0	0.0	0.0	0.0	0.0
FEU	19.25	17.27	30.34	29.55	29.50
MNO	0.19	0.21	0.54	0.23	1.64
MGO	8.90	8.48	16.51	11.90	8.33
CaO	11.34	11.16	0.81	0.57	6.72
Mg <sub>2</sub> O	1.54	1.52	0.0	0.24	0.0
K <sub>2</sub> O	1.50	1.37	0.0	0.0	0.0
TOTAL	98.91	98.27	103.13	100.51	100.00
NO OXYGENS	23	23	0	0	24
Si	6.132	6.240	1.949	1.970	6.064
Ti	0.172	0.174	0.032	0.004	0.031
Al	2.392	2.220	0.072	0.004	2.000
Cr	0.0	0.0	0.0	0.0	0.0
Fe <sup>++</sup>	0.318	0.356	0.0	0.0	0.0
Fe <sup>+++</sup>	2.075	2.190	0.933	0.800	0.774
Mn	0.024	0.027	0.018	0.010	0.218
Mg	2.007	1.931	0.933	0.877	1.012
Ca	1.838	1.827	0.034	0.040	1.129
Mg/Fe	0.452	0.456	0.0	0.010	0.0
K	0.290	0.267	0.0	0.0	0.0
TOTAL IONS	15.811	15.657	4.013	4.004	16.001
X-FE	0.0	0.0	0.5077	0.5011	0.7873
Y-AL	0.0	0.0	1.8377	1.7900	0.5058
Z-MG	0.0	0.0	0.0	0.0	1.7014
W-FE	0.0	0.0	0.0	0.0	0.0712
2-X-AL-GR	0.0	0.0	0.0315	0.0315	0.0
X-AL-TEY	0.0	0.0	0.0256	0.0277	0.0
K-AL-MI	0.0	0.0	0.0210	0.0167	0.0
K-MG-MI	0.0	0.0	0.4810	0.4768	0.1658
K-FE-MI	0.0	0.0	0.0	0.0	0.0554
K-CA-MI	0.0	0.0	0.0	0.0	0.1450
X-MG-M2	0.0	0.0	0.4664	0.4728	0.0
X-FE-M2	0.0	0.0	0.4810	0.4732	0.0
X-CA-M2	0.0	0.0	0.0336	0.0336	0.0
A-ENSIALII	0.0	0.0	0.2130	0.2131	0.0
A-THEMULII	0.000430	0.000490	0.0	0.0	0.0
K-ANORITHI	0.0	0.0	0.0	0.0	0.0
X-ALDITE	0.0	0.0	0.0	0.0	0.0

TABLE 2.2

	hornblende	orthopyroxene	orthopyroxene <	orthopyroxene 3	clinopyroxene
SiO2	45.05	53.19	54.49	54.53	57.41
TiO2	0.77	0.07	0.05	0.07	0.03
Al2O3	12.98	4.00	3.04	3.45	1.26
Cr2O3	0.0	0.0	0.0	0.0	0.0
FeO	0.50	1.11	0.94	0.24	0.21
MnO	5.79	10.34	10.70	11.23	0.05
MgO	0.07	0.23	0.27	0.23	15.97
CaO	16.58	29.81	30.35	30.21	24.97
Na2O	12.61	0.36	0.37	0.22	0.01
K2O	1.19	0.0	0.01	0.0	0.0
TOTAL	96.02	99.00	103.04	103.00	99.01
	23.	6.	6.	6.	6.
MOXIGENS					
Al	6.551	1.894	1.221	1.221	1.867
Ti	0.033	0.002	0.001	0.002	0.002
Al	2.201	0.168	0.124	0.143	0.052
Cr	0.0	0.0	0.0	0.0	0.0
Ca	0.057	0.030	0.022	0.024	0.106
Fe	0.598	0.304	0.315	0.307	0.114
Fe	0.009	0.007	0.003	0.007	0.007
Mn	3.546	1.582	1.593	1.515	0.877
Mg	1.554	0.014	0.014	0.014	0.014
Ca	1.939	0.001	0.001	0.001	0.001
Na	0.331	0.0	0.0	0.0	0.0
K	0.070	0.0	0.0	0.0	0.0
TOTAL	15.415	4.005	4.004	4.001	4.001
FEU/MG	0.0	0.1759	0.1748	0.1722	0.1355
FE/MG	0.0	0.3804	0.3776	0.3724	0.2706
MG/FE	0.0	0.0	0.0	0.0	0.0
AL-AL-CPX	0.0	0.0308	0.0509	0.0500	0.0253
AL-TET	0.0	0.0505	0.0377	0.0347	0.0162
AL-M1	0.0	0.0623	0.0511	0.0473	0.0223
M3-M1	0.0	0.7678	0.7824	0.7712	0.8630
FE-M1	0.0	0.0	0.0	0.0	0.0
CA-M1	0.0	0.0	0.0	0.0	0.0
M2	0.0	0.9070	0.9064	0.9133	0.8165
FE-42	0.0	0.1723	0.1709	0.1700	0.0072
CA-M2	0.0	0.0138	0.0140	0.0143	0.0088
ENSTATTIT	0.0	0.5587	0.5942	0.5717	0.5091
TREMOLIT	0.0222274	0.0	0.0	0.0	0.0
ANORTHIT	0.0	0.0	0.0	0.0	0.0
ALBIT	0.0	0.0	0.0	0.0	0.0



TABLE 12.

	26-5-A feldspar	26-5-A hornblende	26-5-A clinopyroxene	26-5-C feldspar	26-5-E feldspar	26-5-E hornblende	
SiO <sub>2</sub>	45.02	45.02	51.91	48.95	47.56	44.99	0.0
TiO <sub>2</sub>	0.90	0.90	0.12	0.02	0.0	1.16	0.0
Al <sub>2</sub> O <sub>3</sub>	10.09	10.09	2.06	12.16	13.57	5.14	0.0
Cr <sub>2</sub> O <sub>3</sub>	0.0	0.0	0.0	0.0	0.0	0.0	0.0
FeO	0.0	2.46	0.0	0.0	0.0	2.50	0.0
MgO	15.81	13.60	9.95	0.0	0.0	12.14	0.0
MnO	0.21	0.21	0.0	0.0	0.0	0.0	0.0
K <sub>2</sub> O	12.21	12.21	13.12	14.46	5.49	12.50	0.0
CaO	11.74	11.74	22.15	2.47	2.13	12.15	0.0
Na <sub>2</sub> O	1.41	1.41	0.40	0.12	0.06	1.00	0.0
K <sub>2</sub> O	0.75	0.75	0.0	0.12	0.06	1.10	0.0
TOTAL Wt	100.35	98.38	99.71	98.93	99.90	97.88	0.0
NO OXYGENS	32.	33.	32.	33.	32.	32.	0.
Si	5.097	6.631	1.951	9.012	4.730	5.707	0.0
Ti	0.0	0.100	0.003	0.003	0.0	0.130	0.0
Al	2.281	1.750	0.091	7.039	7.715	1.719	0.0
Cr	0.0	0.0	0.0	0.0	0.0	0.0	0.0
Fe <sup>++</sup>	0.0	0.273	0.0	0.0	0.0	0.245	0.0
Fe <sup>3+</sup>	0.030	1.675	0.313	0.072	0.015	1.505	0.0
Mn	0.0	0.026	0.0	0.0	0.0	0.018	0.0
Mg	0.0	2.680	0.735	2.855	3.249	2.777	0.0
Ca	2.283	1.853	0.492	1.855	0.751	2.930	0.0
Na	1.697	0.403	0.029	1.025	0.751	0.289	0.0
K	0.038	0.141	0.0	0.028	0.034	0.504	0.0
TOTAL IONS	20.035	15.530	4.015	19.701	20.074	15.553	0.0
X-FE	0.0	0.0	0.2785	0.0	0.0	0.0	0.0
FE/MG	0.0	0.0	0.6893	0.0	0.0	0.0	0.0
MG/FE	0.0	0.0	0.0	0.0	0.0	0.0	0.0
X-AL-CPX	0.0	0.0	0.0413	0.0	0.0	0.0	0.0
X-AL-TEY	0.0	0.0	0.0245	0.0	0.0	0.0	0.0
X-AL-M1	0.0	0.0	0.0423	0.0	0.0	0.0	0.0
X-MG-M1	0.0	0.0	0.6599	0.0	0.0	0.0	0.0
X-PL-M1	0.0	0.0	0.0	0.0	0.0	0.0	0.0
X-CA-M1	0.0	0.0	0.0	0.0	0.0	0.0	0.0
X-MG-M2	0.0	0.0	0.0553	0.0	0.0	0.0	0.0
X-PL-M2	0.0	0.0	0.0235	0.0	0.0	0.0	0.0
X-CA-M2	0.0	0.0	0.8920	0.0	0.0	0.0	0.0
X-ENSTAIITE	0.0	0.0	0.0352	0.0	0.0	0.0	0.0
X-TREMULITE	0.0	0.004824	0.0	0.0	0.0	0.000278	0.0
X-ANTHOPHILITE	0.0	0.0	0.0	0.0	0.0	0.0	0.0
X-ALBITE	0.4065	0.0	0.0	0.2511	0.0	0.0	0.0



TABLE 23

	hornblende 1	hornblende 2	hornblende 3	hornblende 4	clinopyroxene 1
SiO2	44.80	45.16	45.27	45.27	51.28
TiO2	1.03	1.02	0.99	0.93	0.03
Al2O3	5.44	5.16	5.55	5.27	2.01
CR2O3	0.0	0.0	0.0	0.0	0.0
Fe2O3	2.42	2.36	2.70	2.90	3.11
FeO	13.40	13.03	13.15	13.29	6.17
MnO	0.31	0.25	0.27	0.29	0.47
MgO	12.72	13.36	13.36	13.36	14.28
CaO	11.82	11.77	11.70	11.72	22.55
Na2O	1.16	1.09	1.17	1.11	0.77
K2O	0.89	0.66	0.68	0.68	0.0
TOTAL WGT	97.80	98.16	98.72	98.88	102.23
NO CRYSTALS	23	23	23	23	23
SI	6.637	6.643	6.667	6.670	14.915
TI	0.115	0.113	0.110	0.110	0.000
AL	1.659	1.641	1.650	1.640	0.088
CR	0.0	0.0	0.0	0.0	0.000
FE+++	0.270	0.261	0.245	0.245	0.100
FE++	1.542	1.603	1.893	1.895	0.287
MN	0.030	0.031	0.034	0.034	0.014
MU	2.827	2.929	2.933	2.934	0.795
CA	1.887	1.855	1.878	1.864	0.905
NA	0.335	0.311	0.334	0.333	0.227
K	0.131	0.124	0.124	0.122	0.000
TOTAL IONS	15.612	15.511	15.609	15.605	34.617
X-FE	0.0	0.0	0.0	0.0	0.0784
FE/CMO	0.0	0.0	0.0	0.0	0.000
FL/MU	0.0	0.0	0.0	0.0	0.000
MG/FE	0.0	0.0	0.0	0.0	0.000
Z-X-AL-CPX	0.0	0.0	0.0	0.0	0.000
X-AL-FE	0.0	0.0	0.0	0.0	0.000
X-AL-MI	0.0	0.0	0.0	0.0	0.000
X-AG-MI	0.0	0.0	0.0	0.0	0.000
X-FE-MI	0.0	0.0	0.0	0.0	0.000
X-CA-MI	0.0	0.0	0.0	0.0	0.000
X-MG-M2	0.0	0.0	0.0	0.0	0.000
X-FE-M2	0.0	0.0	0.0	0.0	0.000
X-CA-M2	0.0	0.0	0.0	0.0	0.000
A-ENSTATITE	0.0	0.0	0.0	0.0	0.0272
A-TREMULITE	0.0073532	0.0091107	0.0089230	0.0089230	0.000
X-ANGRIMITE	0.0	0.0	0.0	0.0	0.000
X-ALBITE	0.0	0.0	0.0	0.0	0.000



TABLE 2.83(0085...)

		C clinopyroxene 27	
SiO2	51.75	0.0	0.0
TiO2	0.16	0.0	0.0
Al2O3	2.51	0.0	0.0
Cr2O3	0.0	0.0	0.0
FeO*	7.52	0.0	0.0
MgO	10.35	0.0	0.0
MnO	0.42	0.0	0.0
MgO	13.84	0.0	0.0
CaO	21.90	0.0	0.0
Na2O	0.43	0.0	0.0
K2O	0.0	0.0	0.0
TOTAL WTK	100.97	0.0	0.0
NO OXIGENS			
Si	1.515	0.0	0.0
Ti	0.004	0.0	0.0
Al	0.10	0.0	0.0
Cr	0.0	0.0	0.0
Fe	0.323	0.0	0.0
Mn	0.016	0.0	0.0
Mg	0.769	0.0	0.0
Ca	0.875	0.0	0.0
Na	0.021	0.0	0.0
K	0.0	0.0	0.0
TOTAL TMS	4.644	0.0	0.0
X-Fe	0.5956	0.0	0.0
FeU/M50	0.7478	0.0	0.0
FeVMG	0.0	0.0	0.0
FeVFL	0.0	0.0	0.0
2-X-AL-LPA	0.0457	0.0	0.0
X-AL-TEL	0.0426	0.0	0.0
X-AL-M1	0.0251	0.0	0.0
X-MG-M1	0.6844	0.0	0.0
X-Fe-M1	0.0	0.0	0.0
X-CA-M1	0.0	0.0	0.0
X-MG-M2	0.6566	0.0	0.0
X-Fe-M2	0.0237	0.0	0.0
X-CA-M2	0.8750	0.0	0.0
A-SENSITIV	0.0255	0.0	0.0
A-REMOLIT	0.0	0.0	0.0
A-REHITH	0.0	0.0	0.0
X-ALBITE	0.0	0.0	0.0

### APPENDIX 3: METAMORPHIC PARAMETERS

#### Introduction

The application of various thermodynamic techniques, geothermometers and geobarometers using the analytical data obtained in this study (Appendix 2) is described in this section.

#### Orthopyroxene-clinopyroxene thermometry

The miscibility gap between diopside and enstatite has been the subject of much investigation and experimental calibration (Davis and Boyd, 1966; Wood and Banno, 1973; Nehru and Wyllie, 1974; Saxena and Nehru, 1975; Lindsley and Dixon, 1976; Saxena, 1976; Wells, 1977; Herzberg, 1978; Powell, 1978) and has been applied as an approximate geothermometer. The solid solution of enstatite between orthopyroxene and clinopyroxene:



has been calibrated using the experimental data of Davis and Boyd (1966), and expressions for the equilibration temperature in a two-pyroxene assemblage have been derived. Three of these calibrations (Wood and Banno, 1973; Wells, 1977; Powell, 1978) have been applied to the data obtained in this study, and have yielded a good consistency. These techniques

assume an 'ideal solution' model of the solubility of enstatite in diopside coexisting with orthopyroxene. In this model,  $\text{Fe}^{2+}$  and Mg are randomly distributed over the M1 and M2 octahedrally coordinated sites in the pyroxene molecule. Wood and Banno (1973) found that this made little difference to the results obtained when compared to those obtained using site occupancy calculations involving appropriate values of the standard free energy change of the exchange reaction. The model was able to typically reproduce experimental conditions to within about  $50^\circ\text{C}$ . The expression derived by Wood and Banno (1973, eqn.27) is as follows:

$$T(^{\circ}\text{K}) = \frac{-10202}{\ln \left[ \frac{a_{\text{en}}^{\text{cpx}}}{a_{\text{en}}^{\text{opx}}} \right] - 7,65X_{\text{Fe}}^{\text{opx}} + 3,88(X_{\text{Fe}}^{\text{opx}})^2 - 4,6}$$

and by Wells (1977, eqn.5):

$$T(^{\circ}\text{K}) = \frac{7\,341}{3,355 + 2,44X_{\text{Fe}}^{\text{opx}} - \ln \left[ \frac{a_{\text{en}}^{\text{cpx}}}{a_{\text{en}}^{\text{opx}}} \right]}$$

and by Powell (1978, eqn.22):

$$T(^{\circ}\text{K}) = \frac{- \left\{ 1600 + 80P(\text{kbar}) + (X_{\text{Ca}}^{\text{M2}} - X_{\text{Mg}}^{\text{M2}})_{\text{cpx}} \cdot (6670 - 88P(\text{kbar})) - 1900(X_{\text{Fe}}^{\text{M2}})_{\text{opx}} \right\}}{\ln \left\{ \left[ \frac{X_{\text{Ca}}}{X_{\text{Mg}}} \right]_{\text{opx}}^{\text{M2}} \cdot \left[ \frac{X_{\text{Mg}}}{X_{\text{Ca}}} \right]_{\text{cpx}}^{\text{M2}} \right\}}$$

The Wells calibration utilizes additional more recent experimental data to incorporate a temperature range from 800°C to 1700°C, and considers aluminous pyroxenes. Also, the effect of Fe solubility was calibrated in a more rigorous manner. This thermometer also reproduces the experimental conditions to typically within 50°C. However, the calculated temperatures deviate from those using Wood and Banno's equation (1973, eqn.27) and is attributed to inaccuracies in Wood and Banno's thermometer due to its dependence on experimental data obtained at higher temperatures (mainly over 1000°C) and compositions with lower Fe contents than those pertinent to the data obtained from the study area. Wells uses the same 'ideal solution' mixing model and activity definitions as Wood and Banno. There does not appear to be any systematic variation between the calculated and experimental values, and both thermometers produce values which may be either higher or lower than the relevant experimental value depending on the particular sample. Powell (1978) presents further refinements to these techniques, and considers Ca-Mg exchanges between coexisting pyroxenes. This avoids placing over emphasis on the ferrous iron content of the pyroxenes, since ferric iron proportions of the total iron determined by the microprobe techniques can only be estimated and may introduce inaccuracies. Also, a more rigorous application

of thermodynamic principles by Powell allows the pressure dependence (usually small) of this exchange equilibrium to be considered in the calibration. Thus, pressure estimates must be assumed, or obtained from other sources, in order to solve Powell's thermometer (1978, eqn.22). Alternatively, a PT curve can be calculated for the coexisting pyroxene pair, and intersection with other PT curves using different equilibria may provide a more precise solution of the pressure and temperature of equilibration.

The data and temperature estimates using these geothermometers are summarized in Tables 3.1 and 3.2. The mole fraction and activity data are calculated by a computer program written by the author and are listed together with the other analytical data in Appendix 2. The different methods yield fairly good consistency, where Wood and Banno's method (1973) gives the lowest estimates, and Powell's calibration (1978) gives the highest temperatures. The pyroxenitic amphibolite samples yield temperatures from about 800°C to about 950°C depending on the technique used. Estimates made from the data where Fe<sup>3+</sup> recalculations have been completed differed by usually less than 15°C from those made using the data without Fe<sup>3+</sup> calculations. Using Powell's method (Table 3.2), differences of usually much less than 20°C occurred assuming 4 or 10 kbar pressures, illustrating

Table 3.1: Temperature estimates ( $^{\circ}\text{C}$ ) for pyroxenitic amphibolites (27, X21395, X21399) and a metapyroxenite (20).

Sample number	27	27	X21395	X21395	X21399	20
$a_{\text{en}}^{\text{cpx}}$	0,0292	0,0270	0,0358	0,0278	0,0305	0,0199
$a_{\text{en}}^{\text{cpx}^1}$	0,0293	0,0287	0,0379	0,0301	0,0331	0,0268
$a_{\text{en}}^{\text{opx}}$	0,1564	0,1457	0,1883	0,1944	0,2130	0,5742
$a_{\text{en}}^{\text{opx}^1}$	0,1565	0,1458	0,1885	0,1946	0,2131	0,5738
$X_{\text{Fe}}^{\text{opx}}$	0,5809	0,5965	0,5438	0,5350	0,5077	0,1745
$X_{\text{Fe}}^{\text{opx}^1}$	0,5754	0,5894	0,5361	0,5268	0,5011	0,1659
Data source <sup>2</sup>	Table 2.16 UCT	Table 2.17 WITS	Table 2.18 UCT	Table 2.19 WITS	Table 2.20 UCT	Table 2.12 WITS
$T^3$	811	804	827	798	809	838
$T^{1,3}$	813	814	837	810	821	850
$T^4$	865	857	884	838	850	755
$T^{1,4}$	868	871	898	855	867	764

1: with  $\text{Fe}^{3+}$  recalculation

2: Appendix 2

3: Wood and Banno (1973, eqn.27)

4: Wells (1977, eqn.5)

Table 3.2: Temperature estimates ( $^{\circ}\text{C}$ ) using the method of Powell (1978) for pyroxenitic amphibolites (27, X21395, X21399) and a metapyroxenite (20).

Sample number	27	27	X21395	X21395	X21399	20
T(4 kbar)	960	891	877	868	879	695
T(4 kbar) <sup>1</sup>	959	896	880	875	888	699
T(6 kbar)	963	893	881	871	882	695
T(6 kbar) <sup>1</sup>	962	899	885	879	891	699
T(8 kbar)	966	896	886	874	884	694
T(8 kbar) <sup>1</sup>	965	902	890	882	894	698
T(10 kbar)	969	898	891	877	887	693
T(10 kbar) <sup>1</sup>	967	905	896	885	896	698

1: with  $\text{Fe}^{3+}$  recalculation

Data sources as for Table 3.1.

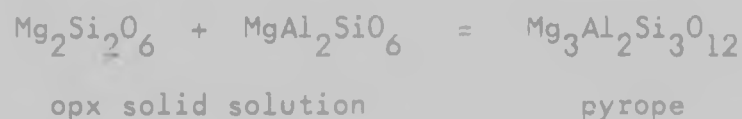
the good pressure insensitivity of this geothermometer. The metapyroxenite sample (no.20) gave less satisfactory correlation between the different methods, where the Wood and Banno estimate is higher (about 840°C to 850°C) and the Powell estimate is lower (about 695°C). Thus, the two-pyroxene pair in this lithology appears to have equilibrated at lower temperatures than those in the pyroxenitic amphibolites. However, the consideration of Ca solubility by Powell's method suggests that the Wood and Banno and Wells temperatures may be too high for this sample. However, all the temperatures are above the minimum melting point of wet granites, and within the field of granulite facies metamorphism.

#### Garnet-orthopyroxene barometry and thermometry

Attempts have been made to calibrate coexisting garnet and orthopyroxene in terms of the temperatures and pressures of equilibration (Wood and Banno, 1973; Wood, 1974; Powell, 1978; Wells, 1979) although it has been shown that these methods often do not provide convincing consistency or credible results (O'Hara and Yarwood, 1978) mainly due to the considerable uncertainty over how aluminium is distributed between octahedrally and tetrahedrally coordinated sites in the orthopyroxene. Wood and Banno (1973, eqn.17) have derived a barometer by extrapolating from experimentally determined phase equilibria in the  $MgSiO_3-Al_2O_3$  system using garnet lherzolite material



(Boyd and England, 1964; Boyd, 1970) for the following reaction:



Their barometer requires a temperature of equilibration to be estimated or assumed before application of their formulation:

$$P = 1 + \left\{ \frac{RT_0 \ln \left[ \frac{X_{\text{Mg}}^{\text{M1}} \cdot (X_{\text{Mg}}^{\text{M2}})^2 + X_{\text{Al}}^{\text{M1}}}{(X_{\text{Mg}}^{\text{gar}})^3} \right] + 4207 - 2,69T_0}{V_{\text{Mg}_3\text{Al}_2\text{Si}_3\text{O}_{12}}^{\circ} - \bar{V}_{\text{Mg}_2\text{Si}_2\text{O}_6} - \bar{V}_{\text{MgAl}_2\text{SiO}_6}} \right\}$$

where  $P$  is in bars,  $T_0$  in  $^{\circ}\text{K}$ ,  $R = 83,143 \text{ cm}^3 \text{ bar}^1 \text{ mole}^{-1} \text{ } ^{\circ}\text{K}^{-1}$ .

and the mole fractions are for multicomponent systems. The volume data (in  $\text{cm}^3$ ) are listed by Wood and Banno (1973) and Wood (1974) for orthopyroxenes with different Al contents.

Wood (1974, eqn.12) refined the above barometer by including additional experimental data on more magnesian systems (for opx: about  $\text{En}_{60}\text{Fs}_{40}$ ) and derived another barometer:

$$P = \frac{RT_0}{\Delta V_r} \cdot \ln \left[ \frac{X_{\text{Al}}^{\text{M1}} \cdot (1 - X_{\text{Al}}^{\text{M1}})}{(1-y)_{\text{gar}}} \right] + \frac{7012 - 3,98T_0}{\Delta V_r} \cdot C(X_{\text{Fe}}^{\text{opx}}) \cdot (1 - 2X_{\text{Al}}^{\text{M1}})$$

where  $C$  is a constant of 10 450 bars derived by Wood (1974),

and  $(1-y)_{\text{gar}}$  is given by  $(X_{\text{Fe}}^{\text{gar}} + X_{\text{Mg}}^{\text{gar}})$  where the mole fractions refer only to the M1 or divalent site in the garnet molecule.

$\Delta V_r$  is given by  $\bar{V}_{\text{Mg}_3\text{Al}_2\text{Si}_3\text{O}_{12}}^0 - \bar{V}_{\text{Mg}_2\text{Si}_2\text{O}_6} - \bar{V}_{\text{MgAl}_2\text{SiO}_6}$  and is tabulated by Wood (1974, Table 1). It must be noted that in order to use this barometer with the same units and constants as in the Wood and Banno equation, it is necessary to multiply the second term on the right-hand side of Wood's expression by 41,86 in order to maintain consistency with the units.

Powell (1978, eqn.26) considers the Ca-Mg exchange between coexisting garnet and orthopyroxene, and by using the experimental data of Wood (1974) and others, has determined another thermometer with a pressure dependence:

$$T^{\circ}\text{K} = \frac{7500 + 63P - (2870 + 50P) \cdot (x_{\text{Mg}}^{\text{gar}} - x_{\text{Ca}}^{\text{gar}}) - 1900(x_{\text{Fe}}^{\text{M2}})_{\text{opx}}}{4,58 - \ln K_D - 2,16(x_{\text{Mg}}^{\text{gar}} - x_{\text{Ca}}^{\text{gar}})}$$

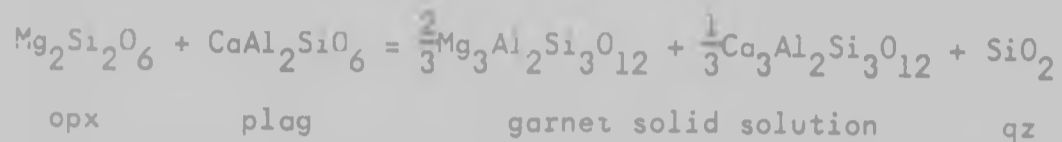
where:

$$K_D = \left[ \frac{x_{\text{Mg}}^{\text{gar}}}{x_{\text{Ca}}^{\text{gar}}} \right] \cdot \left[ \frac{x_{\text{Ca}}^{\text{M2}}}{x_{\text{Mg}}^{\text{M2}}} \right]_{\text{opx}}$$

P is in kilobars, and all garnet mole fractions refer to the M1 or divalent cation site in the garnet molecule. An error of 5 per cent in  $x_{\text{Ca}}^{\text{M2}}$  of the orthopyroxene at 20 kbar propagates in this equation to yield a deviation of only 10°C (Powell, 1978, p.467), and it appears that the uncertainty in the calculated temperature at a particular pressure should not be greater than 75°C.

Wells (1979, eqn.7) has also attempted to calibrate the

coexistence of garnet, orthopyroxene and plagioclase in terms of pressure and temperature. Consideration of the equilibrium:



and use of the data of Hensen (1976) and Newton *et al.* (1977) has enabled the derivation of a barometer with temperature dependence:

$$P = 1 + \left\{ \frac{3300 + 6,26T + RT \ln \left[ \frac{x_{\text{Ca}}^{\text{gar}} \cdot (x_{\text{Mg}}^{\text{gar}})^2}{x_{\text{Mg}}^{\text{M1,opx}} \cdot x_{\text{Mg}}^{\text{M2,opx}} \cdot x_{\text{An}}^{\text{plag}}} \right]}{0,56771} \right\}$$

$$\left\{ \frac{RT \ln \left[ \frac{x_{\text{Ca}}^{\text{gar}} \cdot x_{\text{Mg}}^{\text{gar}}}{x_{\text{An}}^{\text{plag}}} \right]}{0,56771} \right\}$$

The activity-composition data for plagioclase is tabulated by Orville (1972), while activity coefficients for garnet have been assumed as unity. This implies an ideal solution model, and allows a maximum pressure estimate to be obtained.

Results obtained by using these methods of Wood and Banno (1973), Wood (1974), Powell (1978) and Wells (1979) together with the analytical data obtained in this study (Appendix 2) are listed in Tables 3.3, 3.4 and 3.5.

#### Garnet-clinopyroxene thermometry

The coexistence of garnet and clinopyroxene has been

Table 3.3: Pressure estimates for orthopyroxene-garnet pairs using the methods of Wood and Banno (1973) and Wood (1974)

Sample reference	P (Wood and Banno) kbar			P (Wood) kbar			
	500°C	700°C	900°C	500°C	700°C	900°C	
1 {	c	4,1	5,2	6,4	-2,0	5,8	13,7
	r	5,7	7,2	8,8	-2,1	5,7	13,6
2		6,4	8,1	9,9	3,5	12,9	22,3
3 {	c	6,6	8,5	10,3	2,6	11,8	21,0
	r	10,4	13,2	16,1	5,0	14,8	24,6
4		7,3	9,3	11,3	3,0	12,3	21,6
5		18,1	22,9	27,7	21,0	34,7	48,3
6 {	c	8,8	11,2	13,7	8,0	18,1	28,3
	r	5,3	6,8	8,3	9,5	20,0	30,1
7		7,9	10,1	12,2	11,1	22,2	33,4

Sample references: (composition-activity data from Appendix 2)

- 1: sapphirine rock (11-8) - data from Table 2.12;  
 2: garnet-orthopyroxene-plagioclase symplectite (2-8-10A) Table 2.13;  
 3: garnet-orthopyroxene-plagioclase symplectite (2-8-10B) - Table 2.14;  
 4: garnet-orthopyroxene-plagioclase symplectite (2-8-10B) - Table 2.15;  
 5: pyroxenitic amphibolite (27) - Table 2.16;  
 6: pyroxenitic amphibolite (27) - Table 2.17;  
 7: pyroxenitic amphibolite (X21399) - Table 2.20.  
 c: calculated using garnet core composition.  
 r: calculated using garnet rim composition.

N.B. Only data with the Fe<sup>+++</sup> recalculation have been used in determining these estimates.

Table 3.4: Temperature estimates for orthopyroxene-garnet pairs using the method of Pcwel (1978)

Sample reference		Temperature ( $^{\circ}\text{C}$ )			
		5 kbar	6 kbar	8 kbar	10 kbar
1	c	928	945	961	979
	r	820	836	851	861
2		634	649	663	678
3	c	540	554	568	582
	r	623	637	651	665
4		568	582	596	609
5		656	674	692	710
6	c	632	650	668	685
	r	638	656	674	691
7		664	681	698	716

See Table 3.3 for sample references.

Table 3.5: Pressure estimates for orthopyroxene-garnet pairs using the method of Wells. (1979)

Sample reference	Pressure (kbar)		
	500°C	700°C	900°C
2	4,2	3,8	3,4
3 {	c	5,9	5,9
	r	4,7	4,1
5	5,2	5,0	4,9
6 {	c	6,1	6,2
	r	4,6	4,0

See Table 3.3 for sample references.

studied in detail (De Waard, 1965; Green and Ringwood, 1967) due to its relevance in upper mantle rocks, and also high-grade mafic metamorphic rocks. It appears that these minerals may be generated by the following reaction:



and these minerals, together with amphibole, typically make up mafic granulites. Green and Ringwood (1967) have used the above mineral assemblage to make distinctions between low, medium and high pressure granulites and eclogites in PT space. Winkler (1974) has also used this reaction to divide a lower pressure 'hypersthene-plagioclase granulite subzone' from a higher pressure 'clinopyroxene-almandine-quartz granulite subzone' in the 'regional hypersthene zone' (or 'granulite high grade' which contains granulites formed at medium to high pressures, probably more than 4 kbar, and where water partial pressures are considerably less than the total load pressure).

An experimental determination of the pressure and temperature dependence of the iron and magnesium partitioning between garnet and clinopyroxene, particularly for eclogites, has been made by Røheim and Green (1974). They used glasses of typical tholeiitic compositions in their experiments in order to relate to eclogites with basaltic bulk compositions,

and were able to calibrate a distribution coefficient ( $K_D$ ) as a function of temperature and pressure in the range of 600°C to 1 500°C and from 20 kbar to 40 kbar. In this range, the relationship is linear:

$$T(^{\circ}\text{K}) = \frac{3686 + 28,35P(\text{kbar})}{\ln \left[ \frac{\left(\frac{\text{FeO}}{\text{MgO}}\right)_{\text{gar}}}{\left(\frac{\text{FeO}}{\text{MgO}}\right)_{\text{cpx}}} \right] + 2,33}$$

Since this relationship is far more sensitive to changes in temperature than pressure, it may be applied as a geothermometer by assuming a linear extrapolation to lower pressures relevant to mafic granulites.

Ellis and Green (1979) conducted further experimental studies using similar materials and conditions, and considered the effect of Ca upon the garnet-clinopyroxene Fe-Mg exchange equilibria. An improved calibration was produced:

$$T(^{\circ}\text{K}) = \frac{3104X_{\text{Ca}}^{\text{gar}} + 3030 + 10,86P(\text{kbar})}{\ln \left[ \frac{\left(\frac{\text{Fe}^{++}}{\text{Mg}}\right)_{\text{gar}}}{\left(\frac{\text{Fe}^{++}}{\text{Mg}}\right)_{\text{cpx}}} \right] + 1,9034}$$

In addition, Wells (1979) has also produced a geothermometer for coexisting garnet and clinopyroxene using experimental data from several authors:



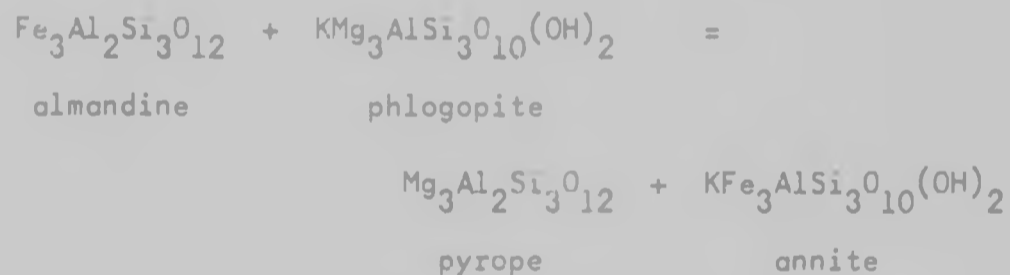
$$T(^{\circ}\text{K}) = \frac{24440 + 0,06524(P - 1)}{13,41 - 3R \ln \left[ \frac{x_{\text{Mg}}^{\text{gar}} \cdot x_{\text{Fe}}^{\text{cpx}}}{x_{\text{Fe}}^{\text{gar}} \cdot x_{\text{Mg}}^{\text{cpx}}} \right]}$$

where P is in bars, and R is the gas constant ( $1,987 \text{ cal}^{\circ}\text{K}^{-1} \text{ mol}^{-1}$ ).

Temperature estimates at various pressures using these three expressions are presented in Table 3.6 using only the analytical data from Appendix 2 where  $\text{Fe}^{+++}$  recalculations have been completed.

#### Biotite-garnet thermometry

A study of the partitioning of Fe and Mg between coexisting biotite and garnet which have compositions close to a binary Fe-Mg system has allowed the experimental calibration in terms of pressure and temperature of the following cation exchange reaction (Thompson, 1976; Ferry and Spear, 1978):



Thompson (1976) applied thermodynamic techniques to natural assemblages to obtain temperature estimates, and demonstrated a linear relationship between the distribution coefficient of the exchange reaction, and temperature (Figure 3.1). A linear regression curve fit to this data has enabled the derivation of a geothermometer:

Table 3.6: Temperature estimates ( $^{\circ}\text{C}$ ) for pyroxenitic amphibolites using coexisting garnet and clinopyroxene

Sample number	27	27	X21399
Data source (Appendix 2)	Table 2.16 UCT	Table 2.17 WITS core rim	Table 2.20 UCT
T1 (4 kbar)	664	675 618	623
T1 (6 kbar)	R&heim and Green (1974)	678 631	636
T1 (8 kbar)		692 645	650
T1 (10 kbar)		706 658	663
T2 (4 kbar)	792	822 701	686
T2 (6 kbar)	Ellis and Green (1979)	798 706	692
T2 (8 kbar)		804 712	697
T2 (10 kbar)		810 718	703
T3 (4 kbar)	770	782 717	723
T3 (6 kbar)	Wells (1979)	776 722	728
T3 (8 kbar)		781 728	733
T3 (10 kbar)		787 733	739

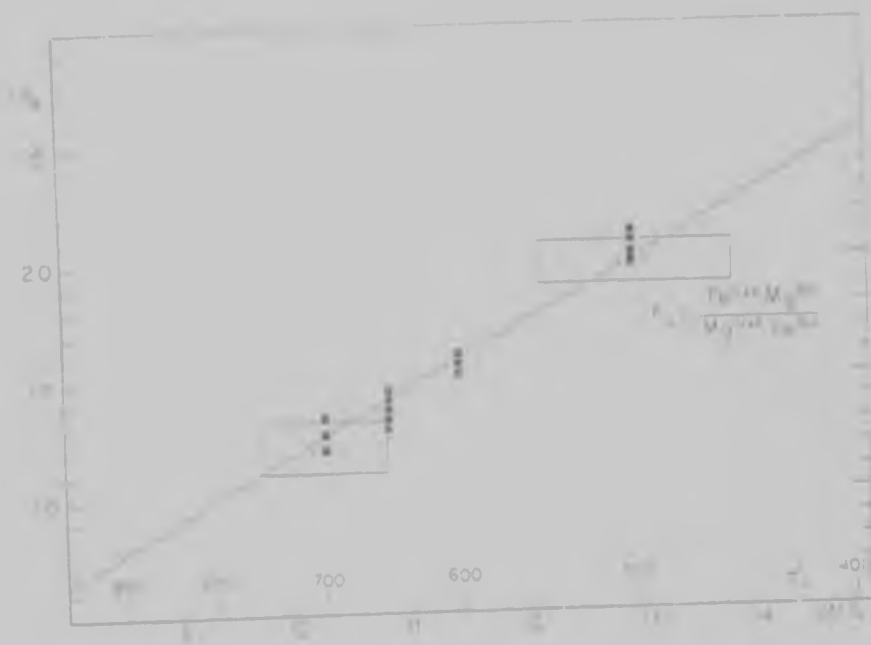


Figure 3.1: Plot of  $\ln K_D$  against  $1/T$  for Fe-Mg exchange between coexisting biotite and garnet (after Thompson, 1976, p.429).

$$T(^{\circ}\text{K}) = \frac{2739,646}{\ln \left[ \frac{\text{Fe}^{\text{gar}}}{\text{Mg}^{\text{gar}}} \cdot \frac{\text{Mg}^{\text{biot}}}{\text{Fe}^{\text{biot}}} \right] + 1,560}$$

However, Thompson (1976) indicates that temperatures determined from this calibration are about  $50^{\circ}\text{C}$  higher than those obtained by  $\text{O}^{18}/\text{O}^{16}$  isotopic thermometers, while garnet-biotite pairs from high grade metamorphic rocks show systematic displacements with increasing Ti in the biotite molecule. Some biotites analysed in this study contain over 4 per cent  $\text{TiO}_2$  (see Appendix 2) and may introduce inaccuracies into this determination.

Ferry and Spear (1978) completed an experimental study on synthetic garnet and biotite in the range of  $550^{\circ}\text{C}$  to  $800^{\circ}\text{C}$  and at about 2 kbar. A linear relationship between the

distribution coefficient (for the binary Fe-Mg exchange equilibrium) and temperature was revealed (Figure 3.2) and numerical analysis of these data has yielded a geothermometer for rock containing biotite and garnet which are close to binary Fe-Mg compounds (largely satisfied by the data obtained in this study):

$$12454 - 4,662T + 0.057P + 3RT \ln K = 0$$

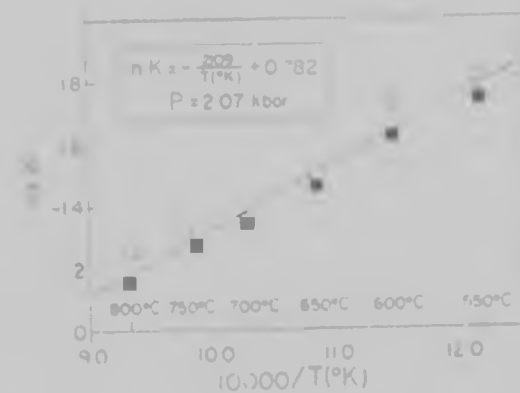


Figure 3.2: Plot of  $\ln K_D$  against  $1/T$  for coexisting biotite and garnet (after Ferry and Spear, 1978, p.115).

where  $T$  is in  $^{\circ}\text{K}$ ,  $P$  is in bars,  $R$  is the gas constant, and  $K$  is the distribution coefficient given by  $(\text{Mg}/\text{Fe})_{\text{gar}}/(\text{Mg}/\text{Fe})_{\text{biot}}$  either on a weight or atomic metal basis. This expression requires a pressure estimate to be made before determining a temperature, though is very insensitive to pressure changes. Ferry and Spear (1978) claim a maximum practical resolution of about  $50^{\circ}\text{C}$ , though point out that caution must be exercised if Ca and Mn fill the divalent metallic sites (M2) by more

than 20 per cent, or if Al and Ti fill the octahedrally coordinated sites (M1) by more than 15 per cent. This will ensure that the condition of a binary Fe-Mg system is largely maintained. The data obtained in this study generally satisfy these constraints.

These two garnet-biotite thermometers have been applied to the data in this study (Appendix 2) and are presented in Table 3.7. Only data where Fe<sup>+++</sup> recalculations (for garnet) have been made are used in determining these estimates, and within the pressure range of 4 to 10 kbar, the thermometer of Ferry and Spear (1978) shows no pressure dependence or effect.

#### Garnet-cordierite thermometry and barometry

It has long been recognized that the coexistence of garnet and cordierite in metamorphic rocks of pelitic composition is controlled by factors such as pressure, temperature and host rock composition. The reaction:



cordierite



garnet

sillimanite quartz

is characteristic of high-grade pelitic rocks, and this assemblage is common in pelitic rocks within the study area.

Table 3.7: Temperature estimates ( $^{\circ}\text{C}$ ) for coexisting biotite and garnet

Sample number	Data source (Appendix 2)	$\left(\frac{\text{Fe}}{\text{Mg}}\right)_{\text{gar}}$	$\left(\frac{\text{Mg}}{\text{Fe}}\right)_{\text{biot}}$	T1	T2
21-7-F	Table 2.2 UCT	2,1329	1,6085	708	764
21-7-G	Table 2.3 UCT	c 1,2601	1,90155	852	989
		r 1,67995		734	802
2-8-12	Table 2.8 UCT	1,0957	4,1914	615	633
2-8-12	Table 2.9 WITS	0,8021	3,8284	748	824
11-8	Table 2.12 UCT	c 0,9010	3,8457	704	759
		r 1,1926		615	633
2-8-10B	Table 2.14 UCT	c 1,7638	2,8158	593	603
		r 1,6044		620	639
2-8-10B	Table 2.15 WITS	1,6980	2,6162	625	646

21-7-F: garnet-cordierite-sillimanite gneiss, Farm Boschrand.  
 21-7-G: garnet-cordierite-sillimanite gneiss, Farm Boschrand.  
 2-8-12: sapphirine bearing rock, Farm Randjesfontein.  
 11-8: sapphirine bearing rock, Farm Randjesfontein.  
 2-8-10B: garnet-orthopyroxene-plagioclase symplectite, Farm Randjesfontein.

c: garnet core composition.  
 r: garnet rim composition.

T1: temperature after Thompson (1976).

T2: temperature after Ferry and Spear (1978).

T2 determined in the pressure range from 4 kbar to 10 kbar.

The dependence of this reaction on the physical parameters of metamorphism has been the subject of much study (Currie, 1971; Hensen and Green, 1971, 1972, 1973; Thompson, 1976; Holdaway and Lee, 1977; Wells, 1979) and several thermometers and barometers have been suggested. Currie (1971) noticed that the volume change in a Mg-Fe exchange equilibrium between garnet and cordierite was negligible, implying that this exchange was not explicitly dependent on pressure, and thus forms the basis of a good geothermometer. However, although the exchange equilibrium is insensitive to pressure, the minerals present in a garnet-cordierite assemblage are very pressure sensitive (Hensen and Green, 1971, 1972, 1973; Thompson, 1976). Currie (1971) conducted an experimental study using cordierites of intermediate composition, and derived the following expression:

$$T(^{\circ}\text{K}) = \frac{4515}{6,37 - \ln \left[ \frac{x_{\text{Mg}}^{\text{cord}}}{x_{\text{Fe}}^{\text{cord}}} \cdot \frac{x_{\text{Fe}}^{\text{gar}}}{x_{\text{Mg}}^{\text{gar}}} \right]}$$

However, Hensen and Green (1971, 1972, 1973) conducted experimental studies on a much wider range of compositions (with Mg/Mg+Fe ratios from 0 to 0,7) and also compositions both with and without excess  $\text{Al}_2\text{O}_3$ , but all with excess  $\text{SiO}_2$ . They were able to demonstrate that garnet and cordierite coexist over a wide range of pressures and temperatures

together with hypersthene, sillimanite, quartz, sapphirine, spinel and olivine:

High P, Low T	gar + cord
	}
	gar + cord + opx + sill + qz
	}
	gar + cord + opx + sapph + qz
	}
	gar + cord + opx + sp + qz
	}
Low P, High T	ol + sp + qz

and where the Mg/Mg+Fe ratio of all the ferromagnesian minerals decreases continuously from the high pressure region to the low pressure region. Consideration of these ratios enabled the calibration of a wide P-T field where garnet and cordierite may coexist (Figure 3.3). Holdaway and Lee (1977) also undertook experimental studies on the stability of cordierite, and were able to produce a calibration of a wide region of P-T space for coexisting garnet and cordierite on the basis of their Fe/Fe+Mg ratios (see Figure 3.4). Thompson (1976) calibrated data from several sources and showed a linear relationship between the distribution coefficient for the exchange equilibrium and temperature (Figure 3.5). The analysis of these data allowed the derivation of a pressure independent thermometer:

$$T(^{\circ}\text{K}) = \frac{2724,948}{\ln \left[ \left( \frac{\text{Fe}}{\text{Mg}} \right)_{\text{gar}} \cdot \left( \frac{\text{Mg}}{\text{Fe}} \right)_{\text{cord}} \right] + 0,896}$$



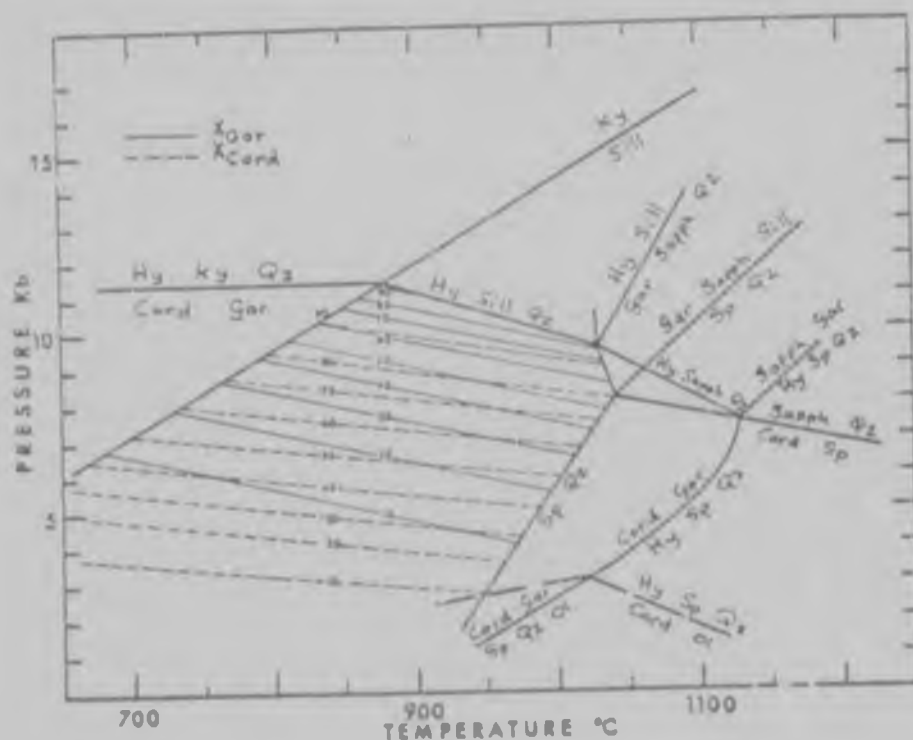


Figure 3.3: P-T field for coexisting garnet and cordierite in the reaction  $\text{cord} = \text{gar} + \text{sill} + \text{qz}$  showing 100Mg/Mg+Fe compositional contours (after Hensen and Green, 1973).

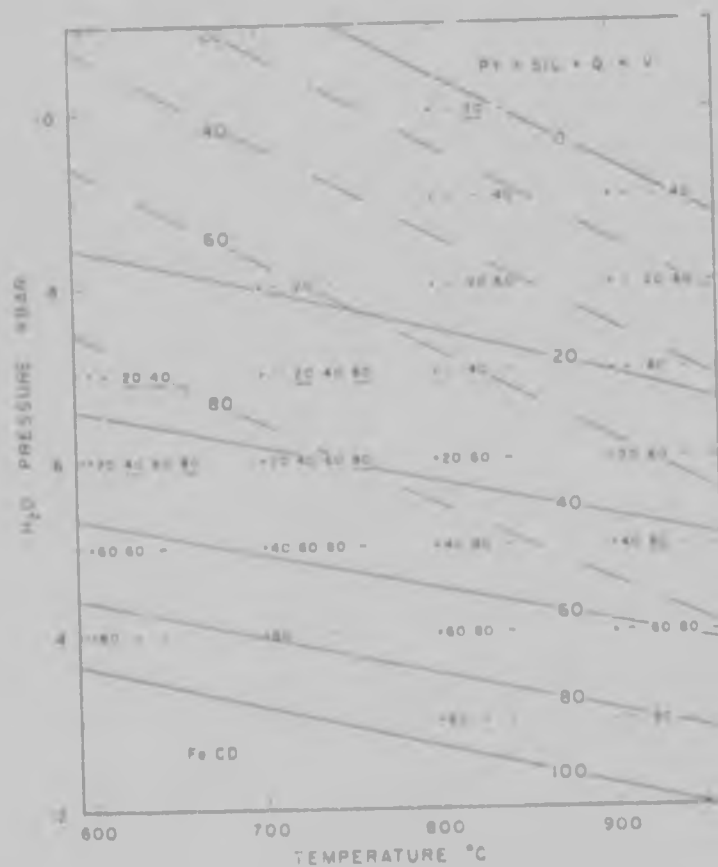


Figure 3.4: P-T field for coexisting garnet and cordierite after Holdaway and Lee (1977). Solid lines (cordierite) and dashed lines (garnet) are 100Fe/Fe+Mg contours. Dots refer to experimental data of Currie (1971).

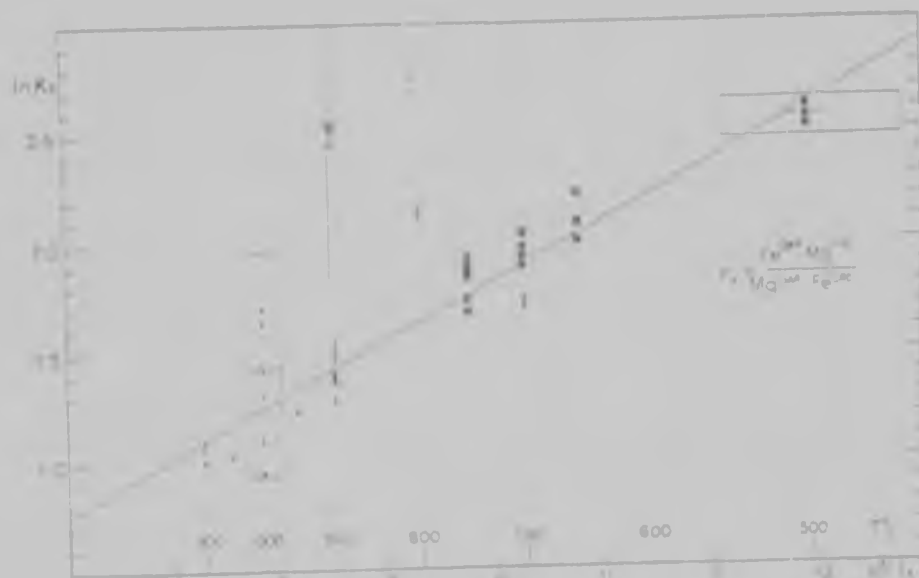


Figure 3.5: Plot of  $\ln K_D$  against  $1/T$  for the Fe-Mg exchange equilibrium between coexisting garnet and cordierite (after Thompson, 1976). Squares are natural assemblages from various sources; solid circles from data of Hensen and Green (1971, 1972); open circles from data of Currie (1971).

Further temperature and pressure calibrations for these minerals has been compiled by Wells (1979) using standard state thermochemical data and experimental results from Hensen and Green (1971, 1972, 1973), Holdaway (1976) and Hensen (1977). The expression for the thermometer is as follows:

$$T(^{\circ}\text{K}) = \frac{33248 - 0.1768(P - 1)}{10.94 + 6R \ln \left[ \frac{x_{\text{Fe}}^{\text{gar}} \cdot x_{\text{Mg}}^{\text{cord}}}{x_{\text{Mg}}^{\text{gar}} \cdot x_{\text{Fe}}^{\text{cord}}} \right]} \quad (P \text{ in bars})$$

In addition, Wells (1979) also calibrated the reaction:



as a barometer for both the Fe and Mg end-members of cordierite and garnet by extracting standard state

thermochemical data from experimental results of several workers:

$$P = 1 + \left\{ \frac{21801 - 9,44T - 6RT \ln \left[ \frac{X_{Fe}^{cord}}{X_{Fe}^{gar}} \right]}{3,6481} \right\}$$

and:

$$P = 1 + \left\{ \frac{16773 + 23,67T + 6RT \ln \left[ \frac{X_{Mg}^{gar}}{X_{Mg}^{cord}} \right]}{3,8256} \right\}$$

where  $P$  is in bars,  $T$  in  $^{\circ}K$ , and  $R$  is the gas constant.

Results obtained using these techniques on the analytical data of this study are presented in Table 3.8 and utilize garnet analyses in which  $Fe^{+++}$  has been recalculated. Good consistencies were obtained between the different methods, though in most cases, the  $Mg/Mg+Fe$  contours of Hensen and Green (1973) intersected out of the sillimanite field (Figure 3.3) for the data in this study. No kyanite has been recognized in samples collected within the study area, although recognized elsewhere in the Limpopo Mobile Belt (e.g. Chinner and Sweatman, 1968), and the temperature and pressure estimates determined using Hensen and Green's data (1973) must be regarded with caution.

Table 3.8: Temperature ( $^{\circ}\text{C}$ ) and pressure (kbar) estimates for coexisting garnet and cordierite

Sample number	21-7-F	21-7-G		2-8-12	11-8	
Data source Appendix 2	Table 2.2 UCT	Table 2.3 UCT		Table 2.8 UCT	Table 2.12 UCT	
		c	r		c	r
T1	783	647	705	802	755	824
T2	638	880	755	616	675	591
T3 P3	- -	850 8,8	- -	- -	- -	- -
T4 P4	690 7,9	870 6,8	815 7,0	550 10,5	630 9,8	550 10,3
T5 (4 kbar)	633	872	749	611	670	587
T5 (6 kbar)	623	860	738	602	659	578
T5 (8 kbar)	613	847	727	592	649	568
P5a ( $500^{\circ}\text{C}$ )	6,8	6,2	6,4	7,8	7,6	8,0
P5a ( $650^{\circ}\text{C}$ )	7,0	6,2	6,5	8,2	7,9	8,3
P5a ( $800^{\circ}\text{C}$ )	7,2	6,2	6,6	8,5	8,3	8,7
P5b ( $500^{\circ}\text{C}$ )	6,8	7,7	7,3	7,6	7,9	7,5
P5b ( $650^{\circ}\text{C}$ )	7,3	8,4	7,8	8,2	8,6	8,1
P5b ( $800^{\circ}\text{C}$ )	7,8	9,0	8,4	8,9	9,2	8,8

21-7-F: garnet-cordierite-sillimanite gneiss, Farm Boschrand.

21-7-G: garnet-cordierite-sillimanite gneiss, Farm Boschrand.

2-8-12: sapphirine bearing rock, Farm Randjesfontein.

11-8: sapphirine bearing rock, Farm Randjesfontein.

c: estimate using garnet core composition.

r: estimate using garnet rim composition.

T1: temperature estimate after Currie (1971).

T2: temperature estimate after Thompson (1976).

T3 & P3: temperature and pressure after Hensen and Green (1973).

T4 & P4: temperature and pressure after Holdaway and Lee (1977).

T5: temperature after Wells (1979).

P5a: pressure using Fe end-members after Wells (1979).

P5b: pressure using Mg end-members after Wells (1979).

Two feldspar thermometry

A geothermometric technique has been developed and successfully applied to quartzo-feldspathic granulites by Stormer and Whitney (1977). Consideration was made of equilibria between coexisting plagioclase and alkali feldspar using experimental data. The partitioning of albite between the two feldspars has been calibrated as a function of pressure and temperature to yield a geothermometer. Two expressions are presented for both high temperature sanidine - high albite series and for microcline - albite series respectively:

$$T = \frac{6326,7 - 9963,2X_{Ab}^{AF} + 943,3(X_{Ab}^{AF})^2 + 2690,2(X_{Ab}^{AF})^2 + P \{ 0,0925 - 0,1458X_{Ab}^{AF} + 0,0141(X_{Ab}^{AF})^2 + 0,0392(X_{Ab}^{AF})^3 \}}{-1,9872 \ln \left[ \frac{X_{Ab}^{AF}}{X_{Ab}^{PF}} \right] + 4,6321 - 10,815X_{Ab}^{AF} + 7,7345(X_{Ab}^{AF})^2 - 1,5312(X_{Ab}^{AF})^3}$$

$$T = \frac{7973,1 - 16910,6X_{Ab}^{AF} + 9901,9(X_{Ab}^{AF})^2 + P \{ 0,11 - 0,22X_{Ab}^{AF} + 0,11(X_{Ab}^{AF})^2 \}}{-1,9872 \ln \left[ \frac{X_{Ab}^{AF}}{X_{Ab}^{PF}} \right] + 6,48 - 21,58X_{Ab}^{AF} + 23,72(X_{Ab}^{AF})^2 - 8,62(X_{Ab}^{AF})^3}$$

where  $T$  is in  $^{\circ}\text{K}$ ,  $P$  is in kilobars, and where  $X_{\text{Ab}}^{\text{AF}}$  and  $X_{\text{Ab}}^{\text{PF}}$  are the mole fractions of albite in alkali feldspar and plagioclase respectively.

Analytical data for a coexisting alkali feldspar and plagioclase are presented for a sample of garnet-cordierite-sillimanite gneiss (sample no. 21-7-F, farm Boschrand, Appendix 2 - Table 2.2) and have been used in the application of Stomer and Whitney's (1977) two geothermometers. From Appendix 2,  $X_{\text{Ab}}^{\text{AF}} = 0,1135$  and  $X_{\text{Ab}}^{\text{PF}} = 0,6772$ , and the temperatures obtained are presented in Table 3.9.

Table 3.9: Temperature estimates for coexisting alkali feldspar and plagioclase.

Solution series	4 kbar	6 kbar	8 kbar
Sanidine-albite	469	469	469
Microcline-albite	515	515	515

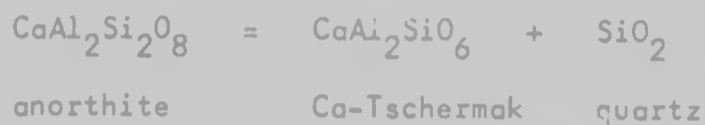
Data for sample no. 21-7-F (garnet-cordierite-sillimanite gneiss - farm Boschrand) from Appendix 2 (Table 2.2).

Temperatures in  $^{\circ}\text{C}$ .

The results of this thermometer display excellent pressure insensitivity. However, the temperature estimates by this method are significantly lower than those obtained by other techniques suggesting that the feldspars equilibrate, probably with the production of perthitic textures, under much lower metamorphic conditions sometime after the peak of the high grade event, or during a later thermal event.

Coexisting plagioclase - clinopyroxene - quartz

The equilibrium:



has been studied by several workers (Hariya and Kennedy, 1968; Wood, 1977, 1978, 1979), and can be used to calculate a P-T curve for this assemblage in rocks of appropriate composition (e.g. basement gneisses, anorthositic and gabbroic gneisses of the Messina Layered Intrusion). Although tabulated heat of formation data for these phases can be used to calculate enthalpies and entropies for this reaction, it is also possible to determine these data from experimental studies, such as those completed by Hariya and Kennedy (1968). At equilibrium, taking standard states of all components to be pure phases at the temperature and pressure of interest, we have:

$$\Delta G_{P,T}^{\circ} = 0 = \Delta H_{1 \text{ bar},T}^{\circ} - T\Delta S_T^{\circ} + \int_1^P \Delta V^{\circ} dp$$

If one assumes that  $\Delta C_p$  is zero and that  $\Delta V^{\circ}$  is a constant, it is then possible to determine  $\Delta H_{1 \text{ bar}}^{\circ}$  and  $\Delta S^{\circ}$  from the equilibrium boundary. However, the experimental data of Hariya and Kennedy (1968) (see Table 3.10 and Figure 3.6) illustrates that experiments on phase equilibria rarely achieve equilibrium between reactants and products, and such equilibrium boundaries can only be 'bracketed', which may introduce errors

Table 3.10: Experimental phase equilibrium results (after Hariya and Kennedy, 1968)  
for the reaction:  $3 \text{ anorthite} \rightleftharpoons 3 \text{ Co-Tschermak's molecule} + 3 \text{ quartz}$   
 $\rightleftharpoons \text{grossularite} + 2 \text{ kyanite} + \text{quartz}$

Number	Reactants	Pressure (K bar)	Temperature (°C)	Time (hours)	Products
85	An	29,5	1450	3	An
57	An	30	1400	8	An
101	Ca-Tsch + Q	30,5	1430	2,2	An
63	An	31,5	1400	3,8	Ca-Tsch + Q
72	An	31,5	1460	3,5	Ca-Tsch + Q
105	An	31,5	1490	2	Ca-Tsch + Q + small amount gl
61	An	33	1400	4,2	Gros + Ky + Q + Ca-Tsch
42	An	33,5	1470	3	Ca-Tsch + Q
106	Gros + Ky + Q	34	1445		Ca-Tsch grew + Q
43	An	35	1400		Gros + Ky + Q + small amount Ca-Tsch (unstable)
44	An	36	1510	1,5	Ca-Tsch + Q + small amount gl
56	An	36,5	1445	3	Gros + Ky + Q + small amount Ca-Tsch (unstable)
55	An	36,5	1475	3	Gros + Ky + Q + Ca-Tsch
45	An	37	1400	3,8	Gros + Ky + Q

An: anorthite; Ca-Tsch: Ca-Tschermak's molecule; gl: glass; Gros: grossularite;  
 Ky: kyanite; Q: quartz.

Starting materials: bot. natural and synthetic minerals.



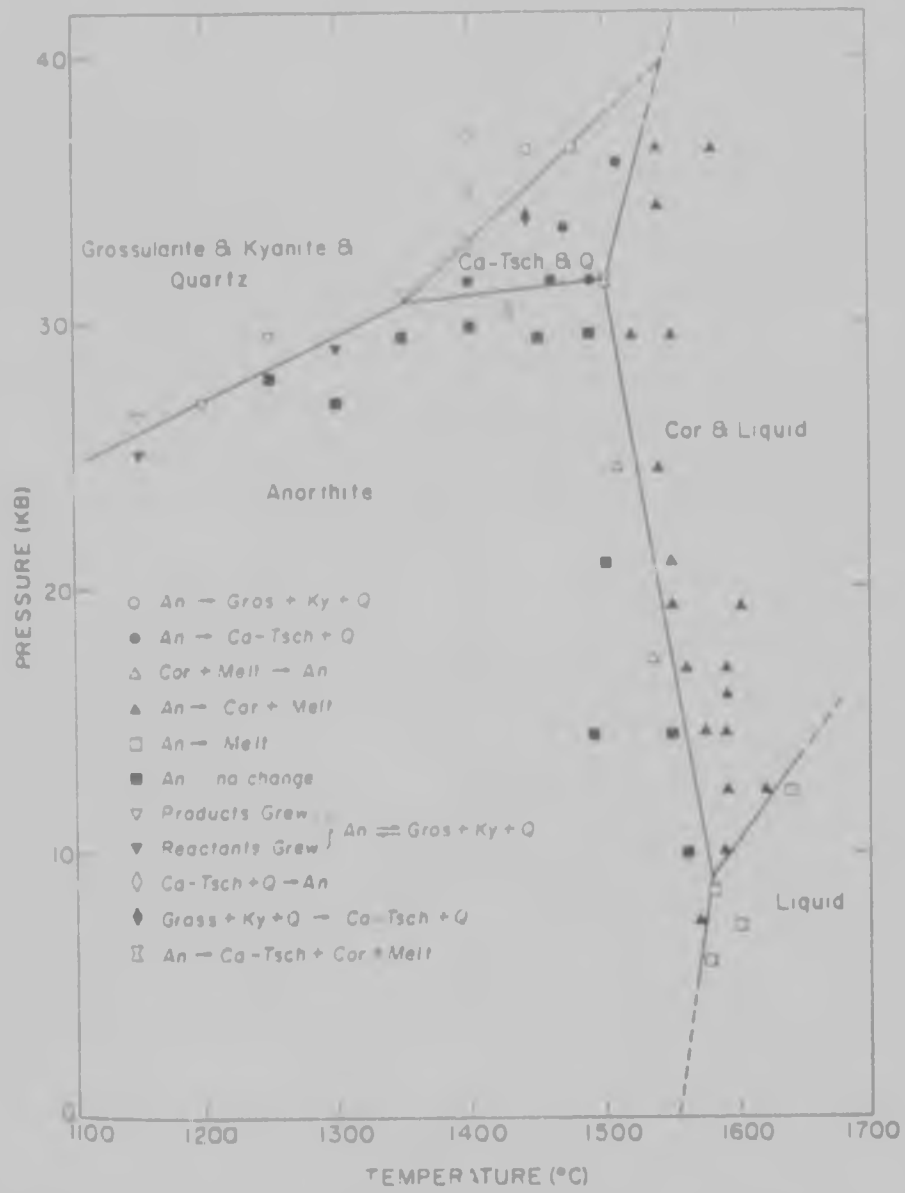


Figure 3.6: The stability field of anorthite at high pressure and temperature (after Hariya and Kennedy, 1968)

in the determination of thermodynamic data. Thus, where products are stable, the following condition will apply (while where the reactants are stable, the reverse condition applies):

$$\Delta G_{P,T}^{\circ} = \Delta H_{1 \text{ bar}}^{\circ} - T\Delta S^{\circ} + (P-1)\Delta V^{\circ} < 0$$

or alternatively,

$$\Delta H_{1 \text{ bar}}^{\circ} - T\Delta S^{\circ} < - (P-1)\Delta V^{\circ}$$

Then, the condition:

$$\Delta H_{1 \text{ bar}}^{\circ} - T\Delta S^{\circ} = - (P-1)\Delta V^{\circ}$$

provides the best internally consistent values of  $\Delta H^{\circ}$  and  $\Delta S^{\circ}$  to be constrained by the experimental results.

Then, using the experimental data of Hariya and Kennedy (1968) (see Table 3.10), these conditions may be derived (Table 3.11) and plotted in  $\Delta H^{\circ} - \Delta S^{\circ}$  space (Figure 3.7) to define a relationship between enthalpy and entropy for this equilibrium. Entropy values for these mineral phases are listed by Robie et al. (1978) for different temperatures, which enables the entropy-temperature relationship for this equilibrium to be determined (Figure 3.8) in the temperature range of interest. By using Figures 3.7 and 3.8 in conjunction, it is therefore possible to determine values for  $\Delta H^{\circ}$  and  $\Delta S^{\circ}$  at a particular temperature, and thus obtain a P-T relationship for this reaction, by substituting into the general condition

Table 3.11:  $\Delta H^\circ - T\Delta S^\circ$  conditions for the experimental data of Hariya and Kennedy (1968) for the reaction:  $\text{anor} = \text{Ca-Ts} + \text{qz}$

Reactants	Products	P(kbar)	T(°K)	$\Delta H^\circ - T\Delta S^\circ \geq -(P-1)\Delta V^\circ$
Ca-Ts + qz	An	30,5	1703	$\Delta H^\circ - 1703\Delta S^\circ > 10641$
An	Ca-Ts + qz	31,5	1673	$\Delta H^\circ - 1673\Delta S^\circ < 10990$
An	Ca-Ts + qz	31,5	1733	$\Delta H^\circ - 1733\Delta S^\circ < 10990$
An	Ca-Ts + qz	31,5	1763	$\Delta H^\circ - 1763\Delta S^\circ < 10990$
An	Ca-Ts + qz	33,5	1743	$\Delta H^\circ - 1743\Delta S^\circ < 11688$
An	Ca-Ts + qz	36,0	1783	$\Delta H^\circ - 1783\Delta S^\circ < 12560$

$$\Delta V^\circ = -0,3489 \text{ cal}^1 \text{ bar}^{-1} \text{ (data from Robie et al., 1978)}$$

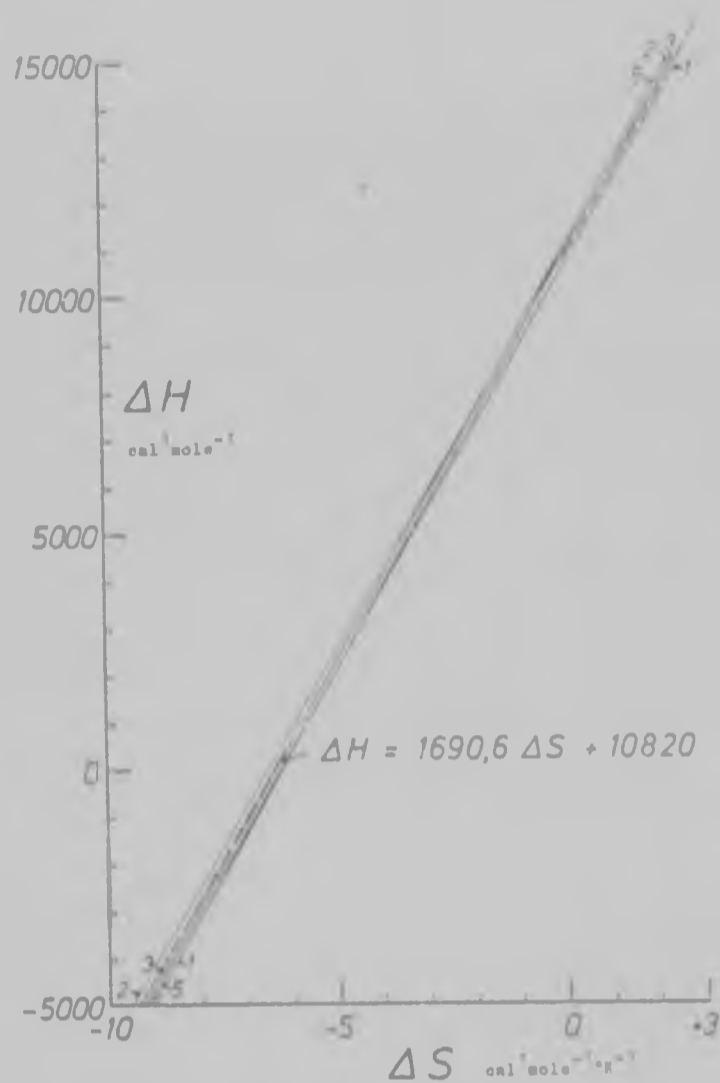


Figure 3.7:  $\Delta H^\circ - \Delta S^\circ$  conditions for the reaction  $\text{an} = \text{Ca-Ts} + \text{qz}$  from the data of Hariya and Keneedy (1968) (after Fripp, 1981c).

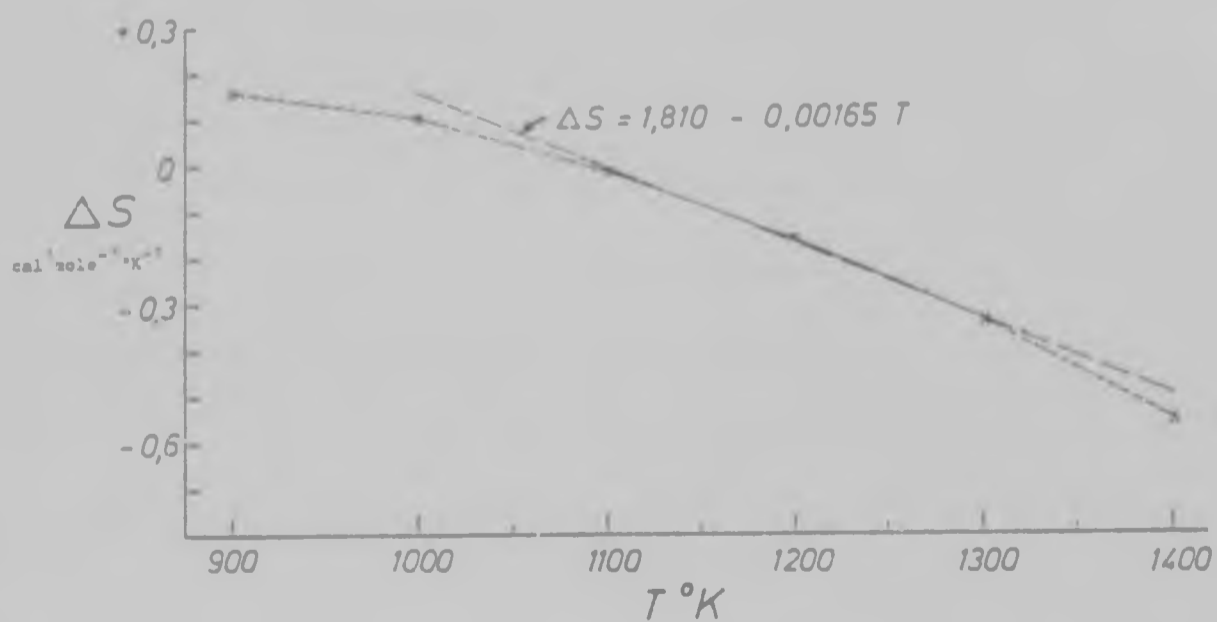


Figure 3.8: Entropy-temperature relationships for the reaction  $\text{an} = \text{Ca-Ts} + \text{qz}$  from the data of Robie *et al.* (1978) (after Fripp, 1981c).

of equilibrium for this reaction:

$$-RT \ln K_D = \Delta H_{1 \text{ bar}, T}^{\circ} - T \Delta S_T^{\circ} + \int_1^P \Delta V^{\circ} dP$$

where  $K_D$  is the equilibrium constant given by:

$$K_D = \frac{a_{\text{Ca-Ts}}^{\text{cpx}} \cdot a_{\text{SiO}_2}^{\text{qz}}}{a_{\text{an}}^{\text{plag}}}$$

Alternatively, a P-T curve can be calculated directly from tabulated heat capacity data without reliance on specific experimental studies. Heat capacity data for minerals can be readily obtained by calorimetric or electrochemical methods and is tabulated by various authors for a wide range of common rock-forming minerals (e.g. Robie *et al.*, 1978; Helgeson *et al.*, 1978). It has been shown that heat capacity at a particular pressure is a function of temperature, which may be represented by the following simple equation:

$$C_p = a + bT + c/T^2$$

where  $a$ ,  $b$  and  $c$  are experimentally determined constants for the phase of interest, and  $T$  is in  $^{\circ}\text{K}$ . Then, since the following relationship between an increase in enthalpy and temperature exists:

$$dH = C_p dT$$

it is possible to determine the enthalpy of a phase at a particular temperature:

$$\int_{298}^T dH = \int_{298}^T C_p dT$$

$$H_T - H_{298} = \int_{298}^T (a + bT + c/T^2) dT$$

$$H_T = H_{298} + \left[ aT + \frac{bT^2}{2} - \frac{c}{T} \right]_{298}^T$$

where  $T$  is the temperature of interest ( $^{\circ}\text{K}$ ) and where  $H_{298}$ ,  $a$ ,  $b$  and  $c$  are experimentally determined parameters for the phase of interest. Increasing the heat content of a phase also increases its entropy, and if an amount of heat  $dH$  is added at constant pressure, the following applies (Wood and Fraser, 1976):

$$dS = \frac{dH}{T}$$

which becomes:

$$dS = \frac{C_p dT}{T}$$

and thus an expression for entropy in terms of the heat capacity may be obtained:

$$\int_{298}^T dS = \int_{298}^T \frac{C_p}{T} dT$$

$$S_T - S_{298} = \int_{298}^T \left( \frac{a}{T} + b + \frac{c}{T^2} \right) dT$$

$$S_T = S_{298} + \left[ a \ln T + bT - \frac{c}{2T^2} \right]_{298}^T$$

Thus, after the calculation of  $H_T$  and  $S_T$  for the relevant mineral phases at the temperature of interest,  $\Delta H$  and  $\Delta S$

may be obtained:

$$\Delta H_T = H_T^{\text{cpx}} + H_T^{\text{qz}} - H_T^{\text{plag}}$$

$$\Delta S_T = S_T^{\text{cpx}} + S_T^{\text{qz}} - S_T^{\text{plag}}$$

and the volume change is given by:

$$\Delta V^0 = V_{\text{cpx}}^0 + V_{\text{qz}}^0 - V_{\text{plag}}^0$$

Then, by substitution into the equation of state at equilibrium:

$$-RT \ln K_D = \Delta H - T\Delta S + (P-1)\Delta V^0$$

or alternatively:

$$P = \left[ \frac{T\Delta S - \Delta H - RT \ln K_D}{\Delta V^0} \right] + 1$$

generates a P-T expression for the assemblage plagioclase + clinopyroxene + quartz. T is given in °K, P is in bars, and  $K_D$  is the equilibrium constant for the reaction given by:

$$K_D = \frac{a_{\text{Ca-Ts}}^{\text{cpx}} \cdot a_{\text{SiO}_2}^{\text{qz}}}{a_{\text{an}}^{\text{plag}}}$$

The activity of  $\text{SiO}_2$  in quartz is unity (trivial), while  $a_{\text{an}}^{\text{plag}}$  is given by Orville (1972) as a function of the readily determined mole fraction  $X_{\text{an}}^{\text{plag}}$ . The activity of Calcium-Tschermak in clinopyroxene is discussed in detail by Wood (1979).

Firstly,  $\bar{X}_{\text{Ca-Ts}}$  is calculated by the following:

$$\bar{X}_{\text{Ca-Ts}} = \frac{4X_{\text{Ca}}^{\text{M2}} \cdot X_{\text{Al}}^{\text{M1}} \cdot X_{\text{Si}}^{\text{Tet}} \cdot X_{\text{Al}}^{\text{Tet}}}{4X_{\text{Ca}}^{\text{M2}} \cdot X_{\text{Al}}^{\text{M1}} \cdot X_{\text{Si}}^{\text{Tet}} \cdot X_{\text{Al}}^{\text{Tet}}}$$

The  $X_{\text{Ca-Ts}}$  is determined by iteration or graphical techniques from:

$$(X_{\text{Ca-Ts}})^2 \cdot (2 - X_{\text{Ca-Ts}}) = \bar{X}_{\text{Ca-Ts}}$$

Then for the temperature range 900°C to 1100°C:

$$a_{\text{Ca-Ts}}^{\text{cpx}} \approx (1,3 - 0,4X_{\text{Fe}}) \cdot X_{\text{Ca-Ts}}$$

where:

$$X_{\text{Fe}} = \left[ \frac{\text{Fe}^{++}}{\text{Fe}^{++} + \text{Mg}} \right]_{\text{cpx}}$$

Results obtained using this method involving heat capacity and other thermodynamic parameters (Table 3.12) for a range of  $K_D$  values from 0,020 to 0,100 are presented in Table 3.13.

Pressure estimates have also been made using the analytical data obtained in this study (Appendix 2) and are presented in Table 3.14. Samples of pyroxenitic amphibolite and gabbroic gneiss (from the Messina Layered Intrusion) were used, and only clinopyroxene analyses with the  $\text{Fe}^{+++}$  recalculation were utilized in the calculation of P-T curves (using the heat capacity technique).

#### Water activity

The activity of water may be calculated for assemblages involving hydrous mineral phases, such as amphibole.

Estimation of the distribution coefficient of a dehydration reaction and the distribution coefficient for the solid phase alone enables the solution of the water activity. One such



Table 3.12: Thermodynamic parameters for anorthite, calcium-Tschermak and quartz (from Helgeson et al., 1978)

Mineral	$V^{\circ}$	$a$	$b \times 10^3$	$c \times 10^{-5}$	$H_{1,298}^{\circ}$	$S_{1,298}^{\circ}$
$\text{SiO}_2$ quartz	22,688	11,220	8,200	2,70	-217,650	9,88
$\text{CaAl}_2\text{SiO}_6$ Ca-Al pyroxene	63,500	54,130	6,420	14,90	-784,013	35,00
$\text{CaAl}_2\text{Si}_2\text{O}_8$ anorthite	100,790	63,311	14,794	15,44	-1007,772	49,10

Units:  $V^{\circ}$ :  $\text{cm}^3 \text{mol}^{-1}$   
 $a$ :  $\text{cal}^1 \text{mol}^{-1} \text{ } ^{\circ}\text{K}^{-1}$   
 $b$ :  $\text{cal}^1 \text{mol}^{-1} \text{ } ^{\circ}\text{K}^{-2}$   
 $c$ :  $\text{cal}^1 \text{mol}^{-1} \text{ } ^{\circ}\text{K}^1$   
 $H^{\circ}$ :  $\text{Kcal}^1 \text{mol}^{-1}$   
 $S^{\circ}$ :  $\text{cal}^1 \text{mol}^{-1} \text{ } ^{\circ}\text{K}^{-1}$

Table 3.13: Pressure estimates (abars) for the reaction  $m \text{ Cu-ly} + g$  for a range in  $K_p$  values from 0.020 to 0.100, and a range in temperatures from 500°C to 1000°C

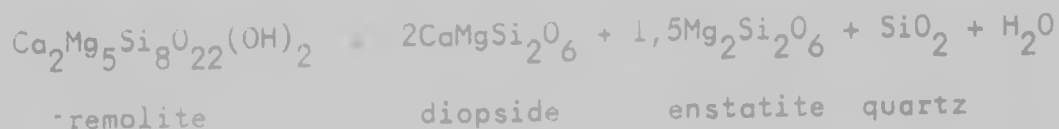
$K_p$	500	550	600	650	700	750	800	850	900	950	1000
0,020	7,106	6,172	5,213	4,247	3,260	2,256	1,240	0,207	3,836	-1,374	-2,961
0,025	8,068	7,218	6,328	5,420	4,497	3,556	2,603	1,634	0,654	-0,340	-1,343
0,030	8,451	8,072	7,235	6,379	5,507	4,618	3,717	2,800	1,872	0,930	-0,022
0,035	9,069	8,795	8,001	7,189	6,351	5,516	4,659	3,786	2,902	2,004	1,096
0,040	10,157	9,421	8,665	7,891	7,101	6,294	5,475	4,640	3,794	2,934	2,064
0,045	10,676	9,973	9,250	8,510	7,764	6,980	6,195	5,394	4,581	3,754	2,918
0,050	11,140	10,467	9,774	9,064	8,338	7,594	6,839	6,067	5,284	4,488	3,681
0,055	11,559	10,913	10,248	9,565	8,866	8,149	7,421	6,677	5,921	5,152	4,372
0,060	11,942	11,321	10,681	10,022	9,348	8,656	7,953	7,233	6,502	5,768	5,003
0,065	12,295	11,696	11,079	10,443	9,791	9,123	8,442	7,745	7,037	6,315	5,583
0,070	12,621	12,044	11,447	10,832	10,202	9,554	8,895	8,219	7,532	6,831	6,121
0,075	12,925	12,367	11,790	11,195	10,584	9,956	9,316	8,660	7,993	7,312	6,621
0,080	13,209	12,670	12,111	11,534	10,942	10,332	9,710	9,073	8,424	7,761	7,089
0,085	13,476	12,954	12,412	11,853	11,278	10,685	10,081	9,451	8,829	8,183	7,528
0,090	13,727	13,222	12,697	12,153	11,594	11,016	10,430	9,826	9,211	8,591	7,942
0,095	13,965	13,475	12,965	12,438	11,894	11,333	10,761	10,172	9,572	8,955	8,334
0,100	14,191	13,715	13,220	12,707	12,178	11,632	11,074	10,500	9,915	9,315	8,706

Table 3.14: Pressure estimates for pyroxenitic amphibolites and samples from the Messina Layered Intrusion using coexisting plagioclase, clinopyroxene and quartz

Sample number	Data source (Appendix 2)	$K_D$	Pressure (kbar)		
			600°C	750°C	900°C
27	Table 2.16 - UCT	0,02636	6,6	3,8	1,0
27	Table 2.17 - WITS	0,03688	8,3	5,8	3,2
X21395	Table 2.18 - UCT	0,06559	11,1	9,2	7,1
X21395	Table 2.19 - WITS	0,06521	11,1	9,1	7,1
X21399	Table 2.20 - UCT	0,06324	10,9	9,0	6,8
26-5-A	Table 2.22 - UCT	0,07034	11,5	9,6	7,6
26-5-A	Table 2.23 - WITS	0,05234	10,0	7,9	5,6
26-5-E	Table 2.22 - UCT	0,05230	10,0	7,8	5,6

27: pyroxenitic amphibolite, Farm Artonvilla.  
 X21395: pyroxenitic amphibolite, Farm Artonvilla.  
 X21399: pyroxenitic amphibolite, Farm Artonvilla.  
 26-5-A: gabbroic gneiss, Farm Shangani.  
 26-5-E: gabbroic gneiss, Farm Shangani.

reaction which has been used in this study involves the dehydration of tremolite:



which has the following distribution coefficient:

$$K_D = \frac{(a_{\text{diop}}^{\text{opx}})^2 \cdot (a_{\text{en}}^{\text{opx}})^{1,5} \cdot (a_{\text{H}_2\text{O}}^{\text{fluid}})}{(a_{\text{trem}}^{\text{amph}})}$$

and thus:

$$a_{\text{H}_2\text{O}}^{\text{fluid}} = \frac{K_D}{K_{\text{solids}}}$$

The activities of tremolite for amphiboles and enstatite for orthopyroxenes are listed in Appendix 2, while the activity of diopside in clinopyroxene is given by:

$$a_{\text{diop}}^{\text{cpx}} = (X_{\text{Ca}}^{\text{M2}}) \cdot (X_{\text{Mg}}^{\text{M1}}) \cdot (X_{\text{Si}}^{\text{Tet}})^2$$

and it is thus possible to determine  $K_{\text{solids}}$  for this equilibrium using the analytical data.  $K_D$  may be calculated for different temperatures and pressures from the equation of state using published thermodynamic parameters. However, the presence of water introduced a complication into what is otherwise a solid-state system. Fisher and Zen (1971) have introduced an approximation by calculating the Gibb's free energy of water ( $G_{\text{H}_2\text{O}}^*$ ). This enables the calculation of

thermodynamic parameters of solid phases from hydrothermal equilibrium data. The equation for the free energy of the system then becomes:

$$\Delta G_o = \Delta G_f^o(1,298)_{\text{solids}} - (T-298)\Delta S_f^o(1,298)_{\text{solids}} + G_{H_2O}^* + (P-1)\Delta V^o_{\text{solids}} + RT \ln K_D$$

and the maximum value of  $K_D$  will occur when  $\Delta G_o = 0$  (i.e. with just enough water to size tremolite). Thus:

$$\ln K_D = \frac{(T-298) \Delta S_f^o(1,298)_{\text{solids}} - (P-1)\Delta V^o_{\text{solids}} - G_{H_2O}^* - \Delta G_f^o(1,298)_{\text{solids}}}{RT}$$

Thermodynamic parameters of the mineral phases are available in the literature (see Table 3.15) to calculate  $K_D$  and together with  $K_{\text{solids}}$  has enabled the determination of the water activity for samples collected in the study area (Table 3.16) at temperatures of 700°C, 800°C and 900°C, and at pressures of 6 kbar, 8 kbar and 10 kbar.

Table 3.15: Thermodynamic parameters for tremolite, diopside, enstatite and quartz, for the reaction:  $\text{trem} = 2 \text{ diop} + 1,5 \text{ en} + \text{qz} + \text{H}_2\text{O}$

Mineral	$\Delta G_f^\circ$ cal/mol	$\Delta H_f^\circ$ cal/mol	$\Delta S_f^\circ$ cal/mol. $^\circ\text{K}$	$V^\circ$ $\text{cm}^3/\text{mol}$
tremolite $\text{Ca}_2\text{Mg}_5\text{Si}_8\text{O}_{22}(\text{OH})_2$	-2770685	-2944478	-583,35	272,92
diopside $\text{CaMgSi}_2\text{O}_6$	-724000	-765598	-139,65	66,09
enstatite $\text{MgSiO}_3$	-348930	-369686	- 69,64	31,28
quartz $\text{SiO}_2$	-204646	-217650	- 43,62	22,69

$\Delta G_f^\circ$ ,  $\Delta H_f^\circ$ , and  $V^\circ$  data from Helgeson et al. (1978).

$\Delta S_f^\circ$  data from Rohie et al. (1978).

Table 3.16: Water activity estimates for pyroxenitic amphibolites and metapyroxenite based on coexisting amphibole, clinopyroxene, orthopyroxene and quartz

Sample number		27	27	X21395	X21395	X21399	20
Data source Appendix 2		Table 2.16 UCT	Table 2.17 WITS	Table 2.18 UCT	Table 2.19 WITS	Table 2.20 UCT	Table 2.21 WITS
T°C	P kbar	K <sub>D</sub>					
700	6	0,0088	0,0144	0,0052	0,0069	0,0034	0,0183
	8	0,0094	0,0153	0,0055	0,0073	0,0036	0,0195
	10	0,0104	0,0169	0,0061	0,0081	0,0040	0,0216
800	6	0,0236	0,0384	0,0138	0,0184	0,0091	0,0489
	8	0,0242	0,0394	0,0141	0,0189	0,0094	0,0502
	10	0,0260	0,0422	0,0152	0,0202	0,0101	0,0539
900	6	0,0543	0,0884	0,0317	0,0432	0,0210	0,1127
	8	0,0541	0,0880	0,0316	0,0414	0,0209	0,1122
	10	0,0564	0,0917	0,0329	0,0439	0,0218	0,1170

27, X21395 and X21399: pyroxenitic amphibolites, Farm Artonvilla.  
 20: metapyroxenite, Farm Artonvilla.

## REFERENCES

- Aibee, A.L. and Ray, L. (1970) Correction factors for electron probe microanalysis of silicates, oxides, carbonates, phosphates and sulfates. *Anal.Chem.* 42, 1408-1414.
- Anastasi <sup>11</sup>, P. and Seifert, F. (1972) Solid solubility of  $Al_2O_3$  in enstatite at high temperatures and 1-5 kbar water pressure. *Contr.Mineral.Petrol.* 3A, 272-287.
- Bahnemann, K.P. (1970) A note on the anorthositic gneiss in the Messina district, northern Transvaal. *Geol.Soc. S.Afr.Spec.Pub.* 1, 715-720.
- Bahnemann, K.P. (1972) A review of the structure, stratigraphy and the metamorphism of the basement rocks in the Messina district, northern Transvaal, D.Sc thesis Univ. Pretoria (unpub.), 156 p.
- Bahnemann, K.P. (1973) The origin of the Singelele granite gneiss near Messina, northern Transvaal, *Geol.Soc.S. Afr.Spec.Pub.* 3, 235-244.
- Bahnemann, K.P. (1975) Garnets as possible indicators of metamorphic grade in the Limpopo folded belt near Messina in the northern Transvaal. *Trans.Geol.Soc. S.Afr.* 78, 251-256.
- Barker, O.B. (1976) Discussion on: The Soutpansberg trough (northern Transvaal) - an aulacogen, by H. Jansen. *Trans.Geol.Soc.S.Afr.* 79, 146-148.
- Barton, J.M. (1979) The chemical compositions, Rb-Sr isotopic systematics and tectonic setting of certain Proterozoic basic igneous rocks, Limpopo Mobile Belt, southern Africa. *Precamb.Res.* 9, 57-80.
- Barton, J.M. (1981) Pb-isotopic evidence for the age of the Messina Layered Intrusion, Central Zone, Limpopo Mobile Belt. *Geol.Soc.S.Afr.Spec.Pub.* (in prep.).
- Barton J.M. and Ryan, B. (1977) A review of the geochronologic framework of the Limpopo Mobile Belt, Botswana *Geol. Surv.Bull.* 12, 183-200.
- Barton, J.M., Fripp, R.E.P. and Ryan, B. (1977) Rb/Sr ages and geological setting of ancient dykes in the Sand River area, Limpopo Mobile Belt, South Africa. *Nature* 267, 487-490.



- Barton, J.M., Ryan, B. and Fripp, R.E.P. (1978) The relationship between Rb-Sr and U-Th-Pb whole-rock and zircon systems in the 3790 m.y. old Sand River Gneisses, Limpopo Mobile Belt, southern Africa, U.S.Geol.Surv.Open-File Report 78-701, 27-28.
- Barton, J.M., Fripp, R.E.P., Horrocks, P.C. and McLean, N. (1979a) The geology, age and tectonic setting of the Messina Layered Intrusion, Limpopo Mobile Belt. Amer J.Sc.279, 1108-1134.
- Barton, J.M., Ryan, B., Fripp, R.E.P. and Horrocks, P.C. (1979b) Effects of metamorphism on the Rb-Sr and U-Pb systematics of the Singelele and Bulai Gneisses, Limpopo Mobile Belt, southern Africa. Trans.Geol. Soc.S.Afr. 82, 259-269.
- Barton, J.M., Fripp, R.E.P. and Horrocks, P.C. (1981) Rb-Sr ages and chemical compositions of some deformed Archaean mafic dykes, Central Zone, Limpopo Mobile Belt, southern Africa. Geol.Soc.S.Afr.Spec.Pub. (in prep.).
- Berg, J.H. (1977) Regional geobarometry in the contact aureoles of the anorthositic Nain Complex, Labrador. J.Petrol. 18, 399-430.
- Bickle, M.J. (1978) Heat loss from the earth: a constraint on Archaean tectonics from the relation between geothermal gradients and the rate of plate production. Earth Planet.Sc.Lett. 40, 301-315.
- Birks, L.S. (1963) Electron Probe Microanalysis. Interscience, 237 p.
- Boyd, F.R. (1970) Garnet peridotite and the system  $\text{CaSiO}_3$ - $\text{MgSiO}_3$ - $\text{Al}_2\text{O}_3$  Mineral.Soc.Amer.Spec.Papers 3, 63-75.
- Boyd, F.R. and England, J.L. (1964) The system enstatite-pyrope. Yearbook Carnegie Inst.Wash.63, 157-161.
- Bridgewater, D., Keto, L., McGregor, V.R. and Myers, J.S. (1976) Archaean gneiss complex of Greenland. In "Geology of Greenland", eds. Escher, A. and Watt, W.S., Geol. Surv. Greenland, 19-75.

- Burke, K. and Kidd, W.S.F. (1978) Were Archaean continental geothermal gradients much steeper than those of today? *Nature* 272, 240-241.
- Carr chael, I.S.E., Turner, F.J. and Verhoogen, J. (1974) *Igneous Petrology*. McGraw-Hill, New York, 739 p.
- Chinner, G.A. and Sweatman, T.R. (1968) A former association of enstatite and kyanite. *Mineral.Mag.* 36, 1052-1060.
- Clifford, T.N. (1970) The structural framework of Africa. In "African Magmatism and Tectonics", Eds. Clifford, T.N. and Gass, I.G., Oliver and Boyd, Edinburgh, 1-26.
- Clifford, T.N., McIver, J.R. and Stumpfl, E.F. (1975) A sapphirine-cordierite-bronzite-phlogopite paragenesis from Namaqualand, South Africa, *Mineral.Mag.* 40, 347-356.
- Coward, M.P. (1976) Archaean deformation patterns in southern Africa. *Phil.Trans.Roy.Soc.Lond.* A283, 313-331.
- Coward, M.P., James, P.R. and Wright, L. (1976) Northern margin of the Limpopo Mobile Belt, southern Africa. *Geol.Soc.Amer.Bull.* 87, 601-611.
- Cox, K.G., Johnson, R.L., Monkman, L.J., Stillman, C.J., Vail, J.R. and Wood, D.N. (1965) The geology of the Nuanetsi igneous province. *Phil.Trans.Roy.Soc.Lond.* A257, 71-218.
- Currie, K.L. (1971) The reaction  $3\text{cordierite} = 2\text{garnet} + 4\text{sillimanite} + 5\text{quartz}$  as a geological thermometer in the Opinicon Lake region, Ontario, *Contr.Mineral. Petrol.* 33, 215-226.
- Davies, G. (1981) The petrogenesis of quartz norites in the area around Buffelspoort Dam, Rustenburg district. Ph.D thesis Univ.Witwatersrand (unpub. in prep.)
- Davis, B.T.C. and Boyd, F.R. (1966) The join  $\text{Mg}_2\text{Si}_2\text{O}_6$ - $\text{CaMgSi}_2\text{O}_6$  at 30 kilobars pressure and its application to pyroxenes from kimberlites. *J.Geophys.Res.* 71, 3567-3576.
- Deer, W.A., Howie, R.A. and Zussman, J. (1966) An introduction to the rock-forming minerals. Longman, London, 528p.

- De Waard, D. (1965) A proposed subdivision of the granulite facies. *Amer.J.Sc.* 263, 455-461.
- Drury, S.A. (1978) Were Archaean continental geothermal gradients much steeper than today? *Nature* 274, 720-721.
- Duchesne, J.C. and Demaiffe, D. (1978) Trace elements and anorthosite genesis. *Earth Planet. Sc.Lett.* 38, 249-272.
- Du Toit, M.C. and Van Reenen, D.D. (1977) The southern margin of the Limpopo Mobile Belt, northern Transvaal, with special reference to metamorphism and structure. *Botswana Geol.Surv.Bull.* 12, 83-97.
- Ellis, D.J. and Green, D.H. (1979) An experimental study of the effect of Ca upon garnet-clinopyroxene Fe-Mg exchange equilibria. *Contr.Mineral.Petrol.* 71, 13-22.
- England, P.C. (1979) Continental geotherms during the Archaean. *Nature* 277, 556-558.
- Ferry, J.M. and Spear, F.S. (1978) Experimental calibration of the partitioning of Fe and Mg between biotite and garnet. *Contr.Mineral.Petrol.* 66, 113-117.
- Fisher, J.R. and Zen, E-An. (1971) Thermochemical calculations from hydrothermal phase equilibrium data and the free energy of H<sub>2</sub>O. *Amer.J.Sc.* 270, 297-314.
- Fripp, R.E.P. (1981a) The geology of the Sand River area near Messina, Limpopo Mobile Belt, South Africa. *Geol. Soc.S.Af.Spec.Pub.* (in press).
- Fripp, R.E.P. (1981b) The ancient Sand River Gneisses, Limpopo Mobile Belt, South Africa. *Geol.Soc.Aust. Spec.Pub.* 7 (in press).
- Fripp, R.E.P. (1981c) The Precambrian geology of an area around the Sand River near Messina, northern Transvaal. Ph.D thesis Univ.Witwatersrand (in prep.).
- Fripp, R.E.P., Lilly, P.A. and Barton, J.M. (1979) The structure and origin of the Singelele Gneiss, Limpopo Mobile Belt, South Africa. *Trans.Geol.Soc. S.Afr.* 82, 161-167.

- Green, D.H. and Ringwood, A.E. (1967) An experimental investigation of the gabbro to eclogite transformation and its petrological implications. *Geochim.Cosmochim. Acta* 31, 767-833.
- Graham, R.H. (1974) A structural investigation of the southern part of the Limpopo Mobile Belt and the adjacent Kaapvaal craton, South Africa. 18th Ann.Rep.Res. Inst.Afr.Geol. Univ.Leeds.
- Horiya, Y. and Kennedy, G.C. (1968) Equilibrium study of anorthite under high pressure and high temperature. *Amer.J.Sc.* 266, 193-203.
- Helgeson, H.C., Delany, J.M., Nesbitt, H.W. and Bird, D.K. (1978) Summary and critique of the thermodynamic properties of rock-forming minerals. *Amer.J.Sc.* 278A, 1-229.
- Hensen, B.J. (1976) The stability of pyrope-grossular garnet with excess silica. *Contr.Mineral.Petrol.* 55, 279-292.
- Hensen, B.J. and Green, D.H. (1971) Experimental study of the stability of cordierite and garnet in pelitic compositions at high pressures and temperatures - I. Compositions with excess alumino-silicate. *Contr. Mineral.Petrol.* 33, 309-330.
- Hensen, B.J. and Green, D.H. (1972) Experimental study of the stability of cordierite and garnet in pelitic compositions at high pressures and temperatures - II. Compositions without excess alumino-silicate. *Contr.Mineral.Petrol.* 35, 331-354.
- Hensen, B.J. and Green, D.H. (1973) Experimental study of the stability of cordierite and garnet in pelitic compositions at high pressures and temperatures - III. Synthesis of experimental data and geological applications. *Contr.Mineral.Petrol.* 38, 151-166.
- Herzberg, C.T. (1978) Pyroxene geothermometry and geobarometry: experimental and thermodynamic evaluation of some subsolidus phase relations involving pyroxenes in the system  $\text{CaO-MgO-Al}_2\text{O}_3 - \text{SiO}_2$  *Geochim.Cosmochim.Acta* 42, 945-957.

- Holdaway, M.J. (1976) Mutual compatibility relations of the  $\text{Fe}^{2+}$ -Mg-Al silicates at 800°C and 3 kbar. *Amer.J. Sc.* 276, 285-308.
- Holdaway, M.J. and Lee, S.M. (1977) Fe-Mg cordierite stability in high-grade pelitic rocks based on experimental, theoretical and natural observations. *Contr.Mineral. Petrol.* 63, 175-198.
- Hor, A.K., Hutt, D.K., Smith, J.V., Wakefield, J. and Windley, B.F. (1975) Petrochemistry and mineralogy of early Precambrian anorthositic rocks of the Limpopo Mobile Belt, southern Africa. *Lithos* 8, 297-310.
- Horrocks, P.C. (1975) The geology of the southern portion of the farm Artonvilla 778, east of Messina, northern Transvaal. B.Sc.Hons.Report Univ.Witwatersrand (unpub.), 59p.
- Horrocks, P.C. (1980) Ancient Archaean supracrustal rocks from the Limpopo Mobile Belt. *Nature* 286, 596-599.
- Horrocks, P.C. (1981) The Precambrian geology of an area between Messina and Tshipise, Limpopo Mobile Belt. *Geol.Soc.S.Afr.Spec.Pub.* (in prep.)
- Jansen, H. (1975) The Soutpansberg trough (northern Transvaal) - aulacogen. *Trans.Geol.Soc.S.Afr.* 78, 129-136.
- Jansen, H. (1976). Author's reply on 'Discussion' by O.B. Barker of 'The Soutpansberg trough (northern Transvaal) - an aulacogen' by H. Jansen (op.cit.), *Trans.Geol.Soc.S. Afr.* 79, 146-148.
- Jansen, H. (1977) Limpopo Belt-Transvaal craton relationships. *Botswana Geol.Surv.Bull.* 12, 99-104.
- Kennedy, W.Q. (1951) Sedimentary differentiation as a factor in Moine-Torridonian correlation, *Geol.Mag.* 88, p.258.
- Keesmann, I., Matthies, S., Schreyer, W. and Seifert, F. (1971) Stability of almandine in the system  $\text{FeO-Fe}_2\text{O}_3\text{-Al}_2\text{O}_3\text{-SiO}_2\text{-H}_2\text{O}$  at elevated pressures. *Contr.Mineral. Petrol.* 31, 132-144.
- Key, R.M. and Hutton, S.M. (1976) The tectonic generation of the Limpopo Mobile Belt and a definition of its western extremity. *Precamb.Res.* 3, 79-90.

- Kratz, R. (1973) Kinetics of the crystallization of garnet at two localities near Yellowknife, Canada. *Mineral.* 12, 1-20.
- Lal, R.K., Ackermann, D., Seifert, F. and Haldar, S.K. (1978) Chemographic relationships in sapphirine-bearing rocks from Sonapahar, Assam, India, *Contr. Mineral. Petrol.* 67, 169-187.
- Leyreloup, A., Lasnier, B. and Marchand, J. (1975) Retrograde corona-forming reactions in high-pressure granulite facies rocks, *Pétrologie*, I, 43-55.
- Light, M.P.R., Broderick, T.J. and Watkeys, M.K. (1977) A preliminary report on the Central Zone of the Limpopo Mobile Belt, Rhodesia. *Botswana Geol. Surv. Bull.* 12, 61-73.
- Light, M.P.R. and Watkeys, M.K. (1978) An outline of the Archaean and early Proterozoic geological history of the region around Beitbridge. *Rhodesia Geol. Surv. Ann.* III, 35-40.
- Lindsley, D.H. and Dixon, S.A. (1976) Diopside-enstatite equilibria at 850°C to 1400°C, 5 to 35 kbar. *Amer. J. Sc.* 276, 1285-1301.
- Luth, W.C., Jahnes, R.H. and Tuttle, O.F. (1964) The granite system at pressures of 4 to 10 kilobars. *J. Geophys. Res.* 69, 759-773.
- MacGregor, A.M. (1953) Precambrian formations of tropical southern Africa. *Int. Congr. Algiers 1952*, 1.
- McCarthy, T.S. (1976) Chemical interrelationships in a low-pressure granulite terrain in Namaqualand, South Africa, and their bearing on granite genesis and the composition of the lower crust. *Geochim. Cosmochim. Acta* 40, 1057-1068.
- McCarthy, T.S. (1977) Geochemical studies of selected granitic terrains in South Africa. Ph.D thesis Univ. Witwatersrand (unpub.).
- Moorbath, S. (1975) The geological significance of early Precambrian rocks. *Proc. Geol. Assoc.* 86, 259-279.

- Nehru, C.E. and Wyllie, P.J. (1974) Electron Microprobe measurement of pyroxenes coexisting with H<sub>2</sub>O-undersaturated liquid in the join  $\text{CaMgSi}_2\text{O}_6\text{-Mg}_2\text{Si}_2\text{O}_6\text{-H}_2\text{O}$  at 30 kilobars, with applications to geothermometry. *Contr.Mineral.Petr.* 48, 221-228.
- Newton, R.C., Charlu, T.V. and Kleppa, O.J. (1977) Thermochemistry of high pressure garnets and clinopyroxenes in the system  $\text{CaO-MgO-Al}_2\text{O}_3\text{-SiO}_2$ . *Geochim.Cosmochim.Acta* 41, 369-377.
- Norrish, K. and Hutton, J.T. (1969) An accurate X-ray spectrographic method for the analysis of a wide range of geological materials. *Geochim.Cosmochim.Acta* 33, 431-453.
- O'Hara, M.J. (1977) Thermal history of excavations of Archaean gneisses from the base of the continental crust. *J.Geol.Soc.Lond.* 134, 185-200.
- O'Hara, M.J. and Yarwood, G. (1978) High pressure-temperature point on an Archaean geotherm, implied magma genesis by crustal anatexis, and consequences for garnet-pyroxene thermometry and barometry. *Phil.Trans.Roy.Soc.Lond.* A288, 441-456.
- Orville, P.M. (1972) Plagioclase cation exchange equilibria with aqueous chloride solution at 700°C and 2000 bars in the presence of quartz. *Amer.J.Sc.* 272, 234-272.
- Pearce, T.H. (1970) Chemical variations in the Palisade sill. *J.Petrol.* 11, 15-32.
- Pettijohn, F.J. (1957) *Sedimentary Rocks*. Harper and Bros (2nd ed.), New York, 718p.
- Powell, R. (1975) Thermodynamics of coexisting cummingtonite-hornblende pairs. *Contr.Mineral.Petrol.* 51, 29-37.
- Powell, R. (1978) The thermodynamics of pyroxene geotherms. *Phil.Trans.Roy.Soc.Lond.* A288, 457-469.
- Raase, P. (1974) Al and Ti contents of hornblende, indicators of pressure and temperature of regional metamorphism. *Contr.Mineral.Petrol.* 45, 231-236.

- and Green, D.H. (1974) Experimental determination of the temperature and pressure dependence of the Fe-Mg partition coefficient for coexisting garnet and clinopyroxene. *Contr.Mineral.Petrol.* 48, 179-203.
- Lyons, R.C. (1967) The estimation of mass absorption coefficients by Compton scattering: improvements and extensions of the method. *Amer.Mineral.* 52, 1493-1502.
- Rhodesia Geological 1 : 1 000 000 Map. 1977 (7th ed.).
- Richardson, S.W., Gilbert, M.C. and Bell, P.M. (1969) Experimental determination of the kyanite-andalusite and andalusite-sillimanite equilibria: the aluminium silicate triple-point. *Amer.J.Sc.* 267, 259-272.
- Robertson, I.D.M. (1968) Granulite metamorphism of the basement complex in the Limpopo metamorphic zone. *Geol.Soc.S.Afr. Annex*, 125-132.
- Robertson, I.D.M. (1973) Potash granites of the southern edge of the Rhodesian craton and the northern granulite zone of the Limpopo Mobile Belt. *Geol.Soc.S.Afr. Spec.Pub.* 3, 265-276.
- Robertson, I.D.M. (1977) Some granulite facies metasediments of the Rhodesian part of the North Marginal Zone of the Limpopo Mobile Belt. *Botswana Geol.Surv.Bull.* 12, 157-176.
- Robie, R.A., Hemingway, B.S. and Fisher, J.R. (1976) Thermodynamic properties of minerals and related substances at 298,15°K and 1 bar ( $10^5$  Pascals) pressure and at higher temperatures. *U.S.Geol.Surv. Bull.* 1452, 456p.
- Ryburn, R.J., Raheim, A. and Green, D.H. (1976) Determination of the P,T paths of natural eclogites during metamorphism - a record of subduction. *Lithos* 9, 161-164.
- Saxena, S.K. (1976) Two-pyroxene geothermometer: a model with an approximate solution. *Amer.Mineral.* 61, 643-652.



- Saxena, S.K. and Nehru, C.E. (1975) Enstatite-diopside geothermometry. *Contr.Mineral.Petrol.* 47, 39-267.
- Schreyer, W. (1968) A reconnaissance study of the system  $MgO-Al_2O_3-SiO_2-H_2O$  at pressures between 10 and 25 kbar. *Carnegie Inst.Wash.Year Book* 66, 380-392.
- Schreyer, W. and Seifert, F. (1969) Compatibility relationships of the aluminium silicates in the system  $MgO-Al_2O_3-SiO_2-H_2O$  and  $K_2O-MgO-Al_2O_3-SiO_2-H_2O$  at high pressures. *Amer.J.Sc.* 267, 371-388.
- Schreyer, W. and Abraham, K. (1976) Natural boron-bearing kornierupine and its breakdown products in a sapphirine rock of the Limpopo Belt, southern Africa. *Contr.Mineral.Petrol.* 54, 109-126.
- Schwardtner, W.M., Waddington, D.H. and Stollery, G. (1974) Polycrystalline pseudomorphs as natural gauges of incremental palaeo-strain. *N.Jb.Mineral.Mh.* 4, 174-182.
- Seifert, F. (1974) Stability of sapphirine: a study of the aluminous part of the system  $MgO-Al_2O_3-SiO_2-H_2O$ . *J.Geol.* 82, 173-204.
- Shaw, D.M. (1968) A review of K/Rb fractionation trends by covariance analysis. *Geochim.Cosmochim.Acta* 32, 573-597.
- Shaw, D.M. (1970) Trace element fractionation during anatexis. *Geochim.Cosmochim.Acta* 34, 237-243.
- Shenge, P.G. (1946) The geology of the Messina copper mines and surrounding country. *Geol.Surv.S.Afr.Mem.* 40, 272p.
- Shenge, P.G., Le Roex, H.D. and Nel, H.J. (1948) The geology of the country around Messina. *Geol.Surv.S.Afr. Explan.Sheet* 46.
- Stormer, J.C. and Whitney, J.A. (1977) Two-feldspar geothermometry in granulite facies metamorphic rocks - sapphirine granulites from Brazil. *Contr.Mineral.Petrol.* 65, 123-133.

- Touret, J. (1971) Le facies granulite en Norvège Méridionale. *Lithos* 4, 423-436.
- Tracy, R.J., Robinson, P. and Thompson, A.B. (1976) Garnet composition and zoning in the determination of temperature and pressure of metamorphism, Central Massachusetts. *Amer.Mineral.* 61, 762-775.
- Thompson, J.B. (1957) The graphical analysis of mineral assemblages in pelitic schists. *Amer.Mineral.* 42, 842-858.
- Thompson, A.B. (1976) Mineral reactions in pelitic rocks: II. Calculation of some P-T-X(Fe-Mg) phase relations. *Amer.J.Sc.* 276, 425-454.
- Thompson, A.B., Tracy, R.J., Lyttle, P.T. and Thompson, J.B. (1977) Prograde reaction histories deduced from compositional zonation and mineral inclusions in garnet from the Gassetts schist, Vermont. *Amer.J.Sc.* 277, 1152-1167.
- Van Reenen, D.D. and Du Toit, M.C. (1970) The reaction garnet + quartz = cordierite + hypersthene in granulites of the Limpopo Metamorphic Complex in northern Transvaal. *Geol.Soc.S.Afr.Spec.Pub.* 4, 149-177.
- Van Zyl, J.S. (1950) Aspects of the geology of the northern Soutpansberg area. *Ann. Univ. Stellenbosch* 26, 1-95.
- Von Gruenewaldt, G. (1973) The modified differentiation index and the modified crystallization index as parameters of differentiation in layered intrusions. *Trans. Geol.Soc.S.Afr.* 76, 53-61.
- Watkeys, M.K. (1977) The geology of the area west of Beitbridge. *Rhodesia Geol.Surv. Ann.* 2, 1-14.
- Watkeys, M.K. (1979) Explanation of the geological map of the country west of Beitbridge. *Rhodesia Geol.Surv. Short Report* 45, 96p.
- Wells, P.R.A. (1977) Pyroxene thermometry in simple and complex systems. *Contr.Mineral.Petrol.* 62, 129-139.

- Wells, P.R.A. (1979) Chemical and thermal evolution of Archaean sialic crust, southern west Greenland. *J.Petrol.* 20, 187-226.
- Windley, B.F. (1973) Archaean anorthosites: a review with the Fiskenaesset Complex, West Greenland as a model for interpretation. *Geol.Soc.S.Afr.Spec.Pub.* 3, 319-332.
- Winkler, H.G.F. (1974) *Petrogenesis of Metamorphic Rocks.* Springer-Verlag (3rd ed.), New York, 320p.
- Wood, B.J. (1974) The solubility of alumina in orthopyroxene coexisting with garnet. *Contr.Mineral.Petrol.* 46, 1-15.
- Wood, B.J. (1977) The activities of components in clinopyroxene and garnet solid solutions and their application to rocks. *Phil.Trans.Roy.Soc.Lond.* A286, 331-342.
- Wood, B.J. (1978) Reactions involving anorthite and  $\text{CaAl}_2\text{SiO}_6$  pyroxene at high pressures and temperatures. *Amer. J.Sc.* 278, 930-942.
- Wood, B.J. (1979) Activity-composition relationships in  $\text{Ca}(\text{Mg,Fe})\text{Si}_2\text{O}_6$ - $\text{CaAl}_2\text{SiO}_6$  clinopyroxene solid solutions. *Amer.J.Sc.* 279, 854-875.
- Wood, B.J. and Banno, S. (1973) Garnet-orthopyroxene and orthopyroxene-clinopyroxene relationships in simple and complex systems. *Contr.Mineral.Petrol.* 42, 109-124.
- Wood, B.J. and Fraser, D.G. (1976) *Elementary Thermodynamics for Geologists.* Oxford Univ. Press, 303p.

## EFFECTS OF METAMORPHISM ON THE Rb-Sr AND U-Pb SYSTEMATICS OF THE SINGELELE AND BULU GNEISSES, LIMPOPO MOBILE BELT, SOUTHERN AFRICA\*

by

J. M. BARTON Jr., B. RYAN, R. E. P. FRIPP and F. HORROCKS

### ABSTRACT

The results of Rb-Sr and Pb-Pb zircon whole-rock and U-Pb zircon isotopic studies are presented of the Singelele and Bulu Gneisses of the Central Zone of the Limpopo Mobile Belt. The zircon U-Pb results from the Singelele Gneiss show ages that are consistent with the emplacement age of that unit while the whole-rock results from the Bulu Gneiss indicate that the gneiss is younger than the emplacement age of that unit. The results from both units are consistent with the interpretation that the gneisses are younger than the emplacement age of that unit. The results from both units are consistent with the interpretation that the gneisses are younger than the emplacement age of that unit. The results from both units are consistent with the interpretation that the gneisses are younger than the emplacement age of that unit.

### CONTENTS

	Page
I INTRODUCTION	259
II THE SINGELELE GNEISS	260
III THE BULU GNEISS	260
IV ANALYTICAL TECHNIQUES, SAMPLING LOCATIONS AND RESULTS	260
V DISCUSSION	268
VI CONCLUSIONS	268
Acknowledgments	268
REFERENCES	268

### I. INTRODUCTION

As more and more isotopic age determinations are being made it is becoming increasingly evident that, in some instances, and perhaps in most instances, the ages measured bear little relationship to the actual age of emplacement of the rock unit involved, even though the measured ages are statistically meaningful (see e.g. Allsopp, 1970, 1977; Moorbath, 1975; Roddick and Compston, 1977; Barton *et al.*, 1978; Bell and Blenkinsop, 1978; Cooper *et al.*, 1979; Black *et al.*, 1979; Welke *et al.*, 1980). This relationship involving mica-model, mica whole-rock and other mineral ages using Rb-Sr and K-Ar techniques is well documented (see e.g. Hart, 1964; Armstrong, 1968; Faure and Powell, 1972; Faure, 1973). In the cases of Rb-Sr, Th-Pb, Sm-Nd and  $^{207}\text{Pb}/^{204}\text{Pb}$  versus  $^{206}\text{Pb}/^{204}\text{Pb}$  (Pb-Pb) whole-rock and U-Pb zircon dating, this relationship is sometimes less obvious, especially in metamorphic rocks of Precambrian age that lack fossils for stratigraphic comparison. Nevertheless, ages determined by these latter techniques are often different than their "true ages" of emplacement as deduced by other means (see Roddick and Compston, 1977; Barton *et al.*, 1978; Allsopp *et al.*, 1979; Black *et al.*, 1979). In the instances of smaller ages, these may often be equated with subsequent metamorphic events affecting the rocks or with the passing of the rocks through some conditions of temperature

and, to a lesser extent, pressure whereby they become closed systems with respect to the parent and daughter isotopes (regional uplift and consequent erosion to a new level). Larger ages may result from analysing rocks composed of two radically different isotopic natures or from analysing rocks representing different sized isotopic domains within a single unit (Roddick and Compston, 1977; Welke *et al.*, 1980). Where other criteria are lacking, to distinguish between "true ages" of emplacement and younger or older ages is a subjective business, at best, and more probably is impossible (Allsopp, 1977). Hence, to blindly accept isotopic ages as ages of emplacement or as ages of metamorphism is rife with risk.

To illustrate this risk, the results of Rb-Sr and Pb-Pb whole-rock and U-Pb zircon isotopic studies are presented of the Singelele and Bulu Gneisses of the Central Zone of the Limpopo Mobile Belt. These isotopic dating techniques are the ones most commonly applied to Precambrian rocks. The Central Zone of the Limpopo Mobile Belt is a highly deformed polymetamorphic terrain situated between the Rhodesian and Kaapvaal Cratons (Barton and Kev, 1980) and the emplacement ages of the two gneissic units into this terrane are reasonably well known from other criteria. The present "state of the art" multiple technique approach to isotopic studies in Precambrian terranes is discussed. This approach is designed to minimise the uncertainties of interpretation inherent in such studies.

\*A South African Contribution to the International Geodynamics Project, No. 55

II. THE SINGELELE GNEISS

The Singelele Gneiss (Fig. 1) (Söhnge, 1945; Söhnge *et al.*, 1948; Bahnemann, 1972; Fripp *et al.*, 1979) is a lithologically defined unit of distinctive brownish weathering, fine- to coarse-grained pink quartzofeldspathic gneiss. It forms a layer or layers within the sequence of supracrustal rocks of the Central Zone of the Limpopo Mobile Belt and is believed to have originally been either a pyroclastic rock or an arkosic sandstone (Fripp *et al.*, 1979). Being part of the sequence of supracrustal rocks implies that the Singelele Gneiss was emplaced some time during the interval of time between about 3 300 m.y. ago, when the older suite of dykes was emplaced into the Sand River Gneisses of the basement complex, and about 3 150 m.y. ago, when the Messina Layered Intrusion was emplaced into the supracrustal rocks (Barton *et al.*, 1979, 1979; Barton, unpubl. data). The Singelele Gneiss, the remaining supracrustal rocks and the Messina Layered Intrusion were subjected to four periods of deformation: the first one prior to about 3 150 m.y. ago, the second one (the principal fabric-forming event) occurring about 3 150 m.y. ago and the third and fourth ones occurring between about 2 700 m.y. ago and about 2 600 m.y. ago (Barton *et al.*, 1979; Barton and Key, 1980). The terrain in which the Singelele Gneiss occurs was raised to approximately its present crustal level by about 1 950 m.y. ago (Barton and Ryan, 1977), but it was locally involved

in the copper mineralisation in the Messina area, which may have occurred about 1 700 m.y. ago (Söhnge, 1945; Jacobsen, 1966; Jacobsen *et al.*, 1975; Barton, 1979).

III. THE BULAI GNEISS

The Bulai Gneiss (Söhnge, 1945; Söhnge *et al.*, 1948) is a distinctive brown weathering, pinkish, coarse-grained porphyritic gneiss occurring primarily west of Messina (Fig. 1). Small outcrops of a lithologically similar rock also occur near Tshipise (Fig. 1). This unit is an orthogneiss of granitic composition, containing appreciable hornblende and biotite, and it was intruded into the sequence of supracrustal rocks of the Central Zone of the Limpopo Mobile Belt, including the Singelele Gneiss, after the second penetrative deformation of these rocks about 3 150 m.y. ago (Barton and Key, 1980). It contains xenoliths of deformed supracrustal gneisses and was affected by the third and fourth regional deformational events between about 2 700 m.y. ago and about 2 600 m.y. ago. As with the Singelele Gneiss, the terrain in which the Bulai Gneiss occurs was raised to approximately its present crustal level by about 1 950 m.y. ago (Barton and Ryan, 1977).

IV. ANALYTICAL TECHNIQUES, SAMPLING LOCATIONS AND RESULTS

The analytical techniques utilised in this study are fairly standard and are described in Barton *et al.* (1977) and Bar-



Figure 1. Geological map of the Central Zone of the Limpopo Mobile Belt, Rhodesia (modified from Fig. 1 of Fripp *et al.*, 1979). M - Messina; T - Tshipise; 1 - Type locality of the Bulai Gneiss; 2 - Farm Skulpfontein; 3 - Type locality of the Singelele Gneiss (Gja-Tshirungule) including Area-1, 2 and 3; 4 - Singelele Gneiss, Farm Osten; 5 - Singelele Gneiss, Farm Skulpfontein; 6 - Porphyritic 'Bulai-type' gneiss, Farm Skulpfontein.

for 1980). Analytical means of mineral isograds are plotted in these diagrams. Where appropriate, isograds have been fitted to the analytical means by the technique of York (1969) using the regression test in Table V. Ages were estimated using the isograds conditions established by Sengy and Tsig (1971). Where the ratio of  $^{87}\text{Sr}/^{86}\text{Sr}$  is not limited by the number of analyses being regressed means are (N MSWD) or (MSWD) are less than 2; the data were taken as datum on isograds (Hacker et al., 1972). In this case, the initial isotope ratio is used, except when the regression fit was too poor to yield a date; errors produced by the geochemical calculations were. Where  $^{87}\text{Sr}/^{86}\text{Sr}$  or MSWD was greater than 2; the data were taken as datum on isograds (Hacker et al., 1972). In this case, the rocks from which the analyses were taken were subjected to completely closed systems with respect to the isotope  $^{87}\text{Sr}/^{86}\text{Sr}$  isochronization.

The mean low-temperature mineral isotope ratios. These uncertainties mean that corrections are of absolute age to age indicated and percentage "loss" can not be taken as the isotope ratios, the geological uncertainties can be calculated and corrected.

Samples of the Sengy Group were collected at five localities (Fig. 1): (1) Dora locality; (2) Dora locality; (3) Gao-Toumangshan on Maotou, one locality on Farm Doren and one locality on Farm Skulp (near Farm Tampo). Of the five localities in the type area (see text) of rocks was collected from the quarry of Gao-Toumangshan (Area 1), and one rock was collected from the quarry of Dora (Area 2) approximately 300 meters below Area 1, and one piece of rocks was collected from the old railway cutting (Area 3), approximately 300 meters northwest of Area 1. Van Boven and Hinton (1972) collected the summit of the Sengy Group that they analysed from Area 1.

TABLE I  
Whole-Rock  $^{87}\text{Sr}/^{86}\text{Sr}$  and  $^{87}\text{Rb}/^{86}\text{Sr}$  Isotope Ratios

Sample	$^{87}\text{Sr}/^{86}\text{Sr}$	$^{87}\text{Rb}/^{86}\text{Sr}$	Age (Myr)	MSWD	Age (Myr)
<b>Sengy Group - Dora Group - Area 1</b>					
D01	0.7101	0.0454	13.4	0.2	13.4
D02	0.7102	0.0454	13.4	0.2	13.4
D03	0.7103	0.0454	13.4	0.2	13.4
D04	0.7104	0.0454	13.4	0.2	13.4
D05	0.7105	0.0454	13.4	0.2	13.4
D06	0.7106	0.0454	13.4	0.2	13.4
D07	0.7107	0.0454	13.4	0.2	13.4
D08	0.7108	0.0454	13.4	0.2	13.4
D09	0.7109	0.0454	13.4	0.2	13.4
D10	0.7110	0.0454	13.4	0.2	13.4
D11	0.7111	0.0454	13.4	0.2	13.4
D12	0.7112	0.0454	13.4	0.2	13.4
D13	0.7113	0.0454	13.4	0.2	13.4
D14	0.7114	0.0454	13.4	0.2	13.4
D15	0.7115	0.0454	13.4	0.2	13.4
D16	0.7116	0.0454	13.4	0.2	13.4
D17	0.7117	0.0454	13.4	0.2	13.4
D18	0.7118	0.0454	13.4	0.2	13.4
D19	0.7119	0.0454	13.4	0.2	13.4
D20	0.7120	0.0454	13.4	0.2	13.4
D21	0.7121	0.0454	13.4	0.2	13.4
D22	0.7122	0.0454	13.4	0.2	13.4
D23	0.7123	0.0454	13.4	0.2	13.4
D24	0.7124	0.0454	13.4	0.2	13.4
D25	0.7125	0.0454	13.4	0.2	13.4
D26	0.7126	0.0454	13.4	0.2	13.4
D27	0.7127	0.0454	13.4	0.2	13.4
D28	0.7128	0.0454	13.4	0.2	13.4
D29	0.7129	0.0454	13.4	0.2	13.4
D30	0.7130	0.0454	13.4	0.2	13.4
D31	0.7131	0.0454	13.4	0.2	13.4
D32	0.7132	0.0454	13.4	0.2	13.4
D33	0.7133	0.0454	13.4	0.2	13.4
D34	0.7134	0.0454	13.4	0.2	13.4
D35	0.7135	0.0454	13.4	0.2	13.4
D36	0.7136	0.0454	13.4	0.2	13.4
D37	0.7137	0.0454	13.4	0.2	13.4
D38	0.7138	0.0454	13.4	0.2	13.4
D39	0.7139	0.0454	13.4	0.2	13.4
D40	0.7140	0.0454	13.4	0.2	13.4
D41	0.7141	0.0454	13.4	0.2	13.4
D42	0.7142	0.0454	13.4	0.2	13.4
D43	0.7143	0.0454	13.4	0.2	13.4
D44	0.7144	0.0454	13.4	0.2	13.4
D45	0.7145	0.0454	13.4	0.2	13.4
D46	0.7146	0.0454	13.4	0.2	13.4
D47	0.7147	0.0454	13.4	0.2	13.4
D48	0.7148	0.0454	13.4	0.2	13.4
D49	0.7149	0.0454	13.4	0.2	13.4
D50	0.7150	0.0454	13.4	0.2	13.4
D51	0.7151	0.0454	13.4	0.2	13.4
D52	0.7152	0.0454	13.4	0.2	13.4
D53	0.7153	0.0454	13.4	0.2	13.4
D54	0.7154	0.0454	13.4	0.2	13.4
D55	0.7155	0.0454	13.4	0.2	13.4
D56	0.7156	0.0454	13.4	0.2	13.4
D57	0.7157	0.0454	13.4	0.2	13.4
D58	0.7158	0.0454	13.4	0.2	13.4
D59	0.7159	0.0454	13.4	0.2	13.4
D60	0.7160	0.0454	13.4	0.2	13.4
D61	0.7161	0.0454	13.4	0.2	13.4
D62	0.7162	0.0454	13.4	0.2	13.4
D63	0.7163	0.0454	13.4	0.2	13.4
D64	0.7164	0.0454	13.4	0.2	13.4
D65	0.7165	0.0454	13.4	0.2	13.4
D66	0.7166	0.0454	13.4	0.2	13.4
D67	0.7167	0.0454	13.4	0.2	13.4
D68	0.7168	0.0454	13.4	0.2	13.4
D69	0.7169	0.0454	13.4	0.2	13.4
D70	0.7170	0.0454	13.4	0.2	13.4
D71	0.7171	0.0454	13.4	0.2	13.4
D72	0.7172	0.0454	13.4	0.2	13.4
D73	0.7173	0.0454	13.4	0.2	13.4
D74	0.7174	0.0454	13.4	0.2	13.4
D75	0.7175	0.0454	13.4	0.2	13.4
D76	0.7176	0.0454	13.4	0.2	13.4
D77	0.7177	0.0454	13.4	0.2	13.4
D78	0.7178	0.0454	13.4	0.2	13.4
D79	0.7179	0.0454	13.4	0.2	13.4
D80	0.7180	0.0454	13.4	0.2	13.4
D81	0.7181	0.0454	13.4	0.2	13.4
D82	0.7182	0.0454	13.4	0.2	13.4
D83	0.7183	0.0454	13.4	0.2	13.4
D84	0.7184	0.0454	13.4	0.2	13.4
D85	0.7185	0.0454	13.4	0.2	13.4
D86	0.7186	0.0454	13.4	0.2	13.4
D87	0.7187	0.0454	13.4	0.2	13.4
D88	0.7188	0.0454	13.4	0.2	13.4
D89	0.7189	0.0454	13.4	0.2	13.4
D90	0.7190	0.0454	13.4	0.2	13.4
D91	0.7191	0.0454	13.4	0.2	13.4
D92	0.7192	0.0454	13.4	0.2	13.4
D93	0.7193	0.0454	13.4	0.2	13.4
D94	0.7194	0.0454	13.4	0.2	13.4
D95	0.7195	0.0454	13.4	0.2	13.4
D96	0.7196	0.0454	13.4	0.2	13.4
D97	0.7197	0.0454	13.4	0.2	13.4
D98	0.7198	0.0454	13.4	0.2	13.4
D99	0.7199	0.0454	13.4	0.2	13.4
D100	0.7200	0.0454	13.4	0.2	13.4
D101	0.7201	0.0454	13.4	0.2	13.4
D102	0.7202	0.0454	13.4	0.2	13.4
D103	0.7203	0.0454	13.4	0.2	13.4
D104	0.7204	0.0454	13.4	0.2	13.4
D105	0.7205	0.0454	13.4	0.2	13.4
D106	0.7206	0.0454	13.4	0.2	13.4
D107	0.7207	0.0454	13.4	0.2	13.4
D108	0.7208	0.0454	13.4	0.2	13.4
D109	0.7209	0.0454	13.4	0.2	13.4
D110	0.7210	0.0454	13.4	0.2	13.4
D111	0.7211	0.0454	13.4	0.2	13.4
D112	0.7212	0.0454	13.4	0.2	13.4
D113	0.7213	0.0454	13.4	0.2	13.4
D114	0.7214	0.0454	13.4	0.2	13.4
D115	0.7215	0.0454	13.4	0.2	13.4
D116	0.7216	0.0454	13.4	0.2	13.4
D117	0.7217	0.0454	13.4	0.2	13.4
D118	0.7218	0.0454	13.4	0.2	13.4
D119	0.7219	0.0454	13.4	0.2	13.4
D120	0.7220	0.0454	13.4	0.2	13.4
D121	0.7221	0.0454	13.4	0.2	13.4
D122	0.7222	0.0454	13.4	0.2	13.4
D123	0.7223	0.0454	13.4	0.2	13.4
D124	0.7224	0.0454	13.4	0.2	13.4
D125	0.7225	0.0454	13.4	0.2	13.4
D126	0.7226	0.0454	13.4	0.2	13.4
D127	0.7227	0.0454	13.4	0.2	13.4
D128	0.7228	0.0454	13.4	0.2	13.4
D129	0.7229	0.0454	13.4	0.2	13.4
D130	0.7230	0.0454	13.4	0.2	13.4
D131	0.7231	0.0454	13.4	0.2	13.4
D132	0.7232	0.0454	13.4	0.2	13.4
D133	0.7233	0.0454	13.4	0.2	13.4
D134	0.7234	0.0454	13.4	0.2	13.4
D135	0.7235	0.0454	13.4	0.2	13.4
D136	0.7236	0.0454	13.4	0.2	13.4
D137	0.7237	0.0454	13.4	0.2	13.4
D138	0.7238	0.0454	13.4	0.2	13.4
D139	0.7239	0.0454	13.4	0.2	13.4
D140	0.7240	0.0454	13.4	0.2	13.4
D141	0.7241	0.0454	13.4	0.2	13.4
D142	0.7242	0.0454	13.4	0.2	13.4
D143	0.7243	0.0454	13.4	0.2	13.4
D144	0.7244	0.0454	13.4	0.2	13.4
D145	0.7245	0.0454	13.4	0.2	13.4
D146	0.7246	0.0454	13.4	0.2	13.4
D147	0.7247	0.0454	13.4	0.2	13.4
D148	0.7248	0.0454	13.4	0.2	13.4
D149	0.7249	0.0454	13.4	0.2	13.4
D150	0.7250	0.0454	13.4	0.2	13.4
D151	0.7251	0.0454	13.4	0.2	13.4
D152	0.7252	0.0454	13.4	0.2	13.4
D153	0.7253	0.0454	13.4	0.2	13.4
D154	0.7254	0.0454	13.4	0.2	13.4
D155	0.7255	0.0454	13.4	0.2	13.4
D156	0.7256	0.0454	13.4	0.2	13.4
D157	0.7257	0.0454	13.4	0.2	13.4
D158	0.7258	0.0454	13.4	0.2	13.4
D159	0.7259	0.0454	13.4	0.2	13.4
D160	0.7260	0.0454	13.4	0.2	13.4
D161	0.7261	0.0454	13.4	0.2	13.4
D162	0.7262	0.0454	13.4	0.2	13.4
D163	0.7263	0.0454	13.4	0.2	13.4
D164	0.7264	0.0454	13.4	0.2	13.4
D165	0.7265	0.0454	13.4	0.2	13.4
D166	0.7266	0.0454	13.4	0.2	13.4
D167	0.7267	0.0454	13.4	0.	

TABLE II  
Isotopic Data

Loc.	Age <sup>1</sup>	δ <sup>2</sup>	n	SD	Percentage unaffected by A = 0.5
<b>Rock Wholesome Data</b>					
Sequistarite Group - Type Locality - Area 1 and 2	1350 ± 40	0.003 ± 0.0010	2	0.40	2.7
Sequistarite Group - Area 1 (Area 2)	1340 ± 40	0.003 ± 0.0010	2	0.40	2.7
Sequistarite Group - Farn Skulpfontein	1370 ± 40	0.003 ± 0.0010	2	0.40	2.7
Basil Group - Type Locality	1200 ± 40	0.003 ± 0.0010	2	0.40	2.7
Basil Group - Type Locality (excluding the data from Van Meuseveldt and DeWitt 1972)	1200 ± 40	0.003 ± 0.0010	2	0.40	2.7
Perthite "Basil-type" Group - Farn Skulpfontein (Area 1)	1200 ± 40	0.003 ± 0.0010	2	0.40	2.7
Sequistarite Group - Type Locality - Area 1	1360 ± 40		2	0.40	2.7
Sequistarite Group - Type Locality - Area 2	1340 ± 40		2	0.40	2.7
Sequistarite Group - Farn Skulpfontein	1370 ± 40		2	0.40	2.7
Basil Group - Type Locality	1200 ± 40		2	0.40	2.7
Perthite "Basil-type" Group - Farn Skulpfontein	1200 ± 40		2	0.40	2.7

<sup>1</sup> Calculated on the assumed <sup>87</sup>Rb/<sup>86</sup>Rb = 0.0010 ± 0.00010 (DeWitt, 1972)  
<sup>2</sup> Standard deviation (SD) given in parentheses  
<sup>3</sup> n = Number of grains analysed  
<sup>4</sup> Percentage of grains unaffected by A = 0.5

Samples of the Basil Group were collected in two localities (Fig. 1) in the type locality of the Basil Group west of Mosses and in a small outcrop exposed in a road excavation on Farn Skulpfontein (see Tamms, 1966). The samples of Basil Group analysed by Van Meuseveldt and DeWitt (1972) came from the type locality.

Approximately 10 kg samples were collected at each locality and in all cases, except those samples from the type area of the Basil Group, the sample areas came from restricted outcrop areas of not over 1,000 m<sup>2</sup>. Within the

Basil Group, samples were collected from 'cones' separated by several kilometers.

Grains were separated from two samples each of Basil and Sequistarite Group. Each sample was divided into size fractions and between 100 $\mu$  and 500 $\mu$  grain size analysed of each size fraction. It was impossible to further divide the samples according to colour, magnetic susceptibility or morphology. The zircon crystals analysed were in all cases pale brown, inclusion free and subhedral. They were neither normally zoned nor obviously metamict.

TABLE III  
Zircon Isotopic Data

Sample <sup>a</sup>	Age (years)	Age (years)	$\delta^{238}\text{U}/^{235}\text{U}$	$\delta^{238}\text{U}/^{235}\text{U}$	$\delta^{238}\text{U}/^{235}\text{U}$	$\delta^{238}\text{U}/^{235}\text{U}$
<b>Sequistarite Group - Type Locality - Area 1</b>						
S.75.1	1350	1350	0.003	0.003	4.15	0.267
S.75.2	1340	1340	0.003	0.003	4.15	0.267
S.75.3	1370	1370	0.003	0.003	4.15	0.267
S.75.4	1350	1350	0.003	0.003	4.15	0.267
<b>Sequistarite Group - Farn Skulpfontein</b>						
S.75.5	1370	1370	0.003	0.003	4.15	0.267
S.75.6	1340	1340	0.003	0.003	4.15	0.267
S.75.7	1370	1370	0.003	0.003	4.15	0.267
<b>Basil Group - Type Locality</b>						
B.75.1	1200	1200	0.003	0.003	4.15	0.267
B.75.2	1200	1200	0.003	0.003	4.15	0.267
B.75.3	1200	1200	0.003	0.003	4.15	0.267
B.75.4	1200	1200	0.003	0.003	4.15	0.267
<b>Perthite "Basil-type" Group - Farn Skulpfontein</b>						
P.75.1	1200	1200	0.003	0.003	4.15	0.267
P.75.2	1200	1200	0.003	0.003	4.15	0.267
P.75.3	1200	1200	0.003	0.003	4.15	0.267
P.75.4	1200	1200	0.003	0.003	4.15	0.267

<sup>a</sup> Age (years) of sample from 4-point isochron diagram in Table No. 1  
<sup>b</sup> Calculated for assumed <sup>87</sup>Rb/<sup>86</sup>Rb = 0.0010 ± 0.00010 (DeWitt, 1972)

Blank concentrations were sufficiently small that no corrections were made.

The results of Rb-Sr and Pb isotopic analyses of whole-rock samples are listed in Table I and the results of the regression of the analytical results are summarised in Table II. These data are also plotted on Figs 2 through 10. The results of U and Pb analyses of zircons are listed in Table III and are plotted on Fig. 11.

V. DISCUSSION

The simplest, and to most people, philosophically the most satisfying approach to interpreting U-Th-Pb isotopic data is to make the same assumptions that are commonly made for Rb-Sr isotopic dating, i.e. isochrons result when

(1) a system has been closed to parent and daughter elements and (2) a system had a uniform daughter isotopic composition but variable parent-daughter elemental compositions at the time it became closed. The slope of the data array on an isochron diagram is thus related to the time elapsed since the system became closed. This time span may be the time elapsed since a rock unit was emplaced or since it was metamorphosed.

However, it is also possible to obtain statistically significant rectilinear data arrays for both U-Th-Pb and Rb-Sr isotopic data that have no time significance as far as the rock unit is concerned. One possible way is to have the samples composed of two components with homogeneous but distinct compositions. Then a range in measured isotopic compositions is a mixing line between the compositions of these two end member components. A second way is for the rock system to behave regularly in a heterogeneous and/or open manner, i.e. for the initial daughter isotopic ratios to vary exactly proportionally to the parent-daughter elemental ratio and/or for changes in the parent-daughter elemental ratios to be exactly proportional to the values of these ratios. For example, a tertiary Pb-Pb isochron may be generated in this way (Gale and Mussett, 1973).

The lack, in detail, of widespread regularity in geochemical processes argues that the simplest approach of assigning isochrons some age significance is probably the most reliable method of interpreting the data. Secondary chemical changes other than rehomogenisation of the daughter isotopic composition, have a tendency to produce scatter in the data and linear arrays that are error-chrons (see e.g. Roddick and Compston, 1977). It must be remembered, however, that the simplest approach is fallible. Mixing lines may be recognised by the age differences of the end members compared to the age associated with the slope of the mixing line. However, in general, to test for the



Figure 2

Rb-Sr isochron diagram for the samples of the Singelele Gneiss from the type locality (Gi. Ishungulela). Clearly the sample population from Area 1, including the samples analysed by Van der Plighe (1972), are distinct from those from Areas

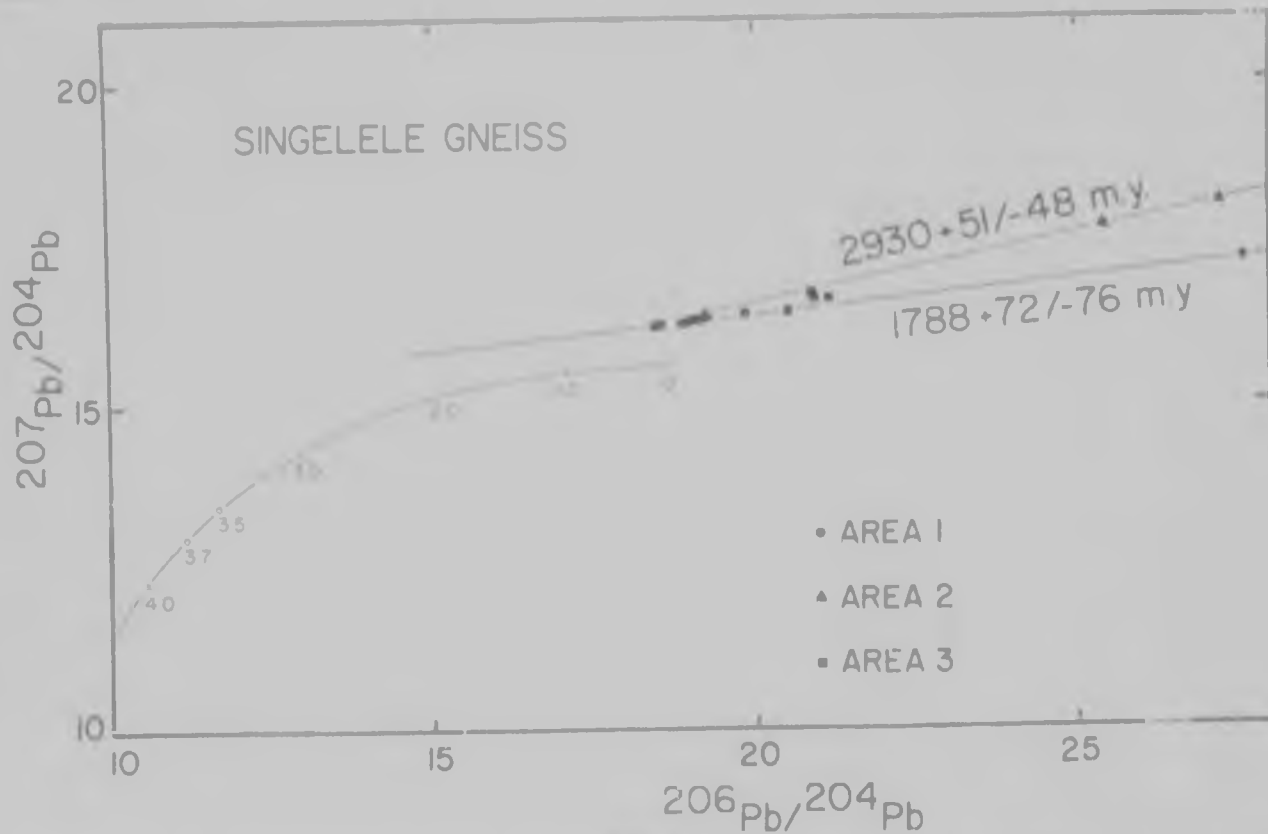


Figure 3

207Pb/204Pb vs 206Pb/204Pb diagram for the samples of the Singelele Gneiss from the type locality (Gi. Ishungulela). The theoretical Pb isotopic growth curve of Blauy and Kretz (1972) calibrated to 20° years is shown for comparison. The samples from Area 1 are characterised as compositions between those from Area 2 and those from Area 3. All of the results plot away from the growth curve, suggesting a larger than average U/Pb ratio in these samples.



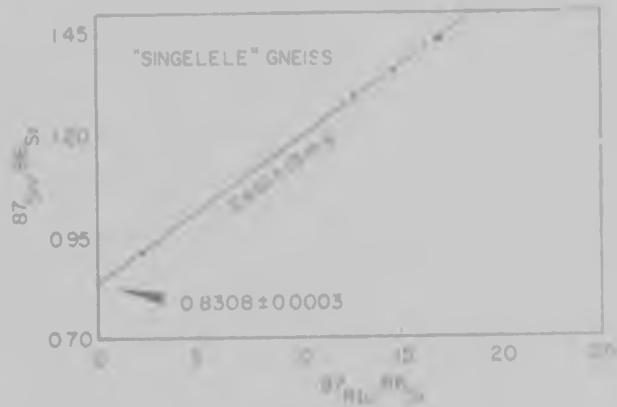


Figure 4

Rb-Sr isochron diagram for the samples of the Singelele Gneiss from Farm Ostend. The very large initial  $^{87}\text{Sr}/^{86}\text{Sr}$  ratio of this isochron is characteristic of rehomogenisation of the Sr isotopes during metamorphism.

ability of other alternative explanations for rectilinear data arrays requires elaborate methods which often are rendered dubious by the number of assumptions necessary to employ them (see e.g. Gale and Mussett, 1973; Welke and Nicolaysen, 1980). For example, U-Pb and Pb-Pb isochrons for a given suite of samples should yield the same ages if the data array is not fortuitous (Gale and Mussett, 1973). However, recent U loss in whole-rock systems has nearly always occurred so that the present U/Pb ratios are often not the correct ones for interpreting the systems. For tertiary Pb-Pb isochrons, testing requires assumptions as to at least one of the following factors: (1) the age of the earth, (2) the original U/Pb ratio of the earth and (3) the time at which the third evolutionary stage began (Gale and Mussett, 1973). Pb-Pb isochrons from systems in which the daughter isotopic composition has been rehomogenised are mathematically indistinguishable from primary or secondary isochrons (Gale and Mussett, 1973).

The suites of samples for each unit analysed for this study were homogeneous on the sample scale, being apparently composed of one rock type with no veins of younger material. In addition, crude estimations of U and Th contents of the whole-rock samples show that the samples are presently active and producing daughter Pb isotopes (Barton, unpubl. data). A mixing line interpretation for the analytical results may thus be discounted.

No internal mathematical tests may be made with the

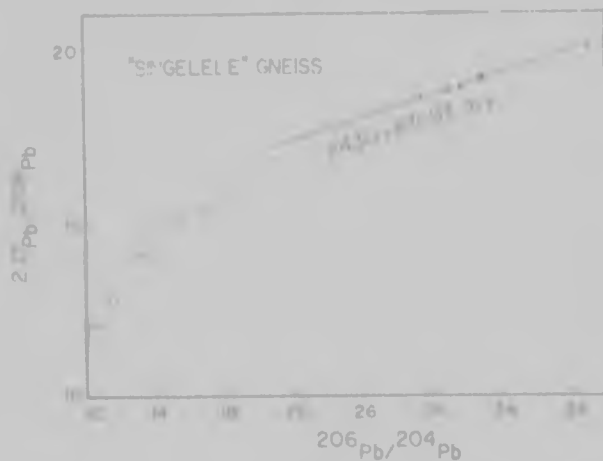


Figure 5

$^{207}\text{Pb}/^{204}\text{Pb}$  versus  $^{206}\text{Pb}/^{204}\text{Pb}$  diagram for the samples of the Singelele Gneiss from Farm Ostend. The terrestrial Pb isotopic growth curve of Stacey and Kramers (1975), calibrated in  $10^9$  years, is shown for comparison and all of the results plot away from this curve, suggesting that these rocks have been in an environment with a larger than average U/Pb ratio.



Figure 6

Rb-Sr isochron diagram for the samples of the Singelele Gneiss from Farm Skullpoint. This is an errorchron.

Rb-Sr whole-rock isotopic data to distinguish whether or not they define isochrons with geologically meaningful ages. Therefore, taken alone, the Rb-Sr data presented here may not be uniquely interpreted.

The Pb-Pb whole-rock isotopic data presented here are not compatible with being primary or secondary isochrons consistent with the terrestrial Pb isotopic evolution models of Stacey and Kramers (1975) or Cumming and Richards (1975). The possible tests are described in Gale and Mussett (1973), but essentially the isochrons do not pass through either the present-day Pb isotopic ratios used in these models nor do they pass through the appropriate Pb isotopic ratios for the ages indicated by the slopes of the isochrons. The data may be interpreted as representing models of two-stage, three-stage, four-stage, etc. development by making the appropriate assumptions including the U/Pb ratios of the rocks prior to the recent U loss. This, however, is a nonconstructive enterprise due to the lack of proper constraints so that unique solutions are impossible.

An alternative approach to interpreting whole-rock U-Th-Pb and Rb-Sr isotopic data is to look at the frequency that specific isochron and mineral ages occur in a given domain composed of several rock units. If clusters of ages occur from units of distinctive stratigraphic ages, then the chances of spurious ages going unrecognised decrease and ages in any given cluster may be assigned, with fair confidence, to at least specific metamorphic events and to possibly emplacement events. This naturally requires a great deal of isotopic age data by numerous techniques as well as a good understanding of the tectonic evolution of the domain by alternative means such as structural analysis. Furthermore, the more complex the history of a domain has been, the more age determinations may be required in order to resolve specific tectonic events.

Clusters of radiometric ages from rocks near Messina in the Central Zone of the Limpopo Mobile Belt that are correlated with tectonic and metamorphic events, occur at  $1150 \pm 50$  m.y.,  $295 \pm 100$  m.y.,  $265 \pm 100$  m.y. and  $195 \pm 50$  m.y. (Barton and Ryan, 1977; Barton *et al.*, 1978; Barton and Key, 1980; Barton, unpubl. data). The majority of the whole-rock isochron ages presented here fall in these clusters (see Table II) and, consequently, they may be equated with isotopic homogenisation during specific tectonic and/or metamorphic events. The data from the Singelele Gneiss on Farm Ostend are anomalous and their significance is unclear. The similarity between the Rb-Sr isochron and the Pb-Pb errorchron ages suggests, however,

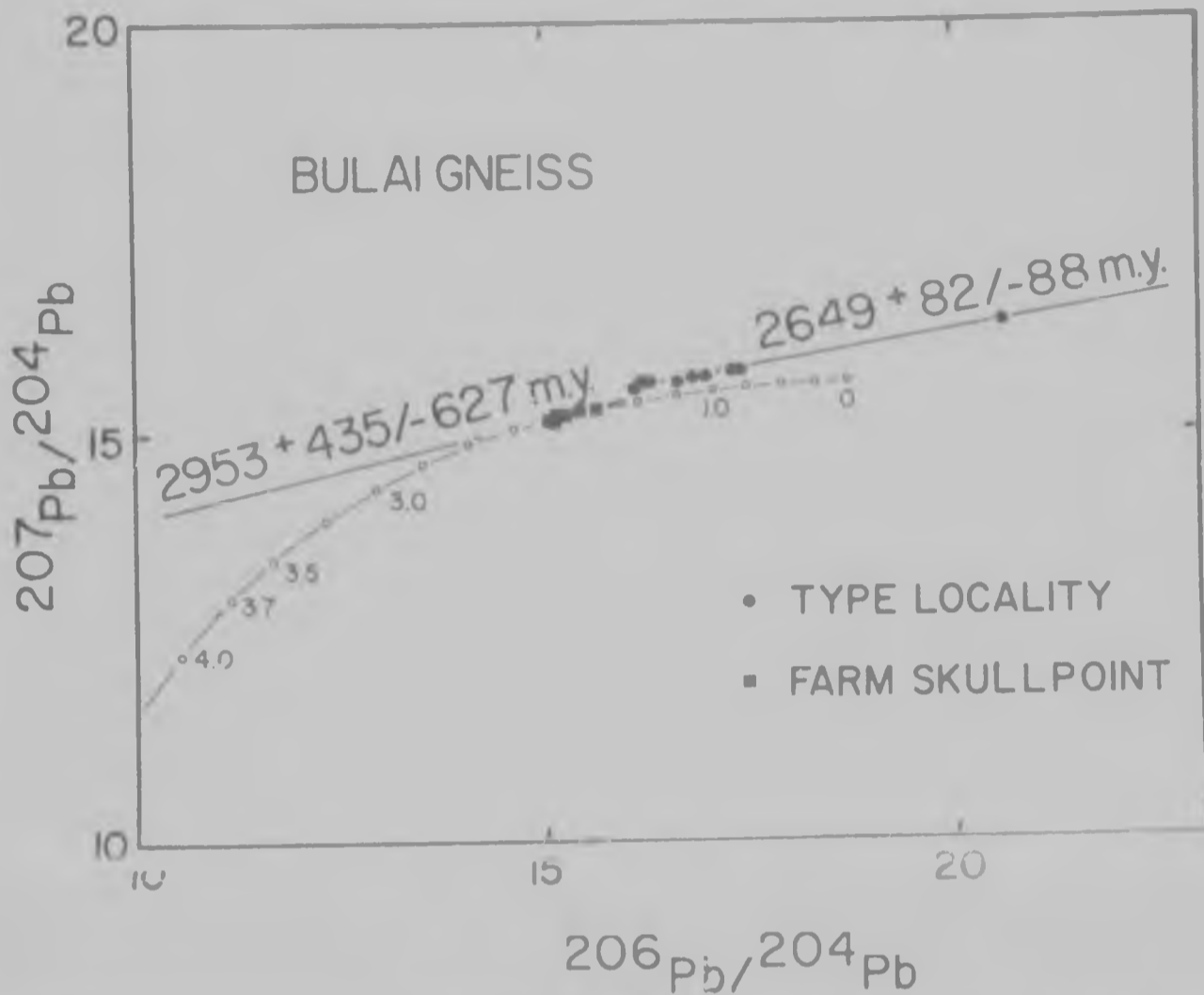


Figure 7  
 $^{207}\text{Pb}/^{204}\text{Pb}$  versus  $^{206}\text{Pb}/^{204}\text{Pb}$  diagram for the samples of Bulai Gneiss from the type locality (the Bulai pluton) and for the samples of polyphyres. "Heliosys" from Farm Skullpoint. The conventional Pb isotopic growth curve of Stacey and Kramers (1975), calibrated in 10<sup>6</sup> years, is shown for comparison. The results plot slightly away from this curve.

that the numbers may not be spurious. The Rb-Sr errorchron age for the Singelele Gneiss on Farm Skullpoint suggests that the Sr isotopes in this unit may have been only partially homogenised about 2 700 m.y. ago. The data from the Singelele Gneiss at Area I are consistent with the Pb isotopes in these rocks being homogenised during copper mineralisation at Messina about 1 770 m.y. ago (Barton, 1977).

It is evident that none of the whole-rock isochron ages measured from the Singelele Gneiss even closely approximate the age of emplacement of this unit. On the other hand, the samples of the Bulai Gneiss from the type locality and from Farm Skullpoint yield whole-rock isochron and errorchron ages of between about 2 950 m.y. and about 2 700 m.y., which are consistent with the span of possible ages of this unit as deduced from other sources. The uncertainty associated with the Pb-Pb whole-rock isochron from the samples from Farm Skullpoint is very large and so this age is of little use. It is, therefore, reasonable to assume, as a working hypothesis, that the Bulai Gneiss was emplaced about 2 700 m.y. ago. However, the possibility exists that this unit was emplaced as much as about 3 150 m.y. ago.

The common Pb isotopic correction values assumed for the zircon age calculations are  $(^{207}\text{Pb}/^{204}\text{Pb})_0 = 14.64$  and  $(^{206}\text{Pb}/^{204}\text{Pb})_0 = 13.52$ . Of necessity, these are only crude estimations of the correct values, and changes in the assumed values of the common Pb isotopic correction

values will make large differences in the positions of some of the analytical results of Fig. 11 (see Table III). However, these differences are not large enough to remove the

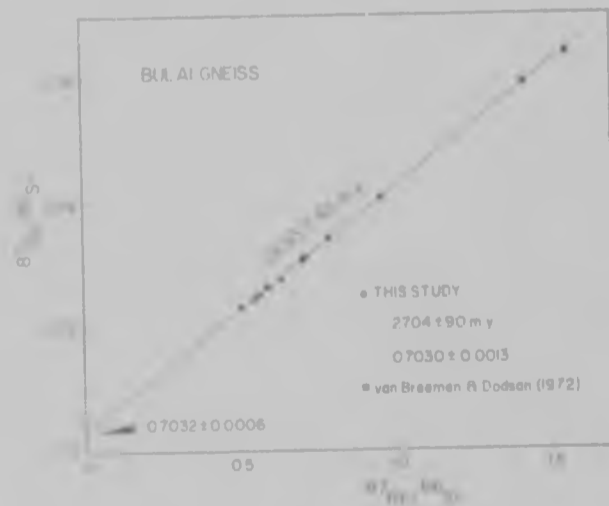


Figure 8  
 Rb-Sr isochron diagram for the samples of the Bulai Gneiss from the type locality (the Bulai pluton).

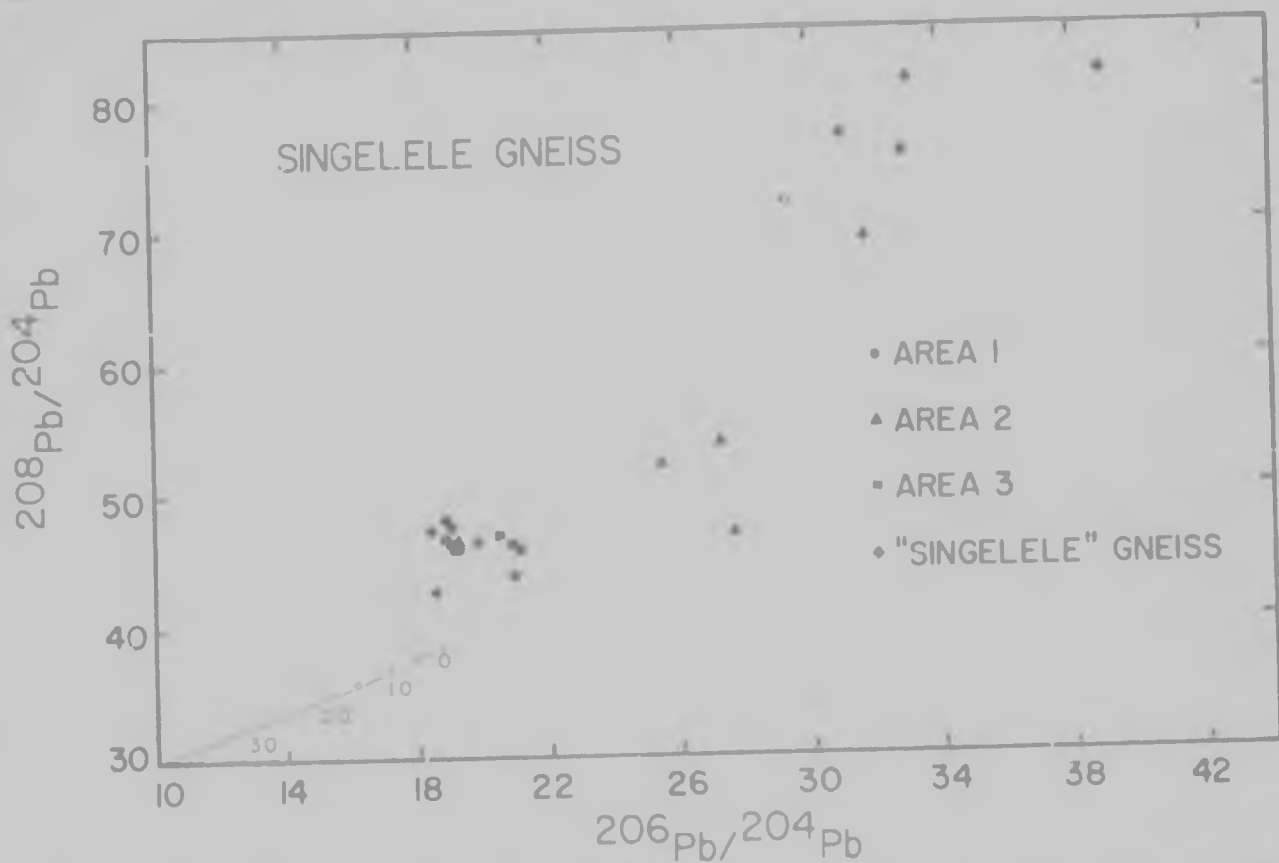


Figure 9  
 $^{208}\text{Pb}/^{204}\text{Pb}$  versus  $^{206}\text{Pb}/^{204}\text{Pb}$  diagram for the Singelele Gneiss from the type locality (the Singelele pluton) and from Farm Skullpoint. The terrestrial Pb isotopic growth curve of Stacey and Kramer (1975), calibrated in  $10^7$  years, is shown for comparison and also the resulting discordance from 10 Ma.

fact that zircons from both the Singelele and Bulai Gneisses have suffered massive Pb loss during their histories. Furthermore, it is obvious from the plotted positions of the data on Fig. 11 that model ages, constructed by projecting individual analytical results on to the concordia curve by straight lines from the origin, are too small for each unit to reflect either emplacement or one of the later deformational events. Three proportional Pb loss curves (Wasserberg, 1963) are shown for comparison on Fig. 11. These have values of 2 000 m.y., 2 700 m.y. and 3 200 m.y. (the last two being minimum ages of emplacement of the Bulai and Singelele Gneisses respectively). The analytical results do not fit well on to any of these curves, indicating that the histories of the zircons have been complicated and irregular. The results do fit reasonably well between the 3 200 m.y. curve and the 2 000 m.y. curve, consistent with the probability that the complicated and irregular behaviour was confined to the time span during which the units were undergoing periodic metamorphism. In addition, the majority of the results plot between the 2 700 m.y. curve and the 2 000 m.y. curve, possibly reflecting Pb loss as a result of a reduction of confining pressure due to regional uplift and erosion (Goidich and Mudrey, 1972). This process occurs most commonly in metamict zircons which the ones analysed for this study are not, but possibly these zircons were annealed at the same time. Nevertheless, zircons with widely discordant compositions such as these are of little use as indicators of precise age, be it of emplacement or of metamorphism. Furthermore, widely discordant compositions are the rule rather than the exception with zircons from polymetamorphic terrains such as the Limpopo Mobile Belt (see e.g. Barton *et al.*, 1978).

The initial  $^{87}\text{Sr}/^{86}\text{Sr}$  ratios of the isochrons from the

Singelele Gneiss are large, suggestive of and consistent with post emplacement homogenisation of the Sr isotopes

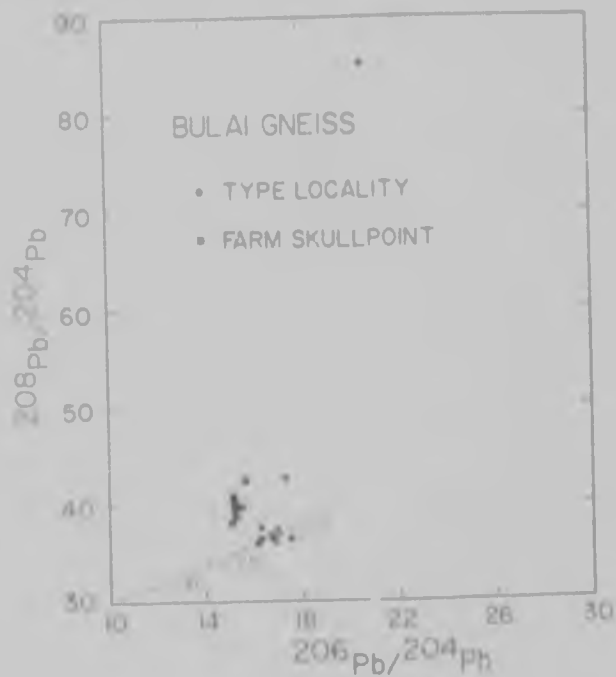


Figure 10  
 $^{208}\text{Pb}/^{204}\text{Pb}$  versus  $^{206}\text{Pb}/^{204}\text{Pb}$  diagram for the samples of the Bulai Gneiss from the type locality (the Bulai pluton) and from Farm Skullpoint. The terrestrial Pb isotopic growth curve of Stacey and Kramer (1975), calibrated in  $10^7$  years, is shown for comparison and most of the results plot away from this curve.



Figure 11

The initial  $^{87}\text{Rb}/^{86}\text{Sr}$  ratios of the isochrons from the Bulai Gneiss are, on the other hand, small enough so as not to be significantly of either a primary or a secondary value.

A method that is often used to estimate a maximum Rb-Sr whole-rock age for a suite of rocks is to calculate the time necessary for a rock with the present average  $^{87}\text{Rb}/^{86}\text{Sr}$  ratio to decay to the  $^{87}\text{Rb}/^{86}\text{Sr}$  ratio calculated from the isochron. This method to the isochron age becomes the maximum age permissible for that unit. This method is a model that assumes (1) isochronal behaviour occurred in the rocks, (2) the average  $^{87}\text{Rb}/^{86}\text{Sr}$  ratio of the rock suite is known, and (3) the estimated minimum possible original  $^{87}\text{Rb}/^{86}\text{Sr}$  ratio for the unit is valid. It is common, if six or more samples of a rock suite are collected and analysed without regard to their Rb/Sr ratios, that the  $^{87}\text{Rb}/^{86}\text{Sr}$  ratio of the suite is a whole is reasonably close to the average  $^{87}\text{Rb}/^{86}\text{Sr}$  ratio of the samples. Samples for this study were collected and analysed this way. In addition, for a rock of an age of about 3500 m.y. or less to have an original  $^{87}\text{Rb}/^{86}\text{Sr}$  ratio less than about 0.7 is unusual. Therefore, for example, for the Singelele Gneiss from the type locality at Agos 1 and 2 to have  $^{87}\text{Rb}/^{86}\text{Sr} = 0.34$  to grow from an  $^{87}\text{Rb}/^{86}\text{Sr}$  ratio of 0.1 in the initial  $^{87}\text{Rb}/^{86}\text{Sr}$  ratio of the isochron requires 329 ± 16 m.y. (2σ). Similarly, for the Singelele Gneiss on Farm Oitend (average  $^{87}\text{Rb}/^{86}\text{Sr} = 13.34$ ), it requires 687 ± 2 m.y. (2σ) and for the Singelele Gneiss on Farm Skulpfont (average  $^{87}\text{Rb}/^{86}\text{Sr} = 14.27$ ), it requires only 34 ± 2 m.y. (2σ). This suggests that the maximum ages for these suites of rocks are about 2921 m.y., 3148 m.y. and 2758 m.y. respectively. In each case, the maximum age is too small and, furthermore, the maximum ages do not agree. This then

shows that the model is invalid and suggests, assuming that the estimated  $^{87}\text{Rb}/^{86}\text{Sr}$  ratios are correct, that some changes in the Rb and Sr contents of each rock suite must have occurred at some time before or during the last resetting of the Rb-Sr "clocks".

Such models predict a maximum age for the Bulai Gneiss at the type locality of 3083 ± 90 m.y. (2σ) (average  $^{87}\text{Rb}/^{86}\text{Sr} = 0.68$ ) and for the porphyritic "Bulai-type" gneiss on Farm Skulpfont of 3003 ± 25 m.y. (2σ) (average  $^{87}\text{Rb}/^{86}\text{Sr} = 0.67$ ) (Barton, 1979). Either of these ages is permissible but neither is compelling for an older age for the Bulai Gneiss. If the Bulai Gneiss is, in fact, older than about 2700 m.y., then there is a very strong probability that suites of this unit also underwent changes in their Rb and Sr contents at some time before or during the last resetting of the Rb-Sr "clocks".

It is interesting to note on Figs. 3, 5, 7, 9 and 10 that the analytical results plot away from the average earth crustal Pb isotopic growth curves of Stacey and Kramers (1975). The same thing is true for the growth curves of Cumming and Richards (1975), although these are not shown on the figure. This implies that both the Singelele and Bulai Gneisses, and other gneisses, have had or were derived from rocks that have had anomalously large U/Pb and Th/U ratios compared to the average of the earth's crust, similar anomalies that have been reported for the Limpopo Gneisses in the Limpopo Mobile Belt (Barton, 1978; Barton, unpubl. data) and the Mesozoic Limpopo Intrusions (Barton, unpubl. data). This suggests that a large portion of the crust and upper mantle of the Central Zone of the Limpopo Mobile Belt around Mesozoic time has anomalously enriched in U with respect to Pb relative to about 4.75 m.y. ago. Pre-500 m.y. anomalous U/Pb ratios have also been reported for the rocks of the Bushveld Complex (Kramers, 1973), but not for the Karooval Complex (see the data in Koppet and Sauer, 1974; Sauer and Kramers, 1973; Sauer and Koppet, 1976). Perhaps the Central Zone of the Limpopo Mobile Belt has more genetic affinity with the Rhodesian Craton than with the Kaapvaal Craton.

Why certain rock units such as the Bulai Gneiss apparently retain isotopic memory of their emplacement age while other units, such as the Singelele Gneiss, do not, is difficult to say. Similarly, it is difficult to say why, within certain rock units such as the Bulai and Singelele Gneisses, individual isotopic dating techniques yield different results. The reasons for these discrepancies probably have something to do with the bulk composition of the individual rock units. It is recognized relationship by contact metamorphism, although not quantitatively documented, that leucocratic quartzofeldspathic and mica-rich rocks tend to be open systems for Rb, Sr, U, Th and Pb at lower temperatures than do rocks containing ferromagnesian minerals such as amphibole and pyroxene. Similarly, coarse-grained rocks tend to be more resistant to isotopic homogenization than do fine-grained rocks, and gabbroic rocks tend to be more resistant than do more siliceous rocks such as granite or andesite (see e.g. Bell and Blenkinsop, 1978; Barton, 1979). Certainly the Singelele Gneiss is a very leucocratic quartzofeldspathic rock while the Bulai Gneiss is an amphibole and biotite-bearing granitic porphyritic rock.

The scale of sampling can also affect the ages obtained from specific rock units (see e.g. Roddick and Compston, 1977). If samples are collected over a large area on the scale of kilometres between samples, there is a possibility that "inherited" ages may be measured that reflects the source of the rocks. Yet, within metamorphic rocks, sampling over an outcrop increases the probability that most ages will be measured. For all of the units studied here, except the Bulai Gneiss from the type locality, the

though where refolded, the same unit is a coherent 'arrowhead' type interference pattern younging away from the D2 and D3 antiformal axial traces. These occurrences, therefore, suggest that thrusting out of some structures occurred post-D2 and syn- and post-D3 folding. Finally, all the gneiss units in the area were folded about east-west trending axial surfaces here designated D1 (fig. 3A).

Mineral fabrics, mainly schistosity involving oriented plagioclase and hornblende crystals, are most readily seen in the gabbroic units of the Messina Layered Intrusion. These are folded about the D2 and D1 hinge zones and are folded about at least some of the D2 hinge zones. Accordingly, it appears that this schistosity was heterogeneously developed during D1 deformation and widely developed during D2 deformation. The D3 and the D1 deformations did not involve penetrative recrystallization of the gneisses.

It is important to recognize that the interpretation of the deformational history of the Messina Layered Intrusion presented here differs from those histories postulated earlier by Graham (1971) and by Coward, James, and Wright (1976) in that the former invoked only three deformational events while the latter invoked five deformational events. Their E2 event along with their E3 event is roughly equivalent to our D2 event. Furthermore, the interpretations presented here of the structure and the 'younging' directions within the Messina Layered Intrusion are at odds with those given by Hor and others (1975), who interpreted the antiformal exposure of the Intrusion immediately south of the Limpopo River (fig. 3A) as being the edge of a single sheet younging from east to west.

**Chondrite-normalized REE patterns.** Fifty-four new major element analyses of rocks from the Messina Layered Intrusion are listed in table 1 (see also app. 1). An AFM diagram (fig. 4) displaying these data combined with analyses previously reported by van Zyl (1950) and by Hor and others (1975) shows a rather broad zone of points crossing from the field of calc-alkaline rocks into the field of tholeiitic rocks as defined by Irvine and Barager (1971). This, no doubt, reflects the primarily cumulus plagioclase nature of these rocks. Unfortunately, however, the scatter of the data is such that very little may be gleaned from this diagram as to the actual chemical nature of the magma giving rise to the Messina Layered Intrusion or to the exact path of its crystallization, although a tholeiitic parental magma of approximately the composition of the samples of gabbro is suggested.

The compositions of some preserved cumulus xenocrysts as well as of the CIPW Norms of the major element analytical results show that plagioclase of a composition of An 75 and An 85 was on the liquidus throughout much of the crystallizational history of the Intrusion. Similarly, the CIPW Norms of the major element analytical results from the melagabbros and from the ultramafic rocks indicate that olivine of a composition of Fo 80 to Fo 85 and/or orthopyroxene of a composition of En 80 to En 86 were on the liquidus during crystallization of these rocks. These data make it possible to delineate a plagioclase fractionation trend (P.F.1) and an olivine fractionation trend (O.F.1) on a plot of wt per

cent MgO versus wt percent AlO<sub>3</sub> (fig. 5A). If it is assumed that essentially isochemical crystallization was taking place and that the volume of the magma was very much greater than the volume of the crystals forming, both the MgO and the AlO<sub>3</sub> contents of the parental magma may be estimated. Similar plagioclase and olivine fractionation trends are illustrated on plots of wt percent CaO versus wt percent AlO<sub>3</sub> (fig. 5B) and of wt percent FeO versus wt percent AlO<sub>3</sub> (fig. 5C), allowing the estimation, in addition, of the CaO and of the FeO contents of the parental magma. In each of these instances, the estimated parental magma has a composition similar to that of some of the gabbroic samples from the Messina Layered Intrusion. Combining these compositions with other fractionation diagrams from analytical results from samples of the Messina Layered Intrusion (figs. 4D to F) yields the estimated composition of the parental magma listed in column A of table 2.

This parental magma is quartztholeiitic in composition, not calc-alkaline as was suggested by Hor and others (1975), and it is low in K<sub>2</sub>O, similar to volcanic rocks in some Archean greenstone belts in the Canadian Shield and to modern oceanic tholeiitic basalts (Hart and others, 1970). The plagioclase-rich rocks have Sr concentrations generally in the range of from 150 to 200 ppm (table 1). As the partitioning coefficient for Sr



FIG. 1. An AFM diagram of the analyses of samples from the Messina Layered Intrusion. The solid line separates the field of tholeiitic rocks from the field of calc-alkaline rocks according to Irvine and Baran (1971).

100

TABLE I  
 The chemical compositions of some rocks from the Mesozoic Layered Intrusion

Sample	R-100	R-110	R-120	R-130	R-140	R-150	R-160	R-170	R-180	R-190
Rock	10	10	10	10	10	10	10	10	10	10
Type	10	10	10	10	10	10	10	10	10	10
SiO <sub>2</sub>	65.0	65.0	65.0	65.0	65.0	65.0	65.0	65.0	65.0	65.0
Al <sub>2</sub> O <sub>3</sub>	15.0	15.0	15.0	15.0	15.0	15.0	15.0	15.0	15.0	15.0
FeO	10.0	10.0	10.0	10.0	10.0	10.0	10.0	10.0	10.0	10.0
CaO	2.0	2.0	2.0	2.0	2.0	2.0	2.0	2.0	2.0	2.0
MgO	10.0	10.0	10.0	10.0	10.0	10.0	10.0	10.0	10.0	10.0
Na <sub>2</sub> O	1.0	1.0	1.0	1.0	1.0	1.0	1.0	1.0	1.0	1.0
K <sub>2</sub> O	0.5	0.5	0.5	0.5	0.5	0.5	0.5	0.5	0.5	0.5
P <sub>2</sub> O <sub>5</sub>	0.1	0.1	0.1	0.1	0.1	0.1	0.1	0.1	0.1	0.1
Water	0.5	0.5	0.5	0.5	0.5	0.5	0.5	0.5	0.5	0.5
Loss	0.5	0.5	0.5	0.5	0.5	0.5	0.5	0.5	0.5	0.5
Total	100.0	100.0	100.0	100.0	100.0	100.0	100.0	100.0	100.0	100.0

TABLE I  
 J. M. Hoover, G. H. P. Fyfe, P. H. G. M. and N. M. L.

6-11-11

Sample	B-500	B-528	B-500B	B-501A	B-528	B-527	B-528	B-528	B-528	B-528
Beck Type	10	10	10	10	10	10	10	10	10	10
SiO <sub>2</sub>	65.0	65.0	65.0	65.0	65.0	65.0	65.0	65.0	65.0	65.0
Al <sub>2</sub> O <sub>3</sub>	15.0	15.0	15.0	15.0	15.0	15.0	15.0	15.0	15.0	15.0
FeO	5.0	5.0	5.0	5.0	5.0	5.0	5.0	5.0	5.0	5.0
CaO	1.0	1.0	1.0	1.0	1.0	1.0	1.0	1.0	1.0	1.0
MgO	1.0	1.0	1.0	1.0	1.0	1.0	1.0	1.0	1.0	1.0
Na <sub>2</sub> O	1.0	1.0	1.0	1.0	1.0	1.0	1.0	1.0	1.0	1.0
K <sub>2</sub> O	1.0	1.0	1.0	1.0	1.0	1.0	1.0	1.0	1.0	1.0
Loss	1.0	1.0	1.0	1.0	1.0	1.0	1.0	1.0	1.0	1.0
Sp. grav	2.65	2.65	2.65	2.65	2.65	2.65	2.65	2.65	2.65	2.65
K. No.	100	100	100	100	100	100	100	100	100	100
R. No.	100	100	100	100	100	100	100	100	100	100

Sample	B-528	B-500B	B-501A	B-528	B-527	B-528	B-528	B-528	B-528
Beck Type	10	10	10	10	10	10	10	10	10
SiO <sub>2</sub>	65.0	65.0	65.0	65.0	65.0	65.0	65.0	65.0	65.0
Al <sub>2</sub> O <sub>3</sub>	15.0	15.0	15.0	15.0	15.0	15.0	15.0	15.0	15.0
FeO	5.0	5.0	5.0	5.0	5.0	5.0	5.0	5.0	5.0
CaO	1.0	1.0	1.0	1.0	1.0	1.0	1.0	1.0	1.0
MgO	1.0	1.0	1.0	1.0	1.0	1.0	1.0	1.0	1.0
Na <sub>2</sub> O	1.0	1.0	1.0	1.0	1.0	1.0	1.0	1.0	1.0
K <sub>2</sub> O	1.0	1.0	1.0	1.0	1.0	1.0	1.0	1.0	1.0
Loss	1.0	1.0	1.0	1.0	1.0	1.0	1.0	1.0	1.0
Sp. grav	2.65	2.65	2.65	2.65	2.65	2.65	2.65	2.65	2.65
K. No.	100	100	100	100	100	100	100	100	100
R. No.	100	100	100	100	100	100	100	100	100

Geological age and volume settings, Missouri Layered Pyroclastic 1921



100

TABLE I (continued)

Sample Rock Type <sup>a</sup>	Q1	Q2	Q3	Q4	Q5	Q6	Q7	Q8	Q9	Q10
	$\bar{x}$	$\bar{x}$	$\bar{x}$	$\bar{x}$	$\bar{x}$	$\bar{x}$	$\bar{x}$	$\bar{x}$	$\bar{x}$	$\bar{x}$
SiO <sub>2</sub>	54.41	56.03	52.94	55.11	55.11	57.81	55.05	56.36	55.4	56.67
Al <sub>2</sub> O <sub>3</sub>	24.52	26.86	23.86	25.75	26.05	26.38	25.11	26.08	25.4	26.2
FeO	0.10	0.07	0.17	0.22	0.15	0.25	0.20	0.15	0.15	0.15
Fe <sub>2</sub> O <sub>3</sub>	7.51	0.93	2.92	7.55	2.5	2.9	6.99	7.98	7.8	6.99
MnO	0.99	0.94	0.60	0.97	0.98	0.98	0.97	0.97	0.97	0.97
MgO	0.99	0.10	1.06	0.95	2.29	1.48	0.7	1.15	1.40	1.40
CaO	11.45	14.36	13.60	13.97	12.35	13.76	13.76	11.55	14.07	14.07
Na <sub>2</sub> O	2.79	1.36	1.08	2.02	7.39	1.61	2.94	1.12	1.87	1.87
K <sub>2</sub> O	0.88	1.86	0.52	0.43	0.41	0.55	0.43	0.43	0.55	0.55
P <sub>2</sub> O <sub>5</sub>	0.04	0.03	0.04	0.00	0.00	0.00	0.00	0.00	0.00	0.00
Rb (ppm)	660	64	64	64	64	64	64	64	64	64
Sr (ppm)	660	64	64	64	64	64	64	64	64	64
K/Rb										
Rb/Sr										

Sample Rock Type <sup>a</sup>	Q11	Q12	Q13	Q14
	$\bar{x}$	$\bar{x}$	$\bar{x}$	$\bar{x}$
SiO <sub>2</sub>	57.96	56.99	56.99	55.54
Al <sub>2</sub> O <sub>3</sub>	26.95	24.45	26.01	23.92
FeO	0.20	0.11	0.10	1.86
Fe <sub>2</sub> O <sub>3</sub>	2.09	1.97	1.39	5.98
MnO	0.46	0.69	0.66	0.66
MgO	0.66	0.79	1.57	1.62
CaO	13.45	13.11	11.24	13.60
Na <sub>2</sub> O	1.92	1.69	1.48	0.40
K <sub>2</sub> O	0.28	0.63	0.48	0.92
P <sub>2</sub> O <sub>5</sub>	0.01	0.00	0.01	0.01
Rb (ppm)	6.0	6.0	6.0	6.0
Sr (ppm)	6.0	6.0	6.0	6.0
K/Rb				
Rb/Sr				

Q11 - J. M. Dawson, Jr.; Q12 - H. W. Phillips; Q13 - H. W. Phillips and A. M. Brown

<sup>a</sup> A - amphibole; H - hornblende; P - plagioclase; Mg - magnetite; and L.M. - ilmenite (L.M. = ilmenite).  
 - Determined by separate analysis from separate sample. - Not determined.

between plagioclase and a basaltic melt is greater than 1 (Philpotts and Schminke, 1970) the parental magma of the Mesoma Layered Intrusion would probably contain less than 100 ppm Sr, a value consistent with the compositions of modern ocean floor tholeiitic basalt and of some Archean gabbros (Hart and others, 1976).

The average composition of the Mesoma Layered Intrusion estimated from the distribution of rock types presently exposed is listed in column B of table 2. This composition is enriched in Al<sub>2</sub>O<sub>3</sub> and CaO and depleted in FeO, TiO<sub>2</sub>, and MgO compared with the estimated parental magma. The fact that the K<sub>2</sub>O content of the estimated parental magma is essentially identical to the average concentration of K<sub>2</sub>O of the Mesoma Layered Intrusion proper may support the contention by Morse (1974) that under conditions of  $\gamma = 0.5$  to 0.6 pressure, the partitioning coefficient for K between plagioclase and a tholeiitic magma is  $\approx 0.5$  to 1.

The major element composition of one sample of a gabbro lamella from within the Sand River Gabbros (B-76-005) is given in table 1 and on figures 1 and 2. In general, the results of this analysis fall within the range of values from the rock types within the Mesoma Layered Intrusion, except that it is enriched in both Na<sub>2</sub>O and K<sub>2</sub>O. Such enrichment could be a result of the reaction between the lamella and the enclosing Sand River Gabbros (p. 6). The chemical composition of these lamellae is therefore consistent with the possibility that they are remnants of the rocks to the Mesoma Layered Intrusion.

No consistent patterns were observed relating chemical or mineralogical composition to stratigraphic position within the Mesoma Layered Intrusion. This might be expected if the volume of magma generating the intrusion greatly exceeded the volume of cumulus crystals normally formed by the intrusion. In this case, compositional changes within the Mesoma Layered Intrusion would likely reflect only metamorphism after crystallization. How and others (1975) did report such compositional changes with stratigraphic position as defined by their interpretation of the structure of the Mesoma Layered Intrusion. However, in the context of the ideas

TABLE 2  
Estimated composition of the magma giving rise to the Mesoma Layered Intrusion (A) and of the average composition of the Mesoma Layered Intrusion (B)

	A	B
SiO <sub>2</sub>	69.2	69.9
Al <sub>2</sub> O <sub>3</sub>	14.9	21.4
FeO	7.1	6.7
TiO <sub>2</sub>	12.8	4.9
MgO	6.26	9.1
MnO	0.05	0.5
CaO	10.0	12.0
Na <sub>2</sub> O	0.5	2.0
K <sub>2</sub> O	0.5	0.5
P <sub>2</sub> O <sub>5</sub>	0.05	0.05

<sup>a</sup> Total Fe as FeO.



Fig. 2. Radio-strontium isotopic analysis results for the samples from the Mesozoic Eocene intrusion from which the compositions of the parental magma were estimated. The open circles represent the present-day compositions, and the solid circles are the values on a more recent time scale. The dashed line represents the trend for an open system, and the solid line represents the trend for a closed system.

the data presented here, their patterns are to be interpreted in terms of the tectonic stratigraphy of the intrusion.

**B. Rb-Sr isotopic studies.**—Nineteen total-rock samples from the Mesozoic Eocene intrusion plus one total-rock sample of a gabbroic boudin from within the Sand River Gneiss (R76-103) were analysed for their Rb-Sr isotopic composition (table 2, see also p. 1172). The 19 samples from the intrusion proper yield an isochron of  $3453 \pm 47$  m.y. (2 $\sigma$ ) with an initial  $^{87}\text{Sr}/^{86}\text{Sr}$  ratio of  $0.70331 \pm 0.00006$  (2 $\sigma$ ) (see fig. 2). The result of the analysis of the one sample from a gabbroic boudin falls on this isochron to within a probability exceeding 99 per cent.



The widely variable K/Rb ratios of these samples (table 1) and the lack of good correlation between either Rb or K<sub>2</sub>O concentration and K/Rb ratios (fig. 7) indicate that post-intrusive variations in the relative proportions of these elements have occurred. In general, these variations appear to have involved the addition of Rb to these rocks, with lesser and sometimes no variation in the amount of K, shifting the K/Rb ratios of some of the leucocratic and aporthocratic from the 0.040 range (usually associated with plagioclase crystalline rocks toward the less than 0.010 range characteristic of trondhjemite rocks. On a plot of wt percent K<sub>2</sub>O versus wt percent Na<sub>2</sub>O versus wt percent CaO (fig. 8), the majority of the analytical results from the Mesoma Layered Intrusion fall in the field of initial tholeiitic crystallization, again indicating that only limited variations in the K contents of these rocks have taken place since crystallization. Consequently, the analysis for the Mesoma Layered Intrusion reflects the post-crystallization alteration in Rb content and can only be considered to be a minimum age for emplacement of the intrusion. Nevertheless, the adjacent Sand River Gneiss has maintained their Rb/Sr isotopic character for the past ~3780 my (Barton and Ryan, unpublished data) and the other series of tholeiitic dikes including those gneisses has maintained its Rb/Sr isotopic character for the past ~3520 my (Barton, Phipps, and Ryan, 1977). Therefore, the blanket resetting of the Rb/Sr

TABLE 1  
Sequences of data from the Mesoma Layered Intrusion

Rock Type and sample Number	Rb (ppm)	Na (ppm)	K/Rb (%)	Na/Rb (%)
<i>Leucocratic</i>				
B 77-20	1.36	11.6	0.0786	0.5682
B 77-28	0.73	6.69	0.0433	0.5221
B 77-21	6.1	19.0	0.0497	0.2977
B 79-03	1.24	10.3	0.0807	0.3974
B 79-09	1.06	18.2	0.0368	0.5307
B 77-04	4.14	12.8	0.0314	0.7861
B 77-06	4.36	18.7	0.0234	0.7168
B 79-08A	0.65	27.5	0.0299	0.7030
B 79-07	0.64	19.1	0.0387	0.7091
B 78-1	0.73	18.1	0.0407	0.6997
<i>Leucocratic</i>				
B 77-11	0.47	21.2	0.0221	0.7152
B 77-14	0.68	14.8	0.0271	0.7117
B 77-22	0.78	19.9	0.0377	0.6883
B 80-1	1.34	14.8	0.0892	0.3495
B 80-11	7.20	14.5	0.0491	0.5977
B 79-08	0.29	14.0	0.0659	0.7468
<i>Orthocratic</i>				
B 77-30	0.63	16.6	0.0397	0.7177
B 79-07	2.89	14.0	0.1799	0.7119
<i>Mylonitic</i>				
B 29-07	0.086	0.031	0.2771	0.7311
<i>Basaltic Di-</i>				
<i>Sand River Gneiss</i>				
B 20-02	11.7	38.0	0.3081	0.7137

\*Normalized to an <sup>87</sup>Rb/<sup>86</sup>Rb ratio of 0.0001.

topic "clocks" occurred within the rocks of this area ~3150 m.y. ago (or occurred more recently), and the alteration reflected in the isochron from the Messina Layered Intrusion must have been primarily restricted to that body of rock. Obvious mechanisms for this type of restricted alteration are (1) reaction of the magma with the wall rock through which it passed and into which it was intruded, and (2) reaction of the solidified rocks with post-crystallization fluids. We favor the latter possibility, but unfortunately, subsequent deformations and recrystallizations of this intrusion make evaluation of these mechanisms exceedingly difficult. However, in either case, this alteration had no noticeable effect on the initial  $^{87}\text{Sr}/^{86}\text{Sr}$  ratio of the intrusion. Consequently, it would likely have occurred, when the coarseness of our present calibration of Archean time and the magnitude of the uncertainty in the isochron from the Messina Layered Intrusion itself are considered, only an indistinguishable period

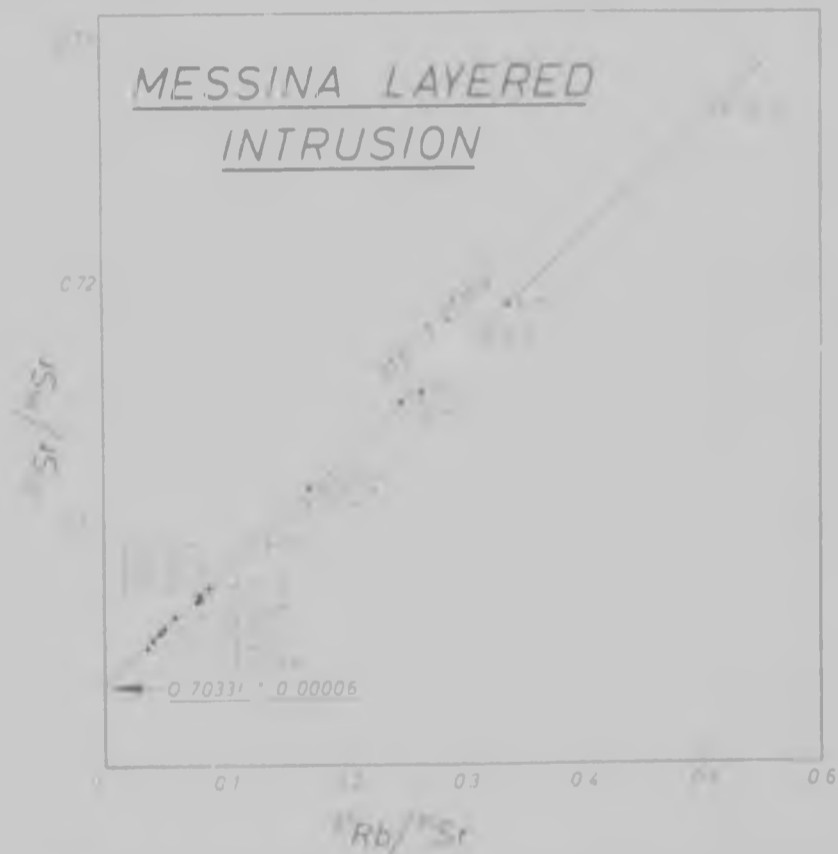


Fig. 6. Rb-Sr total rock isochron for the Messina Layered Intrusion. The symbols are the same as on figure 1. Note the relationship of the analytical results for the gabbroic boudin from within the Sand River Gneisses (sample B 76-103; see pl. 1) to the isochron for the intrusion proper.







Mountain (and see for example, Abajp and others, 1960; and others, 1960; Barton, Fypp, and Ryan, 1971). However, whether these supracrustal rocks are in fact correlative with all the other Supracrustal units exposed in the Central Zone of the Limpopo Metamorphic Belt is a moot question. It has been argued that the rocks of the Messina Layered Intrusion and the immediately surrounding supracrustal rocks and the Sand River Group are found in one and possibly more than one tectonic or thrust sheet. Consequently, they are not necessarily in original part of the regional crustal complex in which they are presently found. Furthermore, the supracrustal rocks surrounding the Messina Layered Intrusion contain banded iron formation and iron-bearing rocks, while in the surrounding areas the supracrustal rocks reported by Solange, le Roux, and Nel (1948), the "Mesma Formation" are characterized by, among other things, continuous massive rocks and very little or no banded iron formation (see, for example, Solange, 1943; Solange, le Roux, and Nel, 1948; Mason, 1971; Walschick, 1976). Granted these rocks may be regional facies within a supracrustal sequence, it is equally possible, however, that on the macro-regional scale, some of the supracrustal assemblages within the Limpopo Mobile Belt are younger than the Messina Layered Intrusion.

**B. *P-T conditions during emplacement of the Messina Layered Intrusion.*** In general, numerical indicators of specific pressure and temperature conditions during emplacement are absent in the Messina Layered Intrusion. As minerals (e.g.,  $\text{Fe}_2\text{SiO}_4$ , pyroxene) of a composition  $\text{An}_{70}$  to  $\text{An}_{55}$ , olivine of a composition  $\text{Fo}_{90}$  to  $\text{Fo}_{85}$ , and/or orthopyroxene of a composition  $\text{En}_{75}$  to  $\text{En}_{60}$  were used at various times in the liquid during crystallization of the intrusion. From experimental melting studies of the assemblages anorthite-forsterite and anorthite-orthopyroxene (Kashiro and Yost, 1960), these liquidus phases indicate that the intrusion was crystallizing at pressures less than about 9 kb and possibly at pressure less than 7 kb. Similar maximum pressure conditions are indicated by crystal-formation studies of tholeiitic magmas by Thompson (1972). Furthermore, constraints from rock deformational studies indicate that it is impossible to inject magmas into horizontal fractures or other discontinuities to form sill-like bodies at confining pressures greater than about 5 kb (less than 9-12 km depth), and probably most sills are formed at considerably smaller pressures (see, for example, Mudge, 1968; Gerner, 1969; Roberts, 1970; Pollard, 1973; Phillips, 1971). If, as it is believed, the Messina Layered Intrusion was emplaced as a sill-like body, its emplacement was an upper-crustal phenomenon, and the supracrustal sequence into which it was intruded was a maximum of about 12 km thick (not probably much thinner).

Sapphirine-kornerupine-corundum bearing mineral assemblages occur locally throughout the Messina Layered Intrusion (Solange, 1945) and analysis of one such assemblage yielded equilibrium pressures greater than 4 kb and temperatures in excess of 700°C for  $P_{\text{H}_2\text{O}} = P_{\text{total}}$  (Schreyer and Abraham, 1976). As this pressure is in excess of that likely present during emplacement of the intrusion, the formation of these mineral as-

semblages must have taken place subsequently and not as simple contact metamorphic reactions. These P-T conditions are verging on those of granulite facies metamorphism. It appears, therefore, that a high grade metamorphic event occurred in this area after the formation of the Messina Layered Intrusion. It is not completely evident at this point exactly when the sapphirine forming reactions occurred. However, the sapphirine-bearing rocks were deformed during the D2 event. The presence of the Messina Layered Intrusion in a high grade metamorphic terrain is, therefore, a fact of fate and not a result of a cause and effect relationship.

*C. The Messina Layered Intrusion and greenstone belt*—The fact that the estimated chemical composition of the parental magma for the Messina Layered Intrusion is different from the estimated average chemical composition of the Intrusion (table 2) suggests either that a large volume of rocks derived from the magma is not exposed at the present erosional level or that some genetically related but geographically distinct mafic rocks have not been included in our present definition of the Intrusion. The latter explanation is a distinct possibility, although at the present erosional level, the area underlain by mafic rocks not included in the Intrusion is small. On the other hand, the first explanation is as possible and presents some scope for speculation. The Intrusion could be composed of phenocrysts derived from and left behind by an ascending body of magma such as might be feeding volcanic eruptions at the surface or forming gabbroic dikes and sills at a higher level in the supracrustal sequence. As was mentioned earlier, the estimated chemical composition of the parental magma is similar to those of many tholeiitic rocks in Canadian Archaean greenstone belts. It is possible, therefore, that the Messina Layered Intrusion is a remnant of the magma feeding a greenstone belt terrain that may have once been extensive in what is now the Limpopo Mobile Belt. In order to explain the paucity of rocks of amphibolitic composition presently exposed in the Central Zone of the Limpopo Mobile Belt, it is necessary that this terrain was removed either by erosion or by some tectonic mechanism. Such removal would have to have taken place prior to the D1 deformation, or else appreciable amounts of greenstone belt material should be incorporated into the D1 folds and nappes.

#### COMPARISON OF THE MESSINA LAYERED INTRUSION WITH THE FISKENAESSET COMPLEX OF WEST GREENLAND

The Messina Layered Intrusion and the Fiskenaesset Complex of West Greenland have many features in common (Windley, 1973; Windley and Smith, 1976), but they differ significantly in two respects. The apparent inverse relationship between the orthite content of the cumulus plagioclase and the hornblende concentrations in the rocks of the Messina Layered Intrusion argues against hornblende being an appreciable primary phase and suggests that the Intrusion formed from a relatively dry magma. However, no such inverse relationship exists in the Fiskenaesset Complex where very calcic plagioclase coexists with abundant hornblende (M. R. Sharpe, personal communication, 1977), suggesting instead that the horn-

blende is a primary phase forming from a hydrous magma (Windley and Smith, 1974, 1976). Secondly, magnetite and chromite layers within the Messina Layered Intrusion are smaller and much less frequent than in the Fiskenaesset Complex (Windley and Smith, 1974, 1976), suggesting that conditions of higher  $P_0$  existed during the crystallization of the latter body. These differences suggest that fundamental genetic differences exist between these bodies. Windley and Smith (1976) have argued that the Fiskenaesset Complex formed from a wet oxidized basaltic magma possibly in a back arc environment; the Messina Layered Intrusion appears to have formed from a dry reasonably unoxidized magma in a continental environment.

#### ACKNOWLEDGMENTS

This study was supported by the Council for Scientific and Industrial Research of South Africa as a part of the South African contribution to the International Geodynamics Project. We thank H. F. Allsopp, C. W. Clark, N. C. Gay, J. B. F. Jacobsen, R. M. Key, J. D. Kramers, J. R. Melver, and E. O. Nicolaysen for critically commenting on an earlier version of this manuscript.

#### APPENDIX 1

##### Major element analytical techniques

Major element concentrations were determined by X-ray fluorescence spectrometry using the technique described by Norrish and Chappell (1967) and Norrish and Hutton (1969). Complete replicate analyses indicate that the precision of the determinations at the confidence level of two standard deviations are: SiO<sub>2</sub> 0.9 percent, Al<sub>2</sub>O<sub>3</sub> 1.3 percent, TiO<sub>2</sub> 2.0 percent, FeO 2.0 percent, MnO 2.0 percent, MgO 2.0 percent, CaO 1.3 percent, Na<sub>2</sub>O 6.0 percent, K<sub>2</sub>O 1.1 percent, P<sub>2</sub>O<sub>5</sub> 6.0 percent, Rb<sub>2</sub>O 2.0 percent, and BaO 2.0 percent. Analyses of common standard rock powders agree with the accepted values to within the precisions of the techniques (McCarthy, 1976).

#### APPENDIX 2

##### Rb-Sr isotopic analytical techniques

An approx 0.2 g portion of powder from each sample was spiked both for determination of the Rb concentration (spike 99.2 percent <sup>87</sup>Rb) and the Sr concentration (spike 99.4 percent <sup>86</sup>Sr) and dissolved with 10 ml of HF and 0.2 ml of HClO<sub>4</sub>. Rb and Sr were concentrated using ion exchange columns. For Rb isotopic determinations, the samples were analysed as chlorides on double Ta filaments. Complete replicate analyses indicate a reproducibility of ±1.0 percent (2σ) for the Rb concentration, and replicate analyses of natural Rb yielded an <sup>87</sup>Rb/<sup>86</sup>Rb ratio of 2.5991 ± 0.0006 (2σ). For Sr isotopic determinations, samples were analysed as nitrates with TaO<sub>2</sub> on single Ta filaments. Replicate analyses indicate a reproducibility of ±1.0 percent (2σ) for the Sr concentration and of ±0.008 percent (2σ) for the <sup>87</sup>Sr/<sup>86</sup>Sr ratios normalized to an <sup>86</sup>Sr/<sup>88</sup>Sr ratio of 8.374. Replicate analyses of the Fomer and Amend standard SrCO<sub>3</sub> yielded a mean value of 0.70802 ± 0.00006 (2σ). Analyses of the NBS SRM 607 K feldspar yielded a Rb concentration of 290 ppm (accepted value 275.31 ppm) and a Sr concentration of 65.185 ppm (accepted value 65.290 ppm). The analytical blanks during this study were 9 nanograms total Rb and 3.5 nanograms total Sr. No blank corrections were made to the data.

The 19 samples from the Messina Layered Intrusion proper yield a M<sub>87</sub>W<sub>87</sub>D of 0.19 by the regression technique of McIntyre and others (1966) and a M<sub>87</sub>Sr<sub>86</sub> of 1.1 by the regression technique of York (1969). As these values are less than the appropriate T<sub>0</sub> ratio for these data (1.7), the actual scatter of the data is less than that predicted by the experimental uncertainties alone, and the data define an isochron (Brooks, Hart, and Wendt, 1972). Following the recommendations of Brooks, Hart, and Wendt (1972), the isochron parameters were calculated utilizing corrected errors by the experimental error technique of McIntyre and others (1966) using  $1.42 \times 10^{-10}$  yr<sup>-1</sup> for the decay constant of <sup>87</sup>Rb.

REFERENCES

- Albritton, H. L., Harris, R. D. & Cooper, A. A. V. and Swadlow, L. O., 1961. Bases of Rhyolite and dacite intrusions from the early Proterozoic sequence in the southern Orange and Namaqualand, South West Africa. *South African J. Geol.* **2**, p. 455-468.
- Barton, J. M. Jr., Harris, R. D. F. and Cooper, B., 1977. Rhyolite and dacite intrusions of ancient dykes in the Sand River area, Transvaal Middle Belt, South Africa. *Nature*, **266**, p. 847-849.
- Bullpenny, D., McGonigle, S. R. and Myers, J. S., 1974. A tectonic orogenic regime in the Appalachians of Greenland and the implications for early tectonic development. *Proceedings Research*, **1**, p. 173-17.
- Brooks, C., Harris, R. D. and Vernon, R. H., 1970. On the possible role of a tectonic orogenic regime as implied in the Namaqualand, South Africa. *Geophysics Research Reports*, **1**, p. 751-777.
- Brooks, C., James, D. F. and Harris, R. D., 1970. A tectonic orogenic regime in the southern African Proterozoic. *Geology*, **8**, p. 680-684.
- Condie, R. C., 1970. Tectonic-climate models for the origin of African volcanic rocks. In Windley, B. F. (ed.), *The Early History of the Earth*. New York: John Wiley & Sons, p. 412-424.
- Conrad, M. P., James, D. F., and Windley, B. F., 1970. Metamorphic isograds in the Limpopo middle belt, southern Africa. *South African J. Geol.*, **3**, p. 903-914.
- Cooper, R. G., Johnson, R. L., Mookerjee, T. J., Williams, C. J., Van der Merwe, D. S., 1969. The geology of the Namaqualand region, province of South West Africa. *Geol. Surv. S. Africa*, **27**, p. 1-218.
- Harris, R. D., Albritton, H. L., Emswiler, S. J. and Marston, W. L., 1970. A tectonic orogenic regime in the southern African Proterozoic. *Geophysics Research Reports*, **1**, p. 777-786.
- Lee, P. W., 1969. Anomalous base composition of the upper mantle. *Jour. Geophys. Research*, **74**, p. 1297-1307.
- James, D. F., 1969. On the development of the tectonic orogenic. *Geophysics Research Reports*, **1**, p. 1419-1449.
- Leitch, R. H., 1974. A tectonic orogenic regime in the southern African Proterozoic. *Geophysics Research Reports*, **1**, p. 1079-1097.
- Queney, P. F., 1977. Neoproterozoic tectonic orogenic regimes in the Transvaal and Namaqualand, southern Africa. *South African J. Geol.*, **30**, p. 1-14.
- Harris, R. D., Brooks, C., Kram, V. E., Davis, G. J. and Nairn, D., 1969. African and possible volcanic rocks: a case of tectonic orogenic. *Earth Planet. Sci. Letters*, **1**, p. 17-28.
- Harris, R. D., 1969. Anomalous base composition of the upper mantle. *Jour. Geophys. Research*, **74**, p. 1297-1307.
- Lee, A. K., Hill, D. V., Smith, J. V., Wakelind, J. and Windley, B. F., 1975. Petrogenetic and tectonic models for the Proterozoic orogenic rocks of the Limpopo middle belt, southern Africa. *Lithos*, **8**, p. 297-310.
- Harris, R. D., Moss, S. R., Albritton, H. L., Emswiler, S. J., Saunders, M. J. and Durr, 1969. *J. Geol. Soc. South Africa*, **72**, p. 1-14.
- James, D. F., 1969. *Geology of the Namaqualand region, province of South West Africa*. *Geol. Surv. S. Africa*, **27**, p. 1-218.
- James, D. F. and Burgess, W. R. A., 1973. A guide to the chemical classification of the common volcanic rocks. *Canadian Jour. Earth Sci.*, **10**, p. 1-17.
- Kram, V. E., 1977. Late Proterozoic orogenic regimes in the southern African Proterozoic and their tectonic significance. *Geophysics Research Reports*, **1**, p. 1079-1097.
- Kram, V. E. and Vernon, R. H., 1969. African volcanic rocks: a case of tectonic orogenic. *Earth Planet. Sci. Letters*, **1**, p. 17-28.
- McCarthy, J. S., 1974. The Limpopo middle belt, southern Africa. *Royal Soc. London Philos. Trans.*, **273**, p. 467-489.
- McCarthy, J. S., Brooks, C., Campione, W. and Furek, S., 1970. The tectonic orogenic regime in the southern African Proterozoic. *Geophysics Research Reports*, **1**, p. 1079-1097.
- McCarthy, J. S., 1976. Chemical compositions of a few proterozoic granites and the composition of the lower crust. *Geology of Zimbabwe*, **3**, p. 196-207.



## Ancient Archaean supracrustal rocks from the Limpopo Mobile Belt

Peter C. Horrocks

Department of Geology, University of the Witwatersrand,  
 Jan Smuts Avenue, Johannesburg 2001, South Africa

A preliminary study has been made to establish pressure, temperature and water activity parameters for the high grade metamorphism of the early Archaean supracrustal rocks exposed in the Limpopo Mobile Belt near Messina, South Africa. The results reported here indicate that a significant orogenic crustal thickness up to 30 km was developed before 3,100 Myr ago in the region.

The high-grade and poly-deformed supracrustal gneisses studied occur south-east of Messina in the Central Zone of the Limpopo Mobile Belt (Fig. 1). They are thought to have been deposited at least partly on a sialic basement made up of the 3,800 Myr old Sand River Gneisses, which are cut by 3,570 Myr old tholeiitic dykes that have not been recognized in the supracrustal gneisses. The supracrustal gneisses were intruded by the anorthositic, gabbroic and peridotitic gneisses of the Messina layered intrusion probably 2,270 Myr ago (J. M. Barton Jr. work in preparation). Subsequently, an important event of igneous and metamorphic activity affected all of these rocks 3,150 Myr ago, and a second suite of 3,060 Myr old tholeiitic dykes were intruded.

The supracrustal gneisses are predominantly quartzo-feldspathic, but contain numerous interlayers and lenses of pyroxenitic amphibolite, quartzite, magnetite quartzite, garnet cordierite gneiss, calc-silicate gneiss and marble. The mafic lithologies commonly preserve orthopyroxene + clinopyroxene + amphibole + plagioclase + quartz + magnetite ± garnet assemblages, and frequently show prograde metamorphic textures in which orthopyroxene has replaced and overgrown amphibole, while some localities show coexisting clinopyroxene and garnet. Kelyphitic coronas predominantly made up of plagioclase are developed around the garnet in lithologies with abundant amphibole, and in some samples, the garnet is almost completely replaced, or remains only as a few scattered optically continuous remnants in the centres of these reaction coronas. Thus, these kelyphitic textures are thought to be the result of retrograde processes (ref. 5, and P. C. H. in preparation), and not due to a second prograde metamorphism as has been described for previously metamorphosed rocks with a resulting low water partial pressure. The metapelitic lithologies contain garnet + cordierite + biotite + sillimanite (+ kyanite) + plagioclase + quartz ± K-feldspar ± amphibole + orthopyroxene. The garnet is commonly distinctly zoned with more inclusion-filled cores, which are more pyrope rich, overgrown by thin more almandine-rich and inclusion-poor rims (work in preparation). Some localities preserve kyanite overgrown by sillimanite. Peraluminous and magnesia-rich rocks within these metapelitic gneisses consist of corundum + spinel + sapphirine + cordierite + garnet + phlogopite ± orthopyroxene + gedrite, and these undersaturated assemblages apparently represent metamorphic residues after the extraction of minimum melt granitic anatectic liquids. Symplectitic coronas about garnet are developed in places where the garnet is replaced by an intergrowth of radial orthopyroxene grains in plagioclase (Fig. 2). This garnet is relatively unzoned, and it is not obvious whether this reaction is prograde or retrograde. However, some samples preserve only spherical knots comprising myrmekitic orthopyroxene grains in plagioclase suggesting the complete breakdown and

replacement of garnet probably by a retrograde process similar to that which is thought to have produced the kelyphitic coronas.

Electron microprobe analyses of the above mineral assemblages mean that several thermodynamic techniques can be used to estimate some of the pressure, temperature and water activity parameters of the high-grade metamorphism these rocks have experienced. The analytical technique used natural and synthetic standards, and was routinely able to repeat known international standards typically to within 2% for all relevant elements. Temperature estimates have been calculated using the following equilibria:

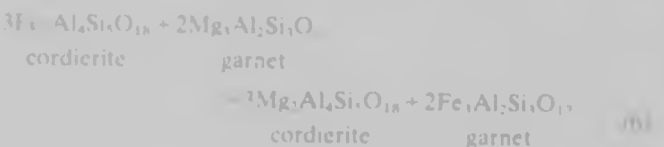
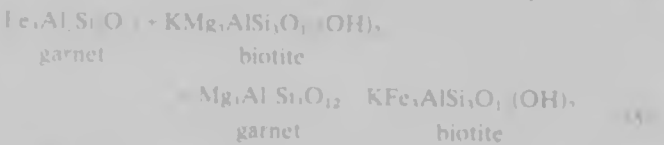
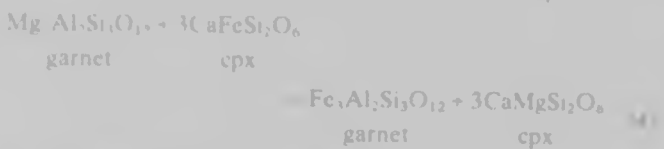
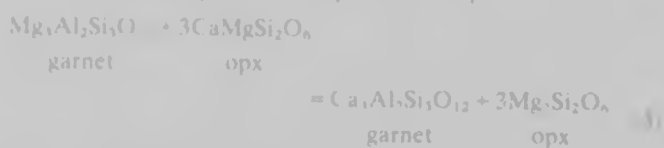
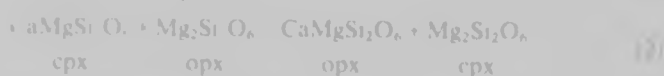


Fig. 1 A simplified geological map of part of southern Africa showing the location of Messina and the Limpopo Mobile Belt.



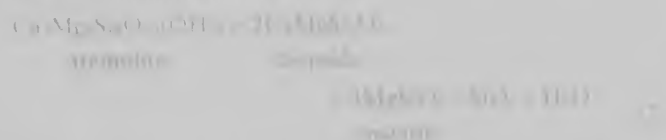
Fig. 2. A dense forest of tall, thin trees, possibly a coniferous forest, with a prominent horizontal line or path cutting across the middle of the scene.

Table 1. Characteristics and measurements of the experimental plots.

Plot No.	Area (m <sup>2</sup> )	Number of trees	Species	Height (m)	DBH (cm)	Volume (m <sup>3</sup> )
1	100	10	Pinus	15	10	150
2	100	10	Pinus	15	10	150
3	100	10	Pinus	15	10	150
4	100	10	Pinus	15	10	150
5	100	10	Pinus	15	10	150
6	100	10	Pinus	15	10	150
7	100	10	Pinus	15	10	150
8	100	10	Pinus	15	10	150
9	100	10	Pinus	15	10	150
10	100	10	Pinus	15	10	150

Notes: The plots were established in a coniferous forest. The trees were measured at the beginning of the experiment and then at regular intervals. The data in this table are the average values for all plots.

The geothermometry derived from three equilibria<sup>13,14</sup> based on experimental data and our own values are typically within 50°C of the experimental conditions. Thus the maximum practical resolution of these techniques is probably about 100°C and about 1 kbar at about 7 kbar.  $T_{\text{max}}$  was estimated to garnet and quartz by a Aluminometric method<sup>15</sup> and was found to be generally a lowering of the temperature estimates more than 50°C in most cases and usually much less than 50°C. Pressure estimates were made from equation (3) and (4) and these geothermometry<sup>16,17</sup> data based on experimental data have given more inconsistent results mainly due to the problems surrounding Al-saturation in pyroxene. A water-saturated system reproducing the experimental values isophysical data and 1.20 mol H<sub>2</sub>O per 100 mol of the garnet-quartz equilibrium. Typically, the best solution for practical purposes is probably listed in Table 1 (4). The water activity was calculated using equilibria (7)–(9). Remantion pressure estimates in the mafic gabbros.



top may vary quite dramatically, approximately<sup>18</sup> based on hydrous and anhydrous data. The water fugacity and equilibrium summarized in Table 1 and Fig. 7.

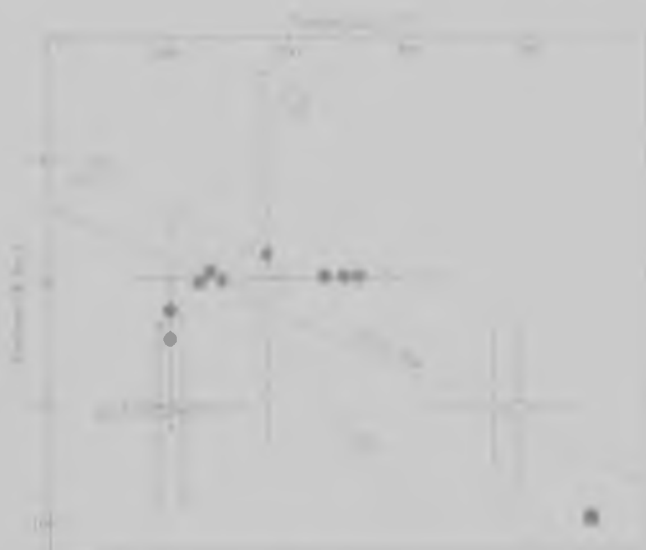


Fig. 3. A pressure-temperature diagram showing the stability fields for Table 1. (●)  $T_{\text{max}}$  and  $P_{\text{max}}$  for garnet-quartz; (□)  $T_{\text{max}}$  and  $P_{\text{max}}$  for garnet-clinopyroxene-quartz; (○)  $T_{\text{max}}$  and  $P_{\text{max}}$  for garnet-clinopyroxene-quartz-water; (△)  $T_{\text{max}}$  and  $P_{\text{max}}$  for garnet-clinopyroxene-quartz-water. The solid lines represent the stability fields for the various mineral assemblages.

The  $P_{\text{max}}$  and  $T_{\text{max}}$  values suggested for the various rocks in the region of Fig. 3 are consistent with the mineralogical features of the study and that of other studies in the region<sup>19</sup> particularly with regard to the association of corundum + kyanite + quartz, kyanite overgrowth on kyanite<sup>20</sup>, prograde amphibole-quartz replacement of amphibole (that is, granitic bodies, metamorphic, mid- to high-grade kyanite-bearing gabbro) in the mafic rocks, and the garnet zonation of the mafic rocks. The early phase of the metamorphism which produced the orthopyroxene-bearing assemblages in the mafic rocks, and the prograde rich corundum and rutile in the mafic rocks occur in preparation, and characterized by temperatures in excess of 800°C and probably pressures up to 10 kbar (Fig. 3). Water fugacity in the mafic rocks were low (with H<sub>2</sub>O making up 10% of the fluid phase) during the high-grade phase of the metamorphism. It was probably the fluid phase or fluid present during this time, based

on a comparison with a study of liquid inclusions in granulites from southern Africa<sup>21</sup>. A retrograde retrogression to a lower temperature of cooling suggests a retrograde development of the kyanite-quartz from garnet in the mafic lithologies, the orthopyroxene-bearing gabbros, and the spinel amphiboles, particularly associated with the preparation in the mafic rocks, and probably also the production of the samples, the mafic rocks garnet (Fig. 3). The retrogression of between 4 and 7 kbar were achieved at temperatures of 600–800°C (Fig. 3).

The early phase of the high-grade metamorphism, the supra-crustal tectonics response, sometime between 3,500–4,000 Myr ago and the emplacement of the Mesozoic layered intrusion, 2,200 Myr ago, was supposed to rapid burial or depths probably greater than 10 km (Fig. 3) of the lower crust either by subsidence or tectonic erosion. A further study of an orthopyroxene-quartz association from Zimbabwe also suggested pressures of up to 10 kbar and temperatures above 950°C with the corundum having an  $\delta^{18}\text{O}$  composition of about 3‰. These data also show that the orthopyroxene reflects an average geothermal gradient of about 10°C/km in the lower crust of the crust. This is compatible with some suggested African geotectonics<sup>22</sup>. The metamorphic and igneous activity about 3,500 Myr ago, which forms the Rhyolite inclusions in the rocks of the Mesozoic layered intrusion, probably reflects the peak of the phase of the metamorphism. Spinel-bearing orthopyroxene events occurred during the intrusion from 3,100 Myr ago to 2,400 Myr ago<sup>23</sup> through each metamorphic grade. A further study of the mafic rocks from the Zimbabwean layered intrusion was reported on the literature<sup>24</sup>. Although the metamorphic and pressure data currently available do not provide sufficient evidence on the metamorphism, these rocks could probably represent a significant metamorphism of the mafic rocks of the supra-crustal rocks and the resulting pressure and temperature changes. The attainment of peak granulite facies metamorphism at maintained temperatures, probably adequately, and may explain the retrogression as indicated by the kyanite textures and garnet zonation. The end of high-grade metamorphism and the onset of metamorphic reversion stability are evidenced by a kyanite-free mafic gabbro at 2,200 Myr ago<sup>25</sup>. This ancient metamorphic event of high-grade metamorphism may not preclude the development of the granulite facies orthopyroxene-bearing assemblages which comprise much of the Earth's shield areas but perhaps represents a contemporaneous development of lower crustal rocks now and exposed in limited zones of the ancient shields. The geometry of these zones or belts is probably superimposed and not a result of the intrinsic metamorphic history.

This work was sponsored by the South African Council for Scientific and Industrial Research, and is Contribution No. 56 in South Africa's contribution to the International Geodynamics Project. I thank T. N. Clifford, W. Schreyer, K. B. Thompson, H. J. Hill, R. J. P. Fyfe, J. M. Barton, and M. K. Watkeys for criticisms.

#### References

1. H. J. Hill, R. J. P. Fyfe, and K. B. Thompson, *J. metamorphic Geol.*, **1**, 197 (1983).
2. H. J. Hill, R. J. P. Fyfe, and K. B. Thompson, *J. metamorphic Geol.*, **1**, 207 (1983).
3. H. J. Hill, R. J. P. Fyfe, and K. B. Thompson, *J. metamorphic Geol.*, **1**, 217 (1983).
4. H. J. Hill, R. J. P. Fyfe, and K. B. Thompson, *J. metamorphic Geol.*, **1**, 227 (1983).
5. H. J. Hill, R. J. P. Fyfe, and K. B. Thompson, *J. metamorphic Geol.*, **1**, 237 (1983).
6. H. J. Hill, R. J. P. Fyfe, and K. B. Thompson, *J. metamorphic Geol.*, **1**, 247 (1983).
7. H. J. Hill, R. J. P. Fyfe, and K. B. Thompson, *J. metamorphic Geol.*, **1**, 257 (1983).
8. H. J. Hill, R. J. P. Fyfe, and K. B. Thompson, *J. metamorphic Geol.*, **1**, 267 (1983).
9. H. J. Hill, R. J. P. Fyfe, and K. B. Thompson, *J. metamorphic Geol.*, **1**, 277 (1983).
10. H. J. Hill, R. J. P. Fyfe, and K. B. Thompson, *J. metamorphic Geol.*, **1**, 287 (1983).
11. H. J. Hill, R. J. P. Fyfe, and K. B. Thompson, *J. metamorphic Geol.*, **1**, 297 (1983).
12. H. J. Hill, R. J. P. Fyfe, and K. B. Thompson, *J. metamorphic Geol.*, **1**, 307 (1983).
13. H. J. Hill, R. J. P. Fyfe, and K. B. Thompson, *J. metamorphic Geol.*, **1**, 317 (1983).
14. H. J. Hill, R. J. P. Fyfe, and K. B. Thompson, *J. metamorphic Geol.*, **1**, 327 (1983).
15. H. J. Hill, R. J. P. Fyfe, and K. B. Thompson, *J. metamorphic Geol.*, **1**, 337 (1983).
16. H. J. Hill, R. J. P. Fyfe, and K. B. Thompson, *J. metamorphic Geol.*, **1**, 347 (1983).
17. H. J. Hill, R. J. P. Fyfe, and K. B. Thompson, *J. metamorphic Geol.*, **1**, 357 (1983).
18. H. J. Hill, R. J. P. Fyfe, and K. B. Thompson, *J. metamorphic Geol.*, **1**, 367 (1983).
19. H. J. Hill, R. J. P. Fyfe, and K. B. Thompson, *J. metamorphic Geol.*, **1**, 377 (1983).
20. H. J. Hill, R. J. P. Fyfe, and K. B. Thompson, *J. metamorphic Geol.*, **1**, 387 (1983).
21. H. J. Hill, R. J. P. Fyfe, and K. B. Thompson, *J. metamorphic Geol.*, **1**, 397 (1983).
22. H. J. Hill, R. J. P. Fyfe, and K. B. Thompson, *J. metamorphic Geol.*, **1**, 407 (1983).
23. H. J. Hill, R. J. P. Fyfe, and K. B. Thompson, *J. metamorphic Geol.*, **1**, 417 (1983).
24. H. J. Hill, R. J. P. Fyfe, and K. B. Thompson, *J. metamorphic Geol.*, **1**, 427 (1983).
25. H. J. Hill, R. J. P. Fyfe, and K. B. Thompson, *J. metamorphic Geol.*, **1**, 437 (1983).



16. Burke, K. & Kidd, W. S. F. *Nature* 272, 240 (1978).  
 17. Wilson, R. L. *Geology* 6, 100 (1978).  
 18. Wilson, R. L. *Geology* 7, 100 (1979).  
 19. Wilson, R. L. *Geology* 8, 100 (1980).  
 20. Wilson, R. L. *Geology* 9, 100 (1981).

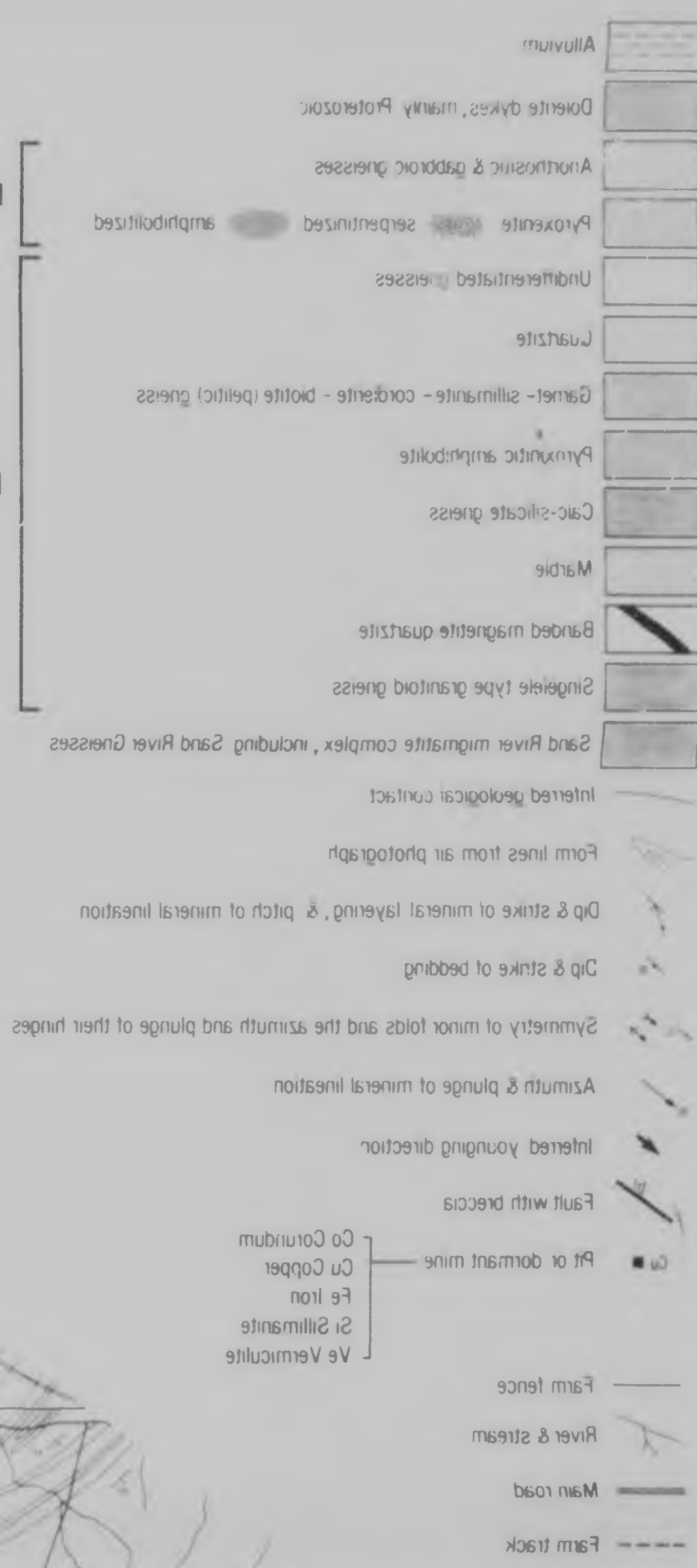
21. Burke, K. & Kidd, W. S. F. *Nature* 272, 240 (1978).  
 22. Drury, S. A. *Nature* 276, 720-721 (1978).  
 23. England, P. C. *Nature* 277, 556-558 (1979).  
 24. Bickle, M. J. *Earth planet. Sci. Lett.* 40, 301-322 (1978).  
 25. McCarthy, T. S. thesis, Univ. Witwatersrand (1978).  
 26. Barton, J. M. Jr. *Precamb. Res.* 9, 57-80 (1979).



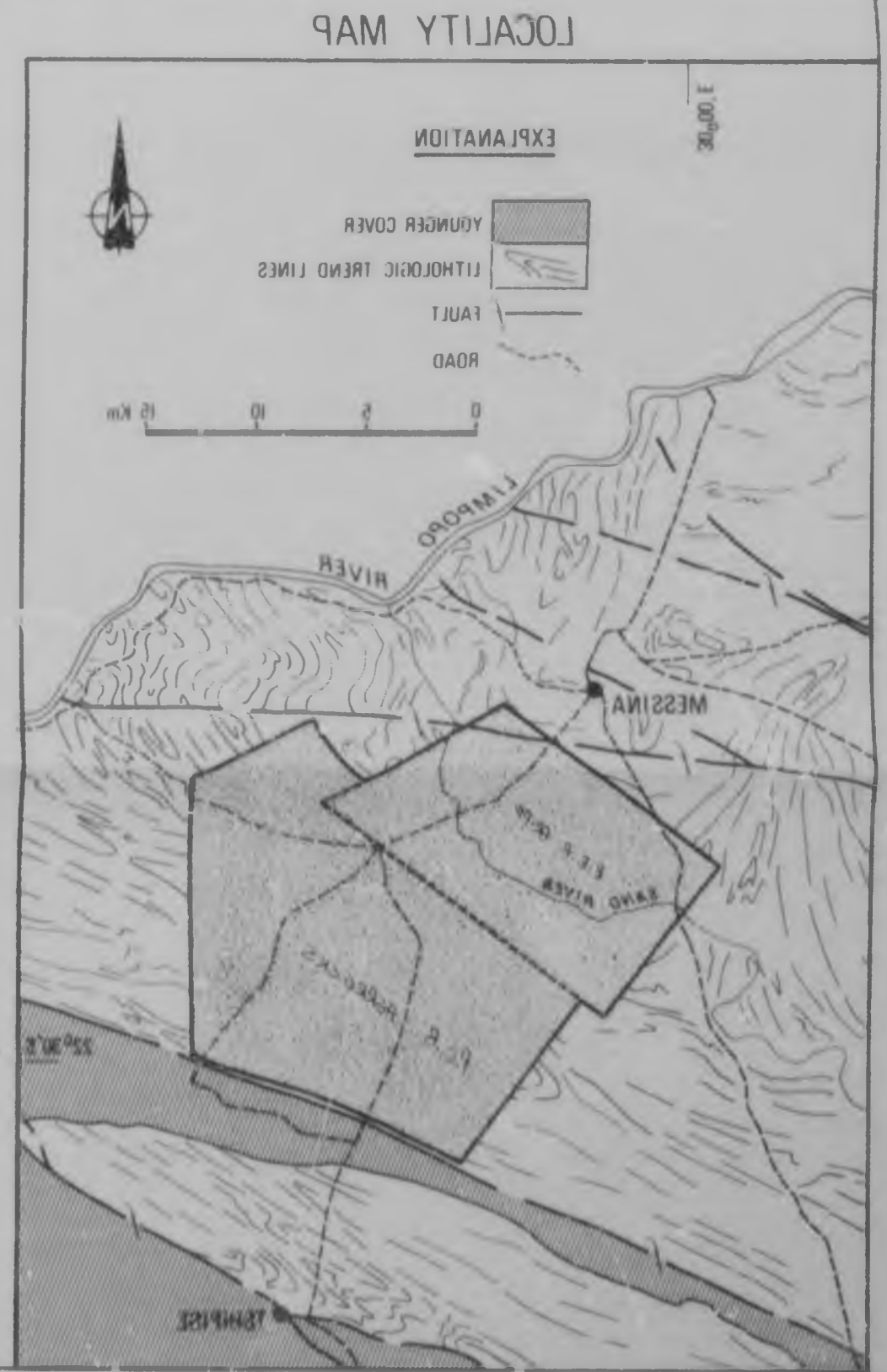


# THE PRECAMBRIAN GEOLOGY OF AN AREA BETWEEN MESSINA & TSHIPISE LIMPOPO BELT

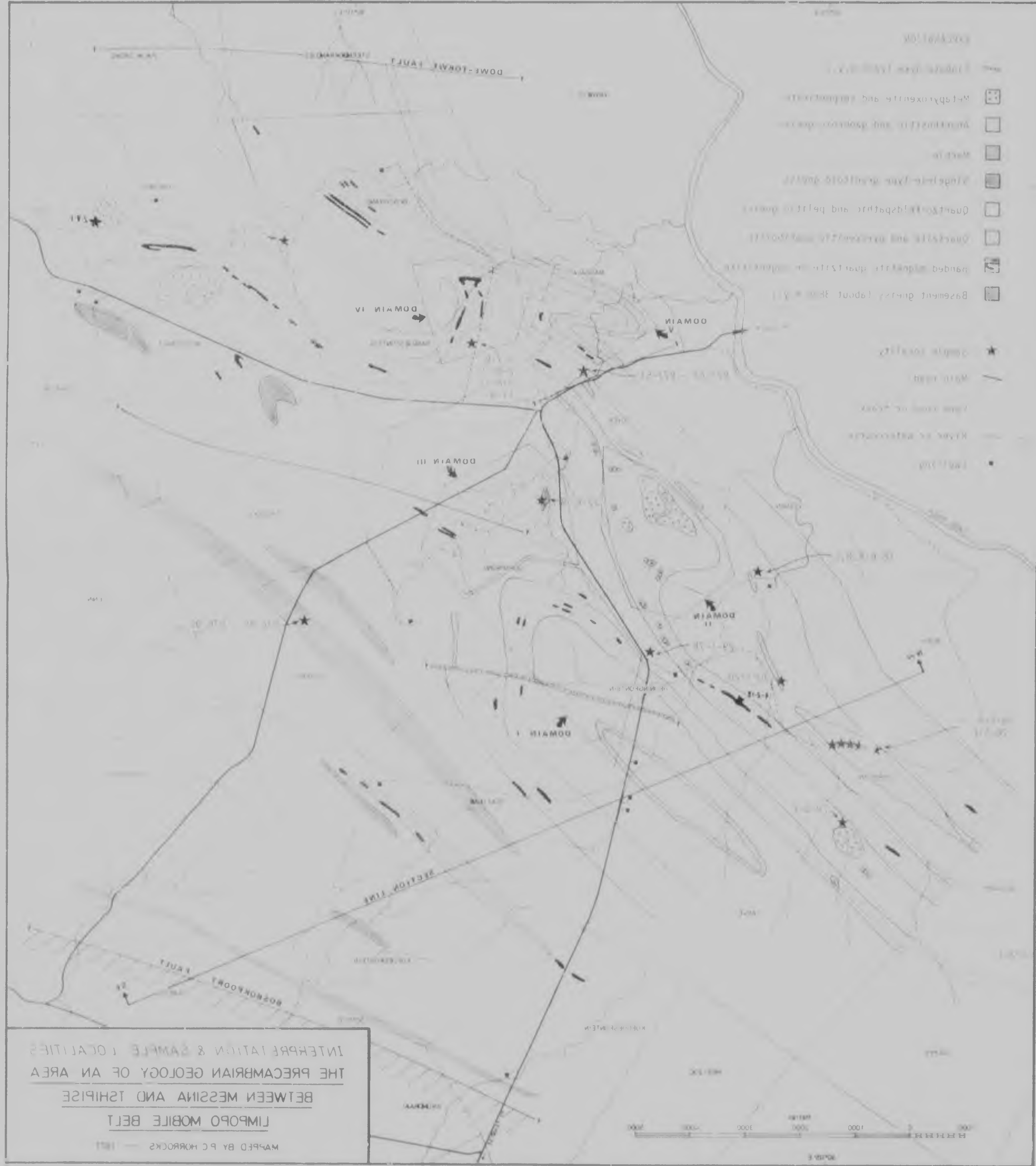
1 : 25 000  
 METERS 0 500 1000 1500 2000 2500 3000 3500 4000 METERS



Messina Layered Intrusion  
 Beit Bridge Complex







**Author** Horrocks P C B

**Name of thesis** The Precambrian Geology of an area between Messina and Tshipise Limpopo Mobile Belt 1981

***PUBLISHER:***

University of the Witwatersrand, Johannesburg

©2013

***LEGAL NOTICES:***

**Copyright Notice:** All materials on the University of the Witwatersrand, Johannesburg Library website are protected by South African copyright law and may not be distributed, transmitted, displayed, or otherwise published in any format, without the prior written permission of the copyright owner.

**Disclaimer and Terms of Use:** Provided that you maintain all copyright and other notices contained therein, you may download material (one machine readable copy and one print copy per page) for your personal and/or educational non-commercial use only.

The University of the Witwatersrand, Johannesburg, is not responsible for any errors or omissions and excludes any and all liability for any errors in or omissions from the information on the Library website.